

**Department of Chemical and Process Engineering**

*Investigation of the effects of flow on crystallisation process*

**Katarzyna Joanna Sypek**

Degree of Doctor of Philosophy

2011

## **Declaration of Authors Rights**

The copyright of this thesis belongs to the author under the terms of the United Kingdom Copyrights Act as qualified by the University of Strathclyde Regulation 3.50. Due acknowledgement must always be made of the use of any material contained in, or derived from, this thesis.

Signed:

Date:

## **Abstract**

It is well known that flow affects nucleation, as well as crystal growth, aggregation and breakage. The overall aim of this work was to investigate causes of the effects of flow on various aspects of the crystallisation process. Results presented in this thesis provide new insight into how flow influences the crystallisation process.

In the first part of the project we investigated the effects of flow conditions on polymorphic outcome of the cooling crystallisation of carbamazepine. It was observed that stirring is the controlling factor for the polymorphic outcome and that depending on the flow regime crystallisation can follow two different paths. For quiescent conditions, a few big crystals of the alpha form are formed from clear solution undergoing transformation into the stable beta form within few hours. Under sufficiently vigorous stirring, turbid suspensions of fine crystals were produced, sometimes preceded by the appearance of a few visible, macroscopically ordered, wire-like structures. A wide range of nucleation times was recorded. At the shortest induction times, numerous small needle-like alpha form crystals initially appeared, quickly transforming into beta form crystals under continuous stirring. For longer induction times, beta form was predominantly observed at the onset of turbidity. Crystal formation under stirring conditions was followed in situ using a novel experimental setup for simultaneous measurement of transmitted and scattered light intensity. Distinct pathways in intensity plots were observed for each respective polymorph.

In the second part of the project, we developed a laboratory based “shear-o-meter” setup to determine a range of flow conditions which can be used for a given crystal suspension in order to avoid crystal breakage. The aim was to investigate the size reduction phenomena that occur in slurries of high aspect ratio crystals passing through a well controlled elongational flow region. It was done by exposing certain volumes of crystal suspensions to controlled flows in the vessel and in a flow-through contraction in the peristaltic pump driven shear-o-meter setup. The breakage behaviour of tyrosine crystals slurries in water was characterised by

focused beam reflectance measurement (FBRM) method and the results shown were obtained from the software as well as calculated values of variously weighted average moments. It has been shown that these crystals are prone to limited breakage and the effect of used nozzle is greatest for biggest value of the entry angle of the nozzle and higher flow rate. The dependence of reduction of the average size of crystals on concentration clearly shows that more concentrated slurries of needle like crystals (like tyrosine) become less prone to breakage with increasing solid loading.

## **Acknowledgments**

I would like to wholeheartedly thank my supervisor Dr Jan Sefcik for the support and guidance he has given and for providing me with the opportunity to present my PhD thesis.

I would like to acknowledge the academic, administrative and technical support of the Department of Chemical and Process Engineering, who made my stay at Strathclyde pleasant and uncomplicated.

I want to thank Prof. Alastair Florence of the Strathclyde Institute of Pharmacy and Biomedical Sciences and the present and past members of his group for a warm welcome in their lab, providing a great working environment, and for their help and encouragement.

I particularly want to thank all friends at the Department of Chemical and Process Engineering for the scientific and often non-scientific support, all our lunches together and of course our after work activities.

I would like to thank my family for all their love and support, especially Colin for his understanding, endless patience and encouragement when it was most required.

Table of contents	i	
List of figures	vi	
List of tables	xiii	
List of abbreviations	xv	
<b>CHAPTER 1</b>		
<b>INTRODUCTION</b>	<b>1</b>	
<b>CHAPTER 2</b>		
<b>THEORERICAL BACKGROUND</b>	<b>3</b>	
2.1	Theory of crystallisation	3
2.1.1	States of matter and crystals	3
2.1.2	Crystalline structure and polymorphism	4
2.1.3	Thermodynamics and phase equilibria	8
2.1.3.1	Solubility (solid – liquid)	9
2.1.3.2	Solid forms and polymorphism (solid-solid)	11
2.1.3.3	Gibbs free energy	12
2.1.3.4	Supersaturation	14
2.1.4	Nucleation	15
2.2	Crystallisation process	19

---

2.2.1	Crystallisation setups	19
2.2.2	Kinetics ruling crystallisation	20
2.2.2.1	Induction time	21
2.2.2.2	MetaStable Zone Width (MSZW)	22
2.2.2.3	Ostwald's rule	23
2.2.3	Parameters affecting crystallisation process	24
2.2.3.1	Effect of solvent	26
2.2.3.2	Effect of seeding	27
2.2.3.3	Effect of flow	27
2.2.4	Crystal growth and crystal habit	29
2.2.5	Particle agglomeration and breakage	30
2.2.5.1	Particle agglomeration	31
2.2.5.2	Particle breakage	31
2.2.6	Post processing of slurries	37
2.2.7	Methods of characterisation of solid state	38
<b>CHAPTER 3</b>	<b>MATERIALS AND METHODS</b>	<b>42</b>
3.1	Materials	42
3.1.1	Tyrosine	42

---

3.1.2	Carbamazepine	43
3.2	Experimental methods	46
3.2.1	Microscopy	46
3.2.2	Focused beam reflectance measurement	47
3.2.3	Light scattering	51
3.2.3.1	Dynamic light scattering	52
3.2.3.2	Turbidity	55
3.2.4	XRD	57
3.3	Data presentation	60
3.3.1	Distributions	60
3.3.2	Weighted distributions and averages	63
3.3.3	Channel grouping	66
3.3.4	FBRM presentation	68
<b>CHAPTER 4</b>	<b>CRYSTALLISATION AND POLYMORPHISM OF CARBAMAZEPINE</b>	<b>70</b>
4.1	The effect of flow on polymorphic outcome of cooling crystallisation of carbamazepine	70
4.1.1	Experimental procedure	70
4.1.2	Effect of stirring	72

---

4.1.3	Effect of cooling rate, supersaturation and air-liquid interface	74
4.1.4	The effect of CBZ source and the transformation into stable form	82
4.1.5	Discussion	85
4.2	In situ monitoring of polymorphic transformation in cooling crystallisation of carbamazepine	89
4.2.1	Experimental procedure	89
4.2.2	Results	91
4.2.3	Discussion	96
<b>CHAPTER 5</b>	<b>BREAKAGE OF CRYSTALS IN FLOW</b>	97
5.1	Experimental procedure	97
5.2	Effect of stirring	101
5.3	Effects of solid loading and sampling	104
5.4	Effect of peristaltic pump	108
5.5	Comparison of effects of stirring, pumping and flow through contractions	111
5.5.1	Effect of stirring and flow on 2.7 wt% slurries	111
5.5.2	Effect of stirring and flow on 5.4 wt% slurries	115
5.5.3	Effect of stirring and flow on 9.0 wt% slurries	119
5.6	Discussion	123

---

<b>CHAPTER 6</b>	<b>CONCLUSIONS</b>	126
<b>CHAPTER 7</b>	<b>REFERENCES</b>	128
<b>CHAPTER 8</b>	<b>APPENDIX</b>	138
8.1	Additional data for crystallisation of CBZ	139
8.2	Dynamic light scattering experiments	145
8.3	Static light scattering experiments	153
8.4	ATR-UV monitoring of cooling crystallisation of CBZ ethanol solutions	157
8.5	Raman Spectroscopy of CBZ in ethanol	162
8.6	NIR of ethanol with different water content and CBZ solutions	165
8.7	Results of the effect of flow conditions on breakage of tyrosine	166
8.8	Viscosity of tyrosine in water slurries	185

---

**List of figures**

<b>2.1</b>	Phase diagram for single component system	3
<b>2.2</b>	Crystal unit cell	4
<b>2.3</b>	Schematic representations of polymorphs, amorphous state, solvate, co-crystal and salt	7
<b>2.4</b>	Gibbs free energy	12
<b>2.5</b>	Relation between Gibbs free energy for a) enantiotropy b) monotropy. $T_t$ is the transition temperature; $T_{mA}$ and $T_{mB}$ are melting temperatures for each form respectively. Liq- represents the liquid state	13
<b>2.6</b>	Critical radius of nuclei and the energy barrier for nucleation	16
<b>2.7</b>	Nucleation paths copied from Vekilov	17
<b>2.8</b>	Nucleation, induction and latent period in crystallisation	21
<b>2.9</b>	MetaStable Zone Width	22
<b>2.10</b>	Kinetics of polymorphs	24
<b>2.11</b>	Crystal habits: cube, tetrahedron, dodecahedron, octahedron	30
<b>2.12</b>	Collisional/impact stresses	32
<b>2.13</b>	Eddy size $\eta$ (Kolmogorov microscale) related to particle diameter $d$	33
<b>2.14</b>	Schematic representation of the entry flow in a 4:1 axisymmetric contraction with sudden re-entrant corner a) $Ws=0.65$ , b) $Ws=4.0$	35
<b>2.15</b>	Downstream processes in crystallisation	38
<b>3.1</b>	Tyrosine structure	42
<b>3.2</b>	L-Tyrosine crystals	43
<b>3.3</b>	Carbamazepine (CBZ) structure	43
<b>3.4</b>	Microscopic pictures of polymorphs of CBZ a) alpha form, b) beta form	44
<b>3.5</b>	Microscopic pictures of alpha form CBZ crystals and creation of beta form	47
<b>3.6</b>	Principles of FBRM	47
<b>3.7</b>	FBRM probe	48
<b>3.8</b>	Calculated CLDs for needles with $r = 20\mu\text{m}$ and 3 values of length: 50, 100 and $200\mu\text{m}$	49
<b>3.9</b>	Illustration of possible measured chords of needle like crystal	50
<b>3.10</b>	Scattering of small and large particles	51

---

<b>3.11</b>	Calculated normalized autocorrelation function decays a) for 3 different values of diameter at the same temperature b) showing the effect of temperature on the same size (100nm)	54
<b>3.12</b>	Principles of XRD	58
<b>3.13</b>	XRD patterns of three polymorphs of CBZ	59
<b>3.14</b>	Cumulative a) and b) and differential c) and d) frequency particle size distribution	62
<b>3.15</b>	Particle size distribution averages	63
<b>3.16</b>	Representation of channel weighting in FBRM. 0-number weighted, 1-length weighted, 2-square weighted	64
<b>3.17</b>	Distributions in light scattering experiments	65
<b>3.18</b>	Linear vs. logarithmic coordinates	66
<b>3.19</b>	Linear a) semilogarithmic b) differential frequency c) and cumulative frequency d) data presentation of the same set of data	67
<b>3.20</b>	Influence of changed width on presentation of count numbers	68
<b>3.21</b>	Example of fitting functions for obtained PSD data	69
<b>4.1</b>	Schematic diagram illustrating range of experimental conditions investigated. CBZ solubility in EtOH is also shown	71
<b>4.2</b>	XRD reference patterns of CBZ beta form (commercial) and alpha form (prepared in house)	72
<b>4.3</b>	Microscopic images of carbamazepine crystals produced under quiescent and stirring conditions. a) Quiescent: large alpha form crystals slowly appear; b) Quiescent: alpha form crystals are gradually turning into few large beta form; c) Stirring: small beta form crystals appear initially at shorter induction times	73
<b>4.4</b>	Microscopic images of structures observed before the onset of turbidity during cooling crystallisation under stirring conditions a), b), and image of fine beta form crystals in turbid suspensions after induction time c).	74
<b>4.5</b>	Cooling profiles measured in bottles under stirring conditions	75
<b>4.6</b>	Pictures of stirred bottles with vortexes corresponding to various stirring speed for partially filled bottles	76
<b>4.7</b>	Cooling profile for a) partially filled (3.3ml) and b) full (5.1ml) bottle	77
<b>4.8</b>	Induction times for a) 3.2g and b) 3.5g <sub>CBZ</sub> /100ml <sub>EtOH</sub> for three stirring speeds (Low, Medium or High) and for two volumes: full and partially filled bottle	78

---

<b>4.9</b>	Induction time plot. Open symbols for alpha form observed initially, closed symbols for beta form. Circles indicate stirring conditions, triangles correspond to quiescent conditions	81
<b>4.10</b>	Transformation in turbid solution (obtained within 7-30 mins from the start) from alpha form to stable beta form (microscopic images of samples withdrawn from turbid suspensions)	82
<b>4.11</b>	Transformation of turbid alpha solution into beta with characteristic for each form peaks	83
<b>4.12</b>	Distribution of induction times for 3.5g <sub>CBZ</sub> /100ml <sub>EtOH</sub> solutions using two sources of CBZ: commercial and recrystallised in house	83
<b>4.13</b>	Seeds used in experiments a) alpha and b) beta	84
<b>4.14</b>	Turbidity pictures when using seeds at a) 17°C and b) 21° C	84
<b>4.15</b>	Observed pathways of CBZ crystallisation	87
<b>4.16</b>	Proposed possible pathways in development of turbidity depending on the source of carbamazepine	88
<b>4.17</b>	Schematic drawing of the experimental setup	90
<b>4.18</b>	Measured cooling profile for studied samples used for situ monitoring experiments	91
<b>4.19</b>	Typical turbidity measurements results of CBZ solutions and EtOH	92
<b>4.20</b>	Repetition of measurements of a) attenuation coefficient and b) scattering intensity for solutions prepared from commercial CBZ powder (COM 1-3) and recrystallised powder (REC1-5)	93
<b>4.21</b>	Attenuation coefficient vs. scattering intensity	94
<b>4.22</b>	Pictures of crystallising solutions a) at the start of stirring b) at the onset of turbidity c) further development of turbidity d) high turbidity e) maximum turbidity	95
<b>4.23</b>	Pictures of crystallising solutions a) at the start (0.12cm <sup>-1</sup> for 13.4% light transmitted) b) at the onset of turbidity (0.5cm <sup>-1</sup> for 45.1% light transmitted) c) high turbidity (6cm <sup>-1</sup> for 99.9% light transmitted)	96
<b>5.1</b>	Diagram of experimental setup used for crystal breakage studies. Mechanical (PTFE) stirrer used for experiments	98
<b>5.2</b>	Picture of the actual setup showing peristaltic pump, test flask with FBRM probe, mechanical stirrer, and tubing for recirculating crystal slurries with contraction nozzle	98
<b>5.3</b>	Design of contraction nozzles used in experiments with indication of the flow direction, entry angles and diameters	99
<b>5.4</b>	Effect of stirring speed on measured CLD of tyrosine in water slurry at 9wt% shown on a) linear and b) logarithmic scale	101

---

<b>5.5</b>	Average sizes for stirring of 9wt% of tyrosine in water at 700rpm	102
<b>5.6</b>	The effect of stirring at 700rpm on 2.7wt% tyrosine in water shown on a) linear and b) logarithmic scale	103
<b>5.7</b>	Average sizes for stirring of 2.7wt% of tyrosine in water at 700rpm	104
<b>5.8</b>	The effect of solid loading on measured CLD a) and corresponding moments b)	105
<b>5.9</b>	Schematic explanation of representative sample test	106
<b>5.10</b>	The measured CLD for sample test a) and corresponding calculated average sizes b)	107
<b>5.11</b>	The effect of pumping at 400rpm of 2.7wt% of tyrosine in water on a) linear and b) logarithmic	108
<b>5.12</b>	Average sizes for pumping of 2.7wt% of tyrosine in water at 400 rpm pumping power	109
<b>5.13</b>	Average sizes for pumping of 9.0wt% of tyrosine in water	110
<b>5.14</b>	The effect of stirring and 400rpm pumping power on 2.7 wt% of tyrosine in water on a) linear and b) logarithmic scale	111
<b>5.15</b>	Average sizes for 2.7 wt% of tyrosine in water tests at 400rpm pumping power	112
<b>5.16</b>	The effect of stirring and 200rpm pumping power on 2.7 wt% of tyrosine on a) linear and b) logarithmic scale	113
<b>5.17</b>	Average sizes for 2.7 wt% of tyrosine in water pumping tests at 200rpm pumping power	114
<b>5.18</b>	The effect of stirring and 400rpm pumping power of 5.4wt% of tyrosine on a) linear and b) logarithmic scale	115
<b>5.19</b>	Average sizes for 5.4 wt% of tyrosine in water pumping tests	116
<b>5.20</b>	The effect of stirring and 200rpm pumping power of 5.4wt% of tyrosine in water on a) linear and b) logarithmic scale	117
<b>5.21</b>	Average sizes for 5.4wt% of tyrosine in water tests at 200rpm pumping power	118
<b>5.22</b>	The effect of stirring and 400rpm pumping power on 9.0wt% of tyrosine on a) linear and b) logarithmic scale	119
<b>5.23</b>	Average sizes for 9.0 wt% of tyrosine in water tests at 400rpm pumping power	120
<b>5.24</b>	The effect of stirring and 200rpm pumping power of 9.0wt% of tyrosine in water on a) linear and b) logarithmic scale	121
<b>5.25</b>	Average sizes for 9.0 wt% tests of tyrosine with 200rpm pumping power	122

---

<b>5.26</b>	Schematic effects of flow on breakage with angle indicating real angles 180, 118 and 10 deg and indication of pumping power with one arrow as 200rpm and 400rpm as two arrows	123
<b>8.1</b>	Pictures show amorphous and dihydrate forms observed in crystallising solutions	139
<b>8.2</b>	Solubility of CBZ in ethanol and corresponding saturation temperatures for solution concentrations used in DLS experiments	146
<b>8.3</b>	Autocorrelation function for 4.2g CBZ/100ml EtOH solution	147
<b>8.4</b>	Autocorrelation function for 3.5g CBZ/100ml EtOH solution	148
<b>8.5</b>	Autocorrelation function for 3.1g CBZ/100ml EtOH solution	148
<b>8.6</b>	Autocorrelation function for 3.0g CBZ/100ml EtOH solution	149
<b>8.7</b>	Autocorrelation function for 2.8g CBZ/100ml EtOH solution	149
<b>8.8</b>	Autocorrelation functions of pure EtOH	150
<b>8.9</b>	Autocorrelation function of cooling of highly undersaturated solution of carbamazepine in ethanol	150
<b>8.10</b>	SLS intensities for 3.5gCBZ/100ml EtOH commercial and recrystallised solutions and pure ethanol at 45°C	154
<b>8.11</b>	SLS intensities for 3.5gCBZ/100ml EtOH commercial and recrystallised solutions and pure ethanol at 25°C	154
<b>8.12</b>	SLS data for 3.5g/100ml at 45°C	155
<b>8.13</b>	SLS data for 3.5g/100ml at 35°C	156
<b>8.14</b>	SLS data for 3.5g/100ml at 25°C	156
<b>8.15</b>	ATR crystal used in ATR-UV	157
<b>8.16</b>	UV spectrum of CBZ	158
<b>8.17</b>	Calibration of ATR UV probe. This test shows cooling of highly concentrated CBZ solution heated up to 70° and cooled down with different stirring speed: 600rpm, 200rpm and no stirring	159
<b>8.18</b>	UV results of 6.12gCBZ/100ml EtOH test	159
<b>8.19</b>	UV results of 8.27gCBZ/100ml EtOH test	160
<b>8.20</b>	UV results of 3.5gCBZ/100ml EtOH test	160
<b>8.21</b>	UV results of 2.0gCBZ/100ml EtOH test	161
<b>8.22</b>	Raman spectra of EtOH and CBZ solutions	162
<b>8.23</b>	Raman spectra of EtOH and CBZ solutions – zoomed peak	163
<b>8.24</b>	Calibration of Raman shift for CBZ in EtOH solutions	163
<b>8.25</b>	Results of centrifugation of 4.8g/100ml CBZ in EtOH solution	164
<b>8.26</b>	NIR spectra of EtOH and CBZ solutions	165

---

<b>8.27</b>	NIR spectra of EtOH and CBZ solutions –zoomed peak	165
<b>8.28</b>	Effects of concentrations on logarithmic scale	166
<b>8.29</b>	Comparison of results presented on logarithmic scale for stirring in 3 flasks	167
<b>8.30</b>	Fitting functions for RS test	168
<b>8.31</b>	Change in average sizes for weighted functions of stirring of 2.7 wt% of tyrosine at 700rpm	168
<b>8.32</b>	Fitting functions for stirring of 2.7 wt% of tyrosine	169
<b>8.33</b>	Stirring of 5.4 wt% tyrosine at 700rpm plotted on linear and logarithmic scale	169
<b>8.34</b>	Change in average sizes for weighted functions of stirring of 5.4 wt% of tyrosine at 700rpm	169
<b>8.35</b>	Fitting functions for stirring of 5.4 wt% of tyrosine	170
<b>8.36</b>	Stirring of 9.0 wt% tyrosine at 700rpm linear and logarithmic scale	170
<b>8.37</b>	Change in average sizes for weighted functions of stirring of 9.0wt% of tyrosine at 700rpm	171
<b>8.38</b>	Fitting functions for stirring of 9.0 wt% of tyrosine	171
<b>8.39</b>	Pumping of 2.7 wt% of tyrosine at 200rpm plotted on linear and logarithmic scale	172
<b>8.40</b>	Change in sizes for weighted functions of pumping of 2.7wt% of tyrosine at 200rpm	172
<b>8.41</b>	Fitting functions for pumping of 2.7 wt% of tyrosine at 200rpm	173
<b>8.42</b>	Pumping of 2.7 wt% of tyrosine at 200rpm plotted on linear and logarithmic scale	173
<b>8.43</b>	Change in average for weighted functions for pumping of 2.7 wt% of tyrosine	173
<b>8.44</b>	Fitting functions for pumping of 2.7 wt% of tyrosine at 400rpm	174
<b>8.45</b>	Pumping of 5.4 wt% of tyrosine at 200rpm plotted on linear and logarithmic scale	174
<b>8.46</b>	Change in average sizes for functions of pumping of 5.4 wt% at 200rpm of tyrosine	175
<b>8.47</b>	Fitting functions for pumping of 5.4 wt% of tyrosine at 200rpm	175

---

<b>8.48</b>	Pumping of 5.4 wt% of tyrosine at 400rpm plotted on linear and logarithmic scale	176
<b>8.49</b>	Change in average sizes for functions of pumping of 5.4 wt% of tyrosine at 400rpm	176
<b>8.50</b>	Fit for change in average sizes for of pumping of 5.4 wt% of tyrosine at 400rpm	177
<b>8.51</b>	Pumping of 9.0 wt% of tyrosine at 200rpm plotted on liner and logarithmic scale	177
<b>8.52</b>	Change in average sizes for functions of pumping of 9.0 wt% of tyrosine at 200rpm	177
<b>8.53</b>	Fitting functions for pumping of 9.0 wt% of tyrosine at 200rpm	178
<b>8.54</b>	Pumping of 9.0 wt% of tyrosine at 400rpm plotted on linear and logarithmic scale	178
<b>8.55</b>	Change in average sizes for functions of pumping of 9.0 wt% of tyrosine at 400rpm	179
<b>8.56</b>	Fitting functions for pumping of 9.0 wt% of tyrosine at 400rpm	179
<b>8.57</b>	Fitting functions for 2.7wt% for different nozzles at 400rpm	180
<b>8.58</b>	Fitting for comparison of end values for 2.7 wt% of tyrosine at 200rpm	181
<b>8.59</b>	Fitting for comparison of end values for 5.4 wt% at 400rpm	182
<b>8.60</b>	Fitting for comparison of end values for 5.4 wt% at 200rpm	183
<b>8.61</b>	Fitting for comparison of end values for 9.0 wt% at 400rpm	184
<b>8.62</b>	Fitting for comparison of end values for 9.0 wt% at 200rpm	184
<b>8.63</b>	Viscosity of tyrosine for 250 $\mu$ m gap in the 1-1000 [1/s] shear rate range	185
<b>8.64</b>	Viscosity of tyrosine for 250 $\mu$ m gap in the 10-100 [1/s] shear rate range	185
<b>8.65</b>	Viscosity of tyrosine for 500 $\mu$ m gap in the 1-1000 [1/s] shear rate range	186

**List of tables**

<b>2.1</b>	Possible Bravais lattices in 7 crystal systems	5
<b>2.2</b>	Properties of polymorphs that can vary between polymorphs	8
<b>2.3</b>	Methods of sizing of solid state materials	39
<b>2.4</b>	Classification of methods of analysis of polymorphs (solid state materials)	41
<b>3.1</b>	Density of CBZ polymorphs	44
<b>3.2</b>	Calculated parameters for fitted experimental results	69
<b>4.1</b>	Number of experiments, Average value and Standard deviation of induction time (in minutes) for 3.2g <sub>CBZ</sub> /100ml <sub>EtOH</sub>	79
<b>4.2</b>	Number of experiments, Average value and Standard deviation of induction times (in minutes) for 3.5g <sub>CBZ</sub> /100ml <sub>EtOH</sub>	80
<b>8.1</b>	Induction times for cooling crystallisation with stirring	141
<b>8.2</b>	List of experimental conditions used for DLS experiments	146
<b>8.3</b>	Calculated values for apparent hydrodynamic diameter big clusters structures present in solutions for square fitting of autocorrelation functions	151
<b>8.4</b>	FBRM average size for different concentrations	167
<b>8.5</b>	Average sizes for RS test	167
<b>8.6</b>	Percentage changes in average sizes of stirring of 2.7 wt% of tyrosine at 700rpm	168
<b>8.7</b>	Percentage changes in average sizes of stirring of 5.4 wt% of tyrosine at 700rpm	170
<b>8.8</b>	Percentage changes in average of stirring of 9.0 wt% of tyrosine at 700rpm	171
<b>8.9</b>	Changes in average sizes for pumping of 2.7 wt% of tyrosine at 200rpm	172
<b>8.10</b>	Changes in average sizes for pumping of 2.7 wt% of tyrosine at 400rpm	174
<b>8.11</b>	Changes in average sizes of pumping of 5.4 wt% of tyrosine at 200rpm	175
<b>8.12</b>	Changes in average sizes of pumping of 5.4 wt% of tyrosine at 400rpm	176
<b>8.13</b>	Changes in average sizes of pumping of 9.0 wt% of tyrosine at 200rpm	178
<b>8.14</b>	Changes in average sizes of pumping of 9.0 wt% of tyrosine at 400rpm	179
<b>8.15</b>	Average sizes for 2.7 wt% tests at 400rpm	180
<b>8.16</b>	Average sizes for 2.7 wt% tests at 200rpm	181
<b>8.17</b>	Average sizes for 5.4 wt% tests at 400rpm	181

<b>8.18</b>	Average sizes for 5.4wt% tests at 200rpm	182
<b>8.19</b>	Average sizes for 9.0wt% tests at 400rpm	183
<b>8.20</b>	Average sizes for 9.0wt% tests at 200rpm	184

**List of abbreviations**

<b>FBRM</b>	Focused Beam Reflectance Measurement
<b>SCF</b>	Supercritical fluids
<b>CBZ</b>	Carbamazepine
<b>API</b>	Active Pharmaceutical Ingredient
<b>MSZW</b>	MetaStable Zone Width
<b>MSMPR</b>	Mixed Suspension and Mixed Product Removal
<b>PAT</b>	Process Analytical Technology
<b>DLS</b>	Dynamic Light Scattering
<b>SLS</b>	Static Light Scattering
<b>ATR</b>	Attenuated Total Reflectance
<b>UV</b>	Ultraviolet
<b>VIS</b>	Visible
<b>FTIR</b>	Fourier Transform Infra Red
<b>NIR</b>	Near Infra Red
<b>SSA</b>	Solid State Analysis
<b>XRD</b>	X-Ray Diffraction
<b>DSC</b>	Differential Scanning Calorimetry
<b>TGA</b>	Thermo Gravimetric Analysis
<b>NMR</b>	Nuclear Magnetic Resonance
<b>SEM</b>	Scanning Electron Microscopy
<b>HPLC</b>	High Performance Liquid Chromatography
<b>CLD</b>	Chord Length Distribution

## CHAPTER 1 INTRODUCTION

Crystallisation is one of the major unit processes in industrial particle technology used for purification, separation and for particle formation. It is a process of creation of highly ordered molecular solids with well defined structure from randomly organized solutions under specific crystallisation conditions.

There are documented records of evaporation of naturally occurring solutions of sea salt thought to be the oldest and amongst the most important chemical engineering processes [1, 2]. A Chinese print dated to 2700 B.C. shows a process of artificial evaporation and crystallisation of salt. The most characteristic feature of crystals which is an angle between two corresponding facets has been studied on quartz crystals by Dutch physician Nicholas Steno in 1669.

A large number of solid materials surrounding us are crystalline: salt, sugar, diamonds, snowflakes, and a lot of commonly used solid drugs like aspirin, paracetamol etc. Applications that are the best established include precipitation of fine and bulk chemicals, detergents, fertilizers, dyestuffs, catalysts, pharmaceuticals. More recent uses include electronic micro-scale devices, healthcare products, etc. [3-5]. The tonnage and variety of crystal products is massive and crystallisation as a process has been studied and developed from the beginning of human civilization. However with the increase in demand for the production of highly advanced crystalline product it is still an ongoing challenge for chemists and engineers.

Crystallisation is a complex process and it is affected by many factors unique for each individual process. The deep understanding of each step of the process helps to fully control it, the subsequent downstream unit operations and the resulting product. The aim of the work was the study of crystallisation process parameters leading to a better understanding and control of the process at each stage.

This work studies the effect of flow on the crystallisation process mainly focusing on two important steps namely the nucleation (on the example of cooling crystallisation of carbamazepine from ethanol) and the breakage of crystals in slurries (on the example of tyrosine slurries in water).

Following this Introduction, the thesis structure consists of seven chapters as follows.

Chapter 2 contains literature reviews of relevant crystallisation topics. The reader is also referred to appropriate references for further details on respective topics.

Chapter 3 describes methods and materials used as well as key characterization methods for relevant processes and products.

In Chapter 4 the effect of the flow on polymorphic outcome is studied on the example of cooling crystallisation of carbamazepine from ethanol. Second part of this section focuses on the in-situ measurement of transmittance and light scattering during crystallisation and polymorphic transformation under stirring conditions.

Chapter 5 is focused on breakage of crystals in the contraction flow for slurries of tyrosine in water.

In Chapter 6 overall conclusions are presented and recommendations for future work are given.

Chapter 7 shows the list of references used in the work and recommended for further studies.

Chapter 8 is an extensive appendix showing additional data collected in the course of this project.

## CHAPTER 2 THEORETICAL BACKGROUND

### 2.1.1 States of matter and crystals

State of matter can be generally classified into one of four categories based on molecular arrangement, distance between particles, and energy of the particles at given temperatures and pressures. In gases the distances between particles are relatively large and molecular movements are independent of each other. Gases do not have free surface and therefore neither specified volume nor shape. Plasma is an ionized gas; however in comparison to ordinary gases it is a very good conductor of electricity and is affected by magnetic fields. In liquids distances between particles are smaller; interactions among particles are stronger and they do not move independently of each other. Therefore at given temperature and pressure the volume is fixed but shape is indefinite and free surface can be defined. Finally in solids distances between particles are smallest and particles are not free to move around from their equilibrium positions; therefore solids have definite shape and volume. They are not easily compressible because there is little free space between particles. Depending on temperature and pressure pure substances can undergo phase transition between these phases and corresponding processes are called: sublimation, vaporization and fusion [see Figure 2.1]. These phase transitions occur spontaneously always in the direction of lower free energy and increase of total entropy at transition temperatures. They are discussed in detail in physicochemical [6] and crystallisation books [3].

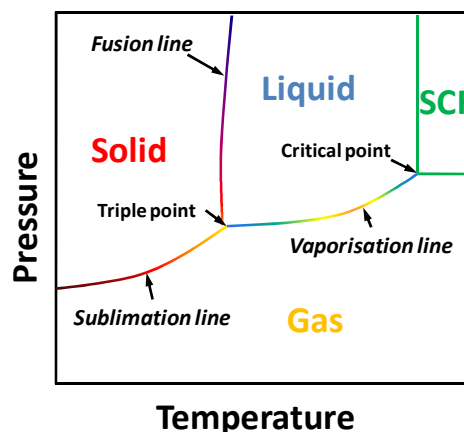


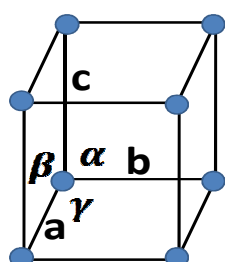
**Figure 2.1** Phase diagram for single component system.

This work focuses on transition from liquid solutions to solid crystalline state where constituent ions, atoms and molecules are regularly packed and located in the characteristic long range three dimensional order [7] for each structure. The process of formation of crystals is called crystallisation. Microcrystalline substance is made of small crystals visible only through a microscope (grains in micrometer range) with the most common including: microcrystalline silicon, microcrystalline cellulose and zeolites.

As a result of crystallisation process solid state materials obtained usually possess anisotropic properties, which means their characteristics (dissolution rate, refractive index, thermal expansion coefficient, electrical conductivity) as well as mechanical properties are directionally dependent. If molecules do not exhibit long range order in their arrangements, when no repeating unit cell can be distinguished, they are amorphous phase solid characterized by higher free energy and therefore greater reactivity in comparison to their crystalline counterparts. Despite the very low stability of amorphous state materials, occasionally their characteristic properties render them of the highest interest amongst all possible structures (glass silica).

### 2.1.2 Crystalline structure and polymorphism

The smallest building constituent of crystal is called a unit cell. It is defined by unique characteristics for each chemical compounds length of crystal axes and specific angles between them which create a crystal lattice in a 3D space.



$\alpha$  – between b and c

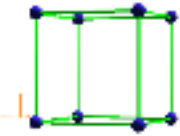
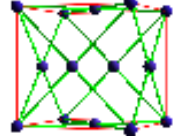
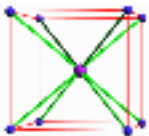
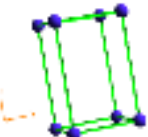
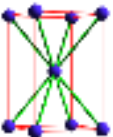
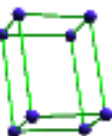
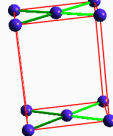
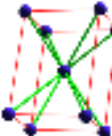
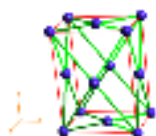
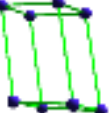
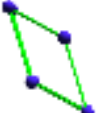
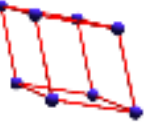
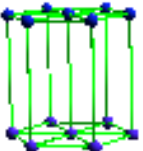
$\beta$  – between a and c

$\gamma$  – between a and b

**Figure 2.2** Crystal unit cell

Each point in the unit cell can represent an asymmetric unit, the atom for atomic or elemental crystal, while in organic structures it is usually a group of atoms. A pattern formed by specific locations in the asymmetric units creates an abstract scaffolding

of crystal structure called space lattice. A structure of crystal is the array of atoms obtained by associating an asymmetric unit cell with each lattice point. The most commonly used classification of crystal structures is based on differences in unit cell symmetry in three dimensional spaces and consists of 14 possible Bravais lattices in 7 crystal systems (crystal classes).

<b>Cubic</b> $a = b = c$ $\alpha = \beta = \gamma = 90^\circ$	  
<b>Tetragonal</b> $a = b \neq c$ $\alpha = \beta = \gamma = 90^\circ$	 
<b>Orthorhombic</b> $a \neq b \neq c$ $\alpha = \beta = \gamma = 90^\circ$	   
<b>Monoclinic</b> $a \neq b \neq c$ $\alpha = \gamma = 90^\circ \neq \beta$	 
<b>Triclinic</b> $a \neq b \neq c$ $\alpha \neq \beta \neq \gamma$	
<b>Trigonal</b> $a = b = c$ $\alpha = \beta = \gamma < 120^\circ, \neq 90^\circ$	
<b>Hexagonal</b> $a = b \neq c$ $\alpha = \beta = 90^\circ, \gamma = 120^\circ$	

**Table 2.1** Possible Bravais lattices in 7 crystal systems [8].

Polymorphism is defined as the ability of one pure chemical compound to exist in two or more crystalline forms differing by arrangements and/or conformations of molecules in the crystal lattice. Two types of polymorphism can be distinguished: packing polymorphism where molecules are packed into different rigid structures and conformational polymorphism where the structure of the same molecule is built from different conformers [9].

A special case of polymorphism related to pure elements is called allotropy and carbon in forms of either graphite or diamond is the simplest example (amorphous carbon is very popular too). Recent publications show other forms of carbon like carbon nanotubes and graphene [10, 11].

Sometimes solvent molecules incorporate into crystal lattice and these are solvates sometimes called pseudopolymorphs, moreover when the solvent is water the obtained crystals are called hydrates [12].

It is possible to co-crystallise two molecular compounds together and resulting co-crystals can possess many interesting features from a pharmaceutical and crystallographic point of view [13]. There is some confusion in literature regarding clear definitions of solvates and co-crystals, but it is seen as appropriate [14] to call compounds co-crystals when all ingredients separately exist in a solid state at room temperature. In both cases chemical structures are usually held together with hydrogen bonds or other directional noncovalent interactions. Co-crystal compounds can benefit from physical and chemical properties of both components and therefore exhibit huge ability to modifications of properties in the resulting crystals [15]. In salts proton is transferred from the acid to the basic functionality of the crystal partner, as the pKa difference between the partners is sufficiently large [16].

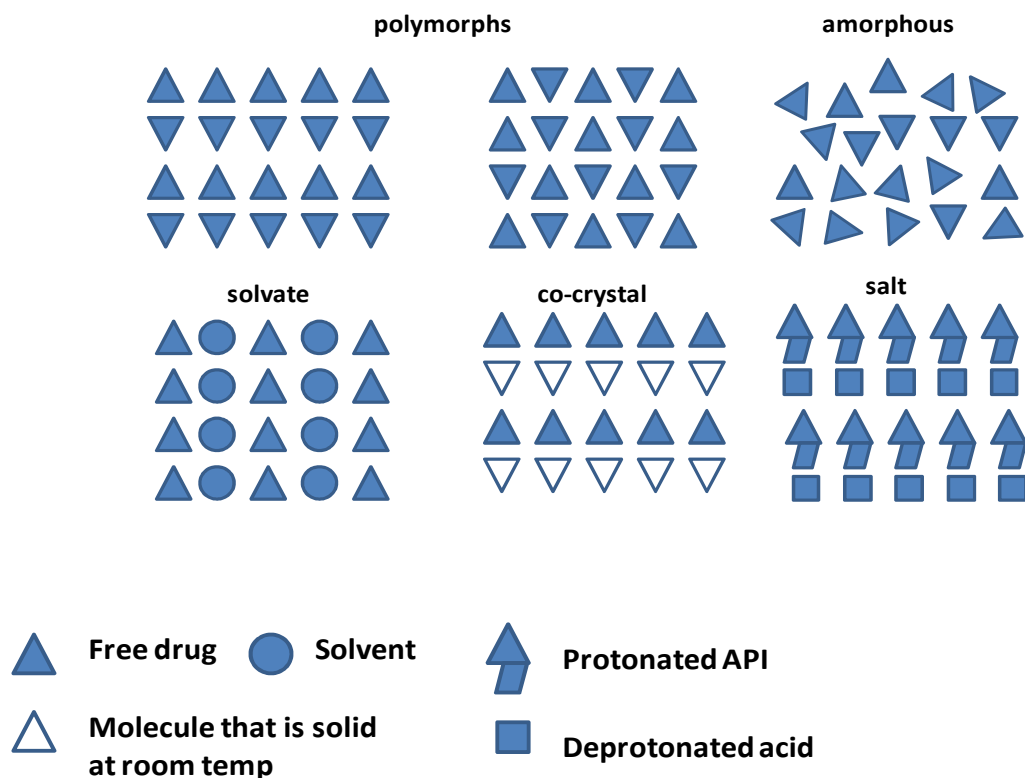


**Figure 2.3** Schematic representations of polymorphs, amorphous state, solvate, co-crystal and salt.

According to Cambridge Structural Database fewer than 5% of organic compounds exhibit polymorphism, however as many as approximately 30% of pharmaceutical solids do. New forms are being discovered constantly and citing the popular McCrone's Law [17] "the number of identified polymorphic forms is proportionally relative to time and money spent on research on the compound".

Differences in molecular packing of polymorphs trigger differences in the variety of physiochemical behaviour and properties [18] [19]. These lead to dissimilarities in solubility, dissolution rate [20] [21] and also regularly in morphology. All these properties affect bioavailability and stability.

The table below shows differences between polymorphs and corresponding features characteristic for each property.

<b>Type of property</b>	<b>Affected characteristic/ feature</b>
Packing properties	Molar volume/density, Refractive index Conductivity, Hygroscopicity
Thermodynamic properties	Melt/sublimation temperature; Enthalpy; Heat capacity; Entropy; Free energy; Thermodynamic activity; Vapour pressure; Solubility
Spectroscopic properties	Electronic transitions, Vibrational transitions, Rotational transitions, Nuclear spin transitions
Kinetic properties	Dissolution rate, Solid state reaction rate, Stability
Surface properties	Surface free energy; Interfacial tensions, Habit (shape)
Mechanical properties	Hardness; Tensile strength; Compactibility / tableting; Handling; Flowability, blending

**Table 2.2** Properties of polymorphs that can vary between polymorphs.

### 2.1.3 Thermodynamics and phase equilibria

A relative stability of phases (solid – liquid, gas – solid and solid – solid) and thermodynamic changes between them are the key challenge when discussing crystallisation process. Referring to the thermodynamics of a crystallising system free energies and the energy relationship between components and phases, as well as basic factors like temperature, pressure and concentration must be considered. Some of the main issues will be discussed below, although deeper analysis and discussions can be found in literature [6, 18, 22].

#### 2.1.4 Solubility (solid –liquid)

Crystallisation from solution is the most commonly used method of obtaining crystalline product in industry. Solubility is a concentration of solute dissolved in solvent resulting in homogeneous solution in equilibrium with given solid state of solute. Therefore it is the maximum concentration of a substance that can be reached in the solution without obtaining more than one phase. In order for dissolution to occur spontaneously the solvation free energy released upon the dissolution must overcome the lattice free energy and the disruptive forces must exceed the attractive forces of solid. It is an outcome resulting from two opposing effects: energy bonding ions, atoms or molecules within a solution against the tendency to create much stronger bonds during crystallisation. On the other hand for a substance to dissolve in a liquid it must be able to disrupt the local structure of a solvent in order to bond to solvent molecules or ions. Solubility depends on the nature of solvent and solute, and is a function of pressure and temperature.

The effect of temperature on solubility is rather complex. For most solids in water solubility usually increases with temperature, although it sometimes decreases for ionic solutes because of the polarity of water. In general like dissolves like e.g. polar dissolves polar and nonpolar will dissolve nonpolar compounds. Gases are more soluble in water with a decrease of temperatures (a lot of oxygen in cold water – better for fish) but less soluble with a decrease of temperature for organic solvents. When choosing suitable solvent its purity, safety hazardous properties as well as physical characteristics: colour, odour are crucial factors. Other important factors in industrial crystallisation are the solvent power and the temperature coefficient [3]. The former one expresses the solubility at a given temperature, thus deciding about the volume of crystallisation in the cooling process, and the latter determines the crystallisation yield.

The most commonly used solvent for inorganic crystallisation is water and it is preferentially chosen in organic crystallisation if possible. However the selection of the best solvent is often complicated, requiring consideration of many factors and it is crucial for antisolvent crystallisation and in cases of possible formation of solvates.

The role of solvent in the crystallisation process especially in the control for polymorphs is rather complex and is further discussed in some detail in section 2.2.3.1.

Polymorphs and solvates have different energy lattices and therefore different solubility values. Usually the less stable form (with marginally amorphous state) has the highest solubility because of highest lattice free energy. During dissolution a higher release amount of energy will thus assist the dissolution process [23, 24]. Special care must be taken if in the process of dissolution polymorphic conversion may occur. In this case the recorded equilibrium solubility of the compound will be the value of the most stable polymorphic form at given temperature.

Solubility will strongly affect the conditions of the crystallisation process and the properties of the resulting product. A special case is the solubility of Active Pharmaceutical Ingredient (API) because it determines the aqueous dissolution rate, therefore having a huge effect on bioavailability. Permeability is the ability of an active drug to diffuse through an intestinal membrane and successfully perform its therapeutic action. It is an essential parameter in classification of drugs because together with solubility it determines the bioavailability and therefore feasibility for a specific compound to successfully perform its therapeutic task.

Very important in pharmaceutical sciences the Biopharmaceutics Classification System (BCS) is a list of guidance regarding the classification of pharmaceutical compounds based on intestinal drug absorption. This system provided by the U.S. Food and Drug Administration allows the classification of drugs into one of four categories [25]:

Class I: High Permeability, High Solubility

Class II: High Permeability, Low Solubility

Class III: Low Permeability, High Solubility

Class IV: Low Permeability, Low Solubility

Details regarding the specification of each class can be found in literature [25, 26].

### 2.1.3.2 Solid forms & polymorphs (solid - solid)

One of the most important relationships for system components in equilibrium applied for crystallising solutions is expressed by the Gibbs phase rule. It helps with understanding the formation of phases and relationships between them.

The Gibbs Phase Rule is expressed in a simple form:

$$P + F = C + 2 \quad 2.1$$

It reflects the relationship between P - the number of phases (physically distinct and mechanically separable domains with boundary surfaces: in gas, liquid or solid state), C - the number of components (species whose concentration can undergo independent variation in different phases) and F – the number of degrees of freedom corresponding to the number of the variables that must be fixed in order for the system to stay in equilibrium, like temperature, pressure and concentration.

In a system of one component (or one polymorph)  $C=1$  being all in one phase  $P=1$  (only in solid state or one polymorphic form) the number of degrees of freedom  $F=2$  meaning both temperature and pressure may be varied without changing the number of phases. If two phases (liquid – solid or two polymorphs) are in equilibrium ( $P=2$ ), the variance is  $F=1$ , means that at chosen pressure, temperature of system must be fixed at the transition temperature. In the case of polymorphism the conclusion of Gibb's phase rule in solution is that only one phase (polymorph) can exist at any temperature and pressure, except the transition temperature, at which providing fixed pressure, usually atmospheric one, two phases (polymorphs) exist in equilibrium. An extreme situation occurs if one component exists as 3 polymorphs (in one phase) and then the system can exist as invariant which will correspond to the triple point.

Hydrates and anhydrates can coexist thermodynamically, because the number of components changes, whereas real polymorphs cannot.

### 2.1.3.3 Gibbs free energy

Gibbs free energy is the driving force (energy that can be used for useful work) for any reaction as it is energy associated with chemical reaction, expressing the direction of process and spontaneous change. A system is in thermodynamic equilibrium only if  $\Delta G$  equals zero and every chemical system will tend to go towards that state.

$$\Delta G = \Delta H - T\Delta S \quad 2.2$$

Where:

G – Gibbs free energy

H – Enthalpy

T – Temperature

S – Entropy of the system

The thermodynamic relations between polymorphs can be represented graphically on an energy – temperature diagram and these are fundamental tools for analysing complex polymorphic systems [18].

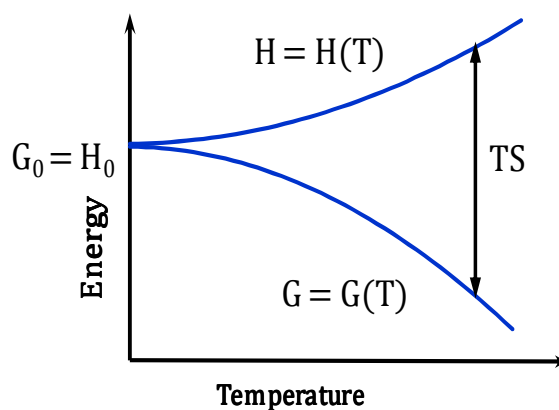


**Figure 2.4** Gibbs free energy.

Plots of Gibbs free energy for each form represent the thermodynamic relationship between possible forms.

Two polymorphs are said to be enantiotropic if one polymorph is more stable at a given temperature and pressure (having the lowest free energy) while the other is stable at different values of temperature and pressure [27].

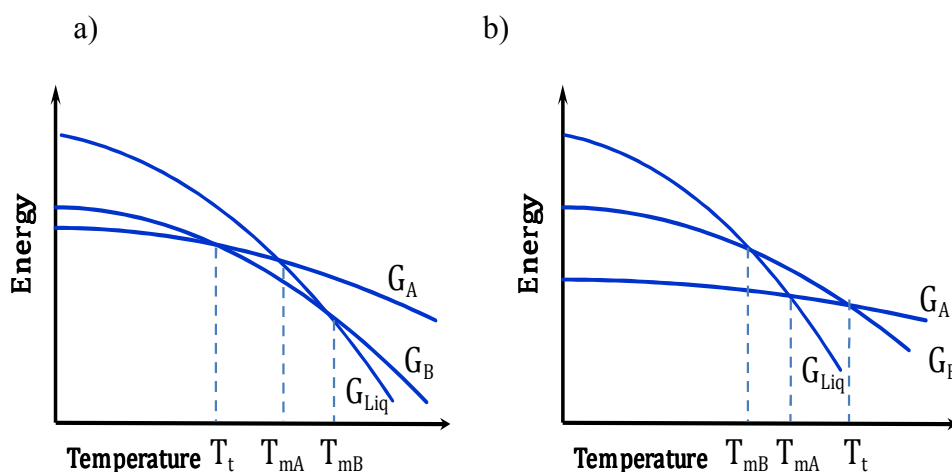


**Figure 2.5** Relation between Gibbs free energy for a) enantiotropy b) monotropy.  $T_t$  is the transition temperature;  $T_{mA}$  and  $T_{mB}$  are melting temperatures for each form respectively. Liq– represents the liquid state.

In the case of enantiotropy at a given temperature two curves intersect below the melting point of each polymorph and at this transition temperature reversible transformation is possible. It can be seen in Figure 2.5a that polymorph A has lower free energy, therefore is stable below  $T_t$ , while above  $T_t$  form B is the more stable one. In the case of monotropy the phase with higher melting point is the stable form [see Figure 2.5b].

The Heat of Fusion Rule states that if a form with a higher melting point has a lower heat of fusion, the two forms are enantiotropic. If the higher melting polymorph has a higher heat of fusion the two are related monotropically. Heat of Transition Rule states that for enantiotropy the polymorphic transition is endothermic but is exothermic for monotropy [28].

The knowledge of these phase diagrams with all possible forms, their relative stability and transition temperatures is very useful for the proper design of a crystallisation process. The change of polymorphic form is accompanied by thermal effects and is commonly studied by DSC (Differential Scanning Calorimetry) and TGA (Thermogravimetric analysis).

### 2.1.3.4 Supersaturation

The crystallisation process consists of three basic steps: supersaturation, nucleation and crystal growth. Supersaturation is a phenomenon where the amount of dissolved solute exceeds the equilibrium value. It can be quantified using either the concentration driving force or the supersaturation ratio:

$$\Delta c = c - c^* \quad 2.3$$

$$\text{or } S = \frac{c}{c^*} \quad 2.4$$

Where:  $\Delta c$  – is a supersaturation or the concentration driving force

$S$  – supersaturation ratio

$c$  - solution concentration

$c^*$  - equilibrium concentration (corresponding to saturation conditions)

Another way of expressing supersaturation is the relative supersaturation [3]:

$$\sigma = \frac{\Delta c}{c^*} = S - 1 \quad 2.5$$

$\sigma$  - relative supersaturation

It is essential to mention that a proper thermodynamic driving force for nucleation is the difference of chemical potentials of the substance in a solution and in solid state.

$$\Delta\mu = \mu_1 - \mu_2 \quad 2.6$$

$$\mu = \mu_0 + RT \ln a \quad 2.7$$

Where  $R$  – gas constant

$T$  – absolute temperature

$a^*$  - activity of saturated solution

$\mu_0$  – reference chemical potential

$$\frac{\Delta\mu}{RT} = \ln \frac{a}{a^*} = \ln S \quad 2.8$$

Supersaturation being intrinsically connected to solubility strongly depends on the temperature and pressure. The effect of supersaturation on crystallisation has been studied in polymorphic crystallisation [29] antisolvent crystallisation [30] and as a factor determining crystal growth and therefore effecting crystal shape [31, 32]. In

general higher supersaturation leads to faster nucleation creating many nucleation sites leading to the formation of many small crystals. Slower crystallisation (slow cooling or slower addition of anti-solvent) will result in a smaller number of bigger crystals.

There are a number of possible methods of obtaining supersaturation. Therefore it is the basis for possible applied methods of crystallisation as described in section 2.2.1.

#### 2.1.4 Nucleation

Crystallisation is a spontaneous, exothermic process and as a result of supersaturation molecules, atoms or ions randomly cluster together. When these nanoscopically generated small formations sometimes called embryos become stable, solid phase is generated [33]. If their size is smaller than the critical radius  $r^*$  they tend to dissolve, but once their size exceeds  $r^*$ , further increases lead to spontaneous decreases in free energy which makes them stable.

Gibbs free energy difference between small solid particles and corresponding solution is equal to the sum of surface excess free energy (between the surface of the particle and the bulk of the particle) and the volume excess free energy (between a very large particle  $r = \infty$  and the solute in a solution) [3].

$$\Delta G = \Delta G_S + \Delta G_V \quad 2.9$$

$$\Delta G_S = 4\pi r^2 \gamma \quad 2.10$$

$$\Delta G_V = - \left( \frac{4\pi r^3}{3V_m} \right) RT \ln(1 + S_B) \quad 2.11$$

$\gamma$  - is the interfacial tension between the developing crystalline surface and the supersaturated solution in which it is located.

$V_m$  - specific volume of solute molecules

$S_B$  – supersaturation of the solution

If these small particles or nuclei are more likely to grow than dissolve i.e. if they are thermodynamically stable they will diffuse in the solution and integrate with other

nuclei or already existing crystal surfaces. Subsequent arrangement of above constituents into the crystal lattice will result in subsequent crystal growth.

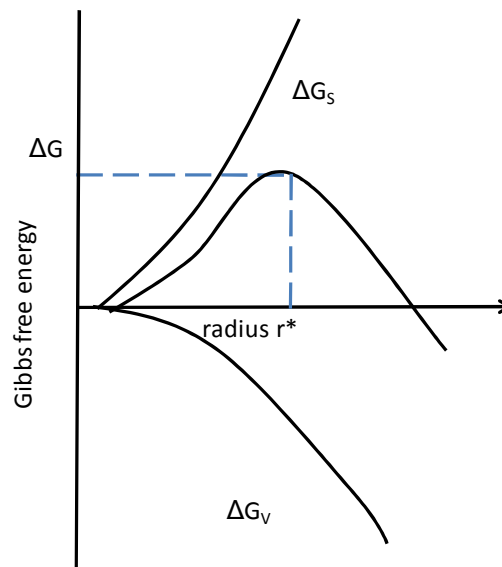


**Figure 2.6** Critical radius of nuclei and the energy barrier for nucleation.

Nucleation is the most important step in crystallisation and the need to understand and control the process motivates extensive research towards better comprehension of this phenomenon.

Due to differences in the solubility of smaller and bigger particles in a crystallising solution smaller clusters tend to dissolve in order to become a part of bigger cluster. This phenomenon called “Ostwald ripening” leads to coarsening crystals and it is a process where the free energy of crystallising solution decreases.

Already existing nuclei in the supersaturated solution can have a catalyzing effect on the process and secondary nucleation can occur under much lower supersaturation than required for primary nucleation [34]. Two approaches to secondary nucleation are proposed: those explaining secondary nuclei as direct derivatives of parent crystal and including breeding of dust, needles or collision and those attributing the presence of possible impurities or fluid shear.

The classical theory of nucleation [35] explains the production of crystals as macroscopic embryos with the same density, molecular arrangements and surface

free energy crystals. This theory assumes that supersaturation does not influence the size of obtained nuclei.

Much recent work gives new evidences that the process of nucleation does not always have to follow this path. The non-classical approaches suggest that the appearance of crystal can be preceded, for example by spinodal decomposition; the spontaneous creation of liquid-like distinct regions with different chemical composition and physical properties. It is thought that creation of metastable liquid phases in the original supersaturated solution is not simultaneously accompanied by change in structure rearrangements [36] and is dependant on the supersaturation. Moreover, inside that spinodal region there is no energy barrier and its decomposition/nucleation will be diffusion limited.

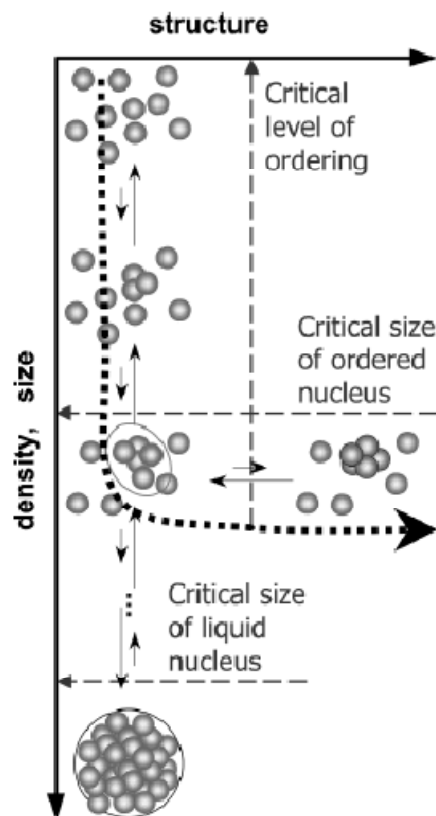


**Figure 2.7** Nucleation paths copied from Vekilov [36].

Creation of these metastable liquids as submicron droplets in protein crystallisation has been extensively studied and reviewed by Vekilov [36]. In his comprehensive

work he concludes that the creation of pre-ordered nuclei (metastable droplets) is a function of structure and density of ordered nucleus and these factors will trigger a variety of possible pathways of crystallisation, either with or without these metastable droplets.

Other research confirms that the proposed mechanism in crystallisation of proteins occurs near critical concentrations. It has been suggested [37] that the structure fluctuation is preceded by density fluctuations therefore helping to explain the height of nucleation energy barrier [38]. This initially observed density fluctuation is the metastable form of two liquids with density and concentration gradients triggering nucleation.

This phenomenon has been observed for other small molecules, not just proteins. Glycine a simple amino acid has been shown [39] to behave contradictory to classical nucleation theory too and the existence of dimers of glycine in a supersaturated solution just before crystallisation indicates two step nucleation process [40]. Contradictory observations and conclusions are reported by Huang [41] that glycine exists mainly as monomers in supersaturated aqueous solutions.

Regions of higher density in crystallising polymer colloidal solution prior to the creation of nuclei have been observed [42] and are the evidence of the existence of the metastable regions. The emulsification of nanoparticles with Ouzo effect as a well known example has been studied by Sitnikowa [43] and Genachaud [44].

Because of many challenges with the full understanding of crystallisation mechanism other alternative theories describing variations from the classical nucleation have been proposed. Mesocrystal formation and orientated attachment mechanism was introduced by Niederberger [45] and illustrates another mechanism different from classical nucleation theory, opening a broad window of new possibilities in bioinspired particles formation.

## 2.2 Crystallisation process

### 2.2.1 Crystallisation setups

Crystallisation process can be carried out in a batch, semi batch or continuous reactors, in stirred or unstirred vessels. At laboratory scale simple agitated vessels are the most commonly used methods however with scaling up significant problems can occur with efficient stirring, heat and mass transfer. Some of the most popular units [3] in industrial crystallisation are vacuum operating draft tube and baffled (DTB), Swenson forced circulation (FC), Oslo fluidized-bed, Mixed Suspension, (theoretical and idealized continuous) and Mixed Product Removal (MSMPR) crystalliser [5]. Factors very important to the process will include high throughput, efficiency and kinetics, all depending on the required scale. A proper design aiming for production with suitable crystal size distribution needs deep analysis of kinetic processes and the crystalliser residence time distribution facilitated by the population balance.

Amongst a number of possible classifications of crystallisation methods the most widely used is based on the way by which supersaturation is achieved; thus there is: reaction, cooling, evaporation, antisolvent (as drowning out), etc. crystallisation [3].

In reaction crystallisation the supersaturation is achieved by chemical reaction. In an example of reaction crystallisation in double jet type reactor it is reported [46] that nucleation occurs instantly while adding the reactants, then the number of stable nuclei gets to constant level and further addition of reactants only results in their growth based on the Brownian motion. The growth of the particles is mostly influenced by the fluid motion in the reactor. This method of obtaining crystals and cocrystals can be advantageous as it is possible to obtain at ambient conditions, during an effective, rapid and relatively environmentally friendly process [47].

In cooling crystallisation supersaturation is achieved by the reduction of temperature causing the change (decrease) of the solubility of solute. This way of obtaining crystals has been shown to be very effective in avoiding secondary nucleation in batch crystallisation by the control of temperature (slow cooling) [48].

Evaporation crystallisation is often used for huge scale inorganic processes like the production of anhydrous soda ash [49], as well as the production of pure, high quality proteins [50, 51]. The crystallising solution is allowed to reduce the amount of solvent by evaporation and this way supersaturation is achieved.

Anti-solvent crystallisation can be used as an alternative to cooling or evaporation for the separation and purification of solid product and it is very commonly used in the pharmaceutical industry. The addition of anti-solvent reduces the solubility of a solute in solution and thereby facilitates the generation of local supersaturation the driving force for nucleation and growth. The big advantage of this method is the low input of energy required as it is usually carried out at room temperature [29] [52]. It has to be considered that the effect of solvent in crystallisation process can affect the resulting habit and creation of possible solvates [53].

Quite often more than one crystallisation method can be combined; for instance cooling combined with antisolvent crystallisation [54]. The resulting process takes advantage of both constituents and is characterized by superior control of the product. This more complicated and expensive procedure is mainly used for highly demanding crystallisations of Active Pharmaceutical Ingredient (API).

In general the crystallisation method will be chosen based on many chemical and physical parameters, including the cost and the scale of crystallisation process.

### **2.2.2 Kinetics ruling crystallisation**

Crystallisation similar to any chemical process is ruled by thermodynamics, but the time scales often trigger which path of reaction is followed. Before the creation of the final, thermodynamically stable form, a kinetic form commonly known as metastable form may be obtained and the transition is kinetically hindered. It is possible that at given conditions the stable form will never be observed.

### 2.2.2.1 Induction time

Instant spontaneous nucleation is not usually observed by achieving common levels of supersaturation and a significant time lag is normally observed. In the case of reaction crystallisation the nucleation occurs instantly when the supersaturation is obtained.

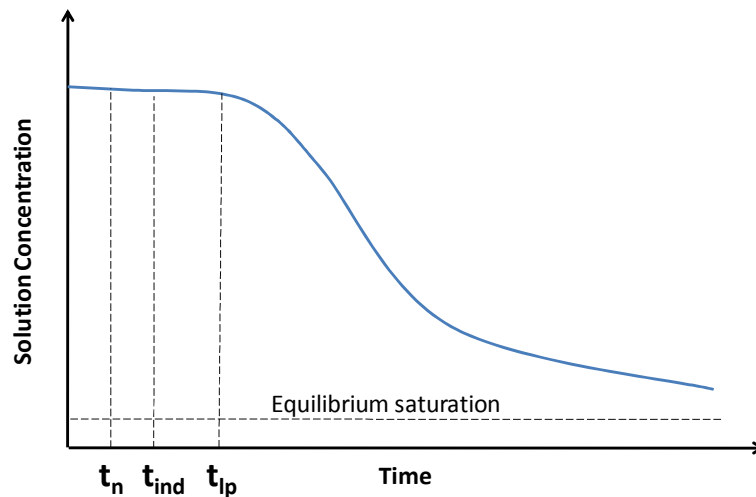


**Figure 2.8** Nucleation, induction and latent period in crystallisation.

Several factors can contribute to the nucleation time lag and these are: relaxation time (a time that cluster distribution needs to get to quasi – steady state distribution and respond to a supersaturation) [3, 55], period when stable nucleus can form and finally time for growth to noticeable sizes. All of these quantities will depend on the components properties: viscosity, supersaturation as well as physical state of the system; cooling rate; stirring etc. Seeding and the presence of impurities will generally decrease the induction time. Induction time is usually delayed relatively to the time when supersaturation point is reached because as mentioned above the system needs time for the stable nuclei ( $t_n$ ) and their growth to detectable sizes ( $t_{ind}$ ). It will be connected to a solution viscosity and hence diffusivity. In some cases, especially at lower concentration, another time lag called latent period ( $t_{lp}$ ) is observed and during this a significant change of the system has been observed. A huge decrease of solution concentration and significant turbidity occurs. Very often it is more practical to record latent periods as more characteristic of the system.

### 2.2.2.2 MetaStable Zone Width (MSZW)

Another very important parameter in the crystallisation process which relates to the kinetics is the Metastable Zone Width (MSZW).

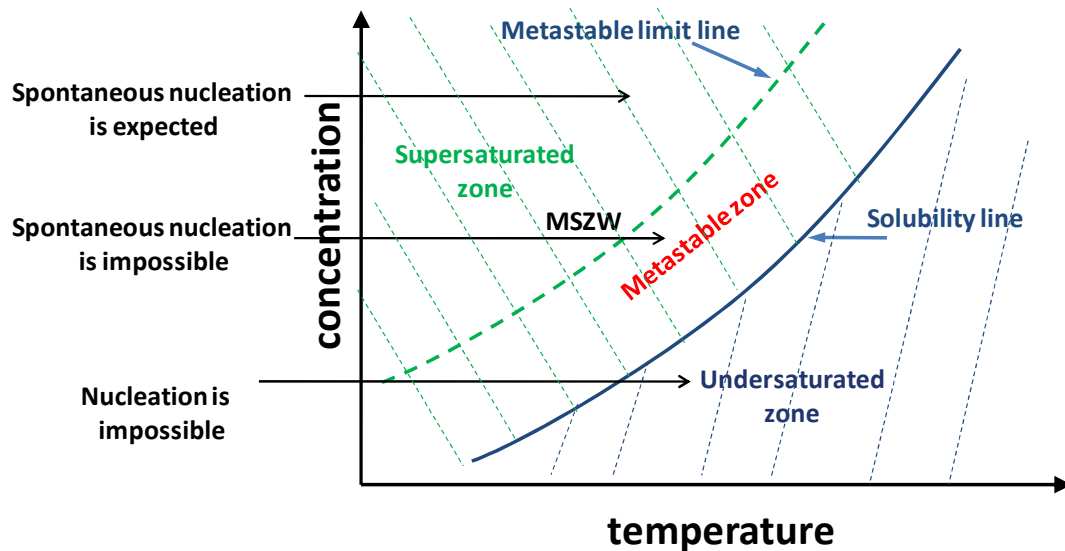


**Figure 2.9** MetaStable Zone Width.

Metastable zone is a region between the solubility line and the metastable limit line and its width depends on processing conditions. In the stable undersaturated region no crystallisation on thermodynamic grounds is expected. In the metastable zone the solution is already supersaturated but spontaneous nucleation is not expected. However it can be induced, by seeding or stirring and crystals can grow in that region. In the supersaturated unstable region above the metastable limit line spontaneous nucleation is expected, after a certain induction time.

MSZW strongly depends on crystallisation conditions: cooling rate, agitation, seeding etc. The control of MSZW will differ significantly depending on the studied system and as an example interesting conclusions come from the work of Nagy [56] where he reported that concentration control is superior to temperature control for the crystallisation process of paracetamol. Crystals obtained in concentration control mode gave much better size distribution, less agglomerates and larger, nicer crystals. In the work of Correia [57] for the process of cooling crystallisation of keto-1,2,3,4-

tetrahydro-6-methylcarbazole (KTMC) from acetone MSZW broadens with the increase of cooling rate. Similar observations were obtained for ketoprofen [58] as for slower cooling, larger MSZW. At the same time the authors observe that the effect of stirring rate on MSZW was not very significant. It has been well known that stirring influences the MSZW [59] and usually with the increase of stirring rate a decrease of the metastable zone width is observed. It is explained as a result of the increased frequency of particles collisions, improvement in solution homogeneity and a reduction in diffusion times [60]. However it is not always the case. Interesting results of the effect of stirring during antisolvent crystallisation show that it may depend on the location of the addition of an antisolvent [61]. Increase of stirring rate narrows MSZW when antisolvent is added close to the impeller, and MSZW becomes wider for the addition of antisolvent near the wall. It is thought that addition near the impeller causes instantaneous homogeneous mixing of components and the increase of probability of contact between solute molecules. However when the antisolvent is added near the wall stirring leads to dissipation of areas of high supersaturation and MSZW gets wider with the increase of stirring speed.

#### **2.2.2.3 Ostwald's rule**

Ostwald's rule is one of the main and most important rules referring to nucleation in polymorphic systems [62]. According to the rule crystallisation of compound will favour not the most but the least stable polymorph with the nearest free energy to that of the supersaturated solution to crystallise first [27].

This is not a universal law but only an often observed tendency in nature.

Thermodynamic path of reaction takes place when the relative thermodynamic stability or the conditions decide in which direction a transformation can occur.

Kinetic path depends on the time it takes for the transformation to occur

(supersaturation, nucleation and crystal growth). Thermodynamics governs the most stable state, but once metastable state is reached then it is kinetics that will determine which form will be created and how long will it survive.

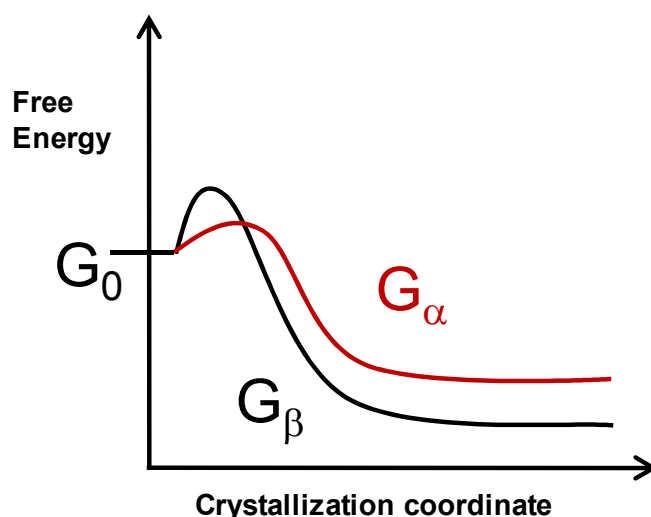


**Figure 2.10** Kinetics of polymorphs.

Looking at the example in the Figure 2.10 it can be seen that it is likely that the first form to crystallise will be the metastable  $\alpha$  form with lower energy barrier  $G_\alpha$  however the form with resulting lowest free energy is  $\beta$  with the lowest  $G_\beta$  and this form will be present in the solution when the solution is in a thermodynamically stable state. For more practical applications according to Ostwald's step rule the stable form will crystallise preferably in lower supersaturation and intuitively metastable form at higher supersaturation. Using a relatively poor solvent for the drug [63] usually metastable form will be obtained.

### 2.2.3 Parameters affecting crystallisation process

The scale, tonnage and variety of crystallisation in industry triggers big demand for effective and profitable processes. That is why process design and optimization are of the highest importance and careful crystallisation control is crucial [64]. The knowledge of the effects of process parameters and establishment of factors limiting obtained size, shape or polymorphism are key elements in process design. A lot of work has been done in order to establish the effect of solvent (see below in 2.2.3.1) on crystal growth and morphology [53], effect of addition of the anti solvent [61], seeding, temperature, stirring etc.

This work focuses on the effect of process parameters on polymorphism and the effect of flow on nucleation and then breakage behaviour of crystals slurries. These areas are described in more details although the other main factors are briefly discussed too.

In the pharmaceutical industry obtaining a desirable polymorphic structure of a drug is crucial as they differ from each other in terms of their physical and mechanical properties. Companies are constantly battling the problem of polymorphism where an active drug can occur in many forms with a series of differences in the drug causing it to act in very different ways. The classical example of unexpected appearance of a new, more thermodynamically stable form of ritonavir [65] has proven that research on polymorphic structures of drugs is crucial as the price can be the risk of human life or at the very least a huge amount of money.

Crystallisation of polymorphs is a thermodynamically very complex process [3-5] and is seen as a sequence of competitive steps of nucleation and growth of possible forms of crystalline API. Crystallisation very often is not an equilibrium process and is driven by kinetic and external factors such as temperature, entropy, solvent, impurities, pressure, etc [66]. As a consequence, the thermodynamically most stable polymorphs may not always be observed because there may be no kinetic pathways to directly obtain these structures or the time scales are far too long. At the same time stable form does not always have to be the preferred choice for manufacturing in cases where relatively higher solubility of metastable or amorphous form is needed.

Physical properties, processing time and dissolution rate must be considered in depth before the decision is taken on which form is the most suitable for manufacture. To capture all these kinetic and external factors determining obtained form it is essential to study the crystallisation process carefully, every single step and each crystallisation process individually.

The most important step for the control of polymorphic structure lies in the nucleation process and it is influenced by many factors that in general can be divided into two groups. The first group of primary factors will be influenced by the nature

of the process: cooling or reactive crystallisation and will consist of: cooling rate, stirring, seeding, temperature, additives, solvent etc. Secondary factors depend on the crystallising system itself, therefore we have: components, solvents, pH and so on.

In the work of Kitamura [67] a wide review on strategies for the control of crystallisation of polymorphs is presented on some examples. The main conclusion is that the controlling factors for specific crystallisation process depend on the studied system and crystallising solutions can and often do but don't always have to follow "Ostwald's step rule". Although the creation of polymorphs is seen as competitive nucleation, polymorphs do not have to nucleate separately; it is known that the stable form can grow on the surface of the metastable form. Nucleation is followed by competitive growth and finally metastable form will then transform into stable form.

Control of polymorphism has been the subject of a review by Llinas and Goodman [68] with many general conclusions about polymorphism. They reported that in components where it was possible to obtain more than one form time scales for nucleation were the key points. If crystals are seen after seconds or minutes it is highly probable that obtained form will be metastable, but if that is extended to a few hours stable form should be found. They reviewed seeding applications for either inducing crystallisation in general or for the support of specific form including enhancement of enantiomer from racemic mixture, templating with SAMs, effect of solvents, supercritical fluids and many others.

The complexity of API crystallisation in many publications focuses mainly on the effect of solvent, temperature, cooling rate and initial solution concentration. A small review of some important factors considered in this work influencing polymorphic and crystallisation process in general is given below.

#### **2.2.3.1 Effect of solvent**

The effect of solvent in crystallisation has been extensively studied [69] and the influence of it seems to be unique for each system. It is seen to play a role only if the process follows the kinetic pathway of crystallisation. The effect of solvent can be crucial where the polarity of the solvent will decide which kind of hydrogen bonding

may be created therefore influencing characteristic aggregation of molecules limiting the creation of a specific form. For example hydrogen bonding sites in the amide molecules will be completed by specific solvents that are donors or acceptors of protons and therefore inhibit chain formation [18]. As a consequence acetone inhibits the growth at the amine end and the carbonyl end will be inhibited by the use of methanol. It has been shown that the chosen solvent may influence the relative nucleation rate and thermodynamic stability of polymorphs of 2-(3-cyano-9-isobutyloxyphenyl)-4-methyl-5-thiazolecarboxylic acid (BPT) from methanol – water solutions [70]. The examples of strategy and importance of controlling polymorphic form in an industrial pharmaceutical company was shown by Müller [63].

#### **2.2.3.2 Effect of seeding**

The addition of small amounts of seed particles into supersaturated solution is a well known method of inducing nucleation and what follows controlling the resulting size of crystalline product. This method is used to control polymorphism of the desired form [71] supporting crystallisation of either stable or unstable form [72]. It can also support transition between polymorphic forms and the surface of one material can act as nucleation inductors for other polymorph [73]. Seeding has been found to support preferential crystallisation of desired enantiomer of racemic mixture [3, 74].

Seeding can also be unintentional and not always desired and the presence of dust or any impurity of crystallisation components or instruments can lead to uncontrolled behaviour of crystallising solutions [3].

#### **2.2.3.3 Effect of flow**

One of the main aims of this work was to study the effect of flow on crystallisation process and its effect on nucleation thereafter to design an experimental test bed for crystal breakage in flows.

Theoretical studies of the influence of a shear flow on the process of nucleation of polymers confirm that the presence of flow changes the isotropy of the crystallising

system [75], influencing size and diffusion coefficient of the created clusters (causing that is not the same in all directions). Research shows direct influence of alignment of chain segments with flow direction of polymer molecules. It results in the control of the course of formation of primary nuclei and hence directs the orientated growth perpendicular to the flow [76]. At the same time it has been reported that at a given shear rate only molecules with bigger than the 'critical orientation molecular weight' will be influenced and orientated. In polymer melts crystallisation shear flow causes acceleration of kinetics leading to changes in crystallisation behaviour therefore changing resulting morphology.

It would also seem logical to expect a strong effect of the flow on crystallisation in cases where metastable liquid phases are present (see nucleation part above).

For colloidal and protein suspensions it was found that rotational shearing fields strongly affect nucleation process and depending on the protein system the strength of the flow will either stimulate or suppress the crystallisation [77]. The existence of the optimal velocity leading to fastest nucleation has been shown for some systems. Induced shear leads to nonuniform surface tension altering the process of adsorption and redistribution of new protein molecules on the surface. The author suggests that shear flow strongly influences the nucleation rate by enhancement of ordering of the metastable droplets leading to faster production of crystal.

The effect of stirring as a controlling factor has been studied in competitive crystallisation of two possible forms of L-Glutamic Acid by Cashell [78]. Stable beta polymorphs were preferably obtained for fast cooling with agitation and slow cooling in conditions without stirring. He analyses the stability of obtained metastable alpha form depending on flow regimes and reports that agitation of already existing alpha slurries can stabilize this form by disruption of nucleation sites of stable beta. This hypotheses is slightly different than presented by Roelands [79] studying the same system. He explains the metastable form as being a result of creation of droplets with two liquid phases and that will trigger the transformation mechanism. For higher

supersaturations liquid-liquid phase separation is observed and a model where stable polymorph is obtained from these droplets is shown.

For the process of antisolvent crystallisation mixing speed has been modelled [80] in the light of the influencing nucleation, crystals growth and finally the resulting PSD. It has been reported that higher number of crystals nucleating are seen for slower mixing, however due to better mass transport faster growth is observed. Summing up faster mixing produces less of bigger crystals. Interestingly, faster desupersaturation at higher mixing rates result in lower number of nucleated crystals.

#### **2.2.4 Crystal growth and crystal habit**

Crystal growth occurs when new atoms and molecules add to stable nucleus already present in the solution with their characteristic arrangement. As with any spontaneous process it leads to a decrease in the total energy of the system. The crystal growth will go towards minimization of total energy for the given volume. In the process of crystal growth surface defects and impurities as well as supersaturation degree play a significant role.

Possible mechanism and detailed descriptions of the process of crystal growth process are given in the literature [3, 35]. A study on crystal morphology distribution in the example of seed crystallisation of potash alum [81] and glycine [82] shows that controlling temperature and supersaturation ratios can be successfully useful for crystal shape tailoring and its control. As mentioned before the effect of saturation is that at higher saturation crystal growth creates many smaller crystals. Inversely lower supersaturation will result in fewer and larger ones.

The aim of crystallisation process design is to obtain desirable product possessing defined quality properties like particle size distribution [83] [84], shape and purity [85]. The particles need to possess desired physicochemical properties for example: chemical purity, crystal habit, structure [86] (polymorphism/hydrates) as well as thermodynamic properties. Other groups are the mechanical properties like flowability, packing, tableting, handling and finally particulate properties like crystal

size and shape. All the above characteristics have an effect on the obtained product bioavailability, solubility as well as chemical and physical stability.

Depending on many factors crystal growth may lead to radically different shapes and sizes for the same unit cell. Crystal habit is one of the crucial characteristic properties influencing many processing behaviours during filtration, tableting etc. There are many different crystal habits. The most commonly occurring are: cubical, octahedral, tabular, fibrous, columnar, lamellar, prismatic, and dendric. The crystal habit is often used by mineralogists to describe a specimen of a particular mineral.

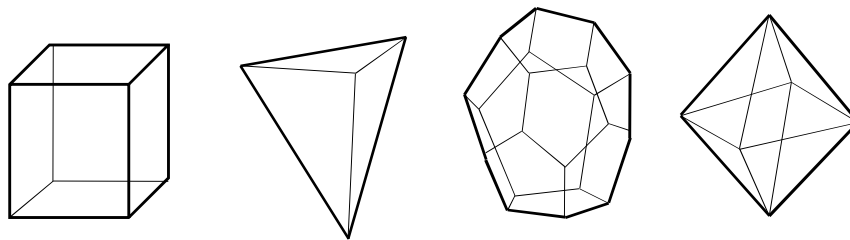


**Figure 2.11** Crystal habits: cube, tetrahedron, dodecahedron, octahedron.

It is important to know how to estimate the importance of each of the controlling factors. The most common are: the rate of growth, the effect of supersaturation, stirring or the used solvent and additives that can be seen on the example of spherical crystallisation of aspirin [87].

### 2.2.5 Particle agglomeration and breakage

The breakage of crystals already existing in the solution is a big issue for industrial crystallisation process [3]. Crystal suspensions pass through a variety of contractions, nozzles and pipes, they are pumped in and out of many vessels and these operations usually have a big influence on crystal size distribution [88] which then affects the resulting product.

Breakage and agglomeration in industrial crystallisation are often seen as secondary processes following primary particle formation (nucleation and growth) and are related to already existing particle systems [5]. These secondary processes can lead

to formation of new structures with different shape and sizes by creation of smaller fragments, or bigger agglomerates changing the overall particle size distribution.

The knowledge of the mechanisms and kinetic studies of breakage and agglomeration are vital for understanding crystallisation as they directly influence the final products characteristics; its filtration, drying, packaging and its behaviour in flows.

#### **2.2.5.1 Particle agglomeration**

Agglomeration process is caused by the physical collision of fine particles. In the close contact between particles Van der Waals forces can become strong enough to exceed the gravitational forces in conditions of sufficient supersaturation permanent bridges are formed and agglomerates are obtained [89, 90]. As a result of particle agglomeration the net particle size distribution moves to larger particles sizes i.e. there are less of smaller particles. Agglomeration mechanism depends on physical properties of crystal slurries (surface charge, pH, medium composition) as well as the supersaturation of the solution. It has been shown that for paracetamol in acetone water mixtures agglomeration will be influenced by solvent composition and its polarity [91], sizes of particle, usually faster stirring will cause destruction of big agglomerates [92]. Higher supersaturation was reported to promote agglomeration of europium oxalate, but the shear flow can inhibit the process [46].

#### **2.2.5.2 Particle breakage**

The opposite situation can occur when some areas on crystal surface are mechanically overloaded, i.e. when the surface undergoes a stress exceeding its fracture strength. Breakage and attrition are influenced by two opposing factors: mechanical strength of crystals and breaking energy supplied by the system. Attrition is the process by which fine fragments are removed from the surface of the parent particles, which gradually change their size [93, 94]. Breakage is the process by which the parent crystals are split into smaller fragments of significant size: therefore the original particles are not present anymore.

Particle break up in flows is the cumulative result of the influence of two groups of stresses: solid – solid and solid – liquid. These are called: collisional impact and fluid mechanical stresses. Collisional/impact stresses originate from particle – particle, particle – wall and particle – impeller collisions.

Synowiec [95] expressed in general form the total rate of fine particles generated in a stirred vessel as the sum of the result of breakage coming from both components:

$$\left(\frac{dn_e}{dt}\right)_{tot} = \left(\frac{dn_e}{dt}\right)_{imp} + \left(\frac{dn_e}{dt}\right)_{turb} \quad 2.12$$

Where  $(dn_e/dt)_{imp}$  describes the rate of fine particles generated by means of impact  
 $(dn_e/dt)_{turb}$  the rate of fine fragments generation by turbulent fluid forces

The first group of collisional stresses will strongly depend on:

- the relative velocity of particles with respect to each other or with respect to the wall or the impeller
- the impact energy of the collisions
- the mechanical properties of the particles, walls and the impeller

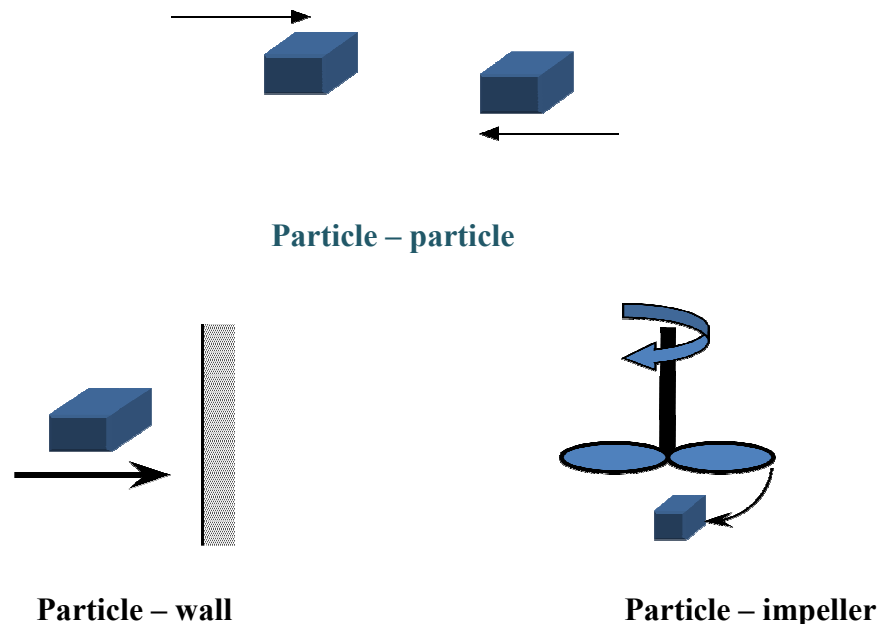


**Figure 2.12** Collisional/impact stresses.

Particle break ups can be the result of stresses caused by turbulent flow. The mechanism of breakage in the flow depends on the size difference between the product particle and the Kolmogorov microscale (eddy size), as represented: [46]

$$\eta = \left( \frac{\nu^3}{\varepsilon} \right)^{1/4} \quad 2.13$$

$\eta$  - turbulent microscale

$\nu$  - kinematic viscosity

$\varepsilon$  - energy dissipation rate of turbulence per unit mass

Kolmogorov microscale is the smallest hydrodynamic scale in turbulent flows.

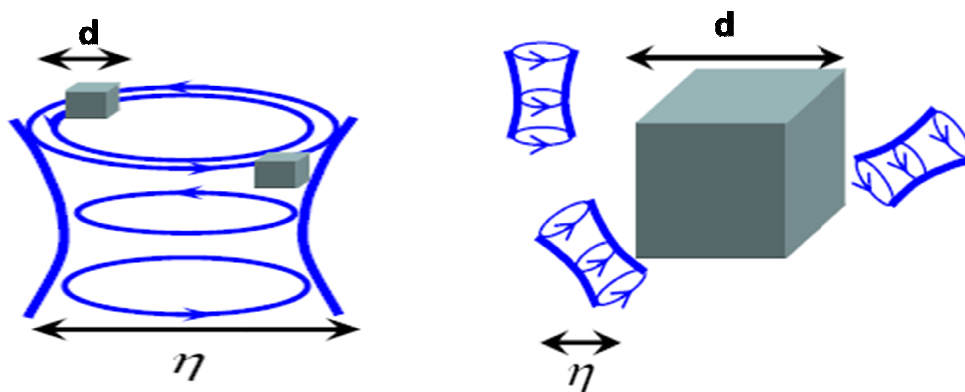


**Figure 2.13** Eddy size  $\eta$  (Kolmogorov microscale) related to particle diameter  $d$ .

The bulk of energy of a turbulent system is contained in the larger eddies. Turbulent attrition is caused by fluid eddies possessing sufficient energy and smaller than critical size. Eddies bigger than critical size will result in a surface stress by to capturing particles. Eddies smaller than particles do not possess sufficient energy to cause significant breakage, but tend to flow over the particles causing particle stresses: shear, surface and pressure stresses (see Figure 2.13).

Fluid mechanical attrition will then be influenced by: the frequency of eddies  $f_e$ , energetic aspect of the breakage and total crystal concentration of the suspension  $n_c$  [95].

$$\left(\frac{dn_e}{dt}\right)_{turb} = f_e \left( \frac{E_n}{e_n} + \frac{E_d}{e_d} + \frac{E_s}{e_s} \right) n_c \quad 2.14$$

subscripts  $n$ ,  $d$  and  $s$  refer to disruption energy generated from pressure (normal), drag and shear forces.

Local shear stress is usually used to express turbulent fluid force acting on particle surface:

$$\tau = \mu \left( \frac{\varepsilon}{\nu} \right)^{1/2} \quad 2.15$$

where  $\mu$  means dynamic viscosity

$\nu$  - kinematic viscosity

$\varepsilon$  - energy dissipation rate of turbulence per unit mass

The effective intensity of stress is equal to eddies fluctuation frequency,  $f_e$  described by Levich in 1962:

$$f' = f_e = 0.258 \left( \frac{\varepsilon}{\nu} \right)^{1/2} \quad 2.16$$

Impact breakage and attrition of particles in diluted suspensions are reported to be mostly referring to collisions of crystals with the wall or impeller and the probability of particle/particle collisions is not significant [34]. The break-up of particles in stirred tanks occurs mostly in the impeller zone due to the maximum value of fluid velocities in this highly inhomogeneous turbulence dissipation system [96].

Synowiec et al [95] have studied crystal break-up in dilute turbulently agitated suspensions and predicted the relative impact of two independent factors which act simultaneously on the crystal surface. They have reported that the crystal attrition is mainly caused by drag – induced fluid turbulence and crystal - impeller collisions, with strong impeller hardness. For particles smaller than around 200 $\mu$ m the contribution of shear forces to turbulent component seems to have the most significant effect while bigger crystals breakage and attrition are mostly influenced by drag forces.

Hydrodynamic mechanism of attrition has been studied by Shamlou [97]. It has been shown, that secondary nucleation of crystals can be generated by turbulent flow having critical eddies in the viscous dissipation subrange of energy spectrum.

Breakage of needle-like crystals during batch crystallisation process has been studied by Sato [98] and he claims that the breakage is proportional to the frequency and the impact energy for all collisional stresses. Those crystals become prone to breakage only when their aspect ratio exceeds a certain limit. Additionally crystal breakage was found to be influenced by liquid properties most importantly viscosity and density. The effect of change of flow by varying the position of impeller in a stirred tank (called impeller clearance) on nucleation and growth was studied by Akrap [99] and Kuzmanic [100].

In the case of real fluid entering axisymmetric contraction, flow can generate vortex (eddies) which can break the particles suspended in the fluid. Experimental studies of the effect of small nozzles (with similar design to these studied in this work experimentally) and numerical simulations of entry flow done by Mitsoulis [101]. He studied the sizes of created vortexes and the dependence of flow rate and design of the entry: rounded and abrupt entry to 4:1 contraction. The results show that the vortex's size increases monotonically with increasing flow rate (or Weissenberg number) and is bigger in the sudden than the rounded entry.

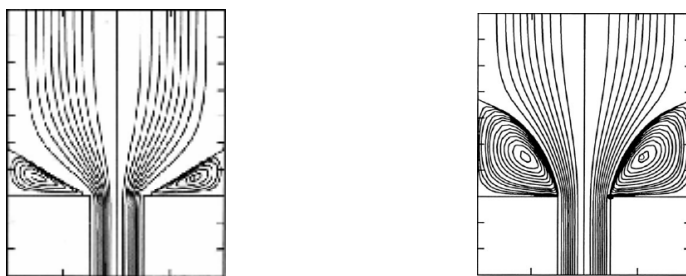


**Figure 2.14** Schematic representation of the entry flow in a 4:1 axisymmetric contraction with sudden re-entrant corner a)  $Ws=0.65$ , b)  $Ws=4.0$ .

As discussed in the nucleation section (2.1.4) secondary nucleation is often a result of processes occurring in already crystallised solution and includes collisions and

fluid shear. Therefore a lot of research on breakage and attrition phenomena has been done not as purely breakage experiments, but in the light of generation of secondary nucleus. The impact attrition in crystallisation process as a means of creation of secondary nuclei in dilute suspensions has been found to be mainly caused by collisions between crystals and the impeller [34]. Thus the process depends on operating conditions as well as material properties.

Model and experimental results of secondary nucleus generation of potassium sulphate crystals in MSMPR crystalliser report [102] that rather than the physical contact the most likely mechanism for attrition is caused by turbulent fluid-dynamic induced breeding.

An extensive review of particle breakage experiments on different materials has been published by Hill and Ng [103]. They presented a method for generating theoretical breakage distribution function for multiple particle breakage. They report that breakage process is very complex and an empirical function describing multiple breakages may be physically unrealistic and needing further work.

An extensive review of nature, mechanism of attrition and test methods for mainly gaseous systems has been given by Bemrose [104]. The aim of this work was to characterise and compare attrition of different materials and to predict particle behaviour during powder use.

The kinetics of breakage and agglomeration in reactive crystallisation [32] and in colloidal dispersion [105] has been the topic of many theoretical studies [106, 107].

Many industrial processes on flocs (aggregates of colloidal particles) involve relatively harsh operating conditions during operations like stirring and filtration that can cause disintegration of the flocs. Shear induced breakage of flocs in contraction flow has been studied by many groups [108]. The flocs strength against break up was measured and the experimental data was analysed as a relationship between floc size and volumetric flow rate [109] and model of the hydrodynamic disrupting force has been evaluated by Blaser [110]. He studied flow fields induced by pumping

water through two different diameter pipes, which were additionally kept stationary or rotated around the axis symmetry. He presented the equation for the maximum elongation rate,  $A_{c,max}$ , acting on a floc moving along the centreline of converging flow:

$$A_{c,max} = \frac{3\sqrt{3Q}}{32\pi R^3} \quad 2.17$$

Where  $Q$  is a volumetric flow rate and  $R$  is a radius of an orifice. The maximum floc size passing through and contraction will be determined by the highest elongation rate in the region surrounding the entry of the flow along the centre axis as it is the weakest from centre to wall. At the same time he found that the flocs were broken apart before they passed the orifice.

### 2.2.6 Post processing of slurries

Usually the intention of a particle production process is to obtain dry powders, easy to store and handle. All steps after the actual crystallisation are called downstream processes. The first process following crystallisation is often solid- liquid separation, and then crystals have to be washed, classified, dried, screened and sorted into appropriate size and quality of product classes.

Crystal slurries are usually separated by filtration but it can be achieved by a range of possible methods from very simple sedimentation via thickeners to various filtrations through which concentrate crystalline slurry is passed. Filtration process can be carried out by many different techniques: from very simple using filter papers and gravity, via support of pressure in Buchner funnels, permeable membranes [5], slurry presses and finally rotary pressure filters using very powerful centrifugal force.

Powders are usually washed and then the resulting cakes are dried either by evaporation, in the oven or slowly at ambient conditions. Recirculation of a filtrate (mother liquor) after filtration and re-dissolution of crystals which do not meet quality requirements are common procedure. In order to avoid crystal caking the moist content must be carefully monitored and possibly removed. Depending on

obtained powder properties some have to be stored in special conditions for example: low humidity conditions (desiccator) or in the case of unstable polymorphic form at special temperature usually lowered (fridge).

A schematic of the post crystallisation downstream processing is shown in Figure 2.15.

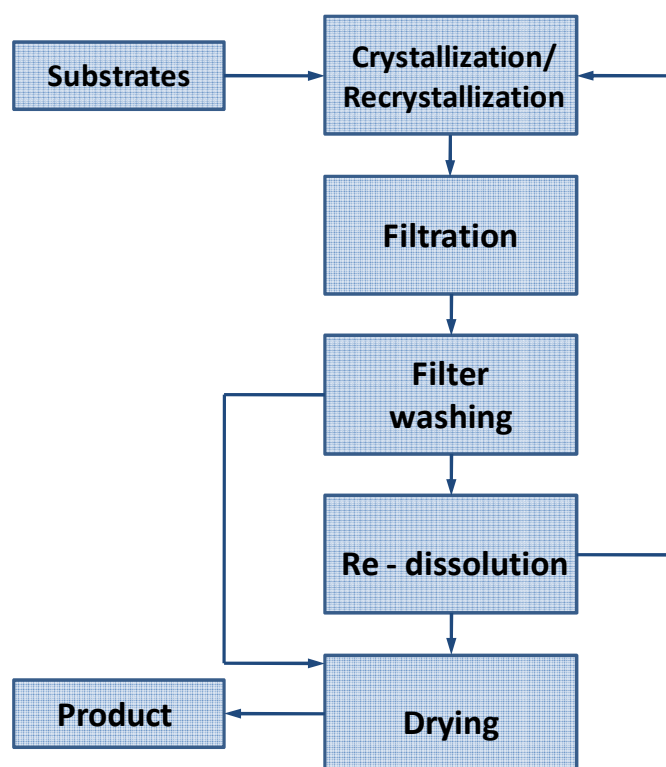


**Figure 2.15** Downstream processes in crystallisation.

### 2.2.7 Methods of characterisation of solid state

Crystal size can vary from several nanometres (active phase in catalysts), up to several millimetres (salt, sugar and diamonds), i.e. from colloidal to coarse dimensions.

Process analysis control provides information about a chemical process and is important for economic, safety and environmental reasons. The information about the process can be obtained in real time, on-line and in-line analysers. The probes can be monitored off-line when the sample is taken manually and transported to the

lab, at-line when the analysis is carried out nearby or on-line when analysers are placed directly in the process. Another very valuable type of analysis is the so called non-invasive analysis however it is very hard to achieve. In this method of analysis no sampling is required and there is no physical contact with the sample. Non – invasive techniques involve designed X-Ray Fluorescence spectrometry, Raman spectrometry, some acoustic techniques as well as within the scope of this project turbidity measurement described in detail in section 3.2.

There are a number of methods for determining the size of solid state particles obtained by crystallisation process [111]. They depend on particle concentration. (solid loading) physiochemical properties and the scale of crystallisation. Some methods like FBRM [112] and ultrasonic attenuation spectroscopy [113] can be used on line. The most commonly used methods for particle sizing with approximate attainable size ranges are listed in the table below.

Techniques	Size range [ $\mu\text{m}$ ]	Size parameter	Solid content [Vol %]
Sieving	5-125000	Sieve aperture diameter of a sphere that would just pass through the aperture	-
Microscopy	0.5-1000	Projected area diameter of a circle that has the same area as projected image	-
Sedimentation	0.1-50	Hydrodynamic diameter	-
Gas adsorption	0.001-10	Surface area	-
Electrical sensing zone (Coulter)	0.6-200	Particle volume	low
Light scattering (DLS, SLS)	0.1-1000	Intensity of the scattered light (fluctuations and angular dependence)	0.01-50 for Malvern
FBRM	1-1000	Chord length distribution	<40
Ultrasonic spectroscopy [113]	0.01-1000	Number/volume size distribution Sound propagation	<70

**Table 2.3** Methods of sizing of solid state materials.

Pharmaceutical manufacturing processes must be carefully monitored and appropriate methods of PAT (Process Analytical Technology) have to be chosen according to requirements [114, 115]. PAT probe based tools include methods in which:

Liquid phase concentration throughout the process is measured by spectroscopic techniques attenuated total reflectance (ATR), visible, ultra-violet (VIS, UV) [116] or near infrared (NIR), Fourier transform infrared (FTIR) [56], or Raman spectroscopy.

Particle size and shape is measured using in-situ, real time FBRM [117], or ultrasonic attenuation spectroscopy [83], particle imaging analysis [118], laser diffraction [119] etc.

Polymorphic forms can be characterised by Raman spectroscopy and corresponding differences in morphology between polymorphs can be characterised with Focused Beam Reflectance Measurement (FBRM), etc.

In the case of solid state forms like polymorphs, solvates, co-crystals etc PAT often is not always comprehensive and Solid State Analysis (SSA) tools must be used [114]. They include: X-ray diffraction (XRD) (often single crystal XRD), solid state nuclear magnetic resonance (NMR), solid state infrared (IR), differential scanning calorimetry (DSC), Thermogravimetric analysis (TGA), scanning electron microscopy (SEM) as well as optical microscopy and many more.

In the example of crystallisation from solution concentration can be checked by ATR-UV [120] and then formation of crystals can be monitored in line using turbidity measurements and FBRM. The same method can be used to study polymorphic or other system conversion and then all in-line analytical methods will be followed by off line characterization of obtained solid forms [121]. A series of methods for characterization and analysis of polymorphs and solvates based on different physicochemical properties [122] allow us to distinguish irregularities in crystal structures. In pharmaceutical unit operation X-Ray diffraction pattern is the criterion of establishing and conformation of new form. It is definitely the first and the best method chosen for a new compound. More analysis may be carried out based on spectral properties of polymorphic structures. At this point it is worth noting that polymorphism is a feature of a solid state only and the substances in gas or liquid phases must be identical.

Details of analytical methods used in this work are described in more detail in section 3.2.

<b>Measured feature</b>	<b>Method of analysis</b>
X-ray diffraction (crystallography)	Powder XRD, Single Crystal XRD
Microscopy	Polarizing Optical Microscopy, Thermal Microscopy, Electron microscopy (SEM), Hot stage microscopy
Thermal analysis (phase transitions)	Thermogravimetry, Differential Thermal Analysis, Differential Scanning Calorimetry
Vibrational Spectroscopy (motions of functional groups)	Infrared Absorption and Raman scattering
Environment of atoms	Nuclear Magnetic Resonance

**Table 2.4** Classification of methods of analysis of polymorphs (solid state materials).

Presented above is a general review of methods available for analysis of solution composition and crystal populations present in crystallising systems. This serves only as a brief summary and the reader is advised to refer to background literature for more details. Despite the fact that there is a wide range of PAT and SSA method used in particle research and manufacturing, it is not always possible to comprehensively characterise systems studied. As will be shown in the section on breakage of crystals in flow, capabilities of available characterisation methods are often limited and data acquired requires careful interpretation. When choosing a suitable analytical method, it is important to consider various practical factors, such as cost and availability of particular techniques, for obtaining the desired measurement.

## CHAPTER 3 MATERIALS AND METHODS

### 3.1 Materials

#### 3.1.1 Tyrosine

Tyrosine is one of the 20 essential amino acids used by cells to synthesize proteins [123]. It is a chiral molecule with D and L stereoisomers differing in solubility [124] and parity violating energy difference (PVED) as result of energy differences between enantiomers as a result of weak forces [125]. No polymorphs have been discovered so far.

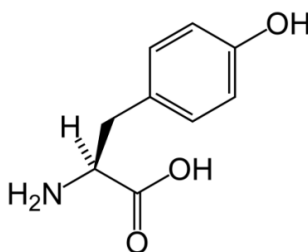


**Figure 3.1** Tyrosine structure.

This work focuses only on properties of L-tyrosine; therefore just a brief review of interesting findings on this stereoisomer is given below.

The main role of L-tyrosine in the human body is to take a part in the biosynthesis of hormones. It is commonly taken for mood enhancement and in the growth hormone stimulation. It has been found to have antioxidant properties and therefore might protect people from coronary disease, cancer development and ageing. Besides the most common feature of being useful in physical and psychological stress related conditions, it is a part of the conventional treatment for drug detoxification patients and in treatment of phenylketonuria. Natural sources products containing L-tyrosine include: soy derivatives, sesame seeds, almonds, avocados, fish, chicken, turkey and dairy like milk, cheese, yogurts, and cottage cheese. Symptoms of tyrosine deficiency are mood disorders, muscle loss, weakness and low proteins levels. The

high importance of L-tyrosine makes it popular and that is why it is marketed and commonly used as a diet supplement.

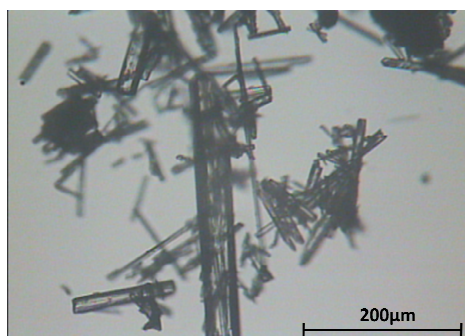


**Figure 3.2** L-Tyrosine crystals.

Tyrosine crystal density is  $1.42\text{g/cm}^3$  [123], with monoclinic space system [126]. The characteristic morphology of L-tyrosine with a high aspect ratio needles together with its non toxic properties made it a perfect model compound to study breakage of crystals in the flow.

### 3.1.2 Carbamazepine

Carbamazepine (CBZ) is a commonly used drug as anticonvulsant to treat epilepsy and trigeminal neuralgia. It has been widely utilized as a model system in pharmaceutical crystallisation research as it is an easily available, non toxic material possessing four different anhydrous polymorphs [127, 128], hydrate [117] as well as many organic solvates. It is often used as one of components in crystallisation of cocrystals [129, 130].

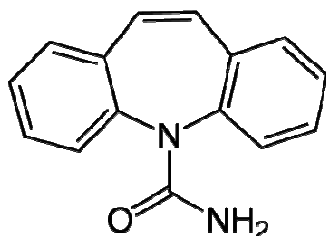


**Figure 3.3** Carbamazepine (CBZ) structure.

The four anhydrous polymorphs possess different physical and mechanical properties for instance solubility, dissolution rate and different densities all resulting in differences in bioavailability.

A very significant fact for this work is that alpha and beta forms are easily distinguishable because of differences in morphology. Crystals of alpha carbamazepine look like long needles while beta as cubes [84].

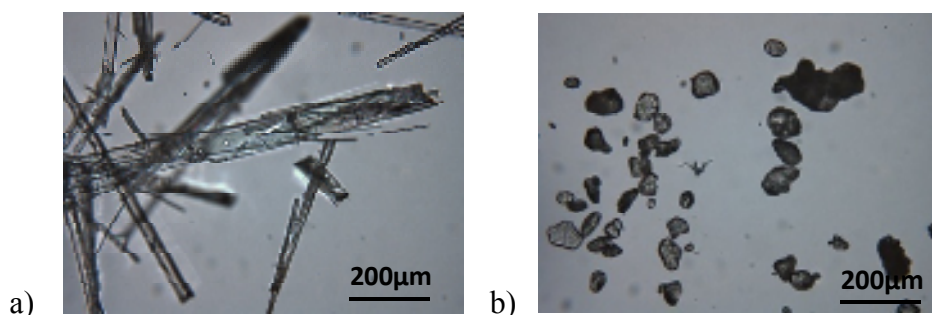


**Figure 3.4** Microscopic pictures of polymorphs of CBZ a) alpha form, b) beta form.

Published data [131] show that carbamazepine form  $\beta$  is the most stable at room temperature, where  $\alpha$  and form IV are metastable,  $\gamma$  is the stable form at temperatures over 130°C.

	$\alpha$ / Form II Trigonal	$\beta$ / Form III P-Monoclinic	$\gamma$ / Form I Triclinic	Form IV C-Monoclinic
Density [g/cm <sup>3</sup> ]	1.24	1.34	1.31	1.27

**Table 3.1** Density of CBZ polymorphs.

An extensive review of crystal structures of carbamazepine, involving 66 solvents in automated parallel crystallisation was given by Florence [127]. His calculations supported by experimental results show the stability order of CBZ polymorphs at 0 K to be: form  $\beta$  > form  $\gamma$  > form C > form  $\alpha$ . It has been concluded that higher concentration thus relatively high crystallisation rate favoured form  $\alpha$  which is the least stable structure of all four anhydrous forms (having the lowest lattice energy and density). Unfortunately no effect of stirring in these conditions has been established. Another important observation is that kinetics rather than

thermodynamics determine the energetically favourable structure during crystallisation of carbamazepine.

It has been shown that form IV can be obtained during evaporation from methanol in the presence of hydroxypropyl cellulose [132], or drying over phosphorous pentoxide at room temperature [133], both with the use of additives in relatively complex processes. In a solvent screening study using cumene [134] (isopropyl benzene), authors obtained 3 polymorphs ( $\alpha$ ,  $\beta$  and  $\gamma$  in temperatures over 80°C).

Ethanol is one the most common organic solvents used in crystallisation of drugs. While crystallising CBZ using ethanol as the sole solvent, so far only two polymorphic forms have been reported in literature:  $\beta$  form by evaporation at room temperature (21°C) and  $\alpha$  by cooling to 4°C and keeping it for a few hours [117]. Triclinic  $\gamma$  form can be obtained at temperatures higher than 80°C therefore ethanol is not suitable as it has a relatively low boiling point of 78.4°C at ambient pressure. Reports in literature on methods of CBZ crystallisation unfortunately do not contain any details of process parameters like stirring. Therefore by following published experimental procedures for CBZ crystallisation different results can be obtained leading to confusing observations and actually different polymorphs from those reported. Moreover even highly cited papers [131] give imprecise descriptions of crystallisation methods so unexpected and unwanted forms can be obtained.

Carbamazepine dihydrate is usually not a desirable product in industrial crystallisation. It has lower dissolution rate than the anhydrous forms which causes decrease in bioavailability. Water present in the system was shown to affect the solubility of CBZ and the purity of obtained form. Water in excess of 19% (by mass) in the crystallising system results always in the formation of dihydrate [135]. Anhydrous form can easily transform into dihydrate in aqueous solutions and the kinetics of that transformation is shown to be strongly affected by grinding and storage of CBZ in humid conditions [136]. Previous research showed [137] that storage of CBZ in humid conditions can significantly decrease its solubility and bioavailability. Profound effect on tablet disintegration and dissolution has been reported after exposing tablets to high humidity conditions [138].

## 3.2 Experimental Methods

### 3.2.1 Microscopy

Optical microscopes are often used for visual observation of crystallisation process and as a method for characterization of polymorphs and solvates [18]. Commonly occurring differences in crystal morphology of polymorphs and solvates make this method the quickest and probably the cheapest method of analysis of crystals.

Optical microscopes usually have magnification of up to 600x allowing visual identification of even some microcrystalline substances. However in order to expand that limited range, electron microscopes can be used with 90000x magnification and much improved visual information.

One of the biggest advantages of microscopy is that it provides rich information including crystal habit, shape and size, requiring only a small amount of sample material.

It must be noted that microscopy should not be used on its own without additional characterisation methods, especially when new forms may be obtained.

In this work an optical microscope was used for observations of many experiments and all crystalline material that has been tested was initially assessed by observation of their shape as well as their size. All crystals obtained by crystallisations in house during numerous experiments were observed and pictures were taken too. In the case of carbamazepine the two most studied forms alpha and beta have different habits, namely alpha has the morphology of needles and beta of small cubes, and both very easily distinguishable (see Figure 3.4). Crystallisation processes of carbamazepine were observed in static and dynamic conditions. Recorded live films show growth of carbamazepine crystals in ethanol from clear supersaturated solutions. By cooling the sample in a sealed cell the creation of small crystals has been observed. Their growth was followed by polymorphic conversion in the solution from metastable alpha to stable beta form. This information has proved crucial towards understanding the processes and related mechanisms.



**Figure 3.5** Microscopic pictures of alpha form CBZ crystals and creation of beta form.

### 3.2.2 Focused beam reflectance measurement

Focused Beam Reflectance Measurement is a method of sizing particles in the range of 1 – 1000 $\mu\text{m}$ , up to 40 percent volume fraction. Obtained data is acquired in situ, in real time and provides us with Chord Length Distribution (CLD) which can be related to particle size distribution and shape [139]. This method is commonly used for monitoring crystallisation processes [140, 141] as well as breakage and agglomeration of crystal suspensions [92, 142].

A beam of laser light travelling at velocity  $V_b$  hits the particle and the duration of the backscattered signal  $\Delta t$  is measured and recorded [143]. From this, the corresponding chord length  $c$  can be calculated as follows:

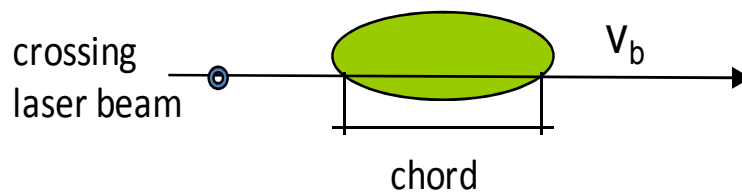


**Figure 3.6** Principles of FBRM.

$$c = \Delta t \cdot V_b \quad 3.1$$

$c$  – chord length

$\Delta t$  – duration of the signal

$V_b$  – circumferential velocity of the beam

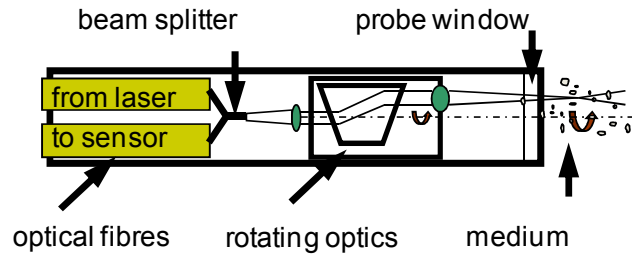


**Figure 3.7** FBRM probe.

Recorded CLDs are gathered in specific channels i.e., intervals with upper and lower values of sizes, and plotted as channel counts i.e., number of particles recorded within a specific channel.

Because of the common irregular shapes of crystals in industrial processes it is often very complicated to define the absolute particle size [119, 144]. Establishment of the “size” for non spherical particles is a complex problem and the analysis of the measurement needs to take into account length, thickness, surface area or the volume of the crystal, as well as its optical properties. In order to relate CLDs to particle size and morphology a lot of theoretical work has been done aiming to model CLD for different shapes (octahedron, needle, platelets and disks) with various aspect ratios [139] [144].

Definition of CLD for needle shaped particles was given by Vaccaro [139]. He came up with a model of CLD dependent on the length and width and it is given by:

$$l^c X_P^c(c) = \begin{cases} \frac{1}{2} \frac{c}{\sqrt{4r^2 - c^2}} \left( 1 - \sqrt{1 - \left(\frac{2r}{l}\right)^2} \right) & c \in [0, 2r[ \\ \frac{1}{\pi} \frac{\left(\frac{2r}{l}\right)^2}{\sqrt{1 - \left(\frac{c}{l}\right)^2}} \frac{1}{2\pi} \frac{l}{c} \frac{\frac{c}{l} \sqrt{1 - \left(\frac{c}{l}\right)^2} + \arccos\left(\frac{c}{l}\right)}{\frac{c}{2r} \sqrt{\left(\frac{c}{2r}\right)^2 - 1}} & c \in ]2r, l[ \\ 0 & c \in [l, \infty[ \end{cases} \quad 3.2$$

Where:

$l^c$  - the thin cylinder characteristic length       $l$  - thin cylinder length  
 $X_p^c(c)$  - single particle CLD of a thin cylinder       $r$  - cylinder base radius  
 $c$  - chord length

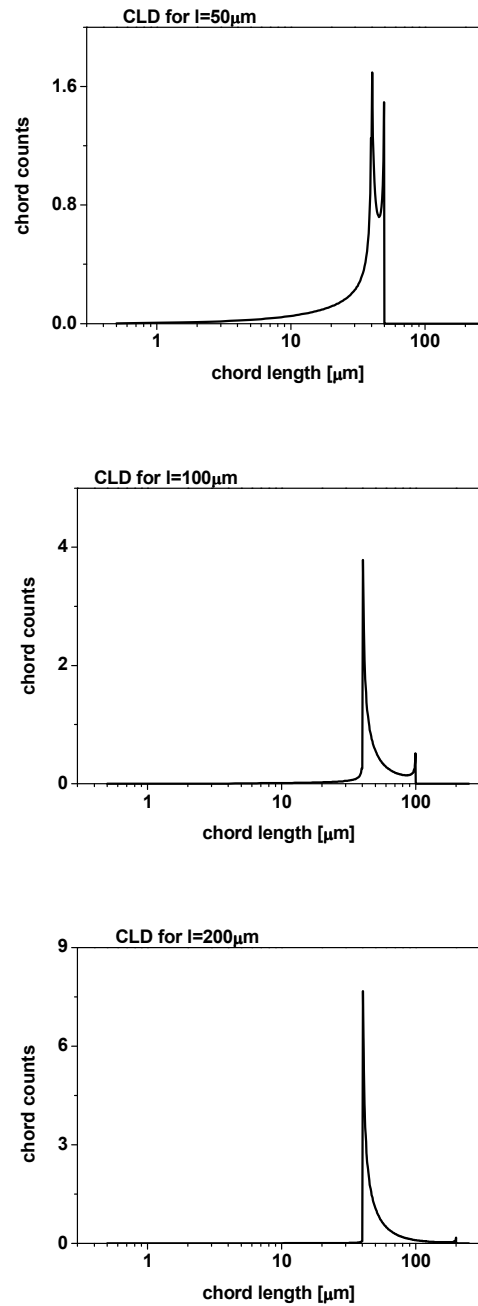


**Figure 3.8** Calculated CLDs for needles with  $r = 20\mu\text{m}$  and 3 values of length: 50, 100 and  $200\mu\text{m}$ .

Plotted CLDs for needle shape crystals with  $20\mu\text{m}$  width and 3 values of lengths show shift of peaks towards large sizes with the increase of length. At the same time the difference in relative height of these 2 peaks representing the width and height becomes larger. Figure 3.8 is a graphical expression of above theoretical equations for two size parameters (width and length) but it is not possible to observe this shape of CLD in real experiments since polydispersity tends to smooth the peak. As said before FBRM measures chord length distribution covering all sizes possible between the main two parameters  $r$  and  $l$ .

Particles move around in suspension and all possibilities of cuts shown below are possible to be recorded.

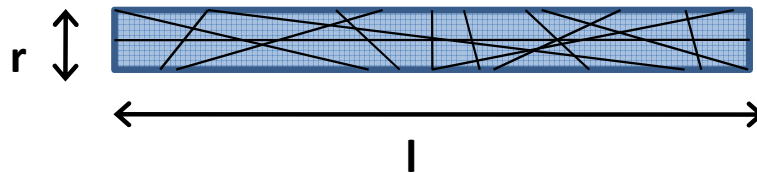


**Figure 3.9** Illustration of possible measured chords of needle like crystal.

In this work FBRM was used to track changes in CLD during breakage experiments of tyrosine crystals. Because of the needle like shape of those crystals we are not trying to fully characterise the dimensions of crystals before and after passing through the contraction nozzle only to observe if and how CLD changes in a sense of general trend.

A Lasentec probe S400E OD: 8 mm, probe length: 91 mm was used for data collection directly placed in the experimental test flask with studied solution described in the results Chapter 5.

### 3.2.3 Light Scattering

Light scattering is a process of absorption and re-emission of electromagnetic radiation by a non-homogeneous medium. It occurs when the wavelength of the light does not correspond to the absorption band (has the ‘wrong’ colour; unlike in absorption spectroscopic methods). In this process the wavelength of the laser light does not undergo any changes. The solution underlying Maxwell’s equations describing oscillating electromagnetic field gave rise to two main theories about light scattering that are in use. They consider two size ranges of particles.

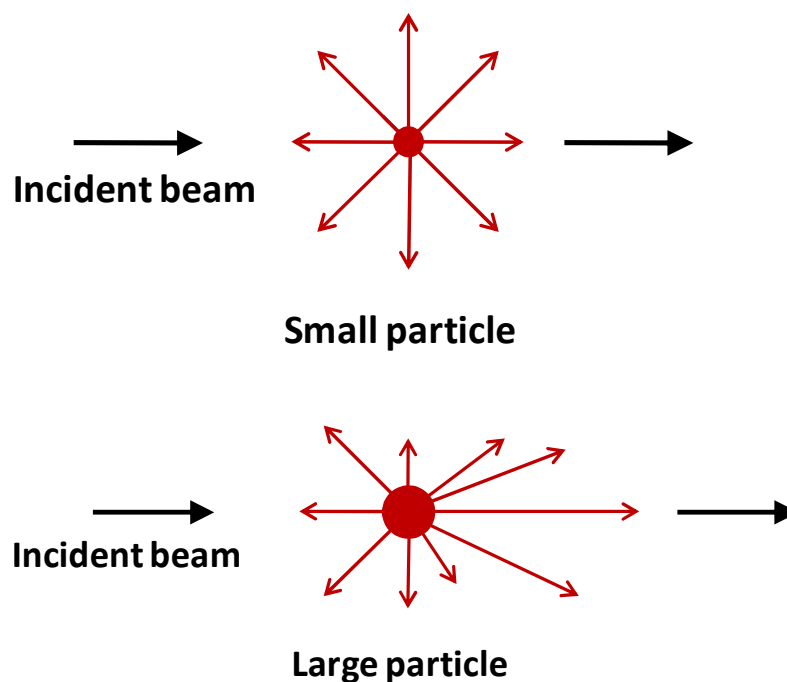


**Figure 3.10** Scattering of small and large particles.

Rayleigh’s scattering theory tells us that particle will scatter light isotropically (equally in all directions) for particles much smaller ( $r$ - radius of particle) than the wavelength of the laser used (less that  $r < \lambda/20$ ). It describes angular intensity distribution for these small particles and says that the scattering will not depend on particle shape nor their concentration but only on their size. In this approximation, the intensities of scattered light follow the equation:  $I \propto d^6$ . In practice this means that for example a particle with diameter of 50nm will scatter a million times

stronger than 5nm size particle, and therefore corresponding scattering signal obscures, overlaps and covers the one from the smaller particles.

Mie's theory describes angular dependence of scattered intensities for particles with sizes similar or larger than the wavelength of the incident laser light. Scattering of electromagnetic radiation by spherical isotropic particle illuminated by monochromatic plane waves can be exactly described [145, 146].

In this work two methods based on light scattering phenomenon, Dynamic Light Scattering (DLS) and Static Light Scattering (SLS) have been used. The main differences between them is that SLS measures time averaged intensity of scattered light at various angles, while DLS correlates scattered intensities (intensity fluctuations) at a given angle due to Brownian motion of particles. DLS and SLS data with theoretical background can be found in the Appendix 8.3. Both are suitable for characterization of particles in the range of 10-1000nm which is suitable for colloidal dispersions of particles.

### 3.2.3.1 Dynamic light scattering

Dynamic Light Scattering is a technique for measuring particle sizes in the sub micron range due to Brownian motion (DLS synonym is PCS - Photon Correlation Spectroscopy). Particle positions undergo fluctuations caused by collisions with solvent molecules resulting in random movements depending on their sizes. Bigger particles move slower, while smaller particles are much more influenced by surrounding solvent molecules and move much further and more rapidly.

A DLS instrument tracks the changes in intensity of scattered light and the fluctuations due to that motion. Fourier transformation of obtained time-domain signal gives the autocorrelation function  $G_2(\tau)$  of the scattered intensity [147-149]. For monodisperse sample it is given by:

$$G_2(\tau) = A [1 + B \exp(-2\Gamma\tau)] \quad 3.3$$

A - the baseline of the correlation function

B - intercept of the correlation function

$\Gamma$  - decay rate

$\tau$  - correlator time decay

Autocorrelation function shows how scattered intensities are mutually correlated at a time delay  $\tau$ .

In order to obtain the size of particles or clusters of particles a decay region of autocorrelation function curve of has to be identified.

Then the decay rate as a factor obtained from trend line (linear, square or cubic) is used and it allows the translational diffusion coefficient to be calculated from:

$$\Gamma = Dq^2 \quad 3.4$$

The scattering vector magnitude  $q$  is a function of a refractive index of solvent, scattering angle and the wavelength of the laser.

$$q = \frac{4\pi n}{\lambda_0} \sin \frac{\theta}{2} \quad 3.5$$

$q$  - scattering vector magnitude

$n$  - refractive index of solvent

$\lambda_0$  - wavelength of laser

$\theta$  - scattered angle

Finally the hydrodynamic diameter  $d_H$  can be calculated from the Stokes Einstein equation:

$$d_H = \frac{kT}{3\pi\eta D} \quad 3.6$$

Where:

$d_H$  - Hydrodynamic diameter

$k$  - Boltzmann's constant

$T$  - Absolute temperature

$\eta$  - Viscosity

$D$  - Translational diffusion coefficient

It is worth noting that for non spherical particles the effective hydrodynamic diameter is a diameter of a sphere with the same translational diffusion coefficient as the given particle.

Examples of calculated plots of normalized autocorrelation function as a function of particle sizes and the temperature are shown below. Figure 3.11a shows the shift of the decay of autocorrelation function as the diameter increases. Figure 3.11b shows how the autocorrelation function is shifted for particles with the same size caused by the increase of temperature.

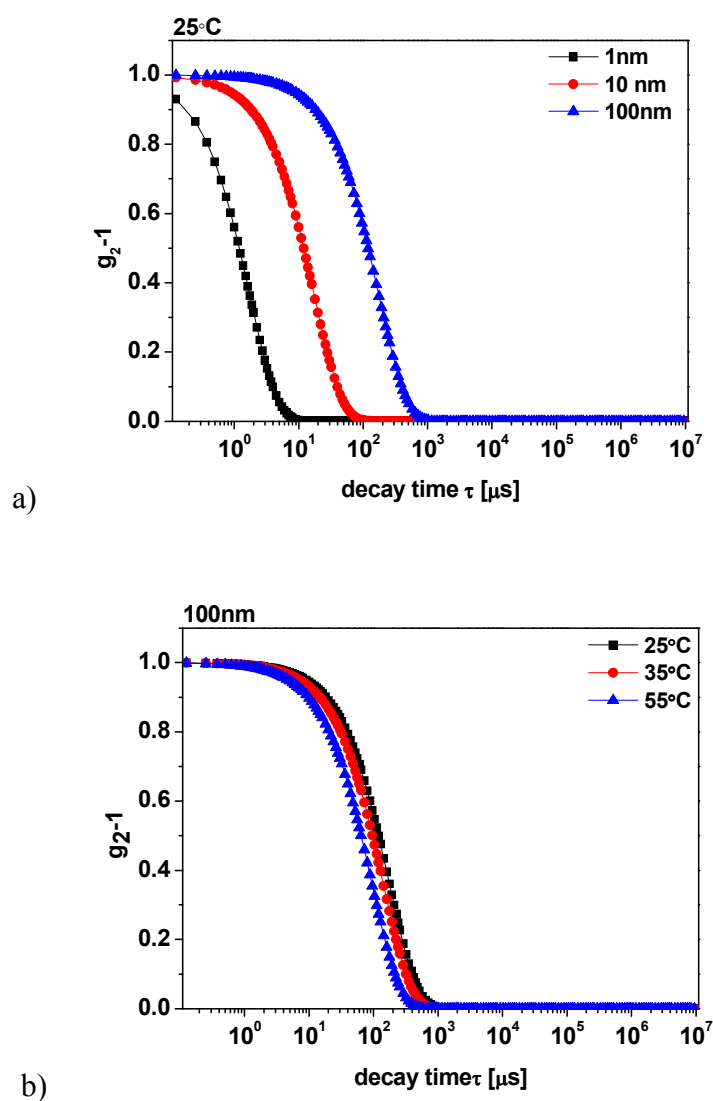


**Figure 3.11** Calculated normalized autocorrelation function decays a) for 3 different values of diameter at the same temperature b) showing the effect of temperature on the same size (100nm).

### 3.2.3.2 Turbidity

Turbidity is associated with solution cloudiness and is due to reduction of transparency caused by the presence of small particles of undissolved matter suspended in a solution. It can be quantified by measuring the intensity of transmitted light passing through the sample,  $I_t$ , which according to the Beer - Lambert law can be expressed by:

$$I_t = I_0 \cdot e^{-(\alpha+\tau)l} \quad 3.7$$

Where:

$I_0$  –incident intensity

$\alpha$  – absorption coefficient

$\tau$  – turbidity

$l$ - light path length

In the case of negligible absorption attenuation coefficient is equal to turbidity  $\tau$  and can be obtained from transmittance  $T$ .

$$\tau = -\left(\frac{1}{l}\right) (\ln T) \quad 3.8$$

Where the transmittance  $T$  is:

$$T = \left(\frac{I}{I_0}\right) \quad 3.9$$

In the light scattering sense the turbidity is a function of the wavelength of used light  $\lambda$ , scattering angle  $\theta$ , the size of particles  $r$ , and optical parameters of the particles and the medium like the refractive index  $n$ .

$$I_t = I_0 (\theta, \lambda, r, n) \quad 3.10$$

More detailed explanations of this scattering phenomenon (including multiple scattering) on aggregates and clusters was modelled and correlated with experiments by Soos [150].

Depending on the size of particles different light sources can be used. An IR turbidity sensor was used for measurement of scattering and transmission of relatively large particles up to 1 $\mu$ m [151]. Forward light scattering and light obscuration setup was made for measurement using monochromatic red light 690nm laser for polydisperse sample in flow through cell setup [152]. Measurement of the turbidity at different operating angles was shown for coagulating polydisperse suspensions [153]. Turbidity was reported to be used to predict the dissolution rate of poorly soluble drugs in submicron size up to 100nm. The measurements were done in the visible light range 500nm and 750nm [154].

Above examples show that different light source have been used for measurements of different sizes of particles. Thus, for example at visible light (350 - 720 nm), the strongest scattering response occurs with particle diameters approximately equal to the wavelength (near 0.4 $\mu$ m).

Relationships below give an indication of the general dependence connecting the wavelength of light and the intensity as functions of the size of particles [151, 155].

$$I_t \propto r^6 / \lambda^4 \quad \text{when } r < \lambda \quad 3.11$$

$$I_t \propto r^4 / \lambda^2 \quad \text{when } r \approx \lambda \quad 3.12$$

$$I_t \propto r^2 \quad \text{when } r > \lambda \quad 3.13$$

These equations can be very useful whilst choosing appropriate light sources for specific size ranges of particles.

### 3.2.4 XRD

X-Ray crystallography is seen as the most powerful technique for structural characterization of crystals in the solid state chemistry and materials science. It is widely used for the recognition of polymorphs and solvates because it gives full information about characteristics and the X-ray pattern unique for each chemical compound.

This analytical method is based on the diffraction phenomenon providing information about the geometry and shape of molecules and their mutual arrangement present in materials. If the dimensions of the diffracting object are comparable to the wavelength of the radiation a phenomenon called diffraction occurs. In order to analyse atoms in crystals X-rays with comparable wavelength (in the range of 0.02Å to 100Å) are used.

Incident X-rays are scattered in all directions by crystal planes, some waves will cancel out each other; some will constructively interfere with others in specific directions, resulting in an XRD pattern. This behaviour has been studied by William Lawrence Bragg, resulting in a law which gives conditions under which scattering signal give desirable diffraction pattern [156]. Bragg came up with an equation based on which we can establish the distance between atomic planes in a crystal structure.

$$n \lambda = 2d \sin \theta \quad 3.14$$

n – an integer number

$\lambda$  – wavelength

d – interatomic spacing between planes

$\theta$  – diffraction angle

This is derived as follows:

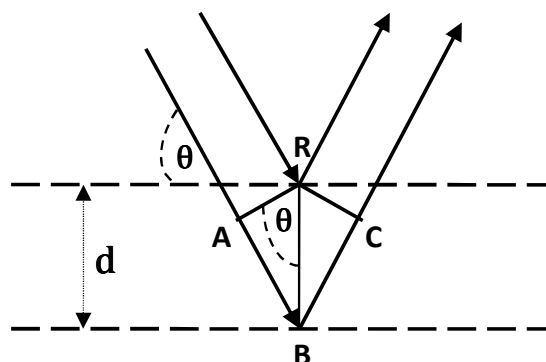


**Figure 3.12** Principles of XRD.

The path length difference  $\delta$  of two shown rays is a condition for them to be constructive at the same time it must be an integral number of wavelengths:

$$\delta = AB + BC = n \cdot \lambda \quad \text{and} \quad BR = d \quad 3.15$$

$$\sin \theta = \frac{AB}{RB} \quad 3.16$$

$$AB = (\sin \theta) \cdot RB = (\sin \theta) \cdot d \quad 3.17$$

$$\sin \theta = \frac{CB}{RB} \quad 3.18$$

$$CB = (\sin \theta) \cdot RB = (\sin \theta) \cdot d \quad 3.19$$

$$\delta = AB + BC = (\sin \theta) \cdot d + (\sin \theta) \cdot d = 2d \sin \theta = n \cdot \lambda \quad 3.20$$

An applet created by Konstantin Lukin available on the web [157] shows visual animation of the phenomenon of constructive and destructive interference of waves, depending on the angle, wavelength and the distance between crystal planes.

In powder XRD randomly orientated sample is irradiated with a monochromatic beam and diffraction at specific angles is measured giving a series of characteristic peaks and information about d- spacing between crystal planes.

Polymorphs differ from each other in their molecular packing trigger different X-ray patterns. As an example powder pattern of different polymorphs of carbamazepine is shown below.

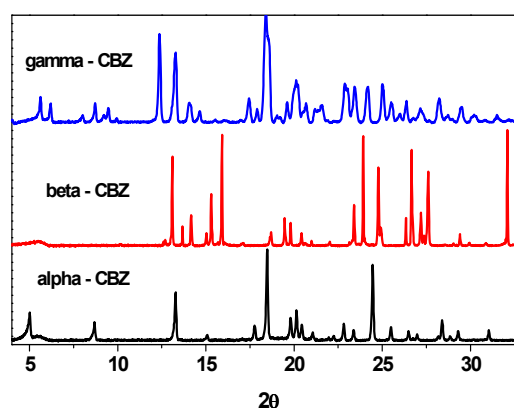


**Figure 3.13** XRD patterns of three polymorphs of CBZ.

Due to long range order in the crystalline material, the diffraction pattern has many sharp peaks corresponding to various crystal planes. Amorphous material has only short range order, but due to small atomic distances (tightly packed) has one or two broad maxima. In order to avoid preferential orientation of material sampled for XRD measurement it is usually grounded. However it is known that grinding can lead to creation of amorphous phase therefore attention must be paid to the preparation procedure.

This work studies crystallisation of the polymorphic system of CBZ. It has been reported [131, 133] that different polymorphic forms of CBZ have unit cells with different symmetries: form alpha is trigonal (Form II), beta p-monoclinic (Form III), gamma triclinic (form I) and form IV unit cell is c-monoclinic. XRD also can be used to determine quantitatively mixtures of polymorphs or solvates as well as the degree of crystallinity.

Transmission foil XRPD data was collected on a Bruker AXS D8-Advance transmission diffractometer equipped with  $\theta/\theta$  geometry, primary monochromated radiation ( $\text{Cu K}_{\alpha 1}$ ,  $\lambda=1.54056 \text{ \AA}$ ). Data was collected in the range  $4\text{-}35^\circ 2\theta$  with a  $0.015^\circ 2\theta$  step size and 1s/step count. Obtained data was compared with reference patterns [127] in program Eva.

### **3.3 Data presentation**

#### **3.3.1 Distributions**

For particles at a given composition, structure and morphology are the most important characteristic influencing their further processing and formulation into final products is their size. In the case of particulate disperse system or powder it is rare to observe all particle sizes to be the same (monodispersity) and most particulate system show distribution of sizes called polydispersity. Carefully planned and conducted particle sizing experiments can generate much useful data. In order to share them with others all results have to be presented in an effective, understandable fashion allowing for meaningful comparison. Data can be presented in tables, charts or diagrams, depending on the nature of the problem and obtained results. Below is a brief introduction to the complex problem of presenting data on Particle Size Distribution (PSD).

Solid particles unlike fluid bubbles or droplets are usually not spherical and in order to define appropriate particle size an equivalent diameter is used. It is defined as a diameter of a sphere having the same value of characteristic property as the particle of our interest.

In the case of realistic, not monodisperse particle suspensions it is not usually possible to specify particle size as a single number and the particle size distribution (PSD) is needed to properly present data [3, 111, 158, 159]. Distribution can be defined as a frequency of occurrence of each size of relevant particles. The quantities that can be used to describe a distribution can be: the number of particles, their surface, mass or volume.

In many literature sources dealing with particles and their sizing there is a degree of confusion in proper definitions for data presentation. The problem of improper presentation of particle size distributions has been highlighted by Sommer [159], who takes issue with an inconsistency in basic definitions of particle size density distribution.

Density distribution is used in a book by Allen [111] as a statistical representation of data and assigns measured values to specific channels or ranges of sizes. The author refers the relative frequency distributions and cumulative distributions.

Mullin [3] shows an example of data presentation on sieving and distinguishes fractional distribution as mass fraction of particles retained on each sieve of cumulative mass as oversize and undersize material.

Rhodes [158] states that PSD can be expressed as relative frequency distribution or differential and cumulative frequency distributions.

Number frequency distribution defined as a number of particle counts within a number of discrete intervals is compared to cumulative number distributions by Seville [2].

Therefore it is not always straightforward to choose the best method of PSD presentation because as seen above there are several ways to do it. However it appears the most appropriate to use is either cumulative or differential frequency distribution.

Cumulative frequency distribution  $Q(x)$  presents the amount of particles lower or equal to specific size (set threshold value). It is a dimensionless quantity ranging from 0 to 1 or 0 to 100% and it is less sensitive to the scatter of data. Therefore it is often preferred to the frequency distribution.

$$Q(x) = \frac{N_{\leq x}}{N_{all}} \quad 3.21$$

$N$  – amount of particles of specified size (lower or equal than  $x$ )

$N_{all}$  – amount of all particles

Differential distribution  $q(x)$  is a derivative of the cumulative distribution  $Q(x)$  with the respect to the characteristic value of  $x$  (described in Channel grouping section below).

$$q(x) = \frac{dQ(x)}{dx} \quad 3.22$$

Therefore the fraction of the number of particles in a specified interval can be obtained from an integral of the area under the curve of  $q(x)$  within those intervals limits. The total area under the curve is unity.

Both distributions may be represented in either discrete (Figure below 3.14 b) and d)) form or as a result of a drawing line between the tops frequency bars at the geometric mean point resulting in a continuous smooth line (Figure 3.14 a) and c)).

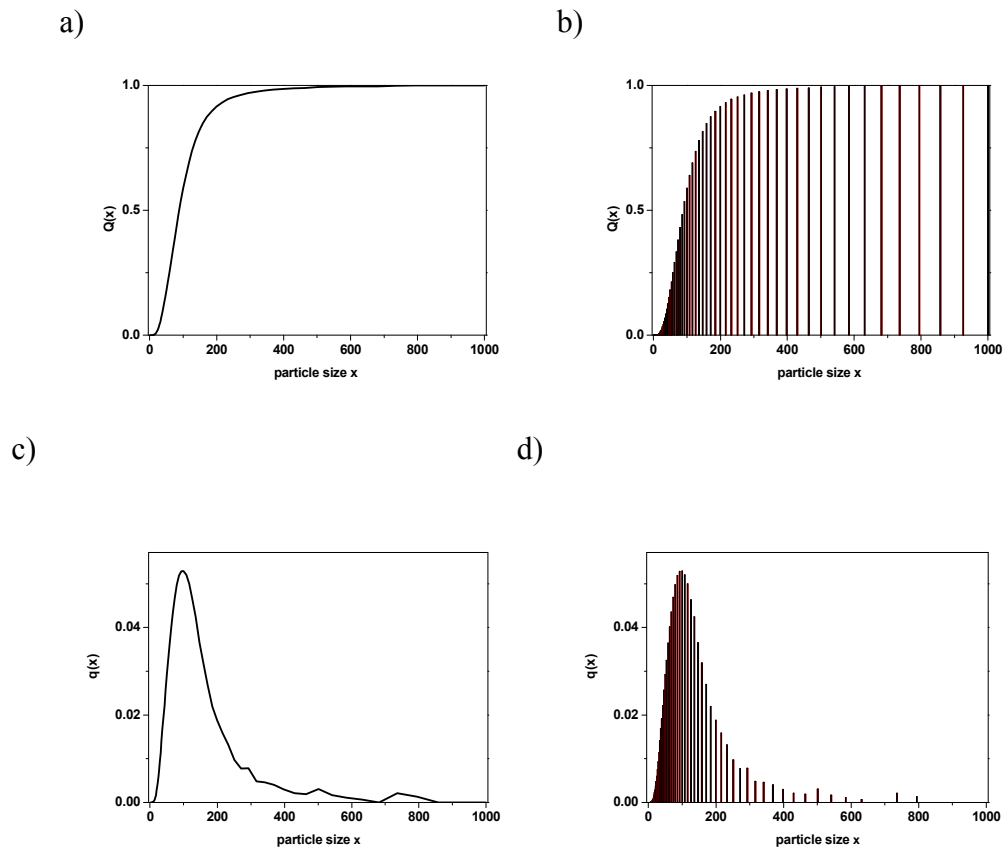


**Figure 3.14** Cumulative a) and b) and differential c) and d) frequency particle size distribution.

Frequently a representation of data as a single number is needed and an appropriate averaging must be done. Averaging is aimed to find a fair representation of a group of individual values in order to understand the group [111]. Thus we have mode, median and mean averaging (see Figure 3.15).

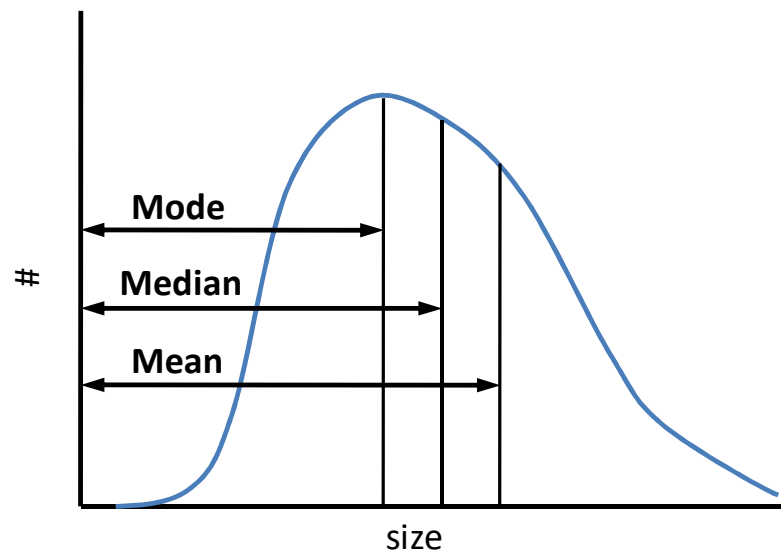


**Figure 3.15** Particle size distribution averages.

The mode is a value that is the most commonly used to present data and is the highest point of the curve. That means the most frequently occurring size.

Median value of particle sizes divides the populations in two equal parts with 50% of particles are below and 50% are above the median (it is the 50% size on the cumulative distribution curve and it splits distribution into two equal parts).

Mean is weighted average of distribution and for a given size distribution many differential ways of averaging can be defined as briefly described below.

### 3.3.2 Weighted distributions and averages

Often it is required to show results in the form of weighted distributions giving data on number, mass or volume distribution of a particulate population. The distribution weighting can be described on the example of data used in this work. As stated previously in section 3.2.2 in FBRM all counts are gathered in specific channels (corresponding to particle size range) and this way the size distribution is obtained unweighted, reflecting PSD (Particle Size Distribution) based on the number of particles of each size range. Appropriate weighting functions can be used to show PSD based on the length, volume, mass and so on. By the use of channel weighting

we can emphasize the change in one region while deemphasizing other region of the distribution. This can be used to track changes in all range of measurements [160] [112]. The  $j$ -th moments of PSD (expressed as  $N_i$  is the number based counts in channel  $i$ ) is defined as:

$$\mu_j = \sum N_i d_i^j \quad 3.23$$

$d_i$  - is the channel size representative (chord length)

Weighted frequency distribution  $w_j$  is defined as:

$$w_j = \frac{N_i d_i^j}{\mu_j} = \frac{N_i d_i^j}{\sum N_i d_i^j} \quad 3.24$$

The 0<sup>th</sup> moment  $\mu_0$  is unweighted equal to the total number of particles. The 1<sup>st</sup> moment is called number weighted, the 2<sup>nd</sup> moment is length weighted, the 3<sup>rd</sup> moment is surface weighted, the 4<sup>th</sup> is mass weighted etc.

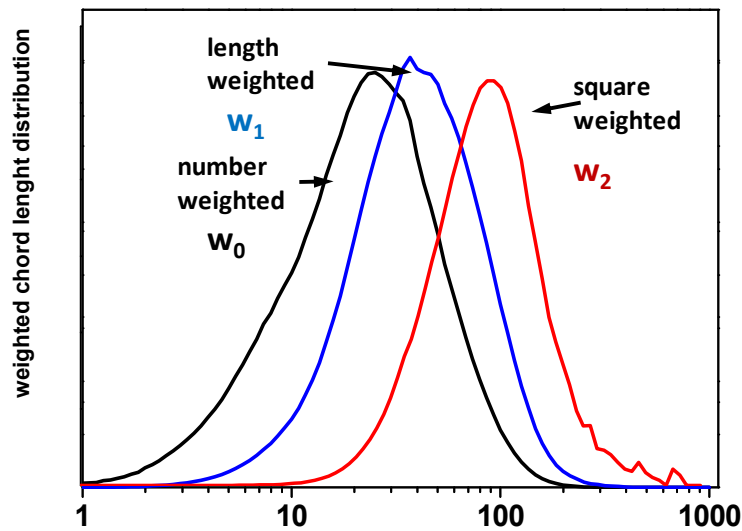


**Figure 3.16** Representation of channel weighting in FBRM. 0-number weighted, 1-length weighted, 2-square weighted.

In order to obtain differently weighted mean diameters, moment ratios of subsequent weightings are used to calculate mean chord length.

$$C_{j/j-1} = \frac{\mu_{j+1}}{\mu_j} = \frac{\sum N_i d_i^{j+1}}{\sum N_i d_i^j} \quad 3.25$$

The number weighted mean chord length  $C_{1/0}$  is sensitive to the smallest crystals in the PSD. With the increasing order  $j$  the mean chord length  $C_{j/j-1}$  we get averages more and more sensitive to bigger particles. We will be using means of order up to 6/5 moment to show ratio contributions of the largest particles.

In the light scattering experiments the size distribution generated by fitting scattering data is the intensity weighted distribution. This distributions can be converted to a volume or number weighted distribution by using Rayleigh – Debye equations [161]. The differences in number, volume and intensity weighted distribution can be shown on the example of two populations in bimodal mixture of particles of 5nm and 50nm present in equal numbers (Figure 3.17).

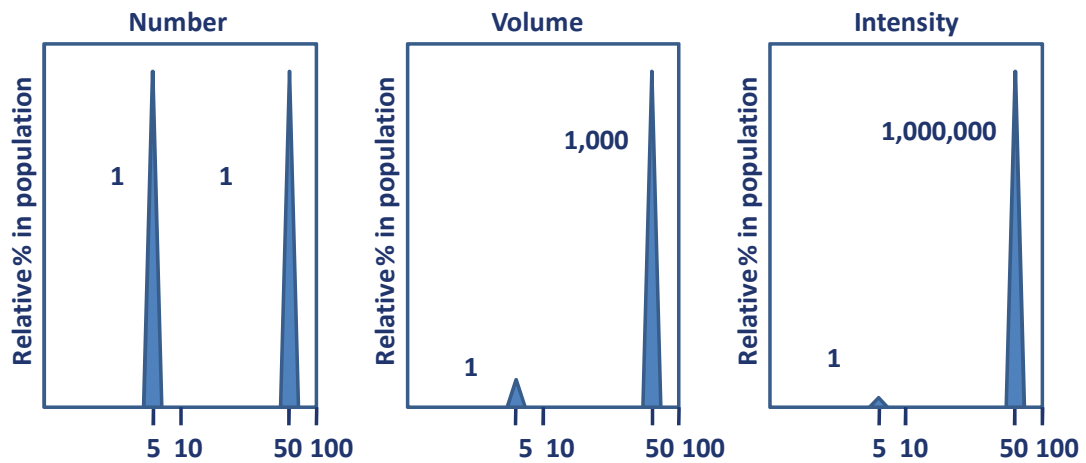


**Figure 3.17** Distributions in light scattering experiments.

### 3.3.3 Channel grouping

The characteristic parameters used to define PSD and the range width between set size points play a crucial role in data presentation. Some instruments allow the user to specify the limits of sizing intervals. Frequently the size range limits however are not set by users and then in order to compare data with different intervals appropriate representations need to be used (see section 3.2.2). Different channel grouping affects the data display and mean size calculations. The most common grouping used for size ranges are linear or logarithmic, former changing linearly and having equal width, while for the latter each channel gets progressively wider by a fixed proportion while they appear to have equal width on the log axis. Semi logarithmic plots are often used when particle size distribution spans over several orders of magnitude, and the size is displayed in logarithmic coordinate.

Logarithmically spaced channels are commonly used in FBRM. This is illustrated in Figure 3.18, where the channel size is plotted as a function of channel number for the size range of 1-1000  $\mu\text{m}$  and 90 channels.

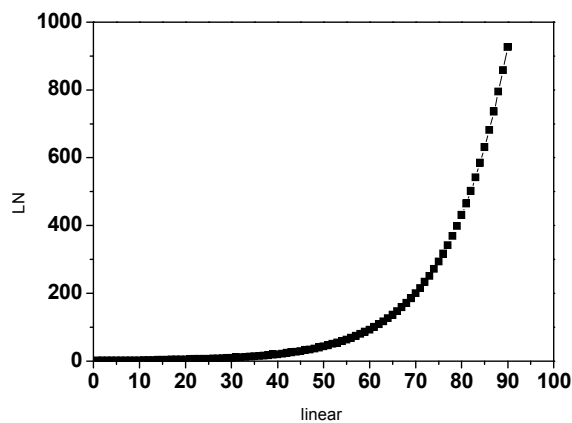


**Figure 3.18** Linear vs logarithmic coordinates.

In logarithmic distribution it can be clearly seen that the channel width is subsequentially increasing and therefore a wider range of particle sizes falls into one channel. Presentation of obtained data will therefore vary significantly depending on the size of channels.

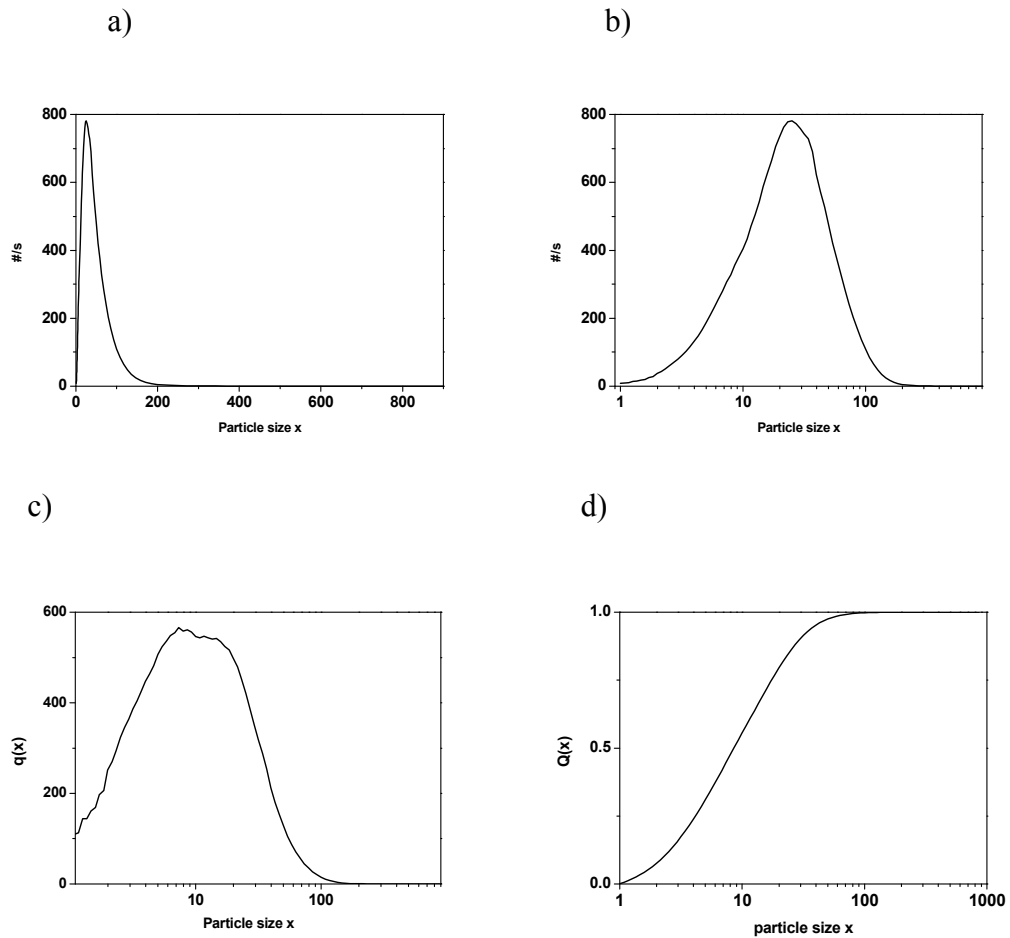


**Figure 3.19** Linear a) semilogarithmic b) differential frequency c) and cumulative frequency d) data presentation of the same set of data.

The Figures 3.19 show how important it is to specify the method in which presented data are gathered and shown.

The channel width has a significant impact on the data display. The plot below shows the same results with logarithmic grouping but for two different types of channel width. They differ in size, the second having a third less channels.

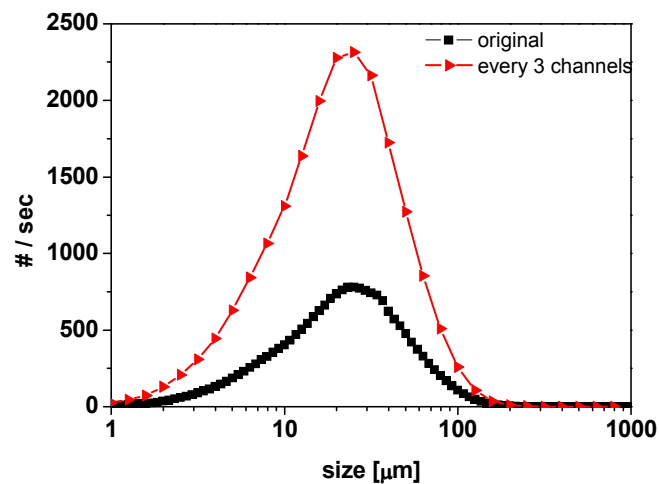


**Figure 3.20** Influence of changed width on presentation of count numbers.

All above examples of the influence of mathematical operations done on obtained data show how important it is to clearly present and interpret the results of the data on the distribution of size of particles. The arrangement of channels, their width, weighting etc are crucial when comparing differently presented results.

It is thought that proper and consistent interpretation of data obtained from different particle sizing is still a big issue requiring a lot of attention [159]. It is recommended that representation of data should be unified to facilitate better understanding of presented results and manufacturers of particle measurement instruments should pay more attention to improve clarity of their data presentation.

### 3.3.4 FBRM presentation

In this work weighted FBRM results are shown on single logarithmic and double logarithmic scale which is most suitable to following the largest crystals. Fitting of the data from the tail of distribution of log – log graph is used to show what is happening to the biggest crystals, as shown in the Appendix.

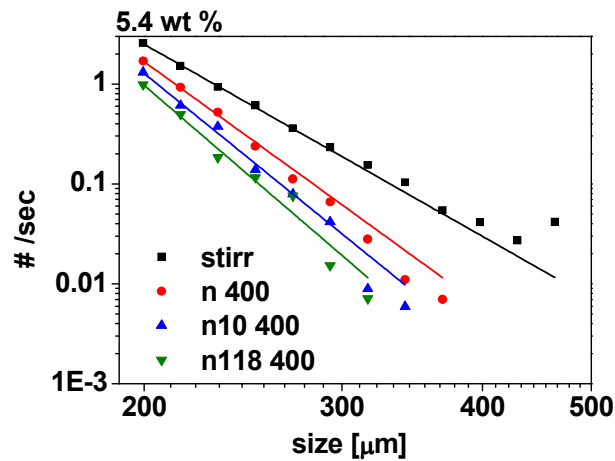


**Figure 3.21** Example of fitting functions for obtained PSD data.

All fits were calculated in Origin8 as allometric first order function with the equation in the following form:

$$y = a \cdot x^b \quad 3.26$$

Obtained values of  $a$  and  $b$  are the best estimates of parameters obtained from fitting experimental data as shown in the table below:

Experiment	Parameter	Value	Standard Error
stirr	a	1.20474E15	6.50938E14
	b	-6.38161	0.10113
n400	a	8.82881E18	8.38082E18
	b	-8.13658	0.17819
n10 400	a	1.1603E21	2.28423E21
	b	-9.1090	0.36995
n118 400	a	1.65858E22	4.13659E22
	b	-9.6626	0.46892

**Table 3.2** Calculated parameters for fitted experimental results.

## CHAPTER 4 CRYSTALLISATION AND POLYMORPHISM OF CARBAMAZEPINE

### 4.1 The effect of flow on polymorphic outcome of carbamazepine crystallisation

Previously reported literature indicates that experimental conditions such as solvent and cooling rate determine the obtained polymorphic form of CBZ. The cooling of supersaturated CBZ solution in ethanol to 5°C and keeping at this temperature for 5h was reported to lead to alpha form [132] while slow evaporation of ethanol solutions at ambient temperature of 21°C gave beta form [131]. Unfortunately no data on the stirring/no stirring conditions were given. In this section we show that it is possible to get different polymorphic outcomes depending on flow conditions when all other parameters are kept constant, and we investigate other factors, such as air-liquid interface and soluble impurities on polymorphic outcome in CBZ crystallisation.

#### 4.1.1 Experimental procedure

Carbamazepine (CBZ) and anhydrous ethanol (99.8% v/v over molecular sieves) were supplied by Sigma-Aldrich. Commercial CBZ powders were kept in the fridge at 4°C. Solutions of carbamazepine in ethanol at concentrations from 3 to 5g<sub>CBZ</sub>/100ml<sub>EtOH</sub> were prepared by dissolution with stirring on a magnetic stirrer in a glass bottle placed in the incubator (Stuart Scientific, Incubator S.I.60) at 56°C. Clear undersaturated solutions were filtered with syringe filters, using 0.45µm PTFE (Nalgene) or 0.1µm Anotop 10 (Whatman) filters. All accessories were kept in the incubator at 56°C to avoid supersaturation of the solution and unwanted nucleation. Filtered solutions were placed in bottles (details given in section 4.1.2) and then cooled under stirring or quiescent conditions as illustrated in Figure 4.1. Solubility data for CBZ in ethanol shown in Figure 4.1 was taken from Qu [162]. Two data points were checked experimentally at 24°C and 35°C by gravimetry and they agreed with the previously published data within 3.5%.

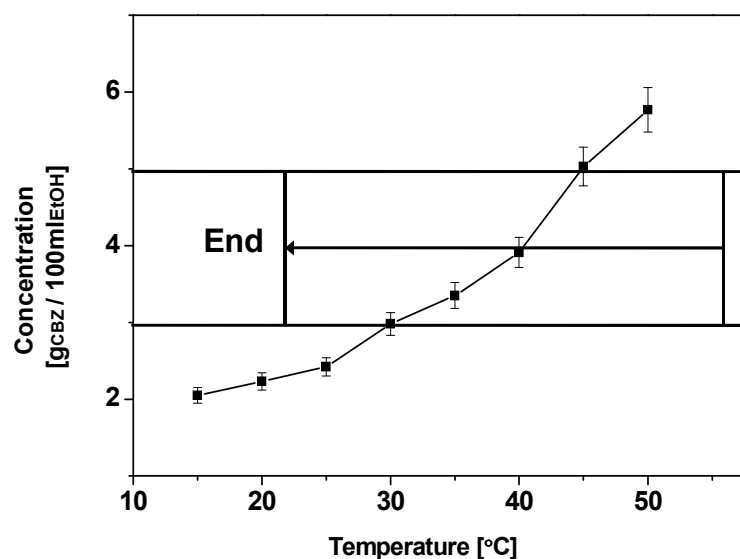


**Figure 4.1** Schematic diagram illustrating range of experimental conditions investigated. CBZ solubility in EtOH is also shown.

Recrystallisation of CBZ was done from ethanol solutions prepared at 56°C by cooling to 21°C with stirring, followed by growth of beta form crystals for around 2 hours, filtration (vacuum Millipore filtration setup with membrane filters HVLP 0.45µm pore size), drying in the oven at 50-70°C for 3 hours and storage in the desiccator at ambient temperature of 21°C. Alpha form crystals were obtained by cooling CBZ solutions in ethanol at 5°C without stirring. Crystals were allowed to grow for around 2-5 hours when 5.0g<sub>CBZ</sub>/100ml<sub>EtOH</sub> solution was crystallised. The obtained crystal slurries were vacuum filtered with 0.45µm PTFE membrane filters, dried and characterised with microscopy and powder XRD. Transmission foil XRPD data were collected on a Bruker AXS D8-Advance transmission diffractometer equipped with  $\theta/\theta$  geometry, primary monochromated radiation (Cu  $K_{\alpha 1}$ ,  $\lambda=1.54056$  Å). Data was collected in the range 4-35° $2\theta$  with a 0.015°  $2\theta$  step size and 1s/step count and compared with reference patterns [127] in the program Eva.

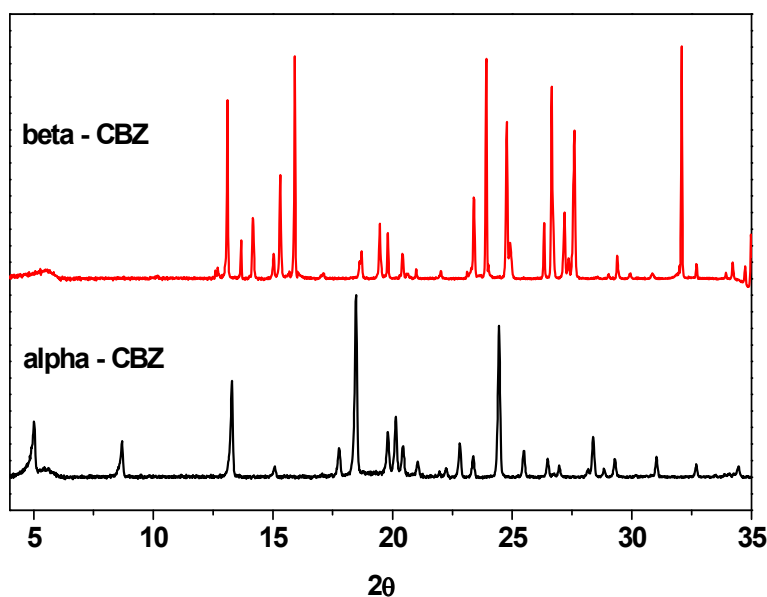


**Figure 4.2** XRD reference patterns of CBZ beta form (commercial) and alpha form (prepared in house).

#### 4.1.2 Effect of stirring

Our investigation was motivated by the initial observations of stirring effects on the polymorphic outcome of cooling crystallisation of CBZ from anhydrous ethanol. We studied carbamazepine solutions of  $3.5\text{g}_{\text{CBZ}}/100\text{ml}_{\text{EtOH}}$  and  $5\text{g}_{\text{CBZ}}/100\text{ml}_{\text{EtOH}}$  using the commercial CBZ source, starting from equilibrated undersaturated solutions prepared at  $56^\circ\text{C}$  in an incubator. In order to induce crystallisation, bottles (glass bottles ID=12.5mm x 36mm height, neck ID=11mm x 8mm height, nominal volume 4.4 ml, total volume 5.1 ml when completely filled, from Chromacol) were stirred on a magnetic stirrer (Magnetic mixer HANNA Instruments HI200M) with identical magnetic stirrer bars (flea micro magnetic spin bar LxD 12x3mm), then removed from the incubator to the lab bench (ambient temperature  $21^\circ\text{C}$ ) and kept there either under quiescent conditions or under magnetic stirring.

In quiescent solutions long needle-like alpha form crystals (Figure 4.3a) appear after hours to days (depending on supersaturation). If left in the solution, they gradually transform over several hours or days to fewer relatively large beta form crystals

(Figure 4.3b). The speed of transformation depends on supersaturation as well as on flow conditions. Even slight shaking of the bottle speeds up the transformation from alpha to beta form significantly.



**Figure 4.3** Microscopic images of carbamazepine crystals produced under quiescent and stirring conditions. a) Quiescent: large alpha form crystals slowly appear; b) Quiescent: alpha form crystals are gradually turning into few large beta form; c) Stirring: small beta form crystals appear initially at shorter induction times.

We note that supersaturated solutions were filtered through submicron size filters before being placed in clean bottles in order to rule out contamination with macroscopic solid impurities. The effect of the filter used was found not to be significant, as indicated by tests where the same solutions were split into two batches, one filtered with 0.45µm PTFE filter and the other one with 0.1µm Anotop filter. No differences of polymorphic outcomes (alpha form in quiescent and beta form under stirring) were observed whether using any of these filters or indeed none at all.

Interestingly, in several magnetic stirring experiments it has been observed that visible (up to couple millimetres), macroscopically ordered, wire-like structures (some curved and some straight) appeared before the induction time. The observed solid structures may be amorphous or poly/crystalline (possibly containing alpha form). These solids disappeared following the onset of turbidity where small beta form crystals formed. Figure 4.4 shows microscopic images of these observed solid forms together with few small beta form crystals, a) and b), and resulting beta crystals formed well after the induction time, c).

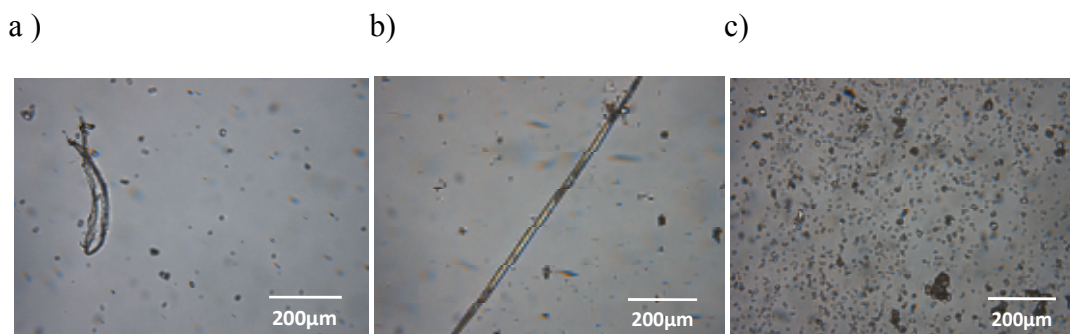


**Figure 4.4** Microscopic images of structures observed before the onset of turbidity during cooling crystallisation under stirring conditions a), b), and image of fine beta form crystals in turbid suspensions after induction time c).

#### 4.1.3 Effect of cooling rate, supersaturation and air-liquid interface

In order to investigate the dependence of polymorphic outcome on the cooling profile, three different cooling profiles have been applied:

-slow cooling: gradual lowering of temperature in the incubator by 5°C every 20 minutes from 56°C to 21°C

-fast cooling: moving the bottle out of the incubator on the lab bench (21°C)

-ice cooling: bottles with crystallising solutions were moved to water – ice bath with 4°C, kept for the whole duration of the crystallisation process.

A typical temperature evolution in the solution measured by a thermocouple inserted inside the bottle is shown in Figure 4.5 and it was found to be similar for both stirred and quiescent solutions for this specific setup.

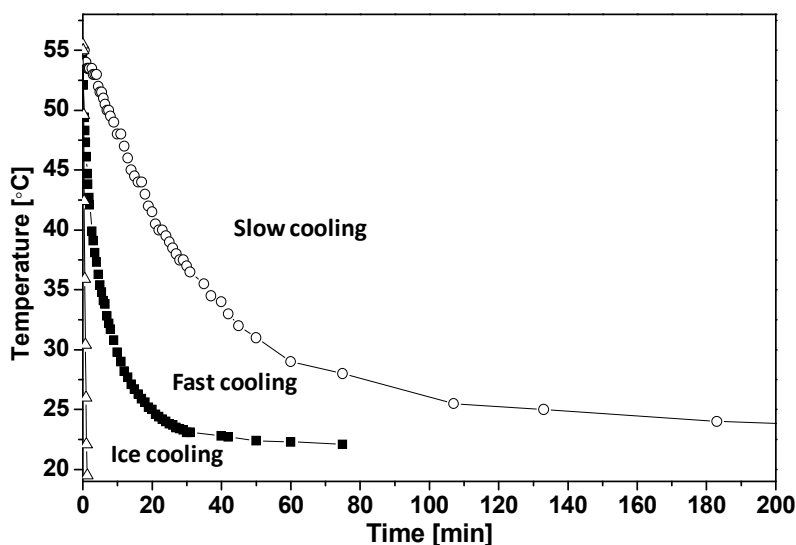


**Figure 4.5** Cooling profiles measured in bottles under stirring conditions.

It was found that while the cooling profile had an impact on the observed induction time as expected (faster cooling resulting in shorter induction time); it did not influence the polymorphic outcome. In all cases, well developed alpha form crystals slowly appeared under quiescent conditions and then underwent transformation to large beta form crystals over an extended period of time. In contrast, stirring typically resulted in the appearance of many small beta form crystals. Therefore we can conclude that stirring appears to be an important factor influencing the initially obtained polymorphic form, while the cooling rate and supersaturation (under the range of conditions investigated here) seems to influence primarily the rates of nucleation and/or subsequent phase transformation.

In order to investigate some other possible effects impacting on polymorphic outcome, we focused on the role of air-liquid interfaces.

The issue of air – liquid interface assisting nucleation of a certain polymorph was studied in a series of experiments using either partially or completely filled bottles for solutions with CBZ concentrations of  $3.5\text{g}_{\text{CBZ}}/100\text{ml}_{\text{EtOH}}$ . The nominal volume of bottles used was 4.4ml but increased to 5.1 when the bottle was completely full (with the neck). Solutions were prepared at  $56^\circ\text{C}$ , filtered with  $0.45\mu\text{m}$  PTFE syringe filters in the incubator and cooled down in constant temperature room ( $22^\circ\text{C}$ ) while

stirred with the speed ranging from 600 to 900 to 1500rpm. During that stirring created vortex had the height of +/- 10mm for partially filled bottles for medium stirring speed (see Figure 4.6) and no visible vortex for completely filled bottles as the volume of air trapped in the bottle was less than 0.3ml.

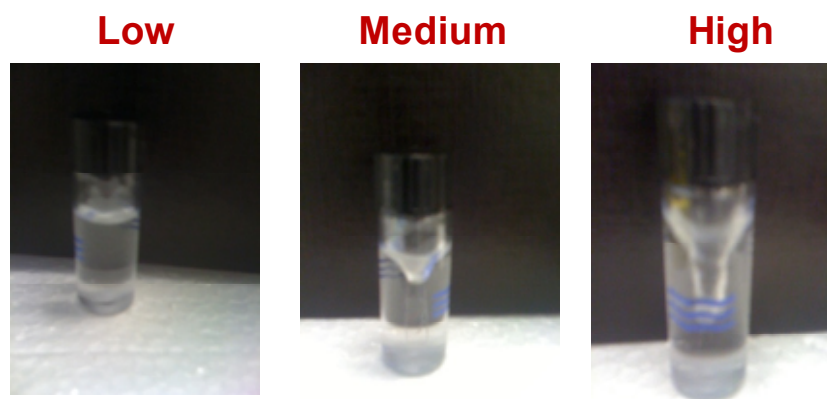
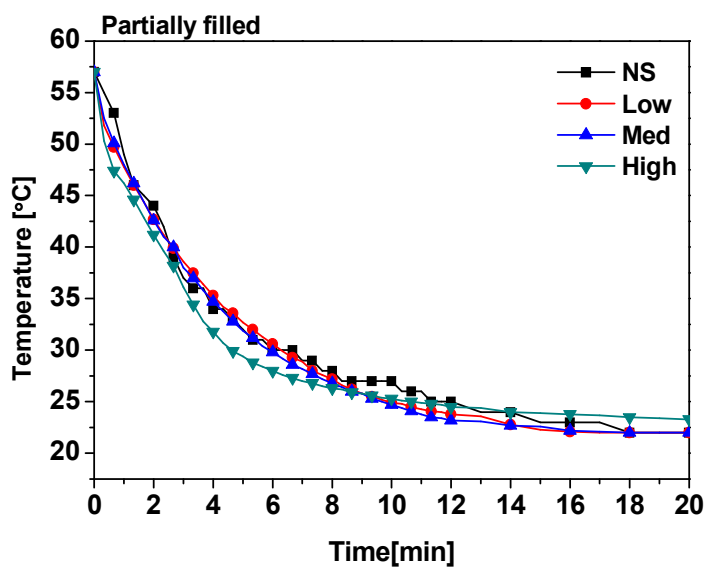
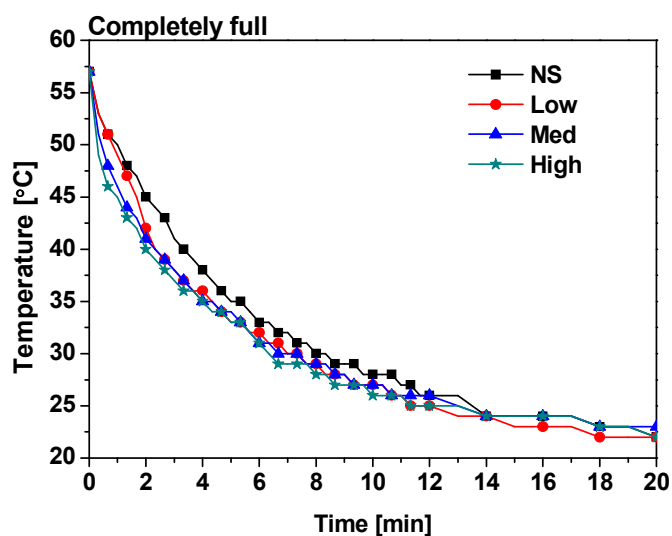


**Figure 4.6** Pictures of stirred bottles with vortexes corresponding to various stirring speed for partially filled bottles.

Corresponding cooling profiles are shown in Figure 4.7 and are similar at all stirring speeds Low (600rpm), Medium (900rpm), and High (1500rpm) speed with an additional cooling profile for unstirred solutions.



a)



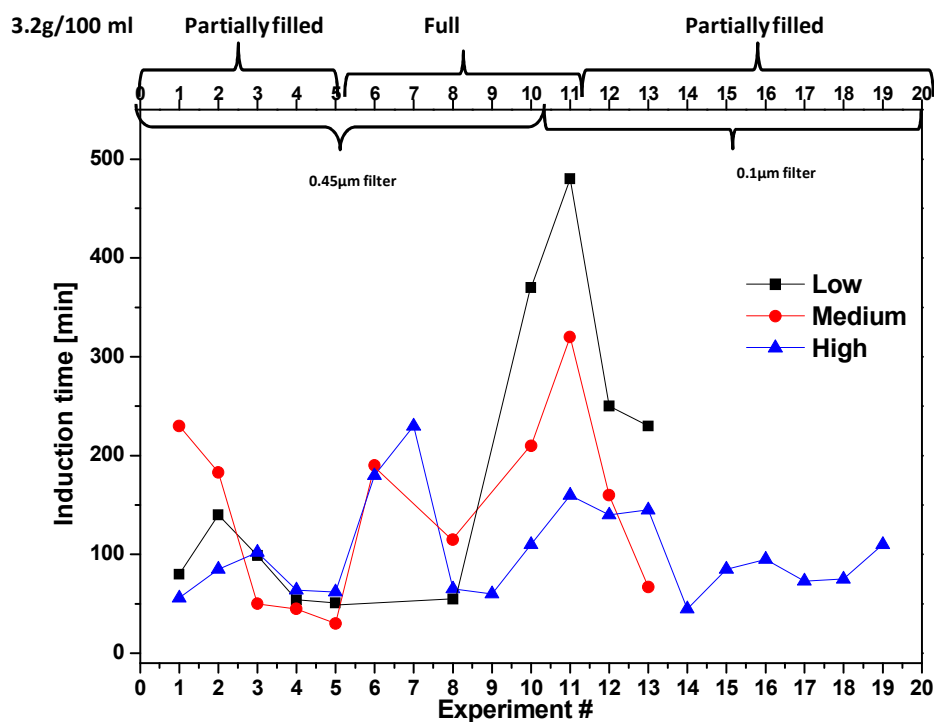
b)

**Figure 4.7** Cooling profile for a) partially filled (3.3ml) and b) full (5.1ml) bottle.

An extensive set of visual observations was conducted to record induction times for a range of solution concentrations, stirring speeds, filtration procedures and volume of crystallising solution (full and partially filled bottles).

Obtained induction times for all experiments are listed in Table 8.1 in the Appendix. Selected results for ambient temperature 21°C and 22°C and 3.2 and 3.5g<sub>CBZ</sub>/100ml<sub>EtOH</sub> are plotted in Figure 4.8, where data are grouped depending on the volume of crystallising solutions partially filled bottle vs. full bottle, used filter and the speed of stirring.

a)



b)

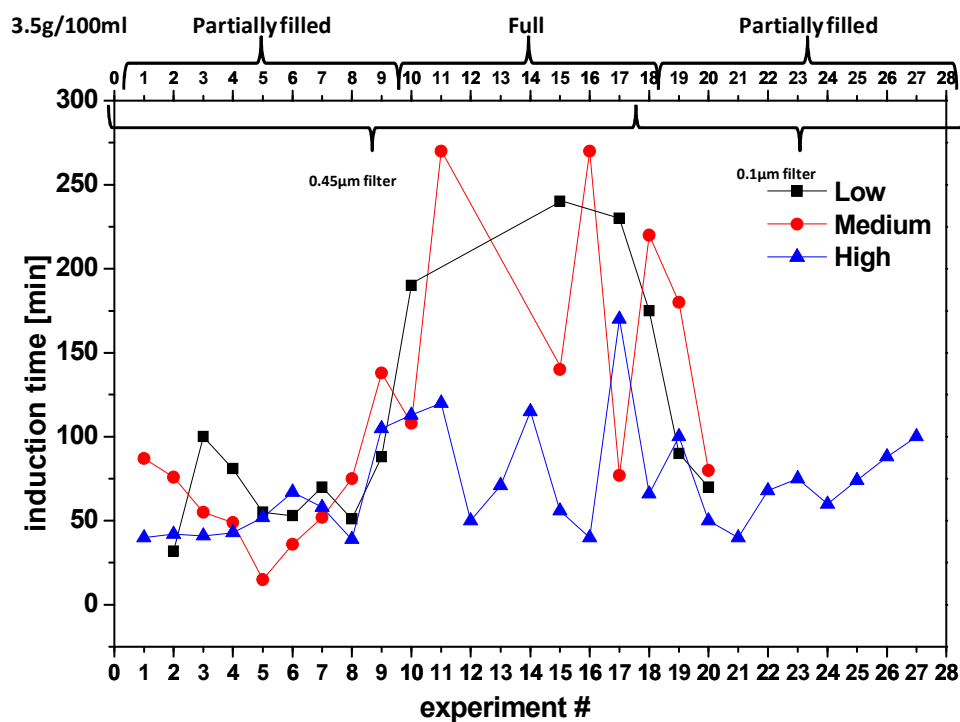


Figure 4.8 Induction times for a) 3.2 and b) 3.5g<sub>CBZ</sub>/100ml<sub>EtOH</sub> for three stirring speeds (Low, Medium or High) and for two volumes: full and partially filled bottles.

Induction times for both values of concentration show significant distribution of values upon repetition as is usual for processes of stochastic nature as nucleation. Narrower distribution of induction times were observed for partially filled bottles at all values of speed. A higher concentration of  $3.5\text{g}_{\text{CBZ}}/100\text{ml}_{\text{EtOH}}$  also resulted in a lower spread of obtained induction time values especially at high stirring speed. The highest values of induction times are observed for filled bottles, at slow and medium stirring speeds. Filtering of solutions was found not to significantly influence obtained induction times.

The table below shows the average induction times and corresponding standard deviations depending on the stirring speed and the presence of air-liquid interface. Induction times were grouped and averaged for all results for each concentration (both partially and fully filled bottles) or separately.

Volume	Low			Medium			High		
	N	A	SD	N	A	SD	N	A	SD
<b>Together</b>	10	177	148	11	145	92	19	102	49
<b>Partially filled</b>	7	123	73	7	109	80	13	88	31
<b>Full</b>	3	302	221	4	209	85	6	134	68

**Table 4.1** Number of experiments, Average value and Standard deviation of induction time (in minutes) for  $3.2\text{g}_{\text{CBZ}}/100\text{ml}_{\text{EtOH}}$ .

A significant variability of results is observed for  $3.2\text{g}_{\text{CBZ}}/100\text{ml}_{\text{EtOH}}$ . It can be seen that the calculated standard deviation values are higher for the full bottles as well as average induction times. Average values of induction times are the highest for the low stirring speed and reach the value of 302 minutes for the full bottle and the low stirring speed. The shortest induction times are observed for the high stirring speed and partially filled vial with the lowest value of standard deviation.

A similar set of results is presented for the higher concentration  $3.5\text{g}_{\text{CBZ}}/100\text{ml}_{\text{EtOH}}$  and three values of stirring speed together with full or partially filled bottles.

Volume	Low			Medium			High		
	N	A	SD	N	A	SD	N	A	SD
<b>Together</b>	15	128	101	17	113	79	27	72	32
<b>Partially full</b>	5	247	21	6	180	47	9	89	23
<b>Full</b>	10	69	90	11	77	84	18	63	43

**Table 4.2** Number of experiments, Average value and Standard deviation of induction times (in minutes) for 3.5g<sub>CBZ</sub>/100ml<sub>EIOH</sub>.

A lower spread of induction times was observed for the higher concentration 3.5g<sub>CBZ</sub>/100ml<sub>EIOH</sub>. It can be seen that the standard deviation is lowest for high stirring speed and the highest for the low speed. Average values of induction times are again higher for the low stirring speed and lower for the high stirring speed. Interestingly, experiments in partially filled bottles and low stirring speed have the highest average induction time but relatively low standard deviation (based on only 5 experiments though).

The purpose of the plot below (Figure 4.9) is to attempt to delineate regions in the time-concentration space where unique patterns of behaviour in terms of polymorphic outcome are observed. To complete the picture, under quiescent conditions, time of appearance of first visible alpha form crystals (few and relatively large, so that suspensions are not appreciably turbid) was taken as the induction time.

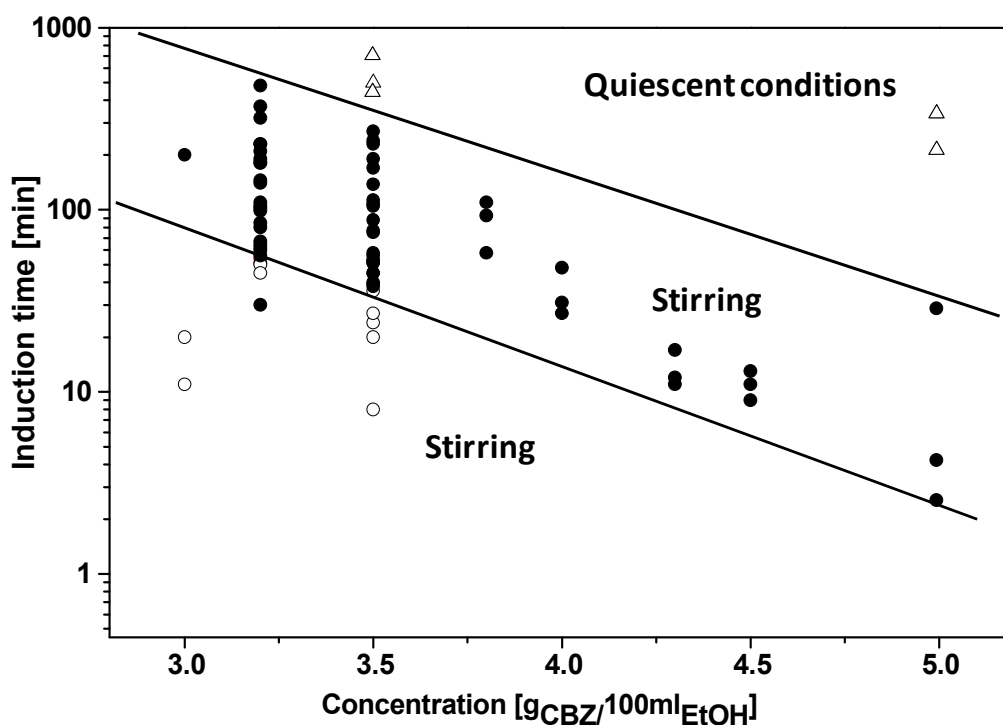


**Figure 4.9** Induction time plot. Open symbols for alpha form observed initially, closed symbols for beta form. Circles indicate stirring conditions, triangles correspond to quiescent conditions.

As noted before there is a significant distribution of induction times due to the fact that the data reported here are aggregated from experiments in partially and fully filled bottles as well as at several stirring speeds.

Induction time results taken for a wider range of concentrations (taken from all in the large Table 8.1 in the Appendix) shows clearly three regions of induction times and resulting forms. The middle region represents all experiments where beta form has been obtained. Outside the middle region alpha form has been obtained under conditions representing two distinct cases. Above the middle region, alpha form is crystallised at relatively long times without stirring, while below many small alpha form needle like crystals are initially observed under stirring conditions when the shortest induction times were recorded (due to faster cooling at lower ambient temperature or when recrystallised (purified) CBZ was used).

#### 4.1.4 The effect of CBZ source and the transformation into stable form

The issue of soluble impurities in the commercial CBZ powder was addressed through purification by recrystallisation. Using of recrystallised in house carbamazepine had a very significant effect on the observed induction times and the appearance of turbidity where the initial turbidity was due to the small alpha form crystals transforming fairly rapidly into small beta form crystals. It was typically observed that for  $3.5\text{g}_{\text{CBZ}}/100\text{ml}_{\text{EtOH}}$  turbidity was developed within less than 30 minutes.

These initially obtained from recrystallised CBZ alpha form crystals would then relatively quickly transform into stable beta form, as illustrated in Figure 4.10.



**Figure 4.10** Transformation in turbid solution (obtained within 7-30 mins from the start) from alpha form to stable beta form (microscopic images of samples withdrawn from turbid suspensions).

The transformation of alpha form to beta form visualized by images above was also monitored by the powder XRD. Samples were withdrawn from turbid suspensions, filtered and dried and characterised. It can be clearly seen that observed powder XRD patterns are in qualitative agreement with visual observations and microscopic images above.

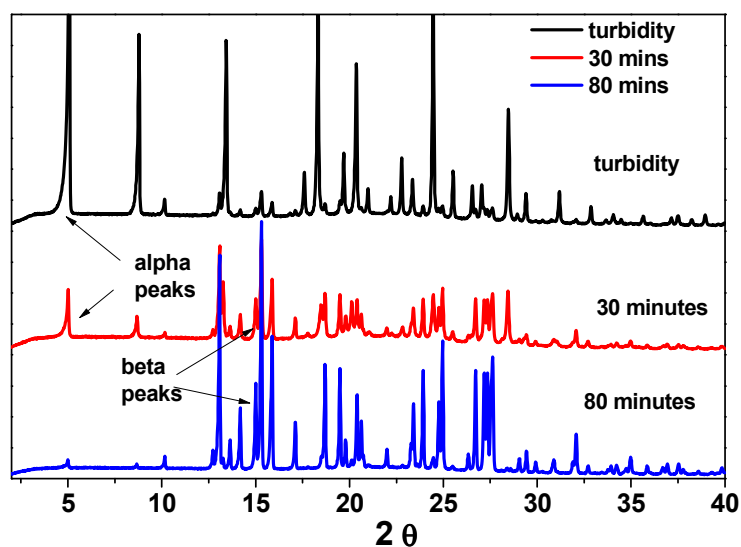


**Figure 4.11** Transformation of turbid alpha solution into beta with characteristic for each form peaks.

On the contrary, solutions that become turbid after more than 30 mins always contained predominantly small beta crystals at the onset of turbidity. The typical induction times for solutions prepared from commercial CBZ powder ranged from 30 minutes up to 3 hours, as seen in Figure 4.12.

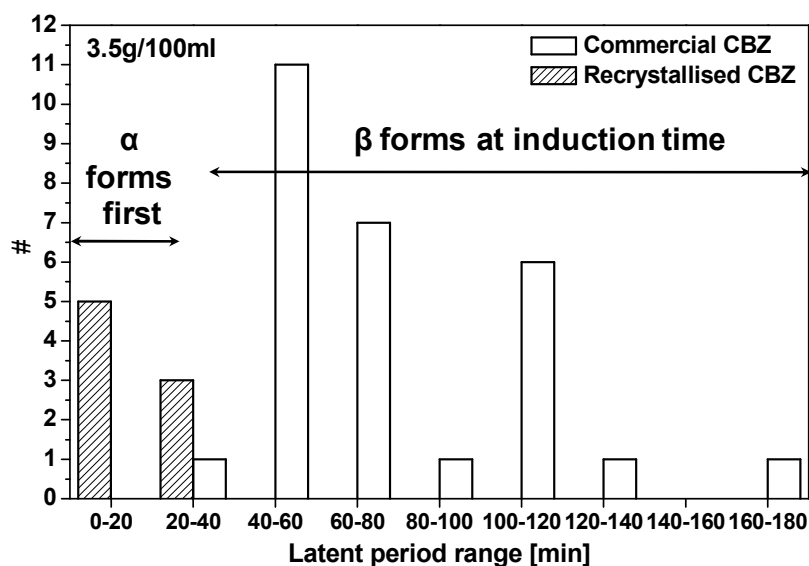


**Figure 4.12** Distribution of induction times for 3.5g<sub>CBZ</sub>/100ml<sub>EtOH</sub> solutions using two sources of CBZ: commercial and recrystallised in house.

In order to exclude the possible seeding effect due to the hypothetical presence of alpha form crystals in recrystallised CBZ, conceivably accelerating nucleation of alpha form, several seeding experiments were performed. Solutions of 3.5g/100ml<sub>EtOH</sub> of the commercial CBZ in ethanol were prepared at 56 °C and filtered with 0.45µm PTFE into identical bottles.

Seeds were added after 5 minutes from the start when the temperature was lower than the solubility of the stable form.

Used seeds are shown in Figure 4.13.

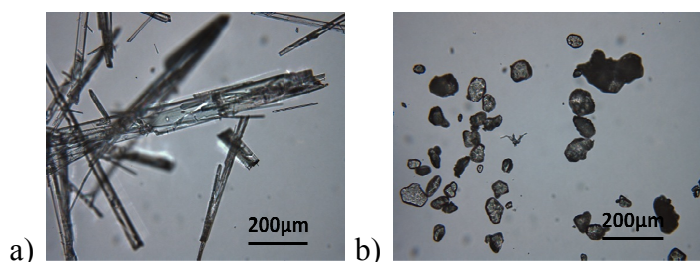


**Figure 4.13** Seeds used in experiments a) alpha and b) beta.

The aim was to assess the effect of seeding in comparison to unseeded solution under stirring conditions.

A resulting form of initial turbidity for results carried at 17°C was the alpha form (Figure 4.14a) and beta form for all experiments at 21°C (Figure 4.14b).

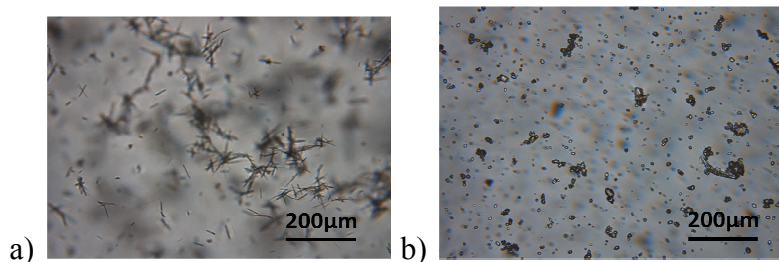


**Figure 4.14** Turbidity pictures when using seeds at a) 17°C and b) 21° C.

The above results show that seeding of unstable alpha form was not the reason for resulting short induction times with alpha turbidity when recrystallised CBZ was used.

The observed change of polymorphic outcome under stirring conditions depending on the source of CBZ is not easy to rationalise. It can be assumed that despite

identical XRD patterns of recrystallised and commercial CBZ there must be some differences between these powders. It is possible that recrystallisation of commercial CBZ results in removal of some unknown impurities present at low or trace levels. Unfortunately it was not possible to obtain any specifications of the production process. There may be impurities present in the commercial CBZ powder coming from industrial manufacturing of carbamazepine [163]. We note a paper on the production of oxcarbazepine indicating that traces of NaOCN/HCl may be present [163].

As mentioned previously humidity/water content can also influence the nucleation process significantly. During crystallisation using recrystallised CBZ when laboratory grade ethanol was used (or when few drops water was added to the HPLC grade ethanol) initial turbidity was coming from the stable beta form. It seems that traces of water may hinder the nucleation of metastable alpha form and/or promote direct nucleation of stable beta form. We also note that solubility of carbamazepine changes dramatically when water is present [135]. Water content in laboratory grade and HPLC grade (used in experiments) has been checked with Karl Fisher analysis (MT DL39) and it was found that in laboratory grade ethanol water content was around 250ppm while in the HPLC grade it was around 50ppm.

#### **4.1.5 Discussion**

Stirring was found to be the key controlling factor for the polymorphic outcome in CBZ cooling crystallisation from ethanol. For quiescent conditions, long needle-like crystals of alpha form were formed from clear solutions, and then further slowly transformed to a few large beta form crystals. In the case of sufficiently vigorous stirring, few well-ordered large precipitates were often observed initially, followed by the onset of turbidity due to formation of a large number of small beta form crystals. Cooling rate under quiescent conditions was found not to affect the polymorphic outcome. However in experiments with the shortest induction times (below 20 minutes for concentrations of 3.5gCBZ/100ml<sub>EtOH</sub>) the onset of turbidity was observed to some from many small needle-like alpha form crystals. Shorter

induction times were recorded either by faster cooling or, more interestingly by using recrystallised CBZ.

Under those circumstances large number of small alpha form crystals were formed rapidly under stirring conditions and then relatively rapidly transformed to small crystals of beta form.

These observations lead to hypothesis that there may be some impurities in the commercial CBZ powder. Seeding experiments excluded the possibility of alpha form seeding when using recrystallised CBZ.

In order to rationalise our observation that stirring influences nucleation of particulate polymorph in CBZ solutions we speculate that the supersaturated carbamazepine solutions may perhaps undergo microphase separation to liquid-like phases at a micron or submicron scale, the denser one of which being a location of subsequent nucleation. The size of denser liquid domains and corresponding interfacial areas can then be expected to be responsive to flow conditions, which may provide a possible explanation of sensitivity of the polymorphic outcome to stirring conditions. Stirring causes flow pattern to change hindering the change in the size of dense liquid domains as well as speeding up mass transfer and the achievement of thermodynamical equilibrium.

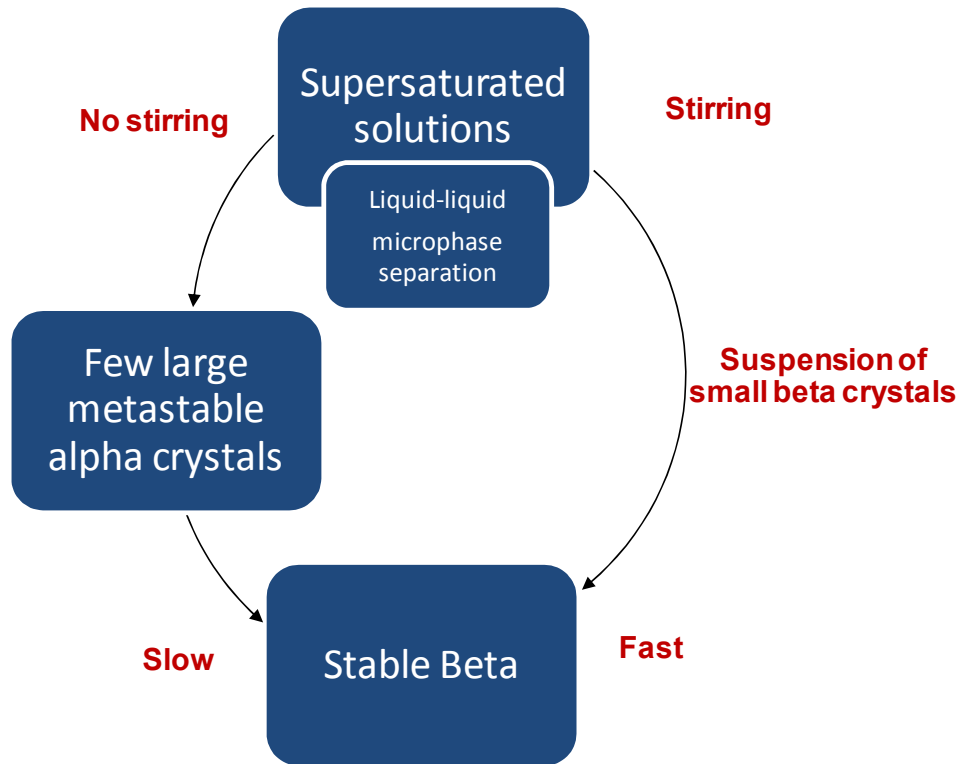


**Figure 4.15** Observed pathways of CBZ crystallisation.

When recrystallised CBZ was used, supersaturated solutions crystallised much faster than commercial samples and different optical turbidity was observed. While commercial CBZ solution generated the bulk of small cubical crystals, recrystallised CBZ solutions produced many alpha crystals which relatively quickly transformed into small beta crystals.

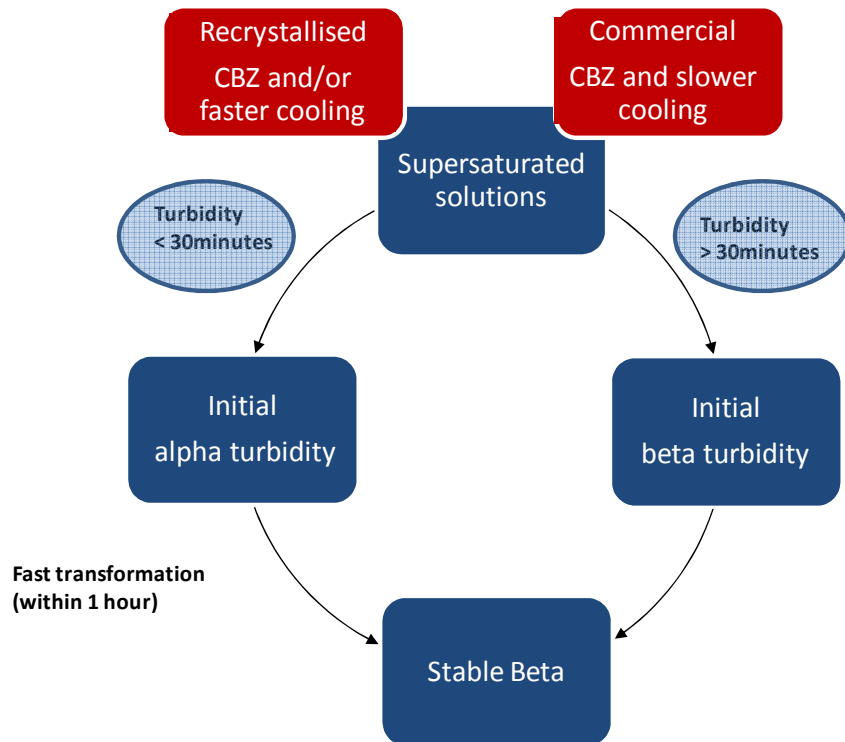


**Figure 4.16** Proposed possible pathways in the development of turbidity depending on the source of carbamazepine.

## **4.2 In situ monitoring of polymorphic transformation in cooling crystallisation of carbamazepine**

In the previous section we investigated polymorphic outcome in cooling crystallisation of CBZ from ethanol. In particular we found that under stirring conditions well defined induction times are observed where turbidity develops in crystallising solutions due to rapid formation of large number of small crystals. Interestingly it was observed that there were two crystallization pathways present under these conditions. In the first one a large number of small crystals of stable beta form was obtained. This was typically observed when commercial CBZ powder was used to prepare solutions, and cooling rate was either slow (in incubator) or fast (in temperature of the lab of 21°C) corresponding to induction times over 30 minutes at CBZ concentration of 3.5g<sub>CBZ</sub>/100ml<sub>EtOH</sub>. The second pathway was typically observed when recrystallised CBZ was used to prepare solutions with induction times below 30 minutes under the same conditions. Obtained turbidity at the induction times was due to many small needles like alpha form crystals, which subsequently transformed into small beta form crystals. A similar outcome was also observed when more rapid cooling was applied for solutions prepared using commercial CBZ powder so that induction time was below 30 minutes. It has been observed that the initial turbidity due to either alpha or beta form at the two distinct pathways can be visually distinguished and so it was shown to be possible to perform optical measurement to monitor the corresponding phase transformations.

### **4.2.1. Experimental procedure**

For this purpose, we developed a novel non-invasive setup for in-situ simultaneous measurement of both transmitted and scattered intensity of light under stirring conditions (see Figure 4.17). HeNe laser (Thorlabs) with the wavelength of 632.8 nm was used as a light source. The setup allows using different vials as well as different stirring speeds. Three detectors: reference, transmittance (both pre-amplified photodiode) and scattering (avalanche photodiode detector) were used to monitor the sample.

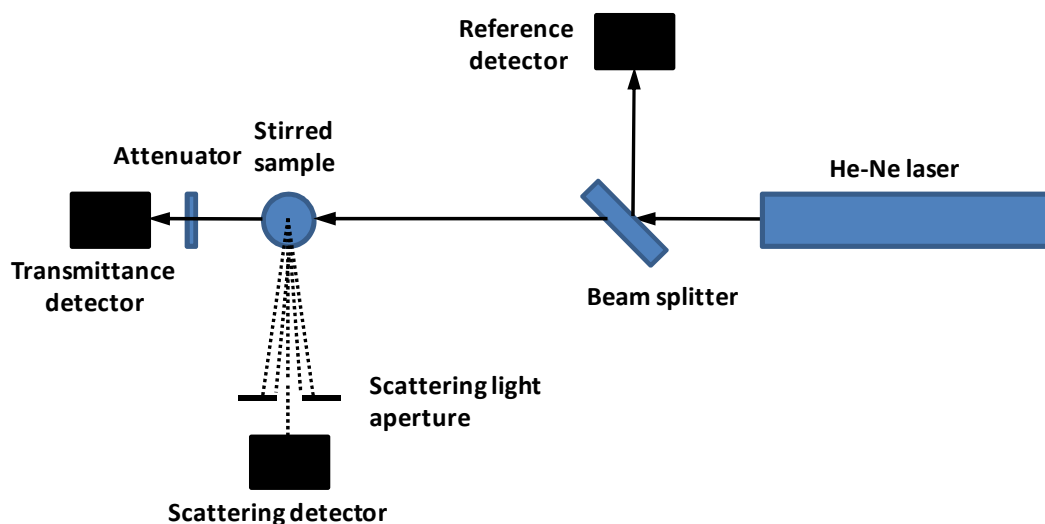


**Figure 4.17** Schematic drawing of the experimental setup.

Attenuation coefficient  $\tau$  was determined from the transmittance measured in the course of crystallisation using the modified Beer-Lambert law:

$$\tau l = -\ln\left(\frac{RT - BT}{RR - BR} x\right)$$

where RT is raw transmittance, RR is raw reference and BT and BR are background transmittance and background reference respectively. These background readings measured when the laser is off were subtracted from all raw values measured in the presence of samples. The calibration coefficient  $x = CR/CT$  was obtained by the measurement of the calibration transmittance CT and calibration reference CR when no sample was present. It was assumed that the ratio of CR to CT (calibration reference to calibration transmittance) is equal to one when all light is transmitted. Scattering intensity I was calculated  $I = RS - BS$ , where RS and BS are raw scattering and background scattering, respectively. Under conditions investigated here, both the attenuation coefficient and the scattered intensity signal are related to turbidity due to formation of crystals in stirred solutions.

Samples were prepared the same way as for the induction time measurements (see section 4.1) and moved quickly to the laser room and spontaneously cooled with the

temperature profile measured in the closed vial under stirring as shown in Figure 4.18.

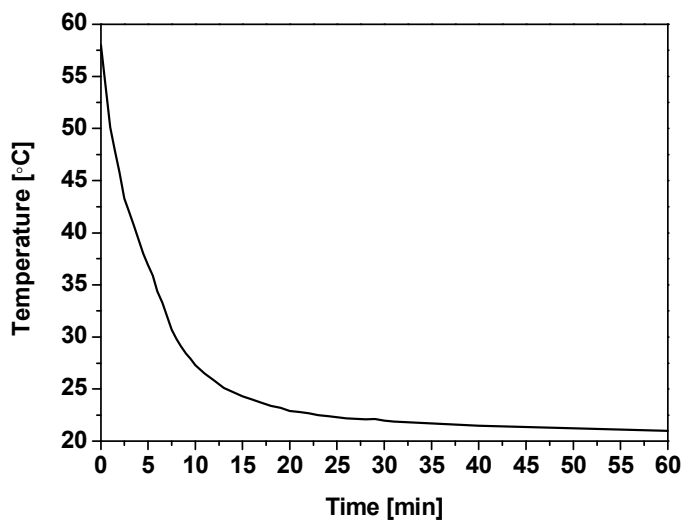


**Figure 4.18** Measured cooling profile for studied samples used for situ monitoring experiments.

#### 4.2.2 Results

Results presented in the previous section 4.1 showed that crystallising solution prepared by dissolution of commercial and recrystallised source of CBZ behaved differently during cooling. Therefore experiments of cooling crystallisation of carbamazepine during stirring were done for two sources of carbamazepine: commercial and recrystallised in house. Solutions of CBZ at the concentrations of  $3.5\text{g}_{\text{CBZ}}/100\text{ml}_{\text{EtOH}}$  were prepared by dissolution in the incubator at  $56^{\circ}\text{C}$ , then filtered with  $0.45\mu\text{m}$  PTFE filters into the 5ml vials and quickly transferred into the measurement setup.

Figures below show the change in attenuation coefficient and scattering intensity while solutions were allowed to cool and crystals formed during continuous stirring. It can be seen that in all cases, for beta commercial and recrystallised sample, the development of turbidity and scattering occurs simultaneously at the induction time,

however the observed induction times in agreement with observations reported in section 4.1 differ significantly depending on the CBZ source used.

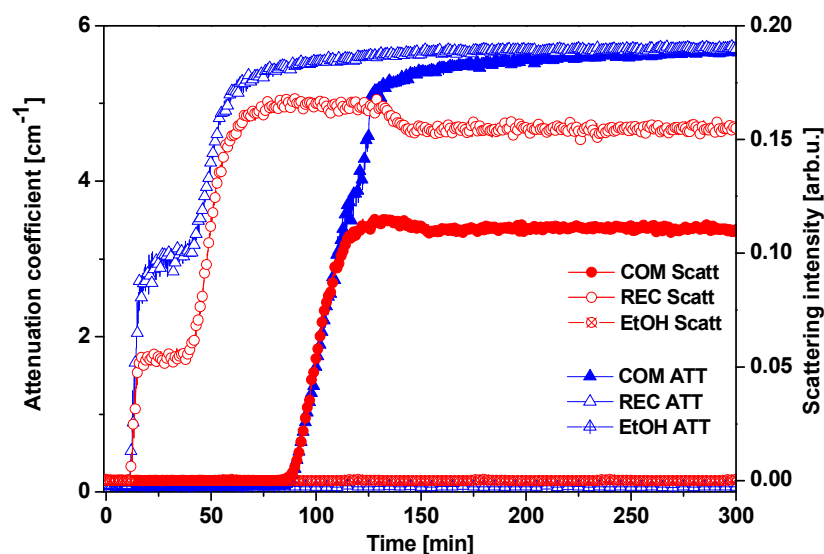


**Figure 4.19** Typical measurement results of CBZ crystallisation from EtOH solution under stirring conditions.

Using recrystallised source of CBZ the sample got turbid much quicker, within the first 30 minutes, while commercial source led to the longer induction times reaching up to several hours. It can also be seen that solutions prepared using recrystallised CBZ exhibit steeper increase in turbidity and scattering intensity at the onset compared to the solutions prepared with the commercial CBZ.

As we can see, the induction time corresponding to the onset of turbidity can be relatively easily monitored with this setup. However, in addition to this capability, which is identical to that of standard turbidity probe, we can also monitor the scattering intensity onset which is always very closely correlated with that for turbidity.

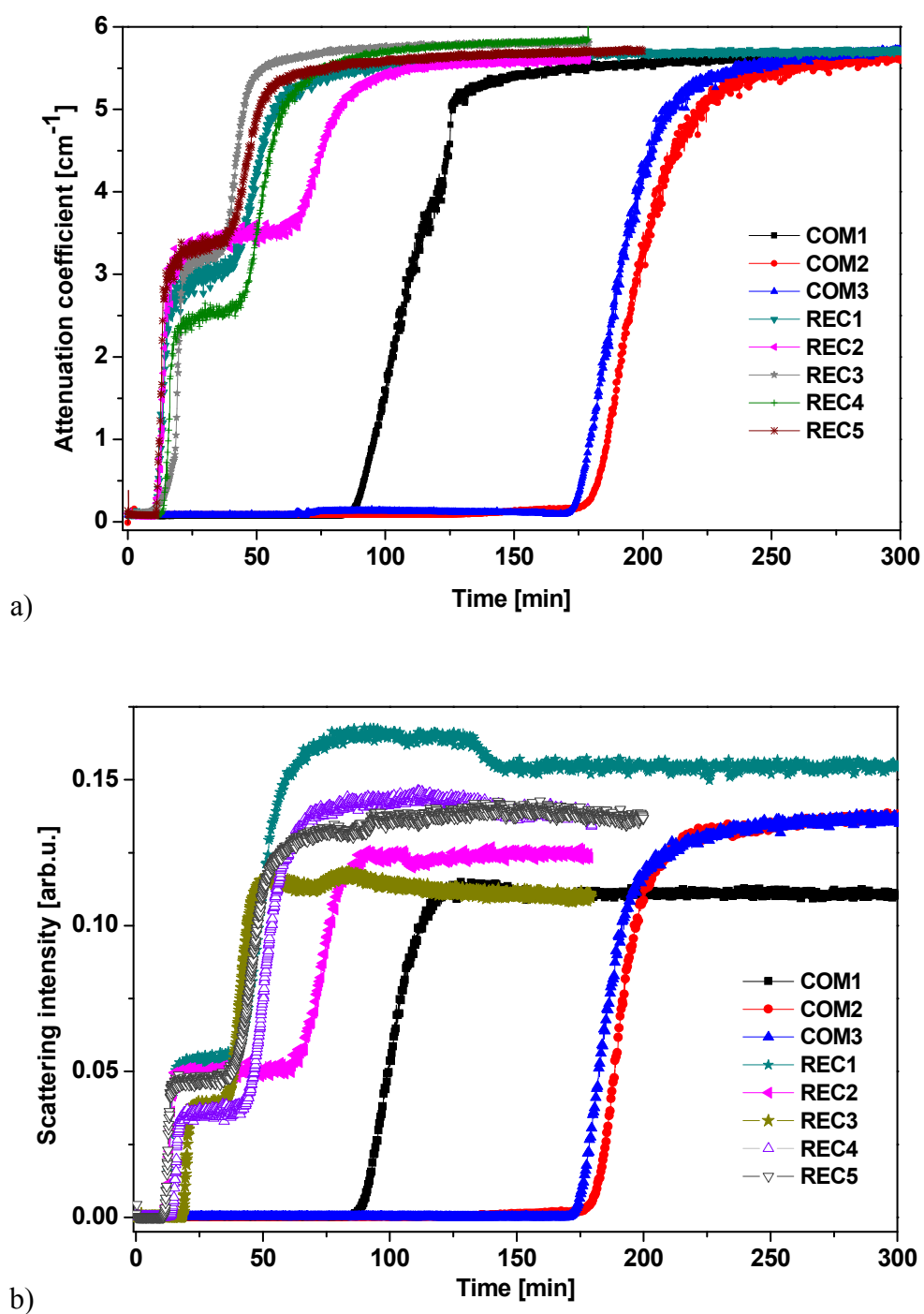


**Figure 4.20** Repetition of measurements of a) attenuation coefficient and b) scattering intensity for solutions prepared from commercial CBZ powder (COM 1-3) and recrystallised powder (REC1-5).

In Figure 4.20 we show results of repetition measurements performed with solutions prepared using commercial CBZ powder (COM1-3) and recrystallised CBZ powder

(REC1-5). For commercial CBZ systems, induction time varied between 1-3 hours and a simple S shape curve was observed for both attenuation coefficient (turbidity) and scattered intensity. For recrystallised CBZ systems, induction time varied between 10 and 20 minutes, and two stages in development of both measured values can be clearly seen. The first stage corresponds to the initial formation of alpha form crystals, and after certain period in the second stage secondary induction time is observed. It corresponds to the transformation to the stable beta form, where both attenuation coefficient and scattering intensity attain plateau values consistent with commercial CBZ systems.

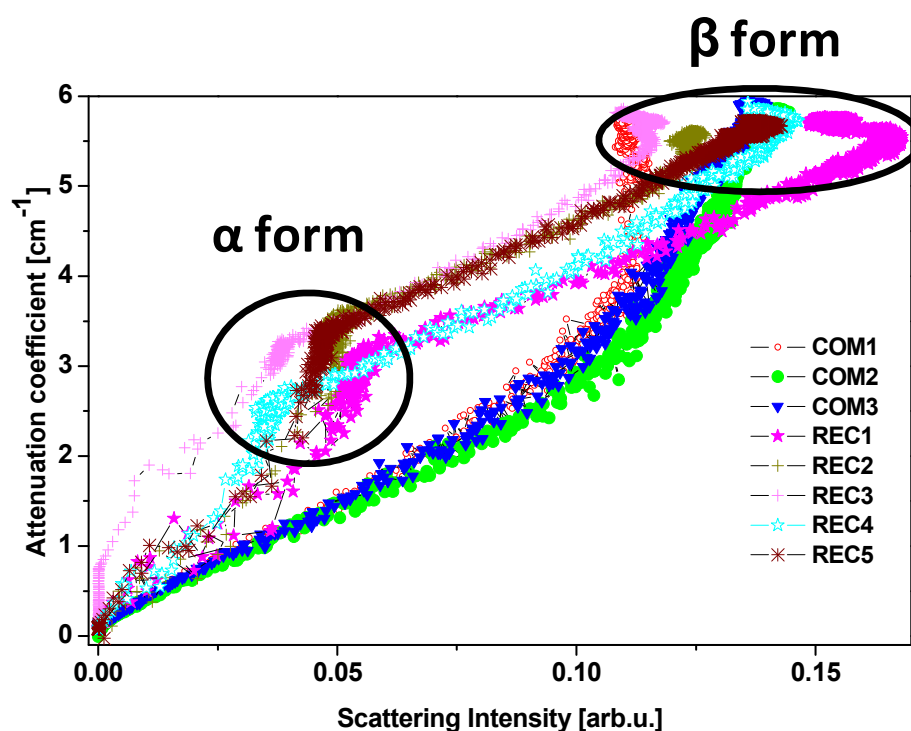


**Figure 4.21** Attenuation coefficient vs. scattering intensity.

Plotting obtained results in terms of the attenuation coefficient against the scattering intensity (Figure 4.21) for all repetitions an interesting trend can be seen distinguishing the two crystallisation paths. For recrystallised CBZ systems a region around  $3.5\text{cm}^{-1}$  of attenuation coefficient and  $0.04$  [arb.u.] of scattering intensity corresponds to the presence of alpha form crystals. From that stage subsequent increase of attenuation coefficient and scattering intensity reach the same region of values as those achieved in commercial CBZ systems, around  $6\text{cm}^{-1}$  attenuation

coefficient and 0.15 [arb.u.] of scattering intensity, corresponding to the presence of beta form crystals. A slight decrease of scattering intensity towards the end of the process (which is thought to be near the thermodynamic equilibrium) is most likely related to the growth of large crystals or agglomeration.

Images of bottles at various stages of the turbidity development are shown in Figure 4.22.

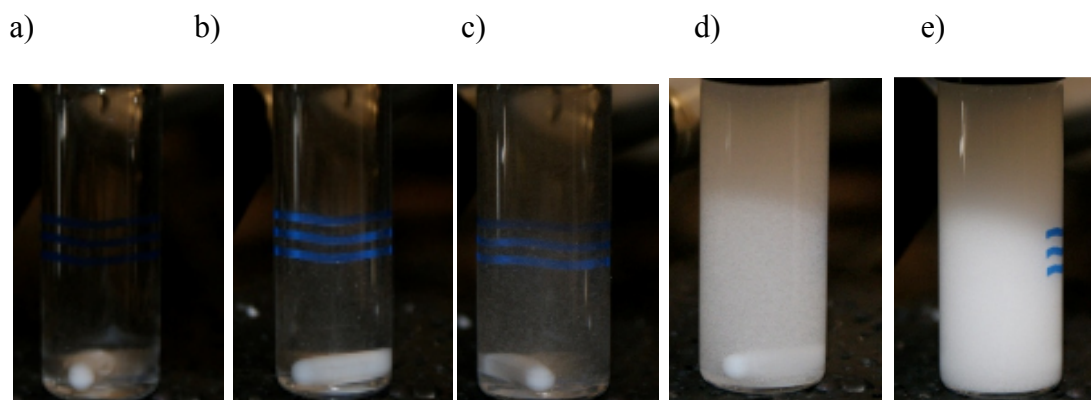


**Figure 4.22** Pictures of crystallising solutions a) at the start of stirring b) at the onset of turbidity c) further development of turbidity d) high turbidity e) maximum turbidity.

Photographs above show the gradual development of turbidity for commercial sample. When recrystallised carbamazepine is used stages b) and c) are almost impossible to catch as the clear solution extremely quickly transforms into stage d) and then into final stage e).

Images below show laser light beam passing through solutions a) at the start of stirring b) at the onset of turbidity c) high turbidity.

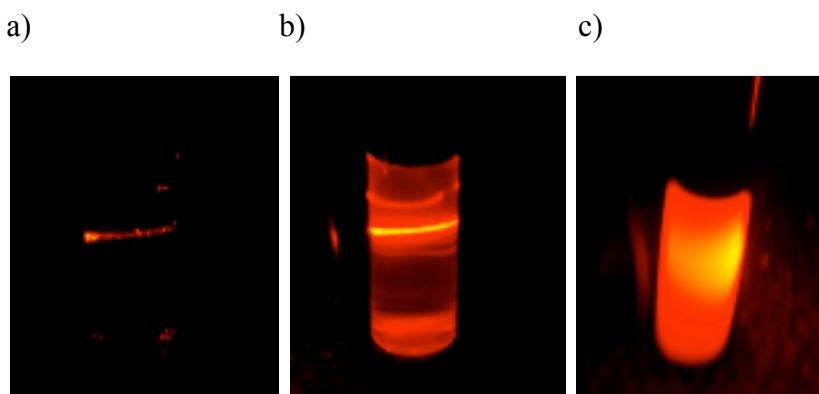


**Figure 4.23** Pictures of crystallising solutions a) at the start ( $0.12\text{cm}^{-1}$  for 13.4% light transmitted) b) at the onset of turbidity ( $0.5\text{cm}^{-1}$  for 45.1% light transmitted) c) high turbidity ( $6\text{cm}^{-1}$  for 99.9% light transmitted).

### 4.2.3 Discussion

In situ simultaneous measurements of transmitted and scattered intensities provided us with an insight into observations reported in section 4.1. It has been clearly demonstrated that there are two separate ways of CBZ crystallisation depending on the source of carbamazepine used.

Our results show that the simultaneous implementation measurement setup can be successfully used to monitor not only the induction time which could be done with a single variable measurement but also can be used to distinguish different polymorphs formed and their mutual transformation. This capability is based on very different morphology of the two polymorphs, which leads to different scattering patterns, which in turn leads to distinct fingerprints when the multiple measurements are recorded.

---

**CHAPTER 5 BREAKAGE OF CRYSTALS IN FLOW**

The objective of this work was to develop a laboratory based approach for the assessment of flow conditions which can be used for a given crystal suspension in order to avoid crystal breakage. In the industrial processes crystal suspensions pass through a variety of flow conditions which may lead to the undesirable crystal breakage or attrition and subsequent deterioration of the particulate product. The specific aim was to investigate the size reduction phenomena occurring in slurries of high aspect ratio crystals passing through a well controlled elongational flow region. This was done by exposing certain volumes of crystal suspensions to controlled flows in the vessel and in a flow-through contraction in the peristaltic pump driven recirculation loop, providing the basis for the “shear–o–meter” setup. This work was done in collaboration with colleagues in Merck, Rahway, N.J., and ETH Zurich, where Computational Fluid Dynamics calculations of flow fields and corresponding strain rates in contractions were carried out. Although these results will not be presented here, they allow relating our observations to the range of strain rates relevant for pilot and plant scale conditions. In this way, results obtained from the laboratory based measurements can be used to inform scale-up consideration in order to manage flow regimes to minimize crystal breakage in downstream processing.

**5.1 Experimental procedure**

The measurement setup consisted of a 3-neck glass (180ml) shallow semi-spherical bottom flask (CG-1576 from Chemglass). To avoid any air-liquid interface to prevent air entrainment and/or foaming the flask was completely filled with crystal slurry. Stirring was provided with a mechanical stirrer and stirrer assembly (CG-2060 from Chemglass). The stirring speed was chosen to provide good suspension of solids and steady state particle size distribution was obtained in the vessel at a given stirring speed after stirring for a certain amount of time. The particle size distribution of the solids was monitored by a FBRM probe inserted in the flask.

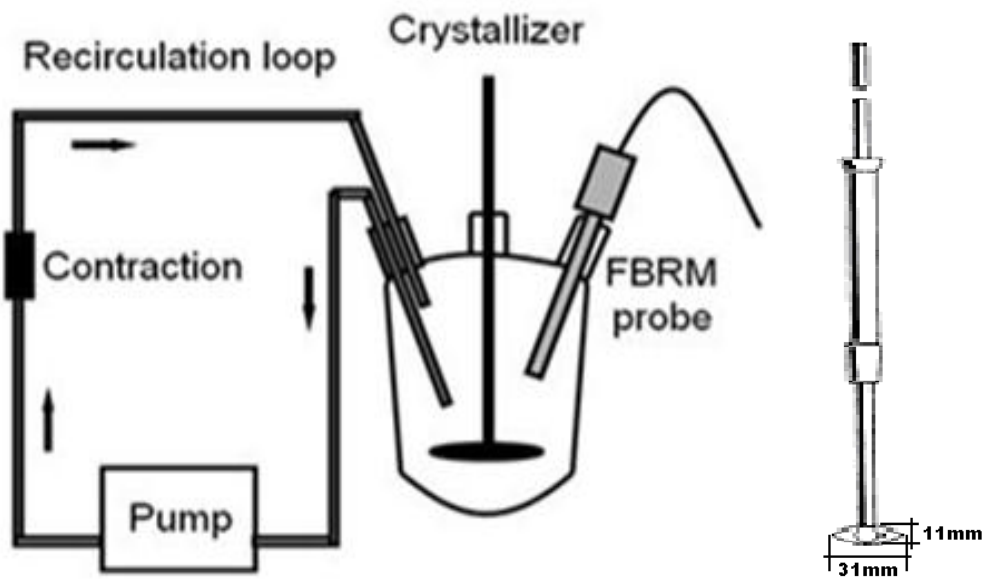


**Figure 5.1** Diagram of experimental setup used for crystal breakage studies. Mechanical (PTFE) stirrer used for experiments.

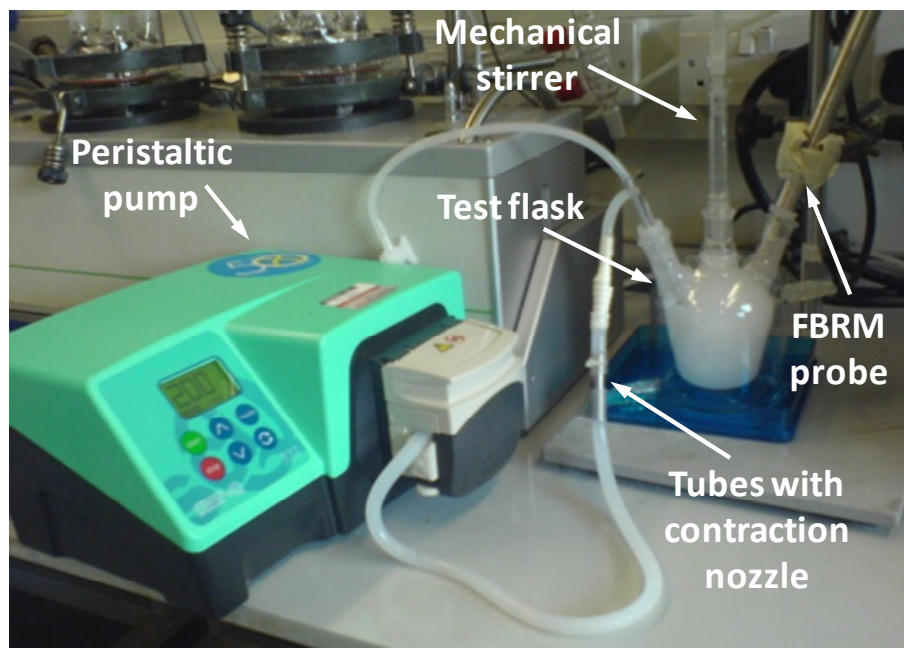


**Figure 5.2** Picture of the actual setup showing peristaltic pump, test flask with FBRM probe, mechanical stirrer, and tubing for recirculating crystal slurries with contraction nozzle.

The effects of flow on particle size distribution were studied by passing the slurry through a recirculation loop (using silicone tubing with I.D. of 0.9 mm) using a Watson Marlow peristaltic pump at 405 and 700ml/min (200 and 400rpm). Initial experiments were performed with the pump only without any contraction in order to assess effect of the pump and the rest of the loop on crystal breakage. Further experiments were then performed with contractions present in the loop. Three types of contraction nozzles were used for the studies:  $10^\circ$  (n10),  $118^\circ$  (n118) and  $180^\circ$  (n180) and the number defines the value of contraction angles.

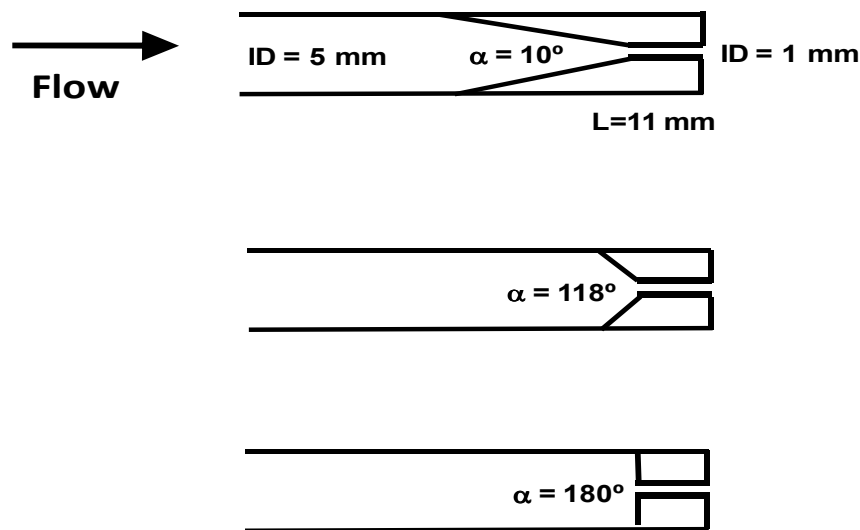


**Figure 5.3** Design of contraction nozzles used in experiments with indication of the flow direction, entry angles and diameters.

Pumping tests followed the general procedure, where slurries were first stirred without pumping and then the pump has been turned on for 6 runs of 10 minutes each, with 5 minute breaks between subsequent runs. Finally, slurries were pumped continuously for 30 minutes. All results from the pumping in the loop experiments shown below correspond to the particle size distributions measured in the flask at the same stirring speed while pumping was stopped, in order to avoid the possible influence of the change of the flow pattern in the flask while pumping on measured results.

Experiments were done using slurries of L- tyrosine (Acros Organics, lot#A0234595) in deionised water. Three concentrations of slurries were used with solid loadings of 2.7, 5.4 and 9.0 wt%. Solubility of tyrosine in water is low and it was established that solid mass dissolved was negligible at the solid loadings used. All experiments were performed at ambient conditions (21°C). FBRM probe used was Lasentec S400E (probe OD: 8 mm, probe length: 91 mm).

The results shown below are divided into several sections. The first one shows the characteristics of the measurement and has been done to explain measuring basics. The effect of solid loading in the resulting CLD in FBRM technique is shown. Representative sample measurements show that the same concentration of tyrosine slurries is taken to the contraction loop therefore exposed to shear flow. These experiments were done on the most concentrated slurries 9wt% as this value was expected to be the potentially very hard to suspend and sucked into the loop.

In following sections results of breakage of tyrosine crystal slurries in the flow are shown. At the beginning a few examples of the effect of stirring in the test flask at 700rpm (the exact conditions were kept throughout all tests) and the effect of a peristaltic pump working at 400rpm on 2.7 and 9.0 wt% slurries are shown. The effects of stirring and the peristaltic pump at 200rpm in the loop as well as the effects of the peristaltic pump and stirring in a test flask on all studied three concentrations is given in the Appendix 8.7. Data shown below are only cumulative results of all breakage tests with the use of three nozzles designs: 10, 118 and 180 degree. All partial, more detailed results with tables of calculated averages and more graphs are shown in the Appendix 8.7.

In the second part initial results of stirring and pumping on chosen examples show what will be the contribution of breakage coming from the stirring as well as the expected breakage caused by the peristaltic pump itself. Finally all results of the partial experiments are compared within each value of concentration for each values of pumping power. The effect of stirring, pumping through the loop and nozzles is shown and the conclusions are given.

## 5.2 Effect of stirring

Stirring was necessary to keep crystals suspended making sure that all crystals are going to be exposed to the flow. Before the main breakage tests a series of experiments was done to establish a suitable stirring speed sufficient to keep all crystals suspended. In this step, the effect of stirring speed on FBRM measurement on 9wt% slurry of tyrosine in water was investigated for stirring speeds from 300 to 900 rpm.

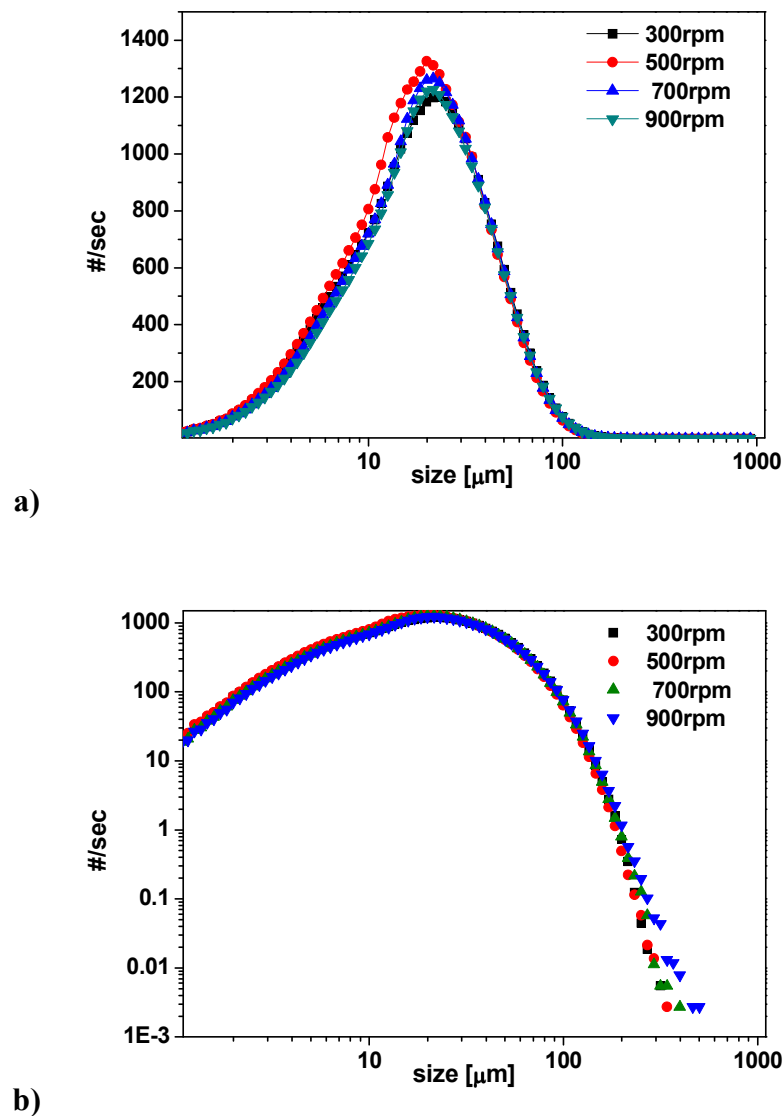


**Figure 5.4** Effect of stirring speed on measured CLD of tyrosine in water slurry at 9wt% shown on a) linear and b) logarithmic scale.

It can be seen that only for the largest suspended particles (with cord lengths higher than  $200\mu\text{m}$ ) there is a difference in chord counts, where higher (and similar) counts are seen at 700 and 900 rpm. Based on these observations, the stirring speed of 700 rpm has been chosen as appropriate and used throughout all subsequent experiments.

The effect of prolonged stirring on slurries with 9.0wt% turned out to be minimal (Figure 5.5). Looking at the calculated average sizes almost no change is observed for lower averaging moment ratios and only slight decrease is seen on the highest average moment ratio. A small amount of the largest crystals were broken during first 10 minutes of stirring and the average shifts from 131 to  $128\mu\text{m}$  for the highest calculated average moment ratio 6/5. Further stirring results in an average of  $121\mu\text{m}$  after 90 minutes of stirring. The lowest average 1/0 remains constant throughout the stirring with the value of  $24\mu\text{m}$ .

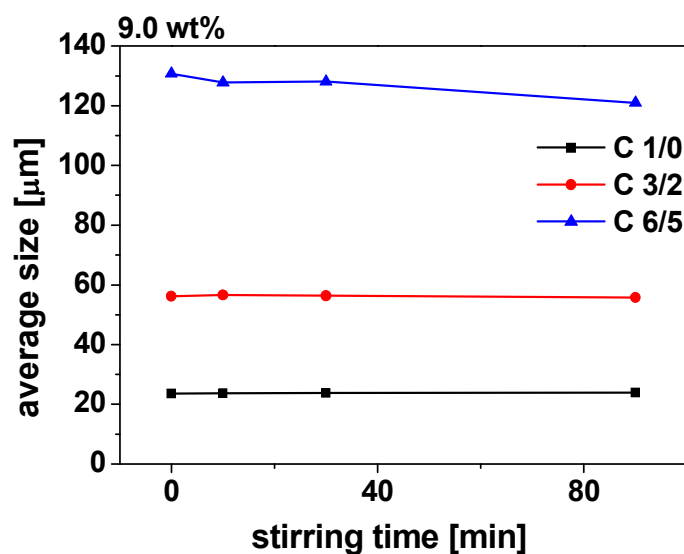


**Figure 5.5** Average sizes for stirring of 9wt% of tyrosine in water at 700rpm.

Stirring of 2.7wt% slurries of tyrosine caused considerable decrease in numbers of counts of the largest particles. Initially there were many particles or aggregates with maximum size approaching 1mm which then was reduced to around  $800\mu\text{m}$  after 30 minutes and after 90 minutes  $650\mu\text{m}$  was the size of the largest crystals (Figure 5.6). Significant increase of fines is seen on the in Figure 5.6a confirms breakage of the

largest crystals which simultaneously increase in the number of smaller crystals coming from attrition.

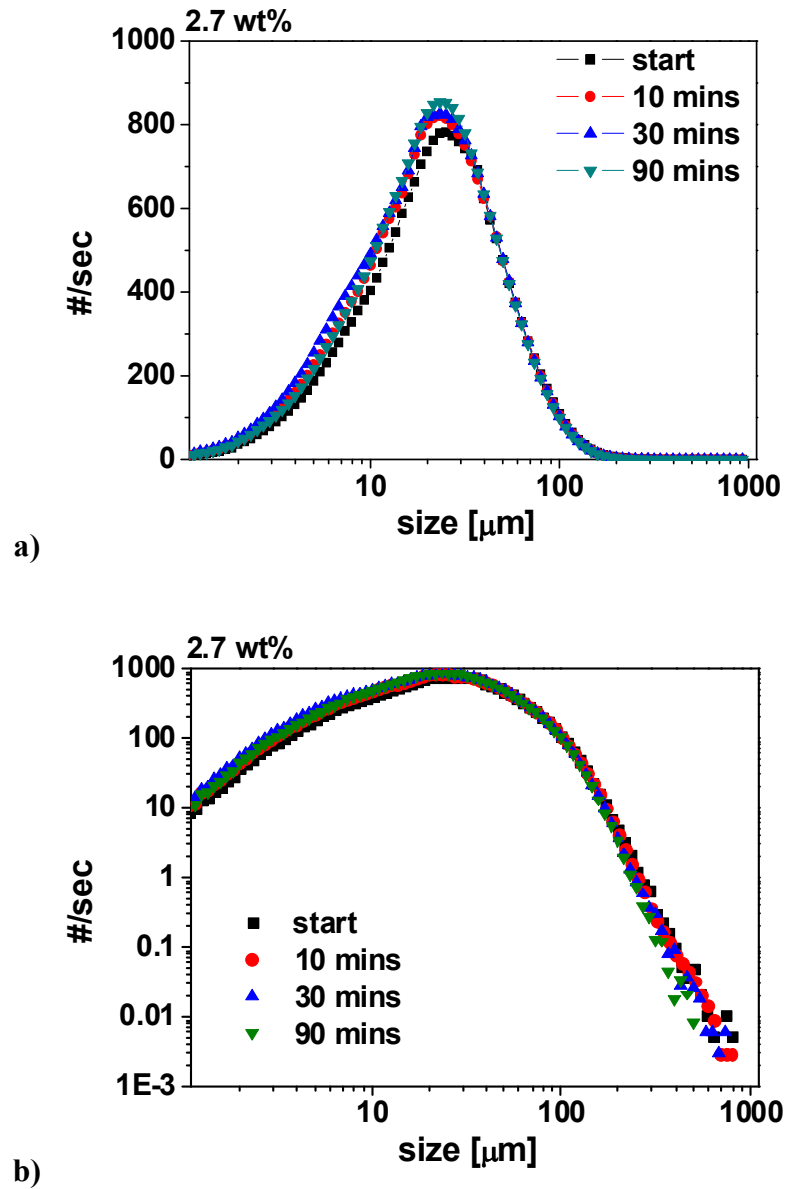


**Figure 5.6** The effect of stirring at 700rpm on 2.7 wt% tyrosine in water shown on a) linear and b) logarithmic scale.

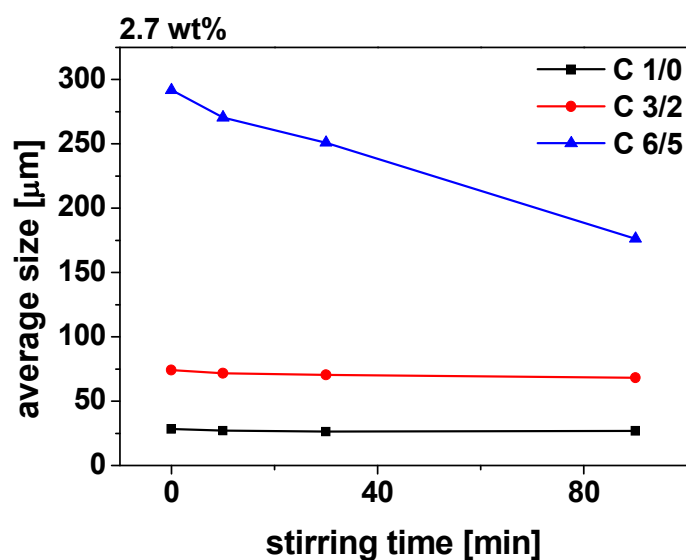


**Figure 5.7** Average sizes for stirring of 2.7 wt% of tyrosine in water at 700rpm.

A significant decrease of average sizes for the biggest averaging moment 6/5 is the evidence of the biggest crystals getting broken. The rate of breakage for 6/5 moment ratio was relatively large reaching 40% of the initial size from 292 to 176 $\mu\text{m}$  (see Appendix 8.7). The lowest calculated average values for 1/0 moment do not show any significant change in the resulting sizes. This may be caused by the fact that this moment ratio is very sensitive to the smallest crystals and their number actually increases throughout the test, shading the decrease in average sizes of large ones.

### 5.3 Effects of solid loading and sampling

This experiment shows the basic feedback of FBRM in response to different solid loading. Stirring of three suspensions with solid loading of 10.5, 5.4 and 2.7wt% at 700rpm of the same volumes in the same vessels are shown in figures below.

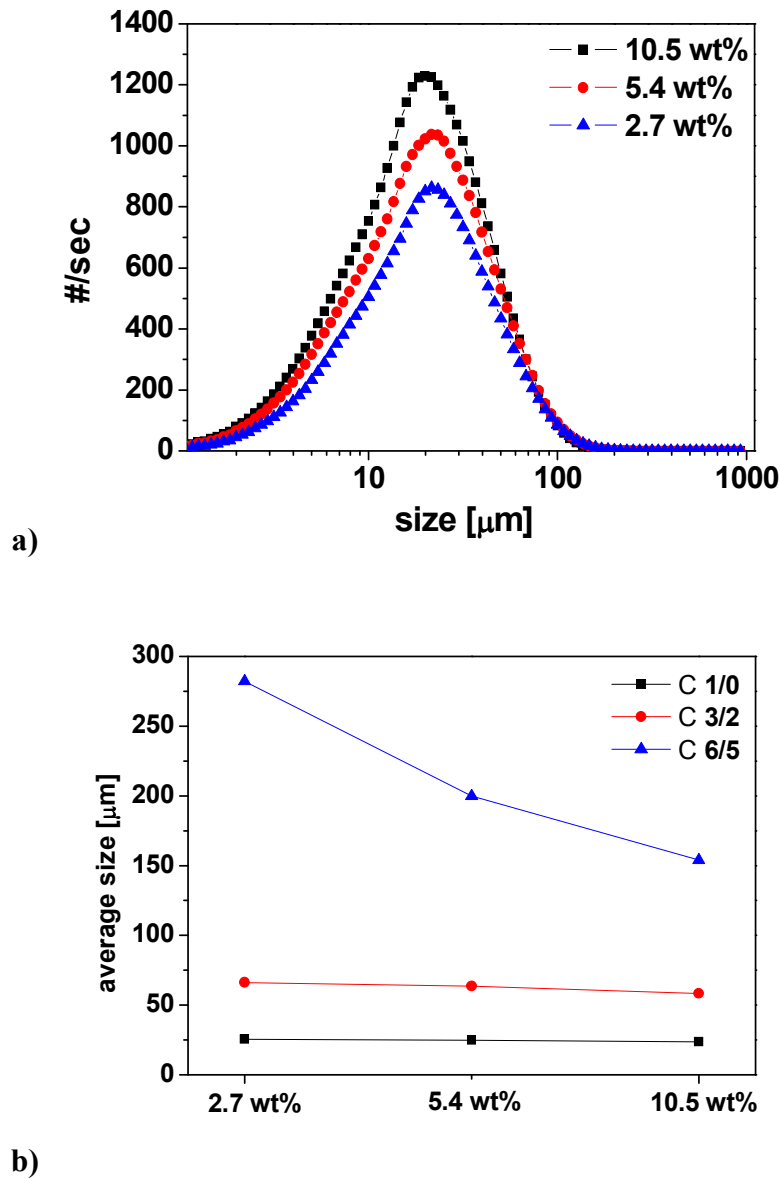


**Figure 5.8** The effect of solid loading on measured CLD a) and corresponding moments b).

It can be seen that for these three studied solid loadings the count number is not proportional to the concentration. Decrease (from proportionality) of the counts for average size with the increase of solid loading is observed as well as the shift of CLD main peak towards the smaller sizes for higher concentration.

Calculates average moments presented in table in the Appendix 8.7 show that exactly for the same crystal lot average sizes differ from over 280 $\mu\text{m}$  for 2.7wt% decreasing

to  $154\mu\text{m}$  for 10.4wt% for the highest moment 6/5. The lowest 1/0 moment differs only slightly from  $25\mu\text{m}$  for 2.7wt% to  $24\mu\text{m}$  for 10.5wt%.

In the case of higher concentrations of slurries it must be noted that smaller particles pass in the front of probe window relatively more times than the large ones (because their number is considerably higher) and the so-called snowstorm effect can be observed, where it is not possible to properly detect larger particles. This feature of the FBRM measurement has previously been described as the shadow or masking effect [144, 164] and this issues must be considered when comparing results of different solid loadings.

The following test was conducted in order to establish whether representative sampling was achieved in withdrawing slurry for circulation through the loop and therefore all crystals are exposed to contraction flow. It is a comparison of measurements from before and after halving the content of primal flask and filling it to full with deionised water.

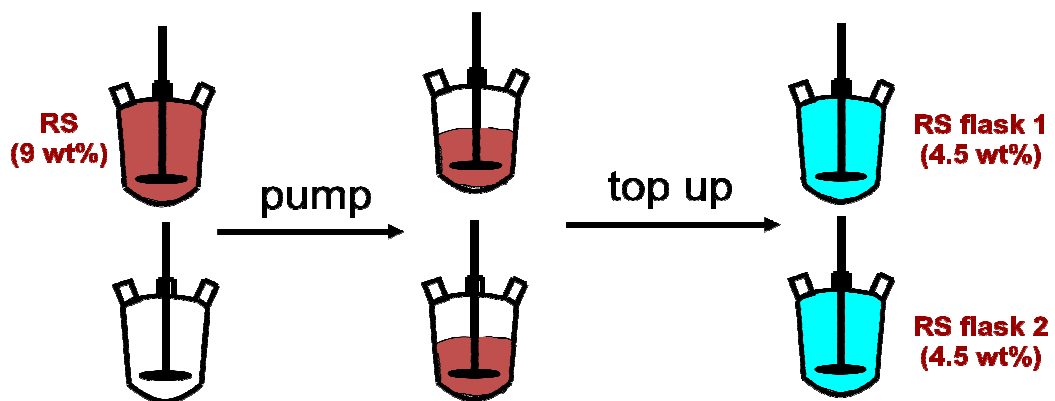


**Figure 5.9** Schematic explanation of representative sample test.

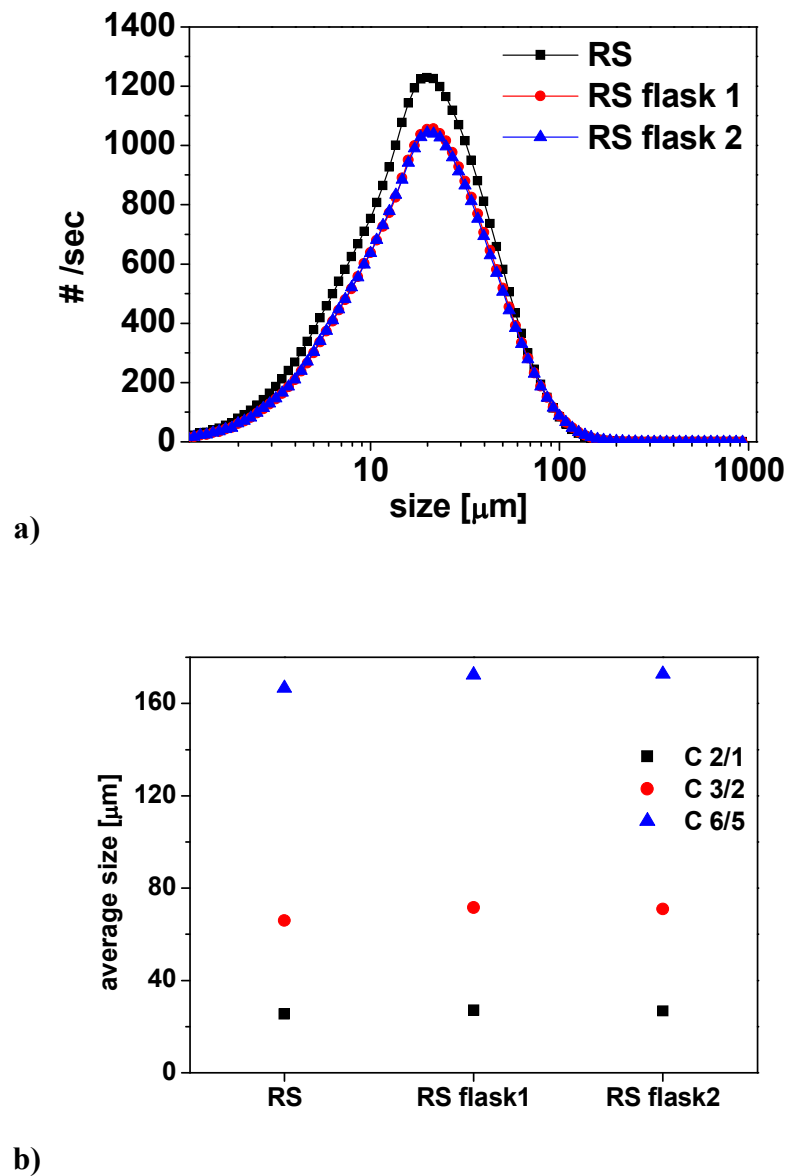


**Figure 5.10** The measured a) CLD for sample test and b) corresponding calculated average sizes.

It can be seen that pumping half of the content of the original flask leads to equitable distribution of sizes of both flasks. The figures above show identical average sizes and moment ratios for both flasks. Previous experiments have proven that with dilution different distribution must be expected and the decrease of concentration compared to the increase of average size at the original flask is observed.

#### 5.4 Effect of peristaltic pump

In this section the result of pumping of tyrosine slurry in water in tubing by a peristaltic pump is shown. The nature of these experiments required the use of a peristaltic pump and the effect of a pump is shown on the example of pumping 2.7wt% slurry at 400rpm (700ml/min pumping flow rate) and compared with 9.0wt%. (see more is in the Appendix 8.7).

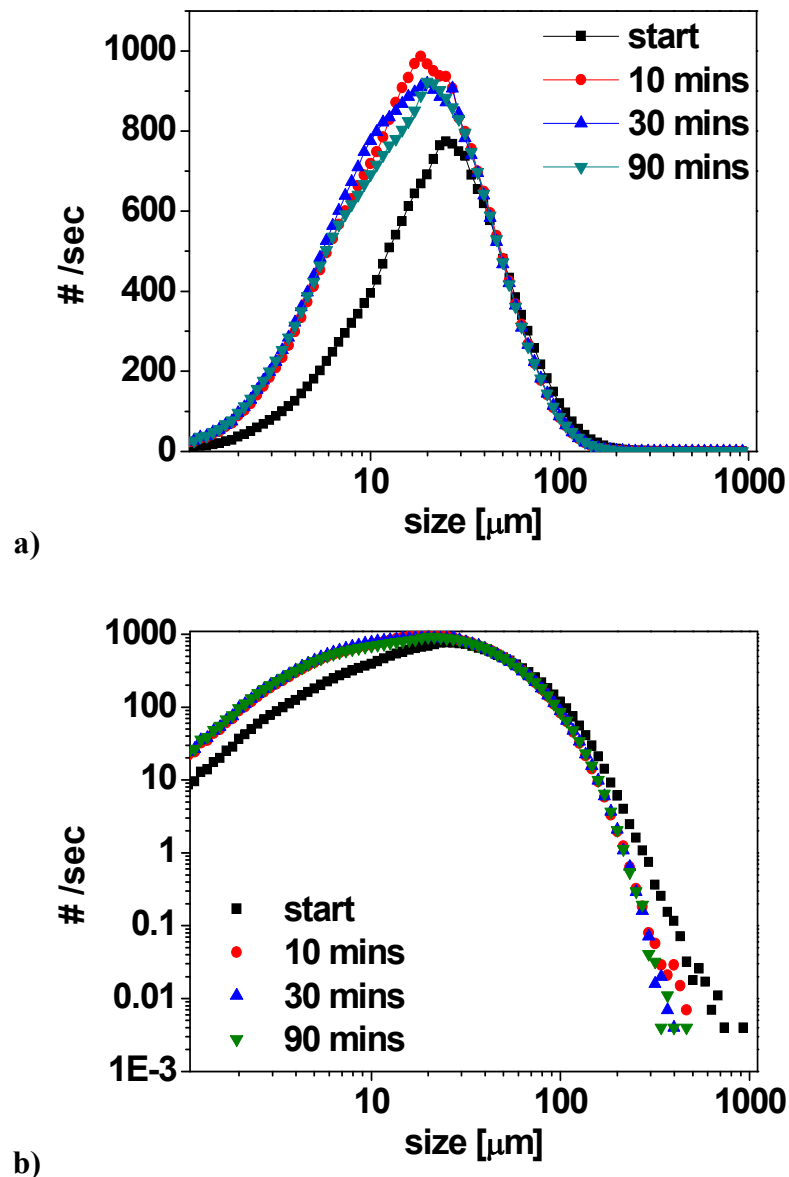


**Figure 5.11** The effect of pumping at 400rpm of 2.7 wt% of tyrosine in water on a) linear and b) logarithmic scale.

The results obtained show a significant rate of breakage of 2.7wt% tyrosine slurry during pumping at 400rpm. Figure 5.11a shows a striking increase of fines already after the first 10 minutes.

In Figure 5.11b it can be seen that the initial crystals with sizes up to 1mm after 10 minutes were completely broken and disappeared and the largest crystals are only up to 500 $\mu$ m maximum size, further pumping cause a total disappearance of any particles bigger than 350 $\mu$ m. It can be seen that the highest breakage was observed during the first 10 minutes of pumping simultaneously with the creation of huge amounts of fines on Fig 5.11a.

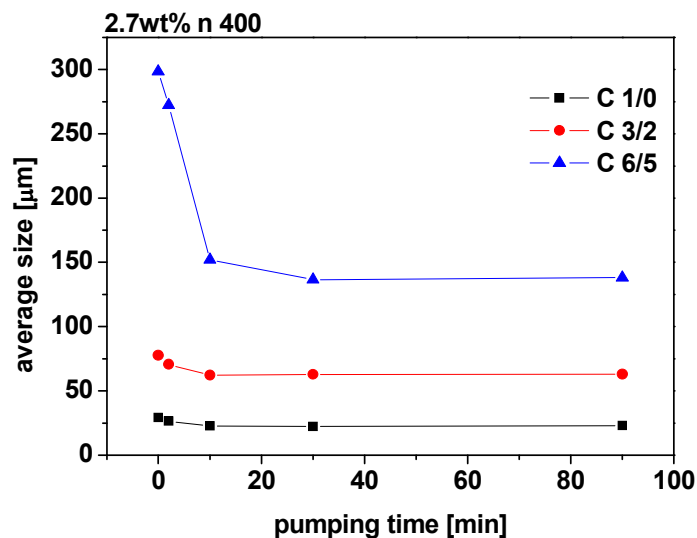


**Figure 5.12** Average sizes for pumping of 2.7 wt% of tyrosine in water at 400 rpm pumping power.

The effect of a pump is clearly visible in all calculated averages. The most significant is for the highest averaging 6/5 where the starting size was nearly 300 $\mu$ m and decreased to a value lower than 140 $\mu$ m. The biggest change occurred during the first 10 minutes where the average decreased by 50%. Even the lowest calculated moment ratio shows a decrease in the average from an initial 29 $\mu$ m to a resulting 23 $\mu$ m at the end of 90 minutes pumping.

The above results show that the peristaltic pump itself can cause a significant rate of breakage for 2.7wt% solid loading of tyrosine.

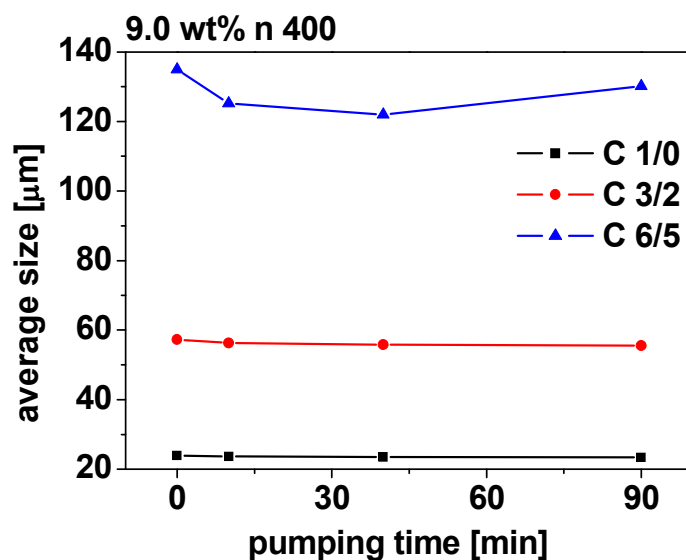


**Figure 5.13** Average sizes for pumping of 9.0wt% of tyrosine in water.

The same testing procedure of pumping crystal slurry through a peristaltic pump at 400rpm applied to the highest value of solid loading (9.0wt%) shows clearly different results.

The effect of the increase of concentration to 9.0wt% again turned out to be much lower with almost no breakage caused by the pump. The highest calculated average moment ratio 6/5 shows only a slight decrease from 135 $\mu\text{m}$  to 130 $\mu\text{m}$  being only 3.5% of the biggest crystals. Average sizes differ only slightly with time with the lowest moment ratio being almost an identical of around 24 $\mu\text{m}$  changing to only 23 $\mu\text{m}$  after 90 minutes of the relatively harsh pumping.

These results show unexpected behaviour of tyrosine slurries being relatively more resistant to operating conditions at higher solid loading. At this point it must be noted that a significant effect of the above results will come from the nature of particle counts by FBRM lowering the averages for higher concentrations significantly.

## 5.5 Comparison of effects of stirring, pumping and flow through contractions

### 5.5.1 Effect of stirring and flow on 2.7 wt% slurries

The significant creation of fines during pumping through a peristaltic pump at 400rpm compared to the effect of stirring and with a contraction nozzle experiment is shown. These results do not mean that less breakage was observed when contraction nozzles were added only that the majority of crystals broken could result in the increase of medium sizes not the smallest.

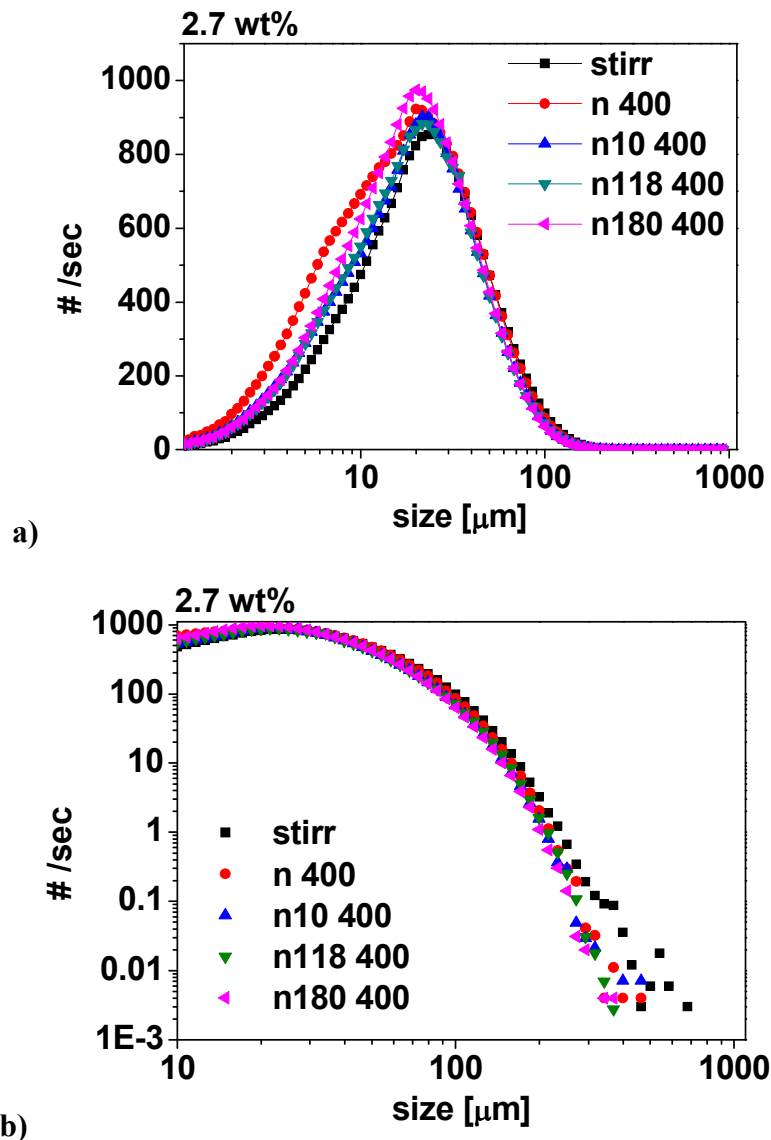


**Figure 5.14** The effect of stirring and 400rpm pumping on 2.7wt% of tyrosine in water on a) linear and b) logarithmic scale.

It is clear on Figure 5.14b that while stirring there were crystals as large as  $650\mu\text{m}$  pumping caused breakage of all crystals bigger than  $400\mu\text{m}$  as well as n10, contraction with n18 angle broke everything bigger than  $300\mu\text{m}$ .

This experiment was the only one allowing the use of contraction of 180 degree angle (because of plugging of the contraction and bursting of tubes for higher solid loadings) and as expected it caused the biggest rate of breakage. Pumping through the 180 degree angle nozzle resulted in the breakage of all crystals larger than  $250\mu\text{m}$ .

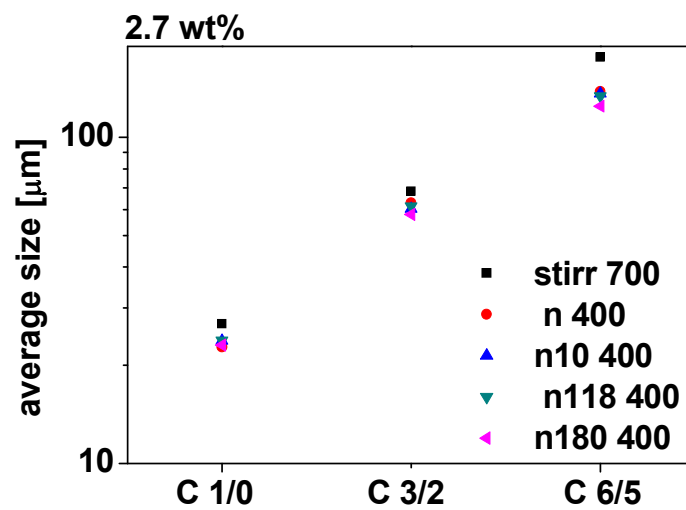


**Figure 5.15** Average sizes for 2.7wt% of tyrosine in water tests at 400rpm pumping power.

The change in the average size of crystals shows an expected reduction in obtained results with the harsher pumping. The highest average sizes are observed after stirring ( $176\mu\text{m}$ ) and lowest for n180 nozzle ( $125\mu\text{m}$ ) although still clearly visible with the lowest of  $27\mu\text{m}$  for stirring and  $23\mu\text{m}$  for n180 nozzle.

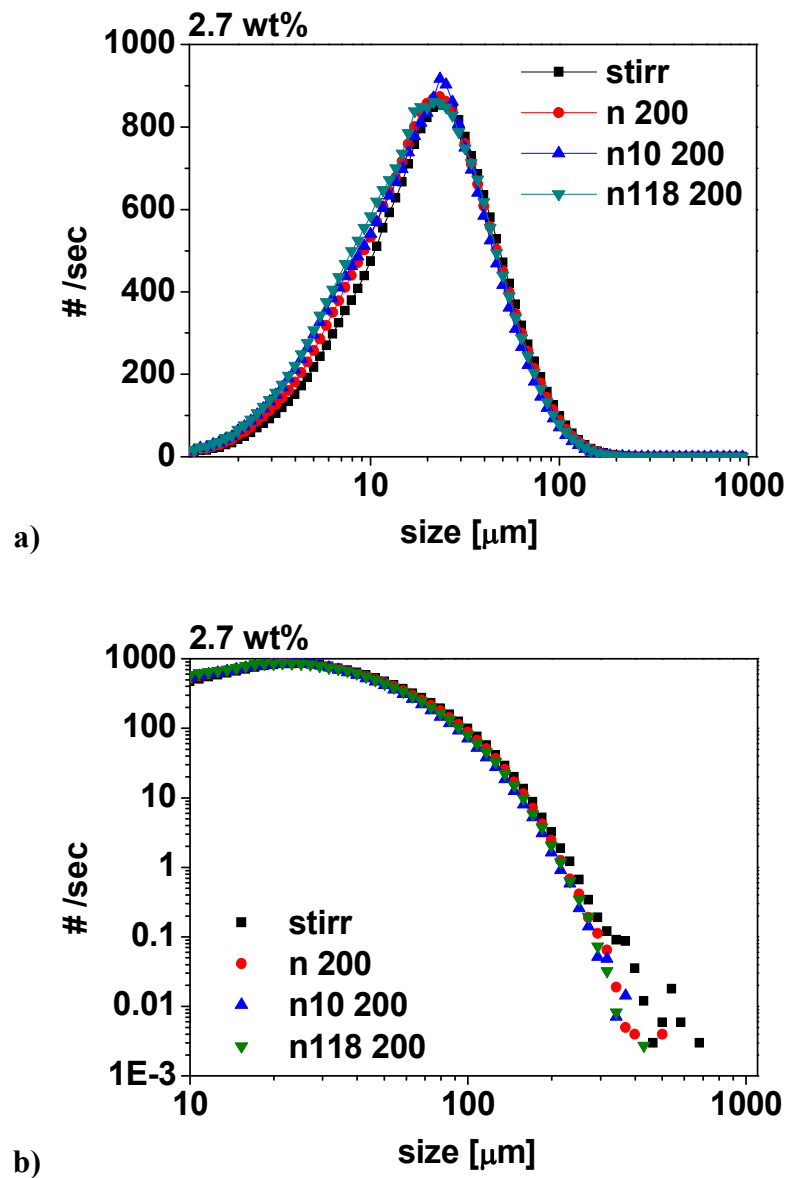


**Figure 5.16** The effect of stirring and 200rpm pumping on 2.7wt% of tyrosine in water on a) linear and b) logarithmic scale.

A significant increase of fines as well as a reduction of the biggest crystals is observed as a result of all of passes through the nozzles.

In Figure 5.16a an increase of smaller crystals can be seen for every additional stressing of crystals by both pump and much more when the nozzle was plugged.

The initial maximum size of 650 $\mu\text{m}$  observed after stirring was significantly reduced by pumping.

Pumping in the loop at 200rpm without a nozzle broke crystals bigger than 500 $\mu\text{m}$  (Figure 5.16b). The addition of nozzle n118 decreased the maximum size to 450 $\mu\text{m}$  and n10 down to 400 $\mu\text{m}$ .

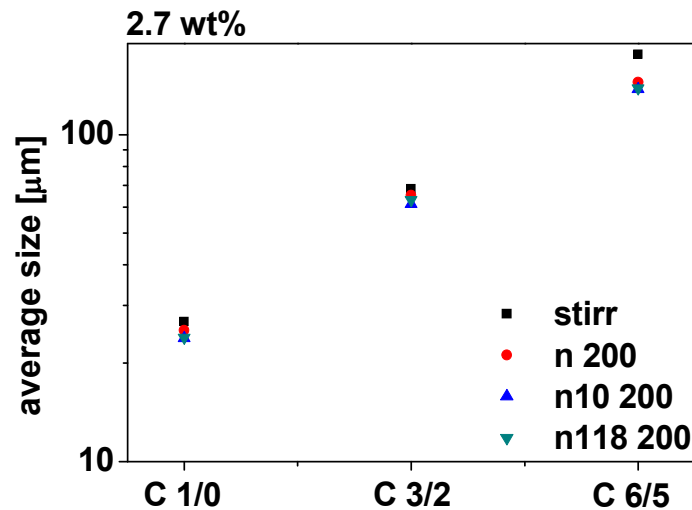


**Figure 5.17** Average sizes for 2.7wt% of tyrosine in water pumping tests at 200rpm pumping power.

Calculated average sizes compared to this one resulting from stirring changed from 27 $\mu\text{m}$  to 24 $\mu\text{m}$  for n118 and n10 from the lowest moment ratio C1/0 which means a reduction of around 10%. The highest averaging moment ratio C6/5 shows the change of more than 20% in relation to n10. It can be seen that those results are more similar to each other meaning that speed of pumping has a relatively significant effect on breakage of the studied crystal slurries.

A decrease of pumping power from 400rpm (750ml/min) to 200rpm (405ml/min) shows a decrease of breakage rate for all experimental procedures.

### 5.5.2 Effect of stirring and flow on 5.4 wt% slurries

By increasing the concentration of studied slurries twice from the 2.7wt% it can be seen that similar rate of breakage has been obtained.

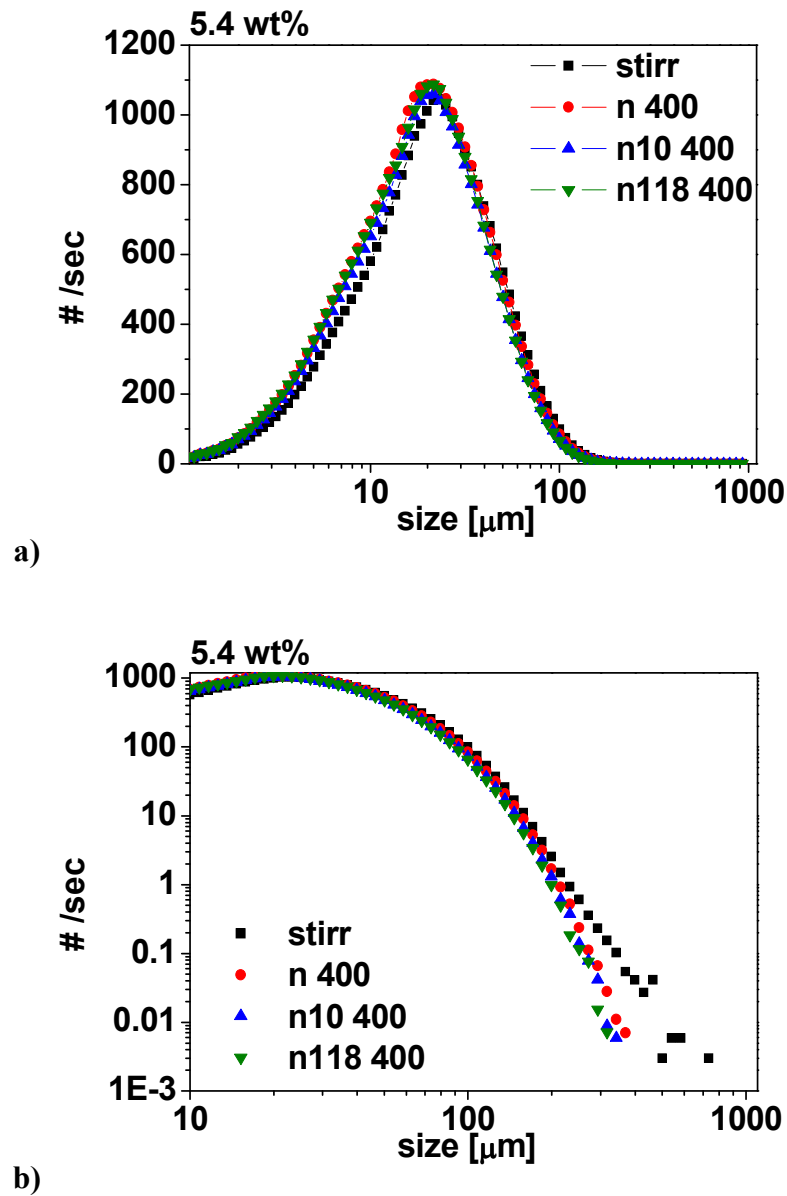


**Figure 5.18** The effect of stirring and 400rpm pumping on 5.4 wt% of tyrosine in water on a) linear and b) logarithmic scale.

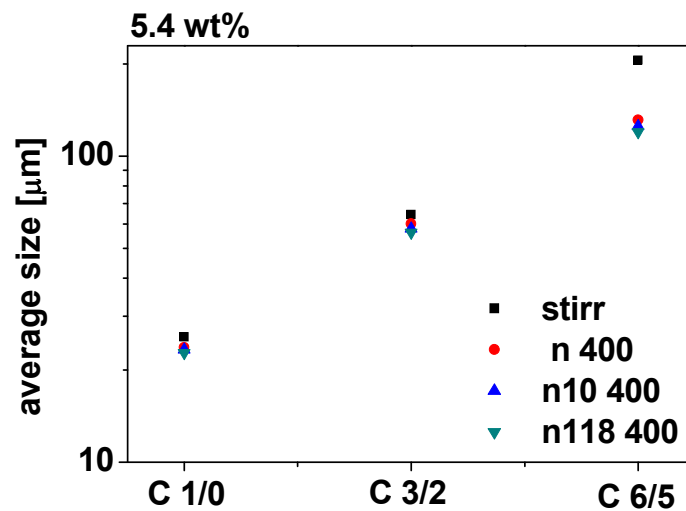


**Figure 5.19** Average sizes for 5.4 wt% of tyrosine in water pumping tests.

Creation of fine crystals similar for all pumping experiments, significantly to stirring is observed. There is a striking reduction of largest crystals for the results of the experiments using just the pump reducing the maximum size from over 700 $\mu\text{m}$  to just below 400 $\mu\text{m}$  and even further reduced after the use of n118 with the loss of anything bigger than 200 $\mu\text{m}$ .

Similar data were obtained by increasing the concentration twice showing the same trend of results. Calculated moments show a decrease for all averages. The greatest you would expect for the highest moment 6/5 changing from 200 $\mu\text{m}$  to around 130 $\mu\text{m}$  similar after all pumping breakage. There is a drop in the lowest 1/0 moment going from 26 $\mu\text{m}$  down to 23 $\mu\text{m}$  which for this moment is significant and the highest from 206 to 120 $\mu\text{m}$ . Resulting averages are very similar for all effects of pumping and contraction nozzles.

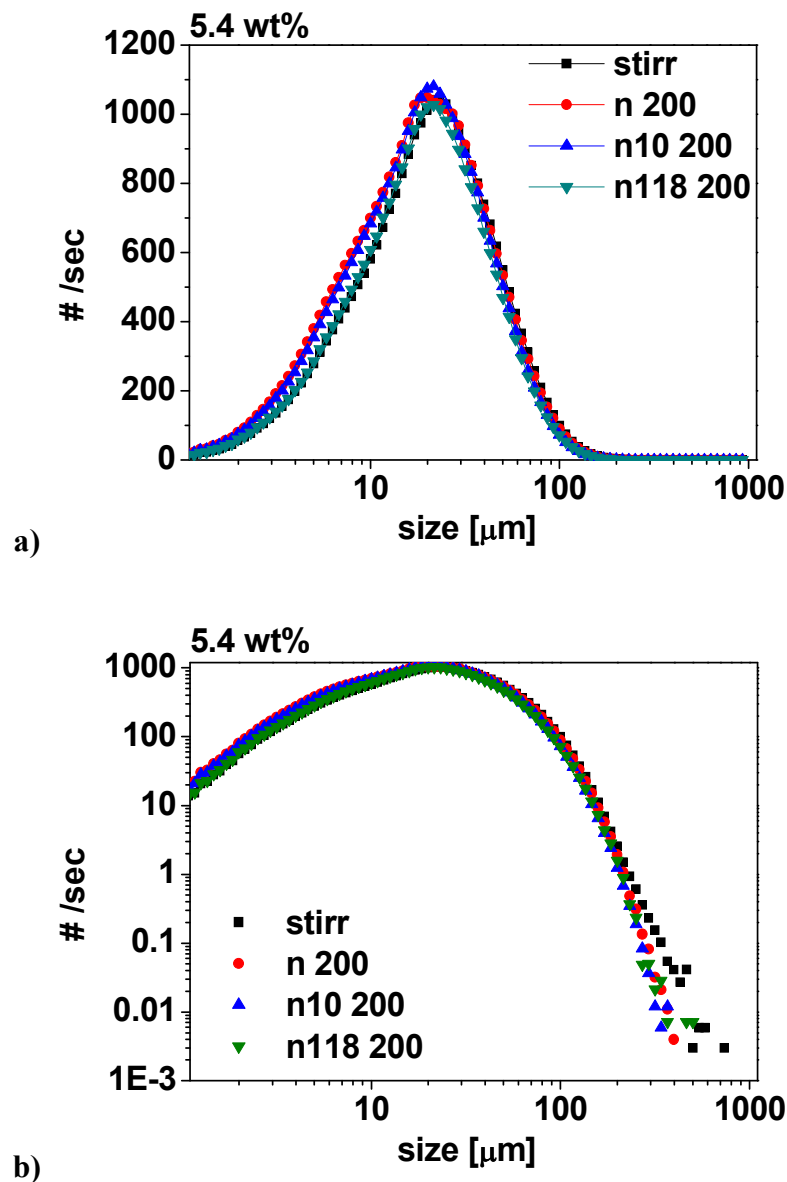


**Figure 5.20** The effect of stirring and 200rpm pumping of 5.4wt% of tyrosine in water on a) linear and b) logarithmic scale.

The above results show that while stirring was gentle for crystals as big as 700 $\mu\text{m}$ , the influence of engaging a peristaltic pump and then a contraction nozzle caused much more significant breakage. Passing the suspension through a contraction with the n118 nozzle angle resulted in the relatively gentle breakage only. Crystals as big as 500 $\mu\text{m}$  survived undamaged and this can be confirmed by no increase of fines in the Figure 5.20a. More significant breakage was observed by the pump itself and

with n118 nozzle. Simultaneously to the increase of fines for both experiments a striking reduction of the largest sizes is observed with the maximum size for n10 being 350 $\mu$ m and 400 $\mu$ m for the pump.

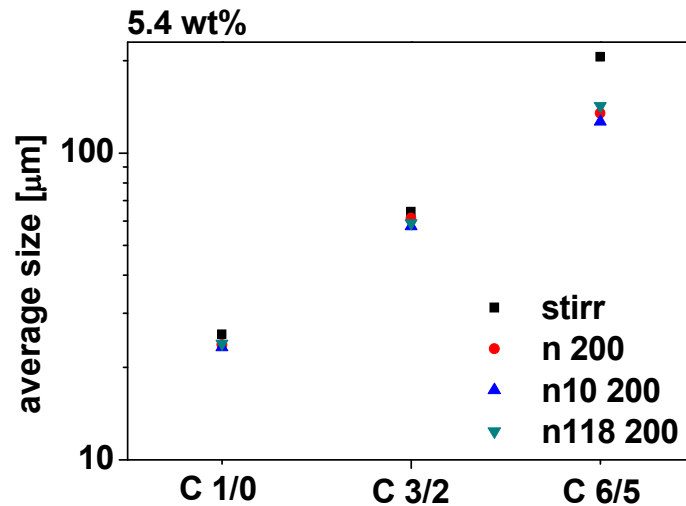


**Figure 5.21** Average sizes for 5.4wt% of tyrosine in water tests at 200rpm pumping power.

It is true that relative changes in lower moment ratios are not likely to be statistically significant. Therefore specific statements relating to them are removed as suggested:

The average sizes show a decrease for all calculated moments. A decrease of the highest 6/5 moment ratio from over 200 $\mu$ m to 140 $\mu$ m for pumping with n118 contraction is seen, and to around 130 for n10 and just pumping.

Gentler pumping at 200rpm results in similar rate of breakage in comparison to 400rpm but it can be concluded that different crystals were broken as a similar number of smaller is seen on Figure 5.20, but not so many of the largest crystals disappeared.

A decrease of the pumping speed from 400rpm to 200rpm caused an overall lower breakage rate for 5.4wt% tyrosine crystal suspension.

### 5.5.3 Effect of stirring and flow on 9.0 wt% slurries

It can be seen that pumping without the nozzle turned out to be relatively gentle, and almost no breakage is observed with crystals around 600 $\mu\text{m}$  sizes. Stirring seemed to be harsher and reduced the highest sizes to near 400 $\mu\text{m}$ . This effect may be caused by shorter residence time and exposition to stirrer blade during pumping.

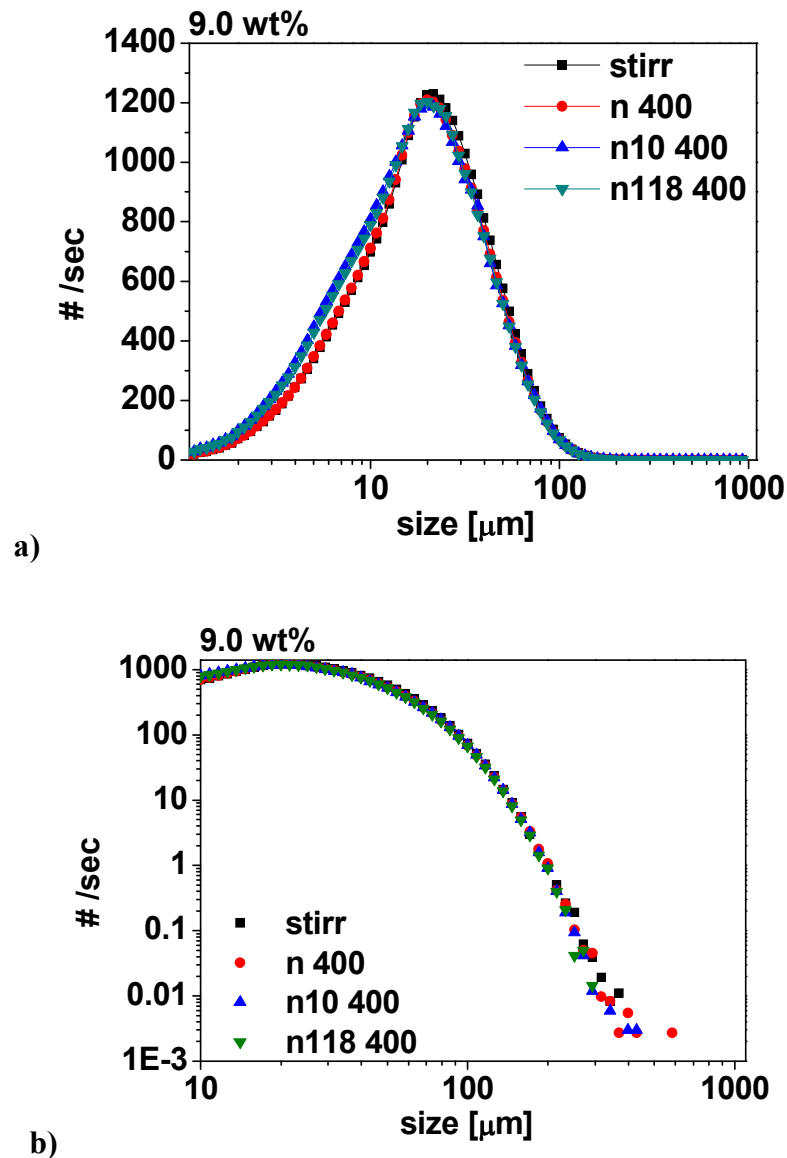


**Figure 5.22** The effect of stirring and 400rpm pumping power on 9.0wt% of tyrosine in water on a) linear and b) logarithmic scale.

The above results unexpectedly show that the highest concentrated slurries are very resistant to the flow conditions they were exposed to and high pumping shows less breakage than expected after lower values of concentrations. A slightly larger effect is observed by passing 9.0wt% slurry by n10 and n118 where obtainable size ranges in around 400 $\mu\text{m}$  and 300 $\mu\text{m}$  respectively. This breakage caused simultaneous creation of fines but not strikingly.

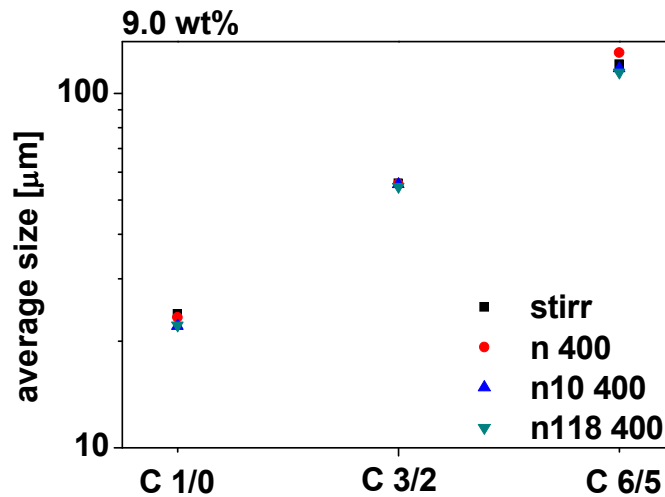


**Figure 5.23** Average sizes for 9.0 wt% of tyrosine in water tests at 400rpm pumping power.

The calculated averages at ratio C 6/5 show the highest average tyrosine crystal with 130 $\mu\text{m}$  after the use of peristaltic pump at 400rpm. There was slightly bigger breakage caused by stirring reducing the average to 121 $\mu\text{m}$ , then 118 $\mu\text{m}$  for n10 and finally 115 $\mu\text{m}$  for n118. The differences in averages calculated by lower moment ratio 1/0 are almost negligible with 24 $\mu\text{m}$  for stirring and 23 $\mu\text{m}$  for the peristaltic pump and 22 $\mu\text{m}$  for both n10 and n118 contraction nozzles.

These suspensions are much less prone to breakage than those at lower concentration. But it has to be taken into consideration that the first test showing the effect of concentration of results proves that we cannot directly quantitatively look at those results.

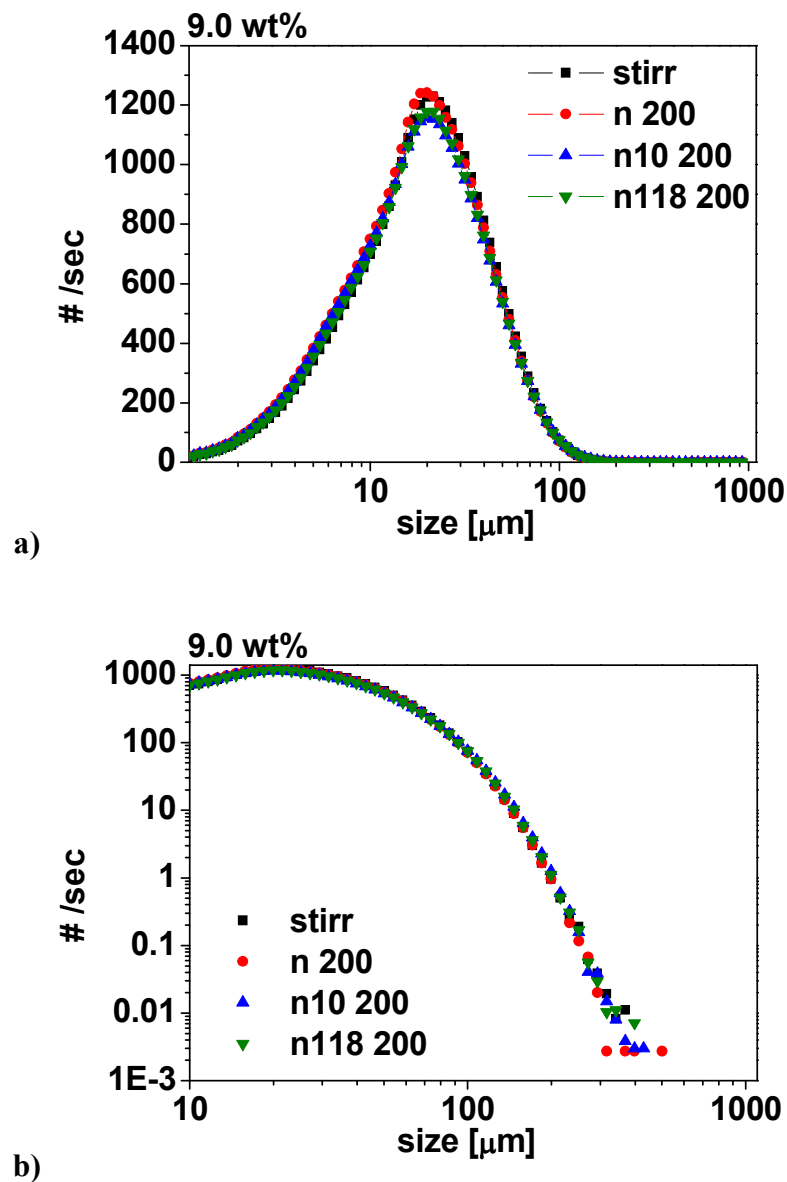


**Figure 5.24** The effect of stirring and 200rpm pumping of 9.0wt% of tyrosine in water on a) linear and b) logarithmic scale.

Decreasing the pumping speed from 400 to 200rpm caused an even smaller rate of breakage of those relatively concentrated 9.0wt% slurries. Figure 5.24a shows no increase in fines caused by each experiment. Looking at Figure 5.24b it is clear that only very slight reduction of the largest sizes is observed after the experiment with the n118 nozzle. While tests with the peristaltic pump were gentle to crystals with the maximum size of around 500μm stirring seemed to break them leaving maximum

380 $\mu\text{m}$ . After n10 and n118 the maximum size of crystals detected in the flask was around 400 $\mu\text{m}$ .

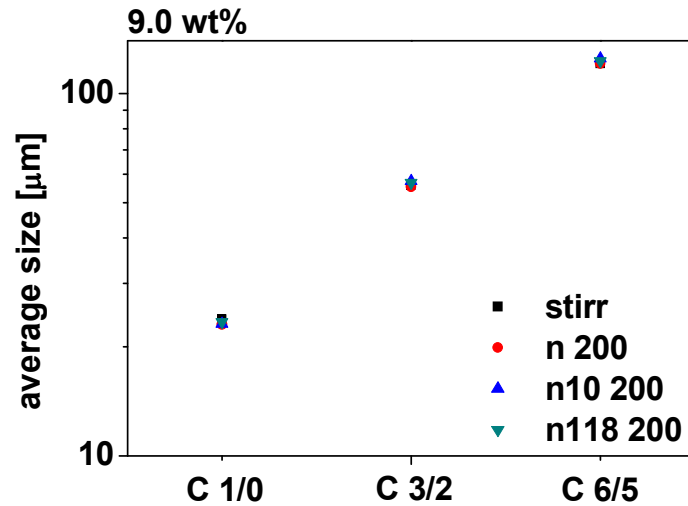


**Figure 5.25** Average sizes for 9.0 wt% of tyrosine in water tests with 200rpm pumping power.

The calculated average moments show almost no additional breakage to stirring for lower pumping power and the highest concentration. The highest moment ratio averages are all in the range of 121 $\mu\text{m}$  to 125 $\mu\text{m}$  after all tests, whilst the lowest moment ratio 1/0 results in even similar averages being 23 $\mu\text{m}$  or 24 $\mu\text{m}$ . This is very visible by all points overlapping each other.

Interestingly these highly concentrated slurries are very resistant to exposure to stirring as well as high shear stresses generated by contraction nozzles.

## 5.6 Discussion

Flow-o-meter concept is based on the exposure of slurries to a well controlled peak stresses over and above those in the rest of the loop. Flow sensitivity of the breakage in tyrosine slurries in (saturated) water was assessed with the flow-o-meter in nominally turbulent flow conditions.

Cumulative results of tests on 2.7%, 5.4% and 9.0wt% concentrated tyrosine suspensions show the effect of stirring, pump and contraction nozzles.

2.7wt% slurries were mostly broken by passing through 180 angle contractions with 400rpm pumping power, then n118 and 400rpm. Nozzle n10 caused similar breakage for with 400rpm and 200rpm followed by n118 at 200rpm and least breakage was a result of stirring.

Effects for 2.7 wt%:

**n180 400 > n118 400 > n10 400 = n10 200 > n118 200 >> stirr700**

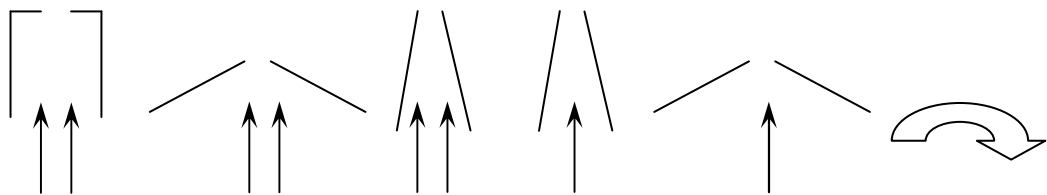


**Figure 4.49** Schematic effects of flow on breakage with angle indicating real angles 180, 118 and 10 deg and indication of pumping speed with one arrow as 200rpm and 400rpm as two arrows.

Similar results were obtained as effects for 9.0 wt% and 5.4 wt%.

**n118 400 > n10 400 > = stirr700 > = n118 200 > n10 200**

The effects of stirring at 700rpm show that the collisional stresses in comparison to the turbulent flow stresses weren't dominant and didn't cause a lot of breakage.

Slurries with the lower concentration of tyrosine were more prone to breakage during stirring in all range of sizes.

The effect of peristaltic pump is not so substantial and varies in the range of 1-3% of crystals for higher concentration but substantially large for low concentration. The effect of flow rate was easy to predict: larger rate of breakage for bigger flow rate.

Presented data show that the biggest breakage occurred during first 10 minutes of stirring and pumping.

The decrease of the mean size of tyrosine crystals while being pumped through a loop with applied well a defined contraction flow is more significant for the higher flow rate (700 ml/min at pump speed of 400rpm), corresponds to a larger extent of crystal of breakage. Since the calculated time for the whole volume of the flask (180 ml) to pass through the contraction is 15 seconds for the 400rpm and 26 seconds for the 200rpm, it is true that at the higher pumping rate the slurry passes through the contraction about twice more times over the same time period. However, once steady state CLDs are achieved, further passing of the slurry through the contraction does not cause any additional measurable breakage, so that the larger steady state extent of breakage at the higher flow rate through the contraction is clearly related to the flow rate effect itself rather than to residence time effects.

In all cases breakage occurred with the most striking effect for the highest value of the entry angle of the nozzle (inertial subrange stresses inside nozzles or collisions?) and for 2.7wt% being the lowest for 10° and highest for 180° value of entry angle of contraction.

The extent of breakage of tyrosine slurries was found not to be proportional to the solid loading and more concentrated tyrosine slurries were found to be less prone to breakage. This behaviour was most likely not due to the change of viscosity, which was relatively minor (see Appendix 8.8), but rather from the flow alignment of the needle-like crystals in more concentrated suspensions due to changing flow patterns with increasing solid concentration. It should be also noted that the total FBRM count rates are not strictly proportional to the solid concentration, so that the count rates increase less than linearly with increasing solid concentration and the peak of the CLD distribution shifts to smaller sizes for more concentrated slurries. This effect

is more pronounced for higher weighted moments and so it appears that indeed it is somewhat less likely to see larger particles at higher slurry concentrations (while assuming that dispersion and stirring is gentle enough that no additional breakage is introduced in more concentrated slurries). This is consistent with the snowstorm effect in the sense that in more concentrated suspensions there could be so many small particles passing in the front of the probe window that they may start obscuring larger particles among them. Therefore one cannot make direct quantitative comparisons between measured CLD distributions at various concentrations. However, we can consider relative changes of CLDs in slurries (at a given concentration) before and after being exposed to the well-controlled contraction flow, since the solid concentration remains constant. If we see that there is only a small change in the overall CLD, we can argue that the extent of the snowstorm effect is the same, and so we can conclude that there is only a small change in the concentration of large crystals, i.e., there is negligible breakage. On the other hand, if we see that there is a significant change in the overall CLD, e.g., a significant increase in counts at small cord lengths and decrease in counts at large cord lengths, we can conclude that there is a significant extent of breakage (or at least attrition) of large crystals, since small cord lengths have to come from breakage or attrition of larger ones.

---

## CHAPTER 6 CONCLUSIONS

The effect of flow has been shown to influence every stage of the crystallisation process from nucleation to crystal growth, aggregation and breakage.

Amongst the key results of this thesis our discovery and careful experimental verification show that the polymorphic outcome of cooling crystallisation of CBZ can be controlled by stirring. We have shown that depending on the flow regime crystallisation can follow two different paths. For quiescent conditions, a few crystals of alpha are formed from clear solution. These large crystals undergo transformation into stable beta form within a few hours. Under sufficiently vigorous stirring, turbid suspensions of fine alpha or beta crystals were produced. A wide range of nucleation times was recorded. At the shortest induction times, small needle-like alpha form crystals initially appeared, quickly transforming into beta form crystals under continuous stirring. For longer induction times, beta form was predominantly observed at the onset of turbidity.

A novel setup for transmittance and scattering light intensity measurement was used for the monitoring of crystal formation under stirring conditions. Distinct pathways in intensity plots were observed for each respective polymorph. It has been shown to be very effective method of studying polymorph transformation pathways in carbamazepine solutions. The initial experiments carried out on the setup lead to successful setting build up and validation of the setup allowing future users to perform more comprehensive measurements.

Unexpected conclusions come from observations of the effect of source of CBZ (recrystallised in house and commercial) on the induction time and the initial polymorphic outcome. The problem of impurities present in either solvent or commercially manufactured powder is a big problem for crystallisation and reproducibility of the outcome of crystallisation process has been highlighted.

The question of WHY flow affects polymorphic outcome is very complex. From a hydrodynamic point of view the flow scale during stirring should only affect much larger structures in solutions than molecules or molecular scale nuclei. Our results

led to preliminary work going deeper into self-association in supersaturated solutions and subsequent nucleation steps searching for the hypothetical larger scale clusters. But this work has not been fully concluded and some preliminary results are reported in the Appendix 8.2.

The breakage phenomenon in extensional flows was investigated on tyrosine in water slurries at different solid loadings. FBRM has been successfully used to monitor changes of crystal size distributions during breakage experiments. It has been shown that tyrosine crystals are prone to limited breakage and the effect of used nozzles is greater for the greater value of the entry angle of the nozzle and higher flow rate. The dependence of the reduction of average size value of crystals on concentration clearly shows that more concentrated slurries are perhaps counter intuitively less prone to breakage in extensional flows however snowstorm effect must be taken into consideration. This is most likely due to more effective alignment of needle-shaped crystals at higher solid loadings.

During the course of this work it was not possible to exhaustively study all problems related the research project topics. Therefore some key suggestions for future work are given below:

- Further development of the turbidity and scattering measurement setup including temperature control, robust probe holder and flow through cell. Studies of other model systems and assessment of capabilities to discriminate wider range of different morphologies and sizes of crystals. Using the setup for MSZW studies.
- Rationalisation of the difference in the behaviour of commercial and recrystallised carbamazepine mainly focusing on impurities by HPLC or other analytical methods. Try to quantitatively assess the effect of water content in ethanol used for crystallisation.
- Studies of crystal breakage could be extended by sampling of slurries and imaging and other sizing technique. Dilution experiments with slurries of different solid loadings before and after being exposed to well controlled flow regimes in order to allow for direct and quantitative comparison of breakage at different solid concentrations.

## CHAPTER 7 REFERENCES

1. Schoen, H., M., C. Grove, S, Jr., and J. Palermo, A., *The early history of crystallization*. Journal of Chemical Education, 1956. **33**(8): p. 373-375.
2. Seville, J.P.K., U. Tuzun, and R. Clift, *Processing of particulate solids*. 1997, London: Blackie Academic & Professional.
3. Mullin, J.W., *Crystallization* ed. t. ed. 2001: Butterworth-Heinemann 594.
4. Davey, R. and J. Garside, *From molecules to crystallizers*. 2000: Oxford University Press
5. Jones, A.G., *Crystallization process systems* 2002: Butterworth-Heinemann 328.
6. Atkins, P.W., *Physical Chemistry*. 9th ed, ed. O.U. Press. 1993. 183-203.
7. Brittain, H.G., *Polymorphism in pharmaceutical solids*, ed. M. Dekker. 1999, New York
8. Rosen, S., <http://phycomp.technion.ac.il/~sshaharr/intro.html>. Last accessed April 2010.
9. Nangia, A., *Conformational polymorphism in organic crystals*. Accounts of Chemical Research, 2008. **41**(5): p. 595-604.
10. Novoselov, K.S., et al., *Electric field effect in atomically thin carbon films*. Science, 2004. **306**(5696): p. 666-669.
11. Novoselov, K.S., et al., *Two-dimensional gas of massless Dirac fermions in graphene*. Nature, 2005. **438**(7065): p. 197-200.
12. Bernstein, J., *Cultivating crystal forms*. Chemical Communications, 2005(40): p. 5007-5012.
13. Vishweshwar, P., et al., *Pharmaceutical co-crystal*. Journal of Pharmaceutical Sciences, 2006. **95**(3): p. 499-516.
14. Almarsson, O. and M.J. Zawortko, *Crystal engineering of the composition of pharmaceutical phases. Do pharmaceutical co-crystals represent a new path to improved medicines?* Chemical Communications, 2004(17): p. 1889-1896.
15. Urbanus, J., et al., *Co-Crystallization as a Separation Technology: Controlling Product Concentrations by Co-Crystals*. Crystal Growth & Design. **10**(3): p. 1171-1179.
16. Black, S.N., et al., *Structure, solubility, screening, and synthesis of molecular salts*. Journal of Pharmaceutical Sciences, 2007. **96**(5): p. 1053-1068.
17. McCrone, W.C., *Polymorphism*. Physics and Chemistry of the Organic Solid State, ed. M.M.L. D. Fox, and A. Weissberger. Vol. 2. 1965, New York: Wiley Interscience. 725-767.
18. Brittain, H.G., *Polymorphism in pharmaceutical solids*. Drugs and the pharmaceutical sciences ; v. 95, ed. M. Dekker. c1999, New York
19. Chow, K., et al., *Engineering of pharmaceutical materials: An industrial perspective*. Journal of Pharmaceutical Sciences, 2008. **97**(8): p. 2855-2877.
20. Kahela, P., et al., *Pharmacokinetics and Dissolution of 2 Crystalline Forms of Carbamazepine*. International Journal of Pharmaceutics, 1983. **14**(1): p. 103-112.
21. Ono, M., et al., *Effects of dehydration temperature on water vapor adsorption and dissolution behavior of carbamazepine*. International Journal of Pharmaceutics, 2002. **239**(1-2): p. 1-12.
22. Bernstein, J., *Polymorphism in Molecular Crystals*, ed. O.U. Press. 2002, Oxford.

23. Marsac, P.J., S.L. Shamblin, and L.S. Taylor, *Theoretical and practical approaches for prediction of drug-polymer miscibility and solubility*. *Pharmaceutical Research*, 2006. **23**(10): p. 2417-2426.
24. Lipinski, C.A., et al., *Experimental and computational approaches to estimate solubility and permeability in drug discovery and development settings*. *Advanced Drug Delivery Reviews*, 1997. **23**(1-3): p. 3-25.
25. Dressman, J.B., et al., *Dissolution testing as a prognostic tool for oral drug absorption: Immediate release dosage forms*. *Pharmaceutical Research*, 1998. **15**(1): p. 11-22.
26. Kasim, N.A., et al., *Molecular properties of WHO essential drugs and provisional biopharmaceutical classification*. *Molecular Pharmaceutics*, 2004. **1**(1): p. 85-96.
27. Rodriguez-Spong, B., et al., *General principles of pharmaceutical solid polymorphism: a supramolecular perspective*. *Advanced Drug Delivery Reviews*, 2004. **56**(3): p. 241-274.
28. Kawakami, K. and Y. Ida, *Application of modulated-temperature DSC to the analysis of enantiotropically related polymorphic transitions*. *Thermochimica Acta*, 2005. **427**(1-2): p. 93-99.
29. Kaneko, S., et al., *Effect of supersaturation on crystal size and number of crystals produced in antisolvent crystallization*. *Journal of Chemical Engineering of Japan*, 2002. **35**(11): p. 1219-1223.
30. Datta, S. and D.J.W. Grant, *Effect of supersaturation on the crystallization of phenylbutazone polymorphs*. *Crystal Research and Technology*, 2005. **40**(3): p. 233-242.
31. Yang, G.Y., et al., *Crystal shape control by manipulating supersaturation in batch cooling crystallization*. *Crystal Growth & Design*, 2006. **6**(12): p. 2799-2803.
32. Lu, J. and J.K. Wang, *Agglomeration, breakage, population balance, and crystallization kinetics of reactive precipitation process*. *Chemical Engineering Communications*, 2006. **193**(7): p. 891-902.
33. Kashchiev, D., *Nucleation : basic theory with applications*, ed. B. Heinemann. 2000.
34. Biscans, B., *Impact attrition in crystallization processes. Analysis of repeated impacts events of individual crystals*. *Powder Technology*, 2004. **143**: p. 264-272.
35. Markov, I.V., *Crystal growth for beginners : fundamentals of nucleation, crystal growth and epitaxy*. 2003, Singapore: River Edge, N.J. : World Scientific.
36. Vekilov, P.G., *Dense liquid precursor for the nucleation of ordered solid phases from solution*. *Crystal Growth & Design*, 2004. **4**(4): p. 671-685.
37. ten Wolde, P.R. and D. Frenkel, *Enhancement of protein crystal nucleation by critical density fluctuations*. *Science*, 1997. **277**(5334): p. 1975-1978.
38. Talanquer, V. and D.W. Oxtoby, *Crystal nucleation in the presence of a metastable critical point*. *Journal of Chemical Physics*, 1998. **109**(1): p. 223-227.
39. Allen, K., et al., *The crystallization of glycine polymorphs from emulsions, microemulsions, and lamellar phases*. *Crystal Growth & Design*, 2002. **2**(6): p. 523-527.
40. Chattopadhyay, S., et al., *SAXS study of the nucleation of glycine crystals from a supersaturated solution*. *Crystal Growth & Design*, 2005. **5**(2): p. 523-527.
41. Huang, J., T.C. Stringfellow, and L. Yu, *Glycine exists mainly as monomers, not dimers, in supersaturated aqueous solutions: Implications for understanding its crystallization and polymorphism*. *Journal of the American Chemical Society*, 2008. **130**(42): p. 13973-13980.

42. Soga, K.G., J.R. Melrose, and R.C. Ball, *Metastable states and the kinetics of colloid phase separation*. Journal of Chemical Physics, 1999. **110**(4): p. 2280-2288.
43. Sitnikova, N.L., et al., *Spontaneously formed trans-anethol/water/alcohol emulsions: Mechanism of formation and stability*. Langmuir, 2005. **21**(16): p. 7083-7089.
44. Ganachaud, F. and J.L. Katz, *Nanoparticles and nanocapsules created using the Ouzo effect: Spontaneous emulsification as an alternative to ultrasonic and high-shear devices*. Chemphyschem, 2005. **6**(2): p. 209-216.
45. Niederberger, M. and H. Colfen, *Oriented attachment and mesocrystals: Non-classical crystallization mechanisms based on nanoparticle assembly*. Physical Chemistry Chemical Physics, 2006. **8**(28): p. 3271-3287.
46. Kim, W.S., et al., *Crystal agglomeration of europium oxalate in reaction crystallization using double-jet semi-batch reactor*. Materials Research Bulletin, 2004. **39**(2): p. 283-296.
47. Rodriguez-Hornedo, N., et al., *Reaction crystallization of pharmaceutical molecular complexes*. Molecular Pharmaceutics, 2006. **3**(3): p. 362-367.
48. Kubota, N., et al., *Seeding policy in batch cooling crystallization*. Powder Technology, 2001. **121**(1): p. 31-38.
49. Oosterhof, H., G.J. Witkamp, and G.M. van Rosmalen, *Evaporative crystallization of anhydrous sodium carbonate at atmospheric conditions*. Aiche Journal, 2001. **47**(10): p. 2220-2225.
50. Dunlop, K.V. and B. Hazes, *When less is more: a more efficient vapour-diffusion protocol*. Acta Crystallographica Section D-Biological Crystallography, 2003. **59**: p. 1797-1800.
51. Talreja, S., et al., *Screening and optimization of protein crystallization conditions through gradual evaporation using a novel crystallization platform*. Journal of Applied Crystallography, 2005. **38**: p. 988-995.
52. Oosterhof, H., G.J. Witkamp, and G.M. van Rosmalen, *Antisolvent crystallization of anhydrous sodium carbonate at atmospheric conditions*. Aiche Journal, 2001. **47**(3): p. 602-608.
53. Lahav, M. and L. Leiserowitz, *The effect of solvent on crystal growth and morphology*. Chemical Engineering Science, 2001. **56**(7): p. 2245-2253.
54. Nagy, Z.K., M. Fujiwara, and R.D. Braatz, *Modelling and control of combined cooling and antisolvent crystallization processes*. Journal of Process Control, 2008. **18**(9): p. 856-864.
55. Gomez-Morales, J., et al., *Nucleation and Polymorphism of Calcium Carbonate by a Vapor Diffusion Sitting Drop Crystallization Technique*. Crystal Growth & Design. **10**(2): p. 963-969.
56. Nagy, Z.K., et al., *Comparative performance of concentration and temperature controlled batch crystallizations*. Journal of Process Control, 2008. **18**(3-4): p. 399-407.
57. Correia, P., et al., *Solubility and metastable zone width of 1-keto-1,2,3,4-tetrahydro-6-methylcarbazole in acetone*. Journal of Chemical and Engineering Data, 2006. **51**(4): p. 1306-1309.
58. Lu, Y.H. and C.B. Ching, *Study on the metastable zone width of ketoprofen*. Chirality, 2006. **18**(4): p. 239-244.

59. Lakshmi, K.U. and K. Ramamurthi, *Growth and characterization of 2,6-dibenzylidenecyclohexanone single crystal*. *Crystal Research and Technology*, 2005. **40**(12): p. 1165-1168.
60. Ludlam-Brown, I. and P. York, *The crystalline modification of succinic acid by variations in crystallization conditions*. *Journal of Physics D: Applied Physics*, 1993. **26**: p. B60-B65.
61. O'Grady, D., et al., *The effect of mixing on the metastable zone width and nucleation kinetics in the anti-solvent crystallization of benzoic acid*. *Chemical Engineering Research & Design*, 2007. **85**(A7): p. 945-952.
62. Van Santen, R.A., *The Ostwald Step Rule*. *J. Phys. Chem.*, 1984. **88**: p. 5768-5769.
63. Muller, M., et al., *Process development strategy to ascertain reproducible API polymorph manufacture*. *Crystal Growth & Design*, 2006. **6**(4): p. 946-954.
64. Fujiwara, M., et al., *First-principles and direct design approaches for the control of pharmaceutical crystallization*. *Journal of Process Control*, 2005. **15**(5): p. 493-504.
65. Bauer, J., et al., *Ritonavir: An extraordinary example of conformational polymorphism*. *Pharmaceutical Research*, 2001. **18**(6): p. 859-866.
66. Blagden, N. and R.J. Davey, *Polymorph selection: Challenges for the future?* *Crystal Growth & Design*, 2003. **3**(6): p. 873-885.
67. Kitamura, M., *Strategy for control of crystallization of polymorphs*. *Crystengcomm*, 2009. **11**(6): p. 949-964.
68. Llinas, A. and J.M. Goodman, *Polymorph control: past, present and future*. *Drug Discovery Today*, 2008. **13**(5-6): p. 198-210.
69. Threlfall, T., *Crystallisation of polymorphs: Thermodynamic insight into the role of solvent*. *Organic Process Research & Development*, 2000. **4**(5): p. 384-390.
70. Kitamura, M., *Controlling factors and mechanism of polymorphic crystallization*. *Crystal Growth & Design*, 2004. **4**(6): p. 1153-1159.
71. Beckmann, W., *Seeding the desired polymorph: Background, possibilities, limitations, and case studies*. *Organic Process Research & Development*, 2000. **4**(5): p. 372-383.
72. Beckmann, W., W. Otto, and U. Budde, *Crystallisation of the stable polymorph of hydroxytriendione: Seeding process and effects of purity*. *Organic Process Research & Development*, 2001. **5**(4): p. 387-392.
73. Yu, L., *Nucleation of one polymorph by another*. *Journal of the American Chemical Society*, 2003. **125**(21): p. 6380-6381.
74. Palacios, S.M. and M.A. Palacio, *Enantiomeric resolution of albuterol sulfate by preferential crystallization*. *Tetrahedron-Asymmetry*, 2007. **18**(10): p. 1170-1175.
75. Reguera, D. and J.M. Rubi, *Homogeneous nucleation in inhomogeneous media. II. Nucleation in a shear flow*. *Journal of Chemical Physics*, 2003. **119**(18): p. 9888-9893.
76. Somani, R.H., et al., *Structure development during shear flow-induced crystallization of i-PP: In-situ small-angle X-ray scattering study*. *Macromolecules*, 2000. **33**(25): p. 9385-9394.
77. Penkova, A., et al., *Nucleation of protein crystals under the influence of solution shear flow*, in *Interdisciplinary Transport Phenomena in the Space Sciences*, S.S. Sadhal, Editor. 2006, Blackwell Publishing: Oxford. p. 214-231.
78. Cashell, C., D. Corcoran, and B.K. Hodnett, *Control of polymorphism and crystal size of L-glutamic acid in the absence of additives*. *Journal of Crystal Growth*, 2004. **273**(1-2): p. 258-265.

79. Roelands, C.P.M., et al., *Precipitation mechanism of stable and metastable polymorphs of L-glutamic acid*. *Aiche Journal*, 2007. **53**(2): p. 354-362.
80. Woo, X.Y., et al., *Simulation of mixing effects in antisolvent crystallization using a coupled CFD-PDF-PBE approach*. *Crystal Growth & Design*, 2006. **6**(6): p. 1291-1303.
81. Wan, J., X.Z. Wang, and C.Y. Ma, *Particle Shape Manipulation and Optimization in Cooling Crystallization Involving Multiple Crystal Morphological Forms*. *Aiche Journal*, 2009. **55**(8): p. 2049-2061.
82. Abu Bakar, M.R., et al., *The Impact of Direct Nucleation Control on Crystal Size Distribution in Pharmaceutical Crystallization Processes*. *Crystal Growth & Design*, 2009. **9**(3): p. 1378-1384.
83. Mougin, P., et al., *On-line monitoring of a crystallization process*. *Aiche Journal*, 2003. **49**(2): p. 373-378.
84. Roberts, R.J., R.S. Payne, and R.C. Rowe, *Mechanical property predictions for polymorphs of sulphathiazole and carbamazepine*. *European Journal of Pharmaceutical Sciences*, 2000. **9**(3): p. 277-283.
85. Mersmann, A., *Supersaturation and nucleation*. *Chemical Engineering Research & Design*, 1996. **74**(A7): p. 812-820.
86. Moulton, B. and M.J. Zaworotko, *From molecules to crystal engineering: Supramolecular isomerism and polymorphism in network solids*. *Chemical Reviews*, 2001. **101**(6): p. 1629-1658.
87. Szabo-Revesz, P., et al., *Crystal growth of drug materials by spherical crystallization*. *Journal of Crystal Growth*, 2002. **237**: p. 2240-2245.
88. Davey, R.J., *Crystallization - How come you look so good?* *Nature*, 2004. **428**(6981): p. 374-375.
89. Pratola, F., S.J.R. Simons, and A.G. Jones, *A novel experimental device for measurement of agglomerative crystallization forces*. *Chemical Engineering Research & Design*, 2002. **80**(A5): p. 441-448.
90. Hounslow, M.J., et al., *A micro-mechanical model for the rate of aggregation during precipitation from solution*. *Chemical Engineering Science*, 2001. **56**(7): p. 2543-2552.
91. Alander, E.M. and A.C. Rasmuson, *Mechanisms of crystal agglomeration of paracetamol in acetone-water mixtures*. *Industrial & Engineering Chemistry Research*, 2005. **44**(15): p. 5788-5794.
92. Yu, Z.Q., R.B.H. Tan, and P.S. Chow, *Effects of operating conditions on agglomeration and habit of paracetamol crystals in anti-solvent crystallization*. *Journal of Crystal Growth*, 2005. **279**(3-4): p. 477-488.
93. Gahn, C. and A. Mersmann, *Brittle fracture in crystallization processes Part A. Attrition and abrasion of brittle solids*. *Chemical Engineering Science*, 1999. **54**(9): p. 1273-1282.
94. Gahn, C. and A. Mersmann, *Brittle fracture in crystallization processes Part B. Growth of fragments and scale-up of suspension crystallizers*. *Chemical Engineering Science*, 1999. **54**(9): p. 1283-1292.
95. Synowiec, P., A.G. Jones, and P.A. Shamlou, *Crystal Break-up in Dilute Turbulently Agitated Suspensions*. *Chemical Engineering Science*, 1993. **48**(20): p. 3485-3495.
96. Illing, S. and S.T.L. Harrison, *The kinetics and mechanism of Corynebacterium glutamicum aggregate breakup in bioreactors*. *Chemical Engineering Science*, 1999. **54**(4): p. 441-454.

97. Shamlou, P.A., A.G. Jones, and K. Djamarani, *Hydrodynamics of Secondary Nucleation in Suspension Crystallization*. Chemical Engineering Science, 1990. **45**(5): p. 1405-1416.
98. Sato, K., et al., *Two-dimensional population balance model with breakage of high aspect ratio crystals for batch crystallization*. Chemical Engineering Science, 2008. **63**(12): p. 3271-3278.
99. Akrap, M., et al. *Effect of off-bottom impeller clearance on nucleation and crystal growth of borax decahydrate on batch cooling crystallizer*. in *13th European Conference on Mixing*. 2009. London.
100. Kuzmanic, N., R. Zanetic, and M. Akrap, *Impact of floating suspended solids on the homogenisation of the liquid phase in dual-impeller agitated vessel*. Chemical Engineering and Processing, 2008. **47**(4): p. 663-669.
101. Mitsoulis, E., *Numerical simulation of entry flow of fluid S1*. Journal of Non-Newtonian Fluid Mechanics, 1998. **78**(2-3): p. 187-201.
102. Shamlou, P.A., A.G. Jones, and K.M. Djamarani, *Attrition of Potassium Sulphate Crystals in Stirred Vessels*, in *Fluid Mixing Iv*, H. Benkreira, Editor. 1990, Inst Chemical Engineers: Rugby. p. 309-325.
103. Hill, P.J. and K.M. Ng, *Statistics of multiple particle breakage*. Aiche Journal, 1996. **42**(6): p. 1600-1611.
104. Bemrose, C.R. and J. Bridgwater, *A Review of Attrition and Attrition Test Methods*. Powder Technology, 1987. **49**(2): p. 97-126.
105. Soos, M., J. Sefcik, and M. Morbidelli, *Investigation of aggregation, breakage and restructuring kinetics of colloidal dispersions in turbulent flows by population balance modeling and static light scattering*. Chemical Engineering Science, 2006. **61**(8): p. 2349-2363.
106. Marchisio, D.L., et al., *Effect of fluid dynamics on particle size distribution in particulate processes*. Chemical Engineering & Technology, 2006. **29**(2): p. 191-199.
107. Karabelas, A.J., *Particle Attrition in Shear-Flow of Concentrated Slurries*. Aiche Journal, 1976. **22**(4): p. 765-771.
108. Sonntag, R.C. and W.B. Russel, *Structure and Breakup of Floccs Subjected to Fluid Stresses .3. Converging Flow*. Journal of Colloid and Interface Science, 1987. **115**(2): p. 390-395.
109. Kobayashi, M., *Breakup and strength of polystyrene latex floccs subjected to a converging flow*. Colloids and Surfaces a-Physicochemical and Engineering Aspects, 2004. **235**(1-3): p. 73-78.
110. Blaser, S., *Break-up of floccs in contraction and swirling flows*. Colloids and Surfaces a-Physicochemical and Engineering Aspects, 2000. **166**(1-3): p. 215-223.
111. Allen, T., *Particle Size Measurement*. 5th edition ed. 1997, London: Chapman & Hall
112. Ehrl, L., M. Soos, and M. Morbidelli, *Sizing polydisperse dispersions by focused beam reflectance and small angle static light scattering*. Particle & Particle Systems Characterization, 2007. **23**(6): p. 438-447.
113. Li, M.Z., et al., *On-line crystallization process parameter measurements using ultrasonic attenuation spectroscopy*. Crystal Growth & Design, 2004. **4**(5): p. 955-963.
114. Howard, K.S., et al., *A Process Analytical Technology Based Investigation of the Polymorphic Transformations during the Antisolvent Crystallization of Sodium Benzoate from IPA/Water Mixture*. Crystal Growth & Design, 2009. **9**(9): p. 3964-3975.

115. Birch, M., et al., *Towards a PAT-Based strategy for crystallization development*. Organic Process Research & Development, 2005. **9**(3): p. 360-364.
116. Billot, P., M. Couty, and P. Hosek, *Application of ATR-UV Spectroscopy for Monitoring the Crystallisation of UV Absorbing and Nonabsorbing Molecules*. Organic Process Research & Development. **14**(3): p. 511-523.
117. Liu, W.J., H.Y. Wei, and S. Black, *An Investigation of the Transformation of Carbamazepine from Anhydrate to Hydrate Using in Situ FBRM and PVM*. Organic Process Research & Development, 2009. **13**(3): p. 494-500.
118. Riebel, U., V. Kofler, and F. Loffler, *Shape Characterization of Crystals and Crystal Agglomerates*. Particle & Particle Systems Characterization, 1991. **8**(1): p. 48-54.
119. Bowen, P., *Particle size distribution measurement from millimeters to nanometers, and from rods to platelets*. Journal of Dispersion Science and Technology, 2002. **23**(5): p. 631-662.
120. Florence, A.J. and A. Johnston. *Applications of ATR UV/vis spectroscopy in physical form characterisation of pharmaceuticals*. Process Column 2004 [cited].
121. Howard, K.S., et al., *Combined PAT-Solid State Analytical Approach for the Detection and Study of Sodium Benzoate Hydrate*. Organic Process Research & Development, 2009. **13**(3): p. 590-597.
122. Brittain, H.G., *Spectral methods for the characterization of polymorphs and solvates*. Journal of Pharmaceutical Sciences, 1997. **86**(4): p. 405-412.
123. Ramachandran, E. and S. Natarajan, *Crystal growth of some urinary stone constituents: I. In-vitro crystallization of L-tyrosine and its characterization*. Crystal Research and Technology, 2002. **37**(11): p. 1160-1164.
124. Shinitzky, M., et al., *Unexpected differences between D- and L-tyrosine lead to chiral enhancement in racemic mixtures - Dedicated to the memory of Prof. Shneior Lifson - A great liberal thinker*. Origins of Life and Evolution of the Biosphere, 2002. **32**(4): p. 285-297.
125. Lahav, M., et al., *Parity violating energetic difference and enantiomorphous crystals - caveats; reinvestigation of tyrosine crystallization*. Origins of Life and Evolution of the Biosphere, 2006. **36**(2): p. 151-170.
126. Fasanella, E.L. and W. Gordy, *Electron Spin Resonance of an Irradiated Single Crystal of L Tyrosine Hydro Chloride*. Proceedings of the National Academy of Sciences of the United States of America, 1969. **62**(2): p. 299-304.
127. Florence, A.J., et al., *An automated parallel crystallisation search for predicted crystal structures and packing motifs of carbamazepine*. Journal of Pharmaceutical Sciences, 2006. **95**(9): p. 1918-1930.
128. Edwards, A.D., et al., *Time-resolved X-ray scattering using synchrotron radiation applied to the study of a polymorphic transition in carbamazepine*. Journal of Pharmaceutical Sciences, 2001. **90**(8): p. 1106-1114.
129. Porter, W.W., S.C. Elie, and A.J. Matzger, *Polymorphism in carbamazepine cocrystals*. Crystal Growth & Design, 2008. **8**(1): p. 14-16.
130. ter Horst, J.H. and P.W. Cains, *Co-crystal polymorphs from a solvent-mediated transformation*. Crystal Growth & Design, 2008. **8**(7): p. 2537-2542.
131. Grzesiak, A.L., et al., *Comparison of the four anhydrous polymorphs of carbamazepine and the crystal structure of form I*. Journal of Pharmaceutical Sciences, 2003. **92**(11): p. 2260-2271.

132. Quist, F., J. Mooney, and A.K. Kakkar, *Self-assembled monolayers: Solidification of carbamazepine in Form II at an interface*. Colloids and Surfaces B-Biointerfaces, 2008. **62**(2): p. 319-323.
133. Harris, R.K., et al., *Structural studies of the polymorphs of carbamazepine, its dihydrate, and two solvates*. Organic Process Research & Development, 2005. **9**(6): p. 902-910.
134. Getsoian, A., R.M. Lodaya, and A.C. Blackburn, *One-solvent polymorph screen of carbamazepine*. International Journal of Pharmaceutics, 2008. **348**(1-2): p. 3-9.
135. Li, Y., et al., *Effect of water activity on the transformation between hydrate and anhydrate of carbamazepine*. Organic Process Research & Development, 2008. **12**(2): p. 264-270.
136. Murphy, D., et al., *Solution-mediated phase transformation of anhydrous to dihydrate carbamazepine and the effect of lattice disorder*. International Journal of Pharmaceutics, 2002. **246**(1-2): p. 121-134.
137. Bell, W.L., I.L. Crawford, and G.K. Shiu, *Reduced Bioavailability of Moisture-Exposed Carbamazepine Resulting in Status Epilepticus*. Epilepsia, 1993. **34**(6): p. 1102-1104.
138. Wang, J.T., et al., *Effects of Humidity and Temperature on in-Vitro Dissolution of Carbamazepine Tablets*. Journal of Pharmaceutical Sciences, 1993. **82**(10): p. 1002-1005.
139. Vaccaro, A., J. Šefcik, and M. Morbidelli, *Modeling Focused Beam Reflectance Measurement and its Application to Sizing of Particles of Variable Shape*. Part. Part. Syst. Charact., 2006. **23**: p. 360-373.
140. Kougoulos, E., et al., *Use of focused beam reflectance measurement (FBRM) and process video imaging (PVI) in a modified mixed suspension mixed product removal (MSMPR) cooling crystallizer*. Journal of Crystal Growth, 2005. **273**(3-4): p. 529-534.
141. Barrett, P. and B. Glennon, *Characterizing the metastable zone width and solubility curve using lasentec FBRM and PVM*. Chemical Engineering Research & Design, 2002. **80**(A7): p. 799-805.
142. Kougoulos, E., A.G. Jones, and M.W. Wood-Kaczmar, *Modelling particle disruption of an organic fine chemical compound using Lasentec focussed beam reflectance monitoring (FBRM) in agitated suspensions*. Powder Technology, 2005. **155**(2): p. 153-158.
143. Kail, N., H. Briesen, and W. Marquardt, *Advanced geometrical modeling of focused beam reflectance measurements (FBRM)*. Particle & Particle Systems Characterization, 2007. **24**(3): p. 184-192.
144. Ruf, A., J. Worlitschek, and M. Mazzotti, *Modeling and experimental analysis of PSD measurements through FBRM*. Particle & Particle Systems Characterization, 2000. **17**(4): p. 167-179.
145. Webb, P.A., *A Primer on Particle Sizing by Static Laser Light Scattering*, in Micromeritics Instrument Corp. 2001.
146. E Vanden Bussche, Y.D.D., P Dubruel, K Vergote, E Schacht and C De Wagter. *The use of static light scattering for the structure analysis of radiosensitive polymer gels: a literature survey*. in *Third International Conference on Radiotherapy Gel Dosimetry*. 2004: Journal of Physics: Conference Series.
147. Pusey, P.N., *Neutrons, X-Rays and Light*, ed. P.L.a.T.Z. (Editors). 2003.
148. Finsy, R., *Particle Sizing by Quasi-Elastic Light-Scattering*. Advances in Colloid and Interface Science, 1994. **52**: p. 79-143.
149. Schurtenberger, P. and M.E. Newman, *Environmental particles*, 1993.

150. Soos, M., M. Lattuada, and J. Sefcik, *Interpretation of Light Scattering and Turbidity Measurements in Aggregated Systems: Effect of Intra-Cluster Multiple-Light Scattering*. Journal of Physical Chemistry B, 2009. **113**(45): p. 14962-14970.
151. Postolache, O., et al., *An IR turbidity sensor: Design and application*, in *Imtc 2002: Proceedings of the 19th IEEE Instrumentation and Measurement Technology Conference, Vols 1 & 2*. 2002, IEEE: New York. p. 535-539.
152. Ebie, K., et al., *New measurement principle and basic performance of high-sensitivity turbidimeter with two optical systems in series*. Water Research, 2006. **40**(4): p. 683-691.
153. Liu, J., S.H. Xu, and Z.W. Sun, *Toward an understanding of the turbidity measurement of floc-coagulation rate constants of dispersions containing particles of different sizes*. Langmuir, 2007. **23**(23): p. 11451-11457.
154. Crisp, M.T., et al., *Turbidimetric measurement and prediction of dissolution rates of poorly soluble drug nanocrystals*. Journal of Controlled Release, 2007. **117**(3): p. 351-359.
155. Richardson, E.G., *Turbidity measurement by optical means*. Proceedings of the Physical Society, 1942. **55**(48).
156. Bragg, W.L., *The Diffraction of Short Electromagnetic Waves by a Crystal*. Proceedings of the Cambridge Philosophical Society, 1913. **17**: p. 43-57.
157. Lukin, K., <http://www.eserc.stonybrook.edu/ProjectJava/Bragg/>. Last accessed May 2010.
158. Rhodes, M., *Introduction to Particle Technology*. Second Edition ed. 2008: John Wiley&Sons, Ltd. 450.
159. Sommer, K., *40 years of presentation particle size distributions - Yet still incorrect?* Particle & Particle Systems Characterization, 2001. **18**(1): p. 22-25.
160. Heath, A.R., et al., *Estimating average particle size by focused beam reflectance measurement (FBRM)*. Particle & Particle Systems Characterization, 2002. **19**(2): p. 84-95.
161. Farias, T.L., U.O. Koylu, and M.G. Carvalho, *Effects of polydispersity of aggregates and primary particles on radiative properties of simulated soot*. Journal of Quantitative Spectroscopy & Radiative Transfer, 1996. **55**(3): p. 357-371.
162. Qu, H., M. Louhi-Kultanen, and J. Kallas, *Solubility and stability of anhydrate/hydrate in solvent mixtures*. International Journal of Pharmaceutics, 2006. **321**(1-2): p. 101-107.
163. Fuenfschilling, P.C., et al., *A new industrial process for oxcarbazepine*. Organic Process Research & Development, 2005. **9**(3): p. 272-277.
164. Abu Bakar, M.R., *Process Analytical Technology Based Approaches for the Monitoring and Control of Size and Polymorphic Form in Pharmaceutical Process*, in *Department of Chemical Engineering*. 2010, Loughborough University.
165. Sedlak, M., *Large-scale supramolecular structure in solutions of low molar mass compounds and mixtures of liquids: II. Kinetics of the formation and long-time stability*. Journal of Physical Chemistry B, 2006. **110**(9): p. 4339-4345.
166. Sedlak, M., *Large-scale supramolecular structure in solutions of low molar mass compounds and mixtures of liquids: 1. Light scattering characterization*. Journal of Physical Chemistry B, 2006. **110**(9): p. 4329-4338.

167. Sedlak, M., *Large-scale supramolecular structure in solutions of low molar mass compounds and mixtures of liquids. III. Correlation with molecular properties and interactions*. Journal of Physical Chemistry B, 2006. **110**(28): p. 13976-13984.
168. Thompson, D.R., et al., *Solute concentration measurement of an important organic compound using ATR-UV spectroscopy*. Journal of Crystal Growth, 2005. **276**(1-2): p. 230-236.
169. Lewiner, F., et al., *On-line ATR FTIR measurement of supersaturation during solution crystallization processes. Calibration and applications on three solute/solvent systems*. Chemical Engineering Science, 2001. **56**(6): p. 2069-2084.

---

**CHAPTER 8 APPENDIX**

Appendixes below contain additional data that can be considered as helpful in deeper understanding of the problems included in the thesis as well as additional data obtained for studied systems, not used in the thesis but having the potential of being helpful for future research.

In section 8.1 all additional data for section 4.1 on crystallization of CBZ are presented with additional images as well as an extensive table with all measured induction times.

Section 8.2 focuses on Dynamic Light Scattering of solutions of CBZ in ethanol. In this section the hypothetical liquid-liquid phase separation is studied.

In section 8.3 Static Light Scattering data are presented aiming for liquid-liquid phase separation study as well.

Section 8.4 ATR-UV monitoring of cooling crystallisation of CBZ ethanol solutions is shown.

In section 8.5 results of Raman Spectroscopy of CBZ in ethanol are shown.

Section 8.6 highlights the possible applications of NIR spectroscopy for the measurement of water content in CBZ in ethanol solutions

Section 8.7 presents all results of the effect of flow conditions on breakage of tyrosine not included in the main results Chapter 5.

And finally section 8.8 shows rheological studies of the viscosity measurements of tyrosine in water slurries.

### 8.1 Additional data for crystallisation of CBZ

In this section relatively important data considering crystallisation of carbamazepine are shown. As mentioned in section 4.1 before turbidity on many occasions a solid form appeared. Its irregular shape can indicate an amorphous structure; however we weren't able to identify it. More images of those structures are shown below.

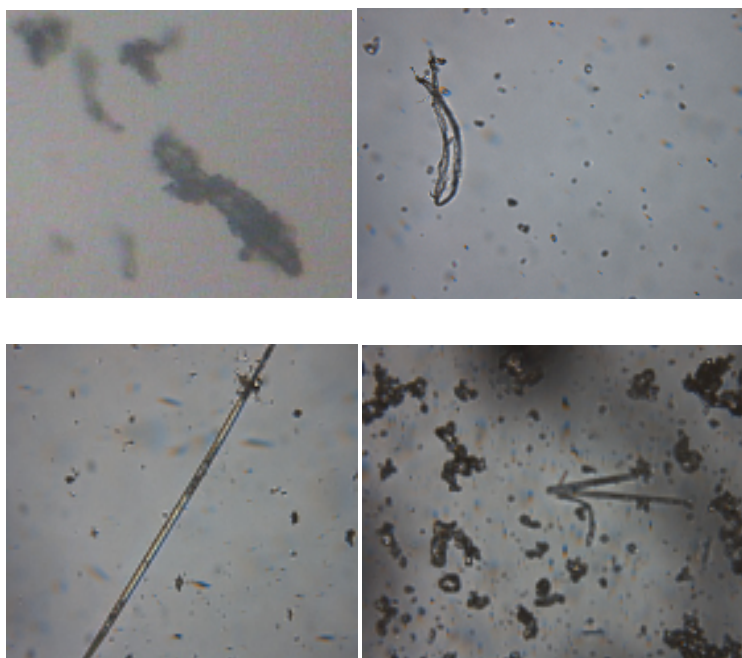


**Figure 8.1** Pictures shows amorphous and dihydrate forms observed in crystallising solutions.

It is thought that those formations can be amorphous solids or other metastable formations created before the appearance of the stable form.

Table 8.1 shows full and detailed results of nucleation studies experiments shown in Chapter 5. Obtained results of induction times are presented for CBZ cooling crystallisation from ethanol in stirred conditions.

Table contains:

In second column concentration values are given (and the beginning of table is arranged according to concentration (3.5 and 3.2 g<sub>CBZ</sub>/100ml<sub>EtOH</sub>). Third column gives names of the test, and then used filter either 0.45µm PTFE or 0.1µm AT that solution before crystallisation was filtered with. Then the date of test, followed by

---

temperature of the experiment (21°C and 22°C were the standard laboratory temperatures). In seventh column the source of used CBZ is shown. Com means commercial, Recr – recrystallised in house carbamazepine (description of the recrystallisation is given in procedure in section. Next column indicates if precipitate was observed before the actual latent state (N means no ? means that is recorded, H M L means is observed for High, Medium or Low stirring speed). Following column states the volume of crystallising solution mainly 3.3ml (partially full) or 5.1ml (totally filled). Next three columns show the resulting latent (turbidity times for Low, Medium of High stirring speed) with indicator of obtained form ( $\alpha$  and  $\beta$ ). The last column shows observations/ interesting findings or other factors important in the tests.

**Table 8.1** Induction times for cooling crystallisation with stirring.

Exp No.	Concentration g <sub>CBZ</sub> /100 ml <sub>EtoH</sub>	file name	Filter used	date	temp	CBZ source	Precipitate observed	Volume crystallised [ml]	Stirring speed			Observations
									Low	Med	High	
1	3.2	Speed_8	0.45	15-Jan	21	com	LH	3.3	80 β	230 β	56 β	
2	3.2	Speed_15	0.45	15-Feb	22	com	N	3.3	140 αβ	183 αβ	85 αβ	
3	3.2	Speed_17	0.45	16-Feb	22	com	N	3.3	99 αβ	50α	102β	
4	3.2	Speed_19	0.45	17-Feb	22	com	N	3.3	54α	45α	64α β	
5	3.2	Speed_22	0.45	18-Feb	22	com	N	3.3	51 αβ	30 β	62 α	
6	3.2	Speed_26	0.45	23-Feb	22	com	n	5.1	>8h	190 β	180 β	
7	3.2	Speed_28	0.45	24-Feb	22	com	N	5.1	-	-	230 β	
8	3.2	Speed_29	0.45	25-Feb	22	com	N	5.1	55	115	65	
9	3.2	Speed_32	0.45	04-Mar	22	com	N	5.1	-	-	60 β	
10	3.2	Speed_35	0.45	05-Mar	22	com	N	5.1	370 β	210 β	110 β	
11	3.2	Speed_14	0.1	10-Feb	22	com	L	5.1	480 αβ	320 αβ	160	Full bottle
12	3.2	Speed_38	0.1	11-Mar	22	com	Y	3.3	>210	160	140	
13	3.2	Speed_40	0.1	16-Mar	22	com	HL	3.3	230	67 αβ	145 αβ	
14, 15, 16	3.2	Speed_43	0.1	17-Mar	22	com	Y	3.3	-	-	45,85, 95	3 high speed
17, 18, 19	3.2	Speed_45	0.1	18-Mar	22	com		3.3	-	-	73,75,110	3 high speed

20	3.5	Speed_1	0.45	07-Jan	21	Com	?	3.3	-	87	40	
21	3.5	Speed_2	0.45	11-Jan	21	Com	?	3.3	32	76	42	
22	3.5	Speed_3	0.45	12-Jan	21	Com	?	3.3	100	55	41	
23	3.5	Speed_7	0.45	14-Jan	21	Com	L	3.3	81 αβ	49 αβ	43 β	
24	3.5	Speed_16	0.45	16-Feb	22	Com	N	3.3	55α	>15 α	52β	
25	3.5	Speed_18	0.45	16-Feb	22	Com	N	3.3	53 αβ	36 α	67 αβ	
26	3.5	Speed_20	0.45	17-Feb	22	com	N	3.3	70 β	52 α β	58β	
27	3.5	Speed_21	0.45	17-Feb	22	com	?	3.3	51 β	75 αβ	39 β	Lab grade EtOH
28	3.5	Speed_23	0.45	18-Feb	22	com	N	3.3	88 αβ	138 αβ	105 αβ	
29	3.5	Speed_27	0.45	23-Feb	22	com	N	5.1	190 β	108 αβ	113 β	
30	3.5	Speed_30	0.45	26-Feb	22	com	L	5.1	400	270	120	
31,												
32,	3.5	Speed_31	0.45	26-Feb	22	com	N	5.1	-	-	50,71,115	3 high speed
33												
34	3.5	Speed_33	0.45	04-Mar	22	com	LM	5.1	240 β	140 β	56 β	
35	3.5	Speed_34	0.45	04-Mar	22	com	LM	5.1	>270	270 β	40 β	
36	3.5	Speed_37	0.45	10-Mar	22	com	Y	5.1	230 β	77 αβ	170 αβ	Distilled EtOH
37	3.5	Speed_13	0.1	04-Feb	22	Com	?	5.1	175	220	66	Full bottle
38	3.5	Speed_39	0.1	11-Mar	22	com	Y	3.3	90	180	100	
39	3.5	Speed_41	0.1	16-Mar	22	com	?	3.3	70	80	50	
40,												
41,	3.5	Speed_42	0.1	17_Mar	22	com	Y	3.3	-	-	40, 68, 75	3 high speed
42												

43	3.5	Seed_3	0.1	17-Mar	22	com	Y	3.3	-	-	60	Seed test
44,												
45,	3.5	Speed_44	0.1	18_Mar	22	com	Y	3.3	-	-	74,88,100	3 high speed
46												
47	3.8	Speed_25	0.45	19-Feb	22	Com	n	3.3	110 β	93 β	58 β	
48	4	Speed_4	0.45	12-Jan	21	Com	?	3.3	27 αβ	48 βα	31 β	
49	4.3	Speed_5	0.45	13-Jan	21	Com	?	3.3	11 αβ	17 β	12 β	
50	4.5	Speed_10	0.45	26-Jan	22	Com	all	3.3	11 β	9 αβ	13 αβ	
51	3.1	Alpha_2	0.1	05-Feb	22	Recr	N	>5	-	106 β	-	
52	3.1	Alpha_2	0.1	05-Feb	18	recr	Y	>5	-	36α	-	
53	3.5	Fridge_2	0.45	01-Feb	22	Recr	N	4	-	24α	-	RCBZ no kept in the fridge
54	3.5	Fridge_2	0.45	01-Feb	22	recr	N	4	-	27α	-	R. CBZ kept in the fridge
55	3.5	Recr_filte	0.1	07-Jan	21	Recr	N	2.5	-	8α	-	
56	3.5	Recr_filte	0.45	07-Jan	21	recr	N	2.5	-	8α	-	
57	3.2	Speed_11	0.45	27-Jan	22	recr	all	3.3	280	230	105 αβ	
58	3.5	Speed_24	0.45	18-Feb	22	recr	N	3.3	45 β	38 β	45 β	Lab grade EtOH
59	3.5	Recr_3	0.45	24-Feb	22	recr	N	>5	-	-	12 α	Wetted and kept in the fridge
60	3.5	Recr_3	0.45	24-Feb	22	recr	N	>5	-	-	20 α	Dried in desiccator
61	3.0	Recr_4	0.45	25-feb	22	recr	N	>5	-	-	20 α	Wetted and kept in the fridge

62	3.0	Recr_4	0.45	25-feb	22	recr	N	>5	-	-	11 $\alpha$	Dried in desiccator
63	3.0	Recr_5	0.45	25-feb	22	recr	N	>5	-	-	200 $\beta$	, Lab Grade EtOH
64	3.5	0.02AT_	0.02	06-Jan	55-30	Recr	N	4	-	210 $\alpha$	-	Very slow cool, crystallised at 30°C
65	3.5	Recr_6	0.1	11Mar	22-20	recr	N	3.3		17 $\alpha$	16 $\alpha$	(for both temp)
66	3.5	Speed_9	0.02	19-Jan	55-21	Com	L	3.5	>360	360 $\beta$	420	Very slow cool in
67	3.5	Temp_1	0.45	02-Feb	22	com	?	3.5	-	85 $\beta$	-	
68	3.5	Temp_1	0.45	02-Feb	18	com	?	3.5	-	23 $\beta$	-	
69	4.0	Temp_2	0.45	02-Feb	22	Com	?	>5	-	22 $\alpha$	-	
70	4.0	Temp_2	0.45	02-Feb	18	com	?	5	-	18 $\alpha$	-	
71	3.5	Filters_3	0.02	05-Jan	21	Com	N	3.3		98 $\beta$		
72	3.5	Filters_3	0.1	05-Jan	21	Com	N	3.3		145 $\beta$		
73	3.5	Filters_3	0.45	05-Jan	21	com	N	3.3		29 $\beta$		3ml
74	3.5	Filters_1	0.02	16-Dec	18	Com	N	2.5		26 $\alpha$		2ml
75	3.5	Filters_1	0.1	16-Dec	18	Com	N	2.5		25 $\alpha$		2ml
76	3.5	Filters_1	0.45	16-Dec	18	com	N	2.5		26 $\alpha$		2ml
77	3.5	TBO_1	0.1	15-Dec	19	Com	?	2	-	65 $\beta$	-	
78	3.5	TBO_1	0.1	15-Dec	19	Com	?	4	-	54 $\beta$	-	
79	3.5	TBO_1	0.1	15-Dec	19	Com	?	>5	-	100 $\beta$	-	
80	3.5	TBO_2	0.45	16-Dec	17	Com	?	3	-	5 $\alpha$	-	17°C lab temp
81	3.5	TBO_2	0.45	16-Dec	17	Com	?	3	-	5 $\alpha$	-	
82	3.5	TBO_2	0.45	16-Dec	17	com	?	>5	-	5 $\alpha$	-	

## 8.2 Dynamic light scattering experiments

In section 4.1 we established that stirring has a strong effect on the polymorphic outcome in cooling crystallisation of CBZ from ethanol solutions.

Since this effect was found to persist even when the influence of other commonly invoked features, such as solution impurities and air-liquid interface, was eliminated we propose that large scale self-association of CBZ in supersaturated solutions to higher density domains or clusters, may be responsible for the sensitivity of polymorphic outcome to macroscopic flow effects. This would provide a possible explanation for the effect of flow on any subsequent phase transition, which is hard to explain for molecularly homogeneous solutions.

If the supersaturated solutions of CBZ in ethanol undergo microphase liquid-liquid separation it should be possible to observe this phenomenon by light scattering experiments due to optical contrast of liquid domains with different refractive index and density. We note that such clusters or domains have been observed previously for supersaturated solutions of other APIs and proteins (see nucleation part in section 2.1.4). Here we used Dynamic Light Scattering (DLS) to characterize density fluctuations in undersaturated and supersaturated solutions of CBZ in ethanol. Results are presented in the form of measured autocorrelation functions for solutions at a given temperature during a stepwise cooling. Calculations of the apparent hydrodynamic diameters were done using equations and methods described in section 3.2.3.1.

### Experimental procedure

Measurements were performed on HPPS (High Performance Particle Sizer) instrument by Malvern at scattering angle of  $173^\circ$  under quiescent conditions.

Solutions were prepared by dissolution of CBZ in anhydrous ethanol (HPLC grade) at temperatures  $\geq 50^\circ\text{C}$  (well above solubility), filtered with syringe filters ( $0.45\mu\text{m}$  PTFE or  $0.1\mu\text{m}$  AT) directly into quartz cuvettes and samples were quickly transferred into the preheated instrument. Solutions were equilibrated to constant

temperature before performing measurement, and then cooled down gradually in-situ in the instrument. Each sample has always been kept under controlled temperature conditions because oscillating temperatures lead to difficulties with measurements where gradients in the temperature trigger undesired convection.

Experiment	CBZ concentration $\text{g}_{\text{CBZ}}/100\text{ml}_{\text{EtOH}}$	CBZ source	Filter used
1	4.2	com	0.45 $\mu\text{m}$ PTFE
2	3.5	com	0.45 $\mu\text{m}$ PTFE
3	3.1	recr	0.1 $\mu\text{m}$ AT
4	3.0	com	0.1 $\mu\text{m}$ AT
5	2.8	com	0.1 $\mu\text{m}$ AT
6	1.2	com	0.1 $\mu\text{m}$ AT
7	0 (pure ethanol)	N/A	0.1 $\mu\text{m}$ AT

**Table 8.2** List of experimental conditions used for DLS experiments.

Majority of experiments were performed at the range of temperatures from 40°C down to 15°C, at which point all solutions were well above their solubility.

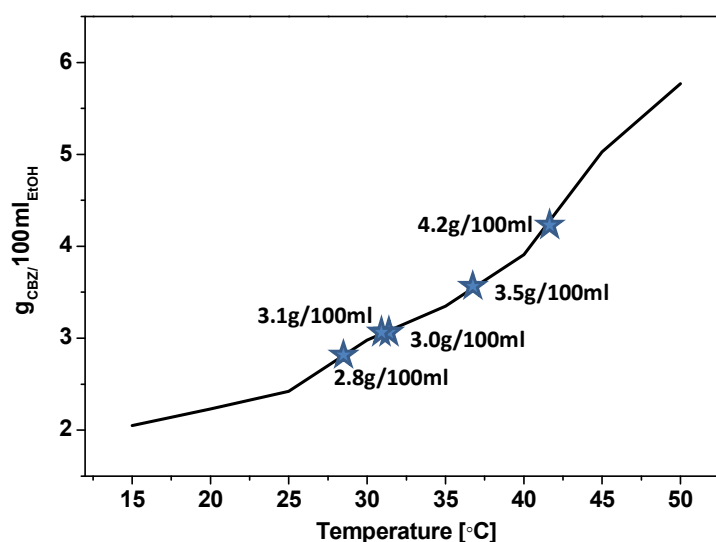


**Figure 8.2** Solubility of CBZ in ethanol and corresponding saturation temperatures for solution concentrations used in DLS experiments.

In Figure 8.2 we show saturation temperature for solutions concentration used in DLS experiments (see Table 8.2).

### Effect of concentration

Here we report results of DLS measurements for carbamazepine solutions in ethanol corresponding to experiments 1-6 in Table 8.2 at six first from the table different values of concentration. When supersaturated conditions are reached solution might nucleate; however since no stirring was present, the metastable zone width can be very large (see chapter 2.4.1) and crystals may not be present throughout the duration of experiment.

**Experiment # 1** 4.2g CBZ/100ml EtOH solution filtered with 0.45 $\mu$ m PTFE filter.

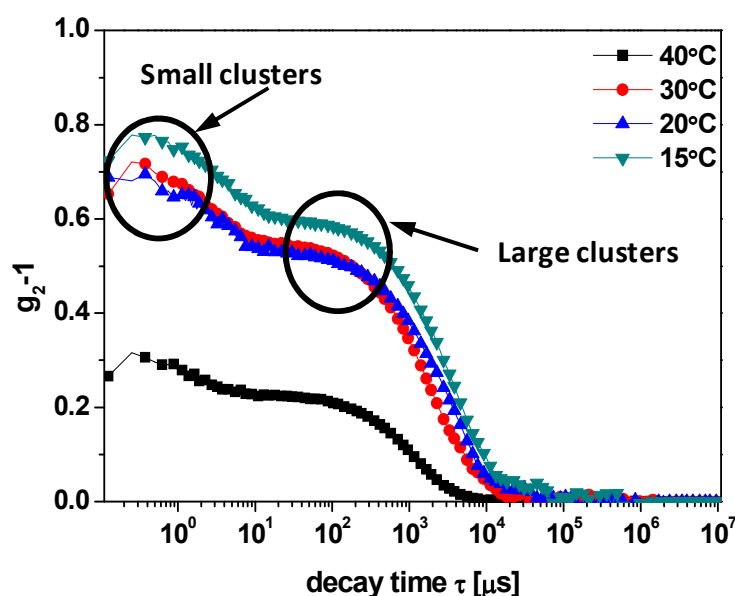


**Figure 8.3** Autocorrelation function for 4.2g CBZ/100ml EtOH solution.

In Figure 8.3 we show results from experiment #1 representing a typical example of the autocorrelation functions measured during step-wise cooling from 40°C to 3°C to 20°C and finally to 15°C. It can be seen that at all temperatures the curves show two well distinguished decays. The first one at the timescale of few  $\mu$ s, represents small molecular clusters, while the second one visible in the region of 100 – 1000 $\mu$ s, comes from large clusters or domains with the size in the order of a micrometer. Very similar results can be seen for other concentrations investigated, corresponding to experiments 2-6 (see below).

**Experiment # 2** 3.5g CBZ/100ml EtOH, solution filtered with 0.45 $\mu$ m PTFE filter.

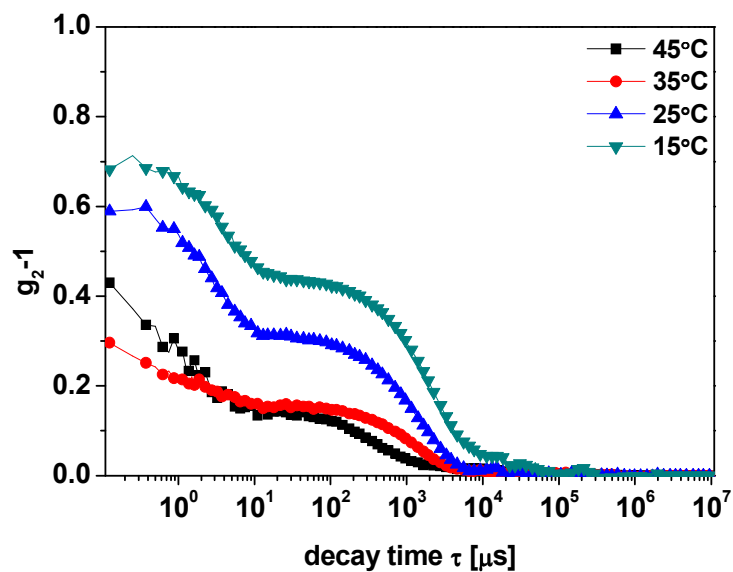


**Figure 8.4** Autocorrelation function for 3.5g CBZ/100ml EtOH solution.

**Experiment # 3** 3.1g CBZ/100ml EtOH, solution filtered with 0.1 $\mu$ m AT filter.

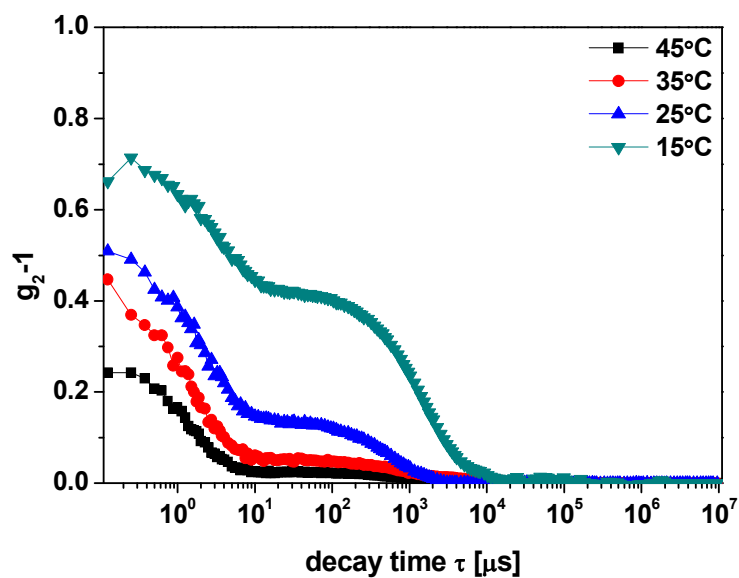


**Figure 8.5** Autocorrelation function for 3.1g CBZ/100ml EtOH solution.

**Experiment # 4** 3.0g CBZ/100ml EtOH, solution filtered with 0.1 $\mu$ m AT filter.

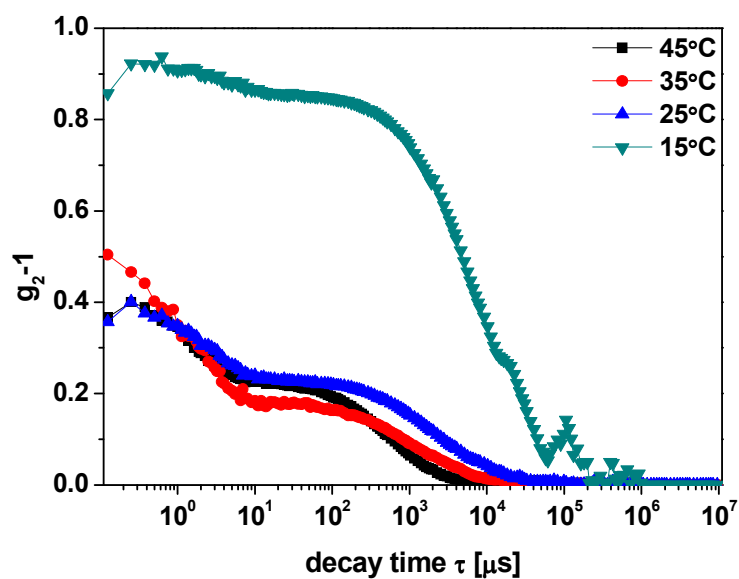


**Figure 8.6** Autocorrelation function for 3.0g CBZ/100ml EtOH solution.

**Experiment # 5** 2.8g CBZ/100ml EtOH, solution filtered with 0.1 $\mu$ m AT filter.

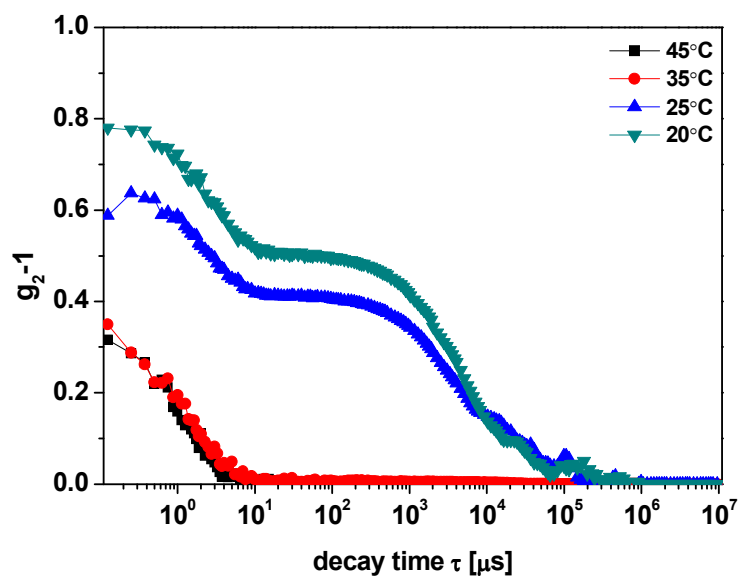


**Figure 8.7** Autocorrelation function for 2.8g CBZ/100ml EtOH solution.

**Experiment # 6**

## Scattering of pure solvent and undersaturated solution

In order to understand properly and interpret above results, we also performed background measurements using the pure solvent (ethanol) and undersaturated solution of carbamazepine 1.2g/100ml (saturation temperature of 10°C) in order to check for possible self association in undersaturation solution.

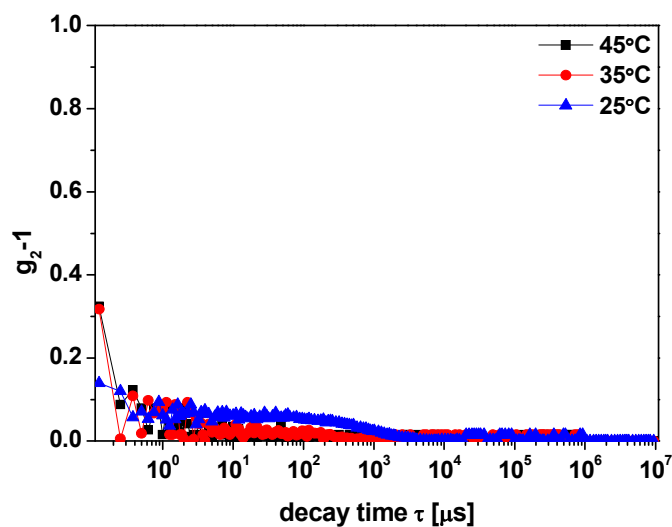


**Figure 8.8** Autocorrelation functions of pure EtOH.

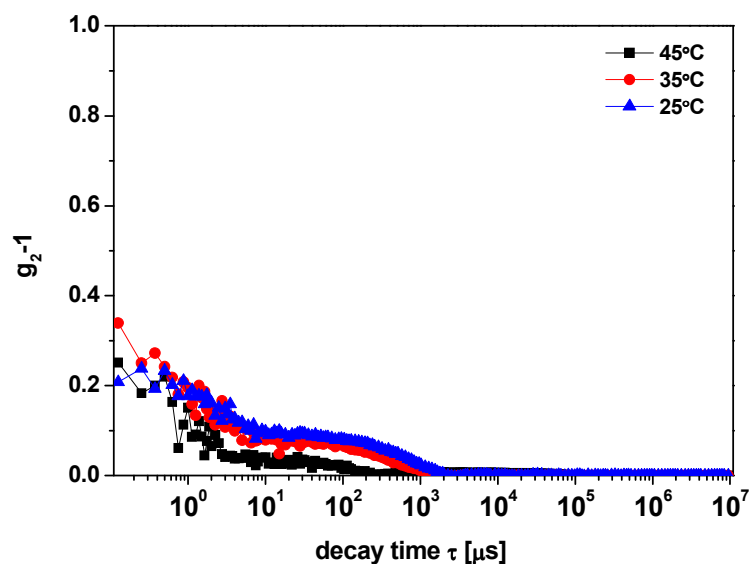


**Figure 8.9** Autocorrelation function of cooling of highly undersaturated solution of carbamazepine in ethanol.

It can be seen that there is considerable structuring in the solution as new decay appears with lowering the temperature. Above results show the existence of some clusters in pure solvent and undersaturated solution at 25°C. Significant oscillations observed especially at higher temperatures are very characteristic for pure solvent autocorrelation functions.

Similar trend for the same for undersaturated solution: 1.2gCBZ/100ml EtOH filtered with 0.1µm AT filter when no smooth decay or autocorrelation was observed.

However slight decays in autocorrelation function can be observed. For example calculated size for 25°C was just above 400nm.

### Conclusions

Above results show that during cooling of carbamazepine solutions structuring is observed. At higher temperatures usually no large agglomerates are visible, however with the decrease of temperature and therefore increase of supersaturation levels large clusters are created. Cooling down to 15°C caused that their sizes vary from just above 700nm reach even up to over 3000nm.

Concentration g <sub>CBZ</sub> /100ml EtOH	Apparent hydrodynamic diameter [nm]					
	40°C	35°C	30°C	25°C	20°C	15°C
4.2	946	--	1892	-	-	1492
3.5	-	882	-	798	-	1056
3.1	-	-	-	372	-	726
3.0	496	-	-	-	1044	3200
2.8					2560	

**Table 8.3** Calculated values for apparent hydrodynamic diameter of big clusters structures present in solutions for square fitting of autocorrelation functions.

In all shown tested solutions a kind of clustering was observed. It can be seen that the maximum size of agglomerates can reach even 3000nm and it is expected that the next step must be the crystallisation. In most cases created clusters grow from 1000

to 3000nm from 3.0g/100ml solution or from 400 to 800nm for 3.1g/100ml, but the highest concentration value 4.25g/100ml show that they change from 100nm at 40°C, via 2000nm at 35°C to 1500nm at 25°C. But not just the size of huge agglomerates is interesting. Above results that the initial part of autocorrelation differs a lot and different sizes of so called small agglomerates varies from 1nm to (2.8g/100) to 10 nm for 3.1g/100. Interesting observation of growth of agglomerates with the decrease of temperature was observed for 2.8g/100 solutions and the size has changed from 1.5 to 36nm i.e. from dimers to significantly large agglomerates. But the opposite trend is seen for 3.1 g/100 solutions where the size of smaller agglomerates decreased from 8.5nm at 45°C to 3.5nm at 15°C.

The appearance of ordered clusters with significant size may be the factor testifying against the classical behaviour of carbamazepine in ethanol solution.

Presented DLS results indicate that CBZ doesn't exist as monomers except highly undersaturated solutions where significant oscillations don't allow calculating the size of molecules or clusters. However this conclusion is only speculative and in order to be sure more evidence should be given.

### 8.3 Static light scattering experiments

Measurements were performed on SLS instrument CGS-3 by ALV GmbH. Measurements were done aiming to see molecular structuring of solution (clusters or aggregates) before crystallisation similar to DLS shown above.

This method can be used for sizing of dispersions of particles (or molecular weight determination for polymers) in solution by the measurement of the time-averaged intensity of scattered light. The dependence of scattering intensity as a function of the angle  $\theta$  over long observation times  $T$  [148] gives information about the shapes of individual particles (in dilute solution) as well or spatial arrangement of particles (in concentrated systems) [147].

$$I(\theta) = \lim_{T \rightarrow \infty} \frac{1}{T} \int_0^T I(\theta, t) dt$$

It has been widely used for determination of molar mass of polymers and their radius of gyration in the solution and recently increasing for studies of protein systems.

SLS has been used to study super molecular structuring (domains) in solutions caused by characteristic interactions between solvent and solute of organic and inorganic molecules commonly seen as homogeneous [165-167].

#### SLS data of cooling CBZ in EtOH – set 1

Two solutions of  $3.5 \text{g}_{\text{CBZ}}/100 \text{ml}_{\text{EtOH}}$  were prepared by dissolution of CBZ in ethanol overnight at  $50^\circ\text{C}$  then filtration with  $0.1 \mu\text{m}$  AT syringe filters. Two sources of CBZ were tested: the commercial one and recrystallised in house (as described in previous results section). Those were compared to HPLC grade ethanol. As previously solutions were gradually cooled down allowing getting to constant temperature.

Specification of all tests:

From 15	to 60	step 5	runs 1	duration 600s
From 65	to 135	step 10	runs 1	duration 600s

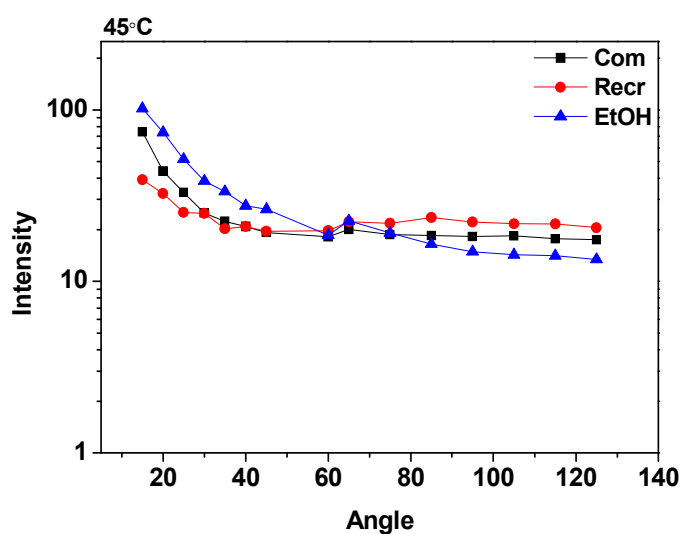


**Figure 8.10** SLS intensities for 3.5gCBZ/100ml<sub>EtOH</sub> commercial and recrystallised solutions and pure ethanol at 45°C.

The angle dependence of scattered light intensities for studied three samples show similar trends. However, the slope of the curves may mean that there are some structures present in the solution only visible at low angles, probably very small in size.

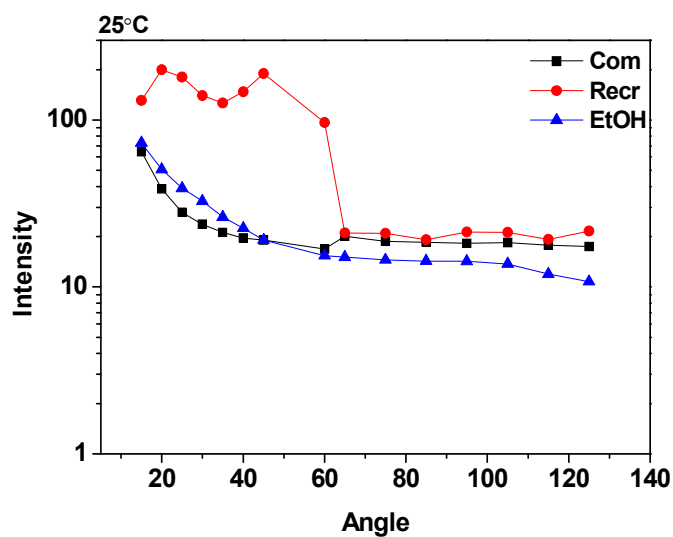


**Figure 8.11** SLS intensities for 3.5gCBZ/100ml<sub>EtOH</sub> commercial and recrystallised solutions and pure ethanol at 25°C.

Cooling of those solutions shows very interesting results. Recrystallised CBZ shows dissimilarities in comparison to commercial CBZ and ethanol. Very important was

that those results were only a repetition of the first, shorter therefore less accurate test and again usage of recrystallised carbamazepine leads to structuring with the decrease of temperature to 25°C visible at lower angles.

### SLS data of cooling CBZ in EtOH – set 2

CBZ Commercial and Recrystallised CBZ and ethanol 3.5g<sub>CBZ</sub>/100ml<sub>EtOH</sub>, filtered on 0.45µm PTFE filter at 3 temperatures. The same test conditions for all 3 samples.

Test specifications: angle 15 to 135°, step 5, runs 5, duration 20s.

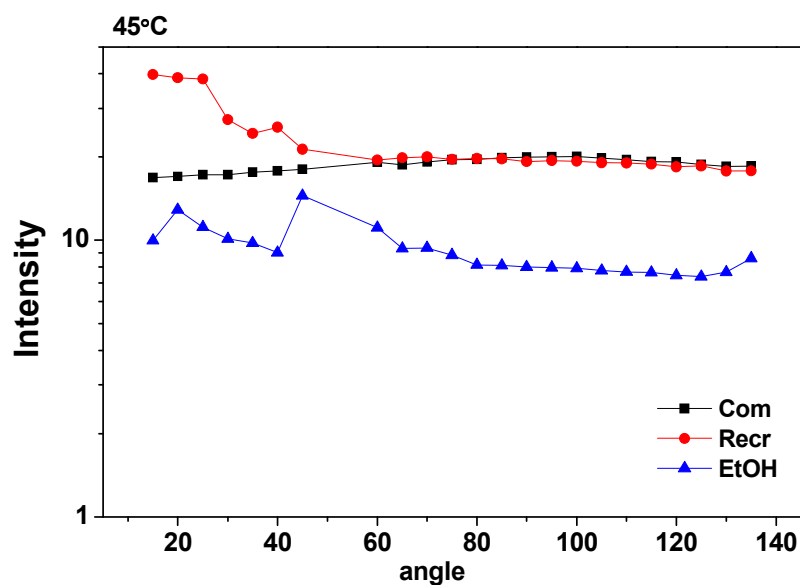


**Figure 8.12** SLS data for 3.5g/100ml at 45°C.

Slightly different pattern of scattering intensity with angle is observed for these three samples. Recrystallised and Commercial carbamazepine shows different trend, and recrystallised CBZ scatters much more than the commercial.

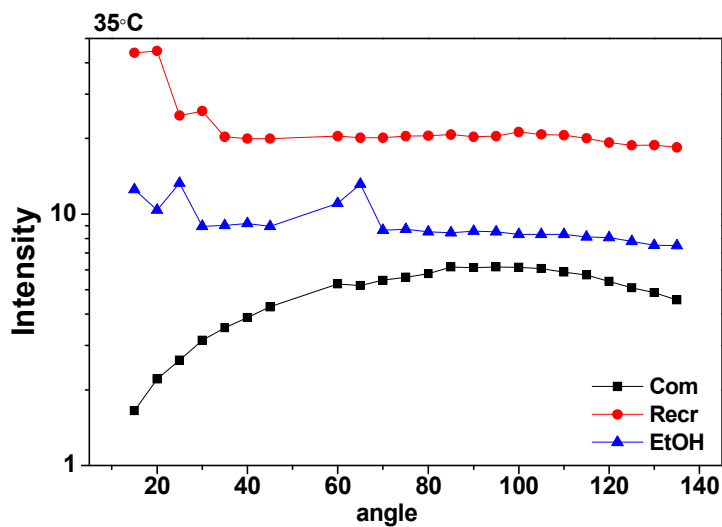


**Figure 8.13** SLS data for 3.5g/100ml at 35°C.

Change in scattering is observed with the decrease in temperature only for carbamazepine solutions, not for pure solvent. What more the differences of scattering of Com and Rec get more significant with the increase of temperature. The scattering of ethanol remains fairly constant.

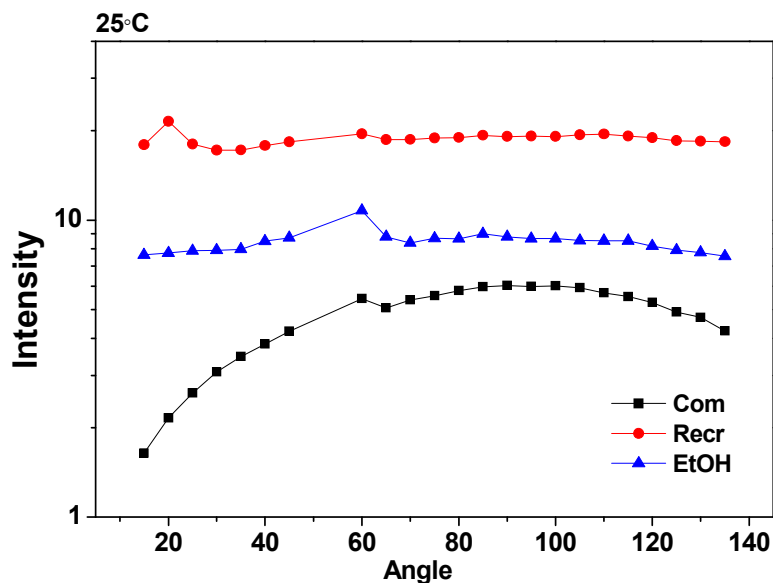


**Figure 8.14** SLS data for 3.5g/100ml at 25°C.

At final temperature 25°C scattering intensity is slightly decreased, and recrystallised solution shows now similar trend to commercial but still is much stronger in intensity.

#### 8.4 ATR-UV monitoring of cooling crystallisation of CBZ ethanol solutions

This part shows ATR UV - results of experiments on the cooling crystallisation of carbamazepine. Series of experiments of cooling crystallisation of CBZ from ethanol were performed. It was expected that regions of highly supersaturated CBZ would be seen a priori to the crystallisation.

UV absorbance spectroscopy is used to measure the concentration of studied liquid solutions of molecules containing chromophore [114, 120, 168]. The big advantage of the attenuated total reflectance ultraviolet (ATR-UV) is that measurement can be performed in situ without necessity of dissolution, moreover in the presence of solid state. It can be used to monitor processes as dissolution, crystallisation [116] and so on. It's used for very easy and rapid measurements of highly absorbing solutions with different attenuation values for the solvent and solute (different UV absorption). ATR is based on the measurement of attenuation of light passing from a material with a high refractive index (attenuated total reflection crystal) to a material with lower refractive index (solution) [169]. It means that part of the light from the probe usually is not totally reflected, but a part of it is absorbed by the solution before reflecting back to the probe and reduction in the output signal is observed. The used ATR probe 661.812 is made of a 3-bounce sapphire ATR crystal, directly immersed into the solution to be measured and connected to via fibre optic cables to UV Spectrometer.

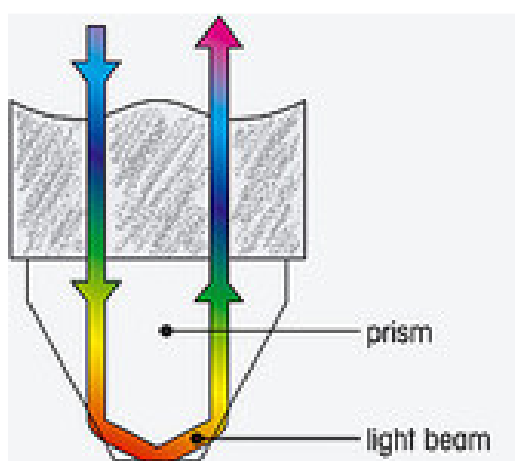


**Figure 8.15** ATR crystal used in ATR-UV.

Measurements were done in Multimax 16 reactor with the probe directly placed in the solution and the changes in the CBZ concentration were tracked through all. Local increase of concentration caused by droplets (as hoped) was expected in supersaturated solutions.

Example of UV spectrum of CBZ in ethanol with visible peaks. Characteristic peak of absorbance at 285nm was chosen to track concentration changes.

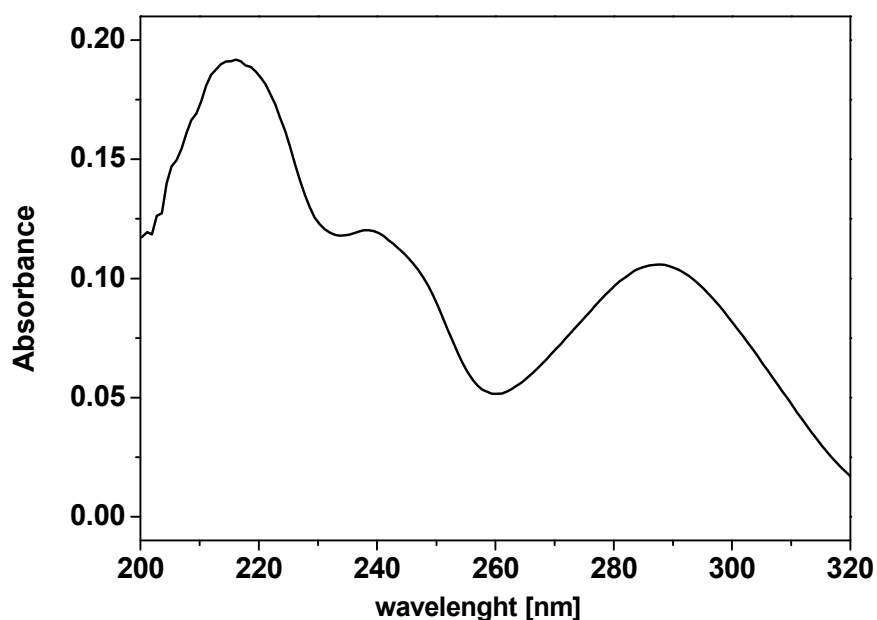


**Figure 8.16** UV spectrum of CBZ.

Calibration of ATR probe was done on 3 values of concentration at 3 temperatures. It can be seen the absorbance highly depends on the temperature.

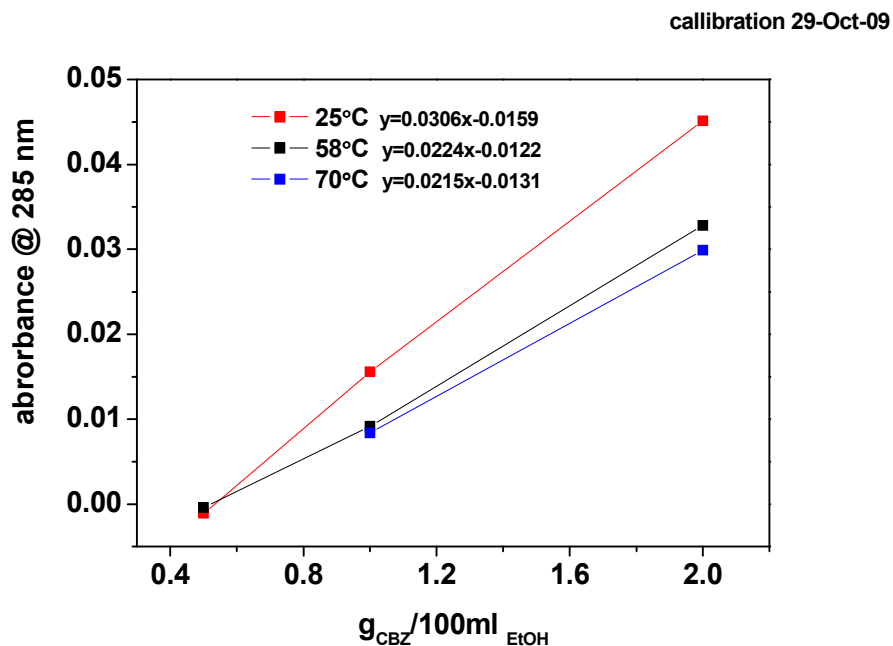


**Figure 8.17** Calibration of ATR UV probe. This test shows cooling of highly concentrated CBZ solution heated up to 70° and cooled down with different stirring speed: 600rpm, 200rpm and no stirring.

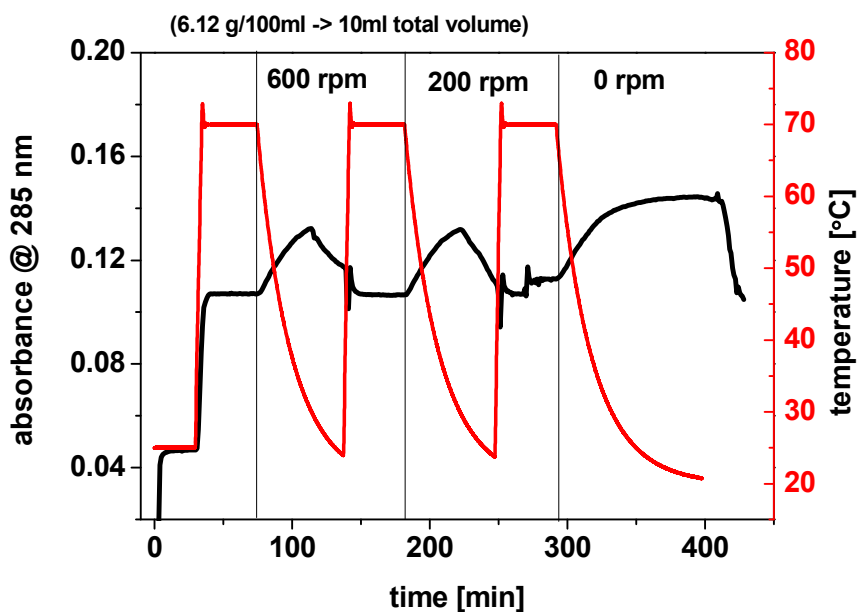


**Figure 8.18** UV results of 6.12gCBZ/100ml EtOH test.

Higher concentration 8.27g/100ml EtOH and the effect of stirring as stirring at 900rpm and no stirring. Dissolution at 70°C.

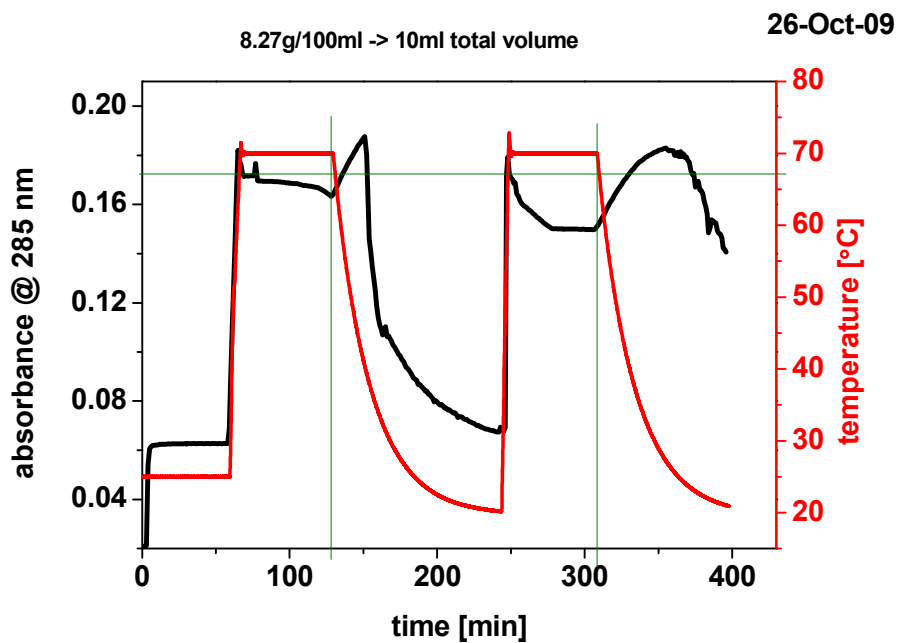


**Figure 8.19** UV results of 8.27gCBZ/100ml<sub>EtOH</sub> test.

Test on the most frequently used concentration 3.5g/100ml show similar behaviour. Heating and cooling log values to exactly repeat the trend. Stirring at 600rpm.

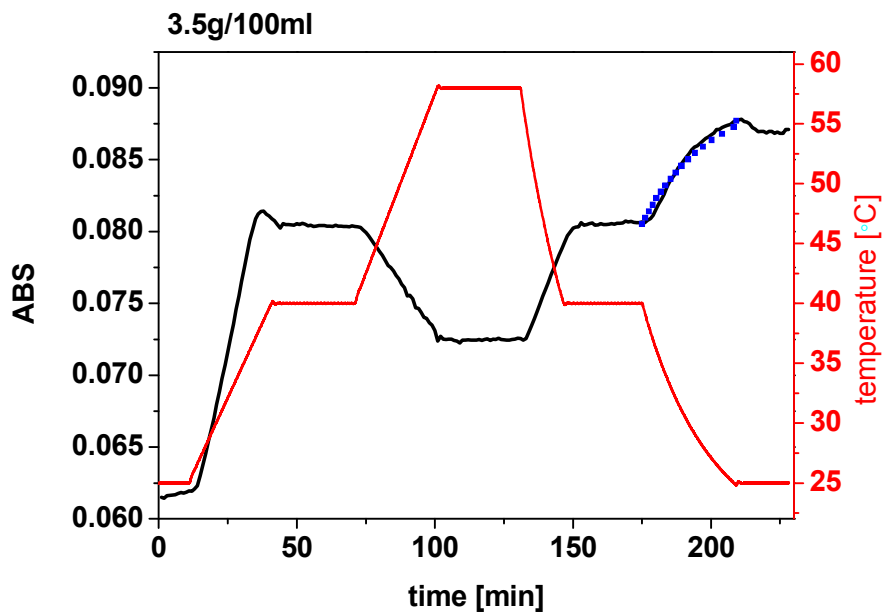


**Figure 8.20** UV results of 3.5gCBZ/100ml EtOH test.

Blue dotted line is a calculated trend as function of temperature and ABS from the calibration.

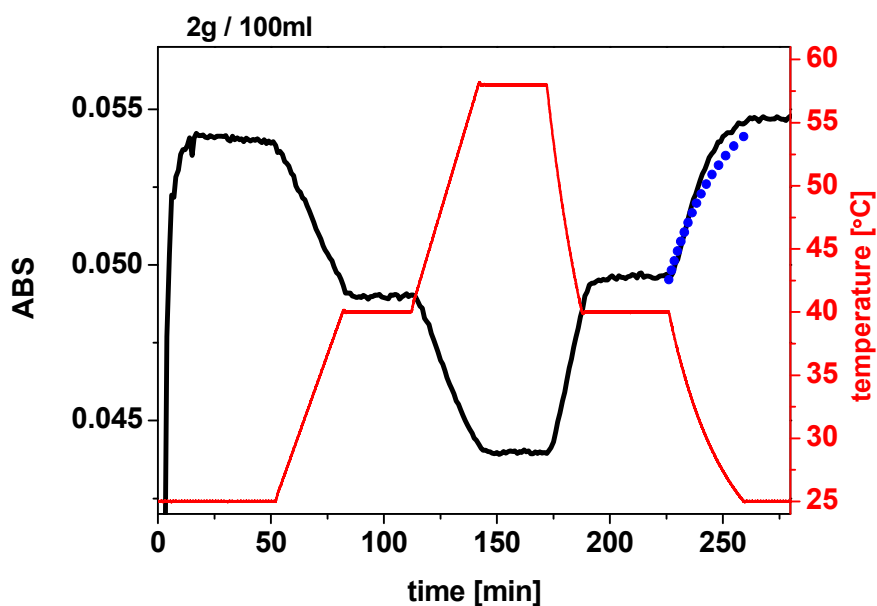


**Figure 8.21** UV results of 2.0gCBZ/100ml<sub>EtOH</sub> test.

It has been observed that the increase of UV signal with the decrease of temperature is a purely effect of temperature. This has been proven by calculation of ABS with decrease of temperature from calibration.

### 8.5 Raman Spectroscopy of CBZ in ethanol

Raman spectroscopy was used to assess the concentration of CBZ in ethanol solutions without dissolution. It was expected that CBZ supersaturated solutions undergo liquid-liquid phase separation with significant difference in concentration of those two phases. Therefore supersaturated solutions before crystallisation were gently centrifuged and samples of the top and the bottom were taken for analysis. First data were aiming for calibration of Raman experimental setup.

Calibration for three concentrations and the pure ethanol has been done.

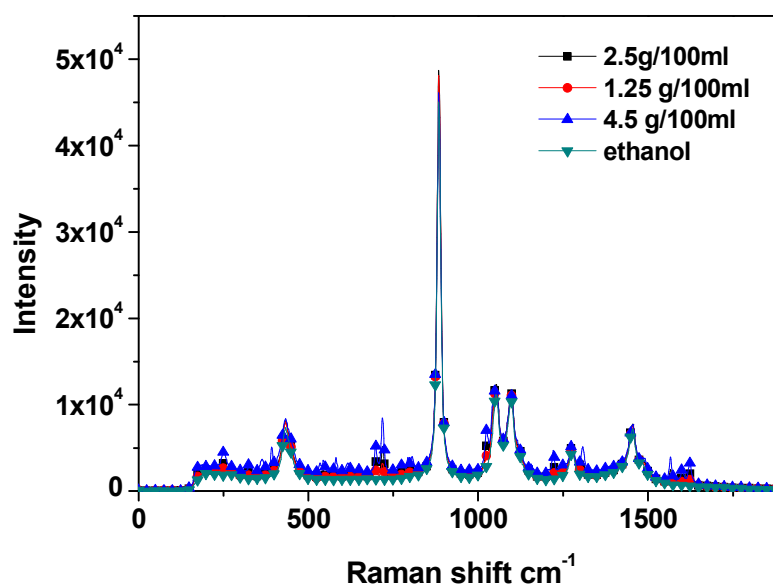


Figure 8.22 Raman spectra of EtOH and CBZ solutions.

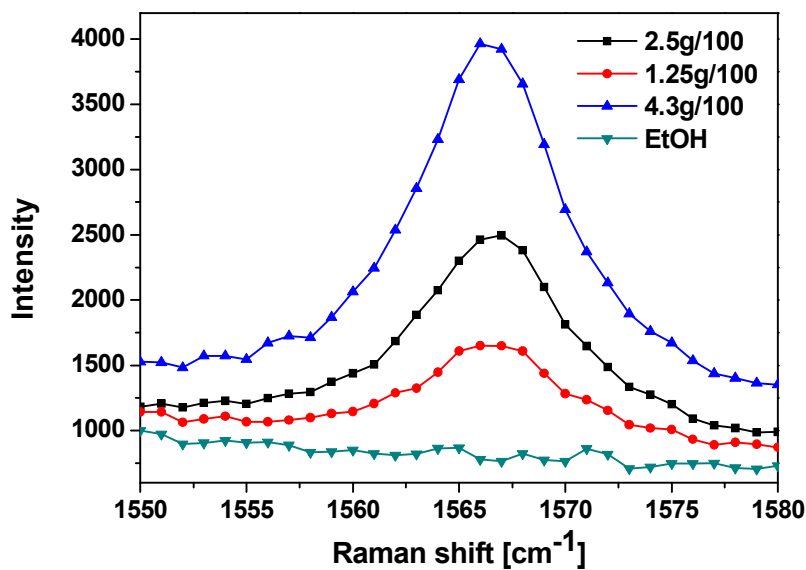


Figure 8.23 Raman spectra of EtOH and CBZ solutions – zoomed peak.

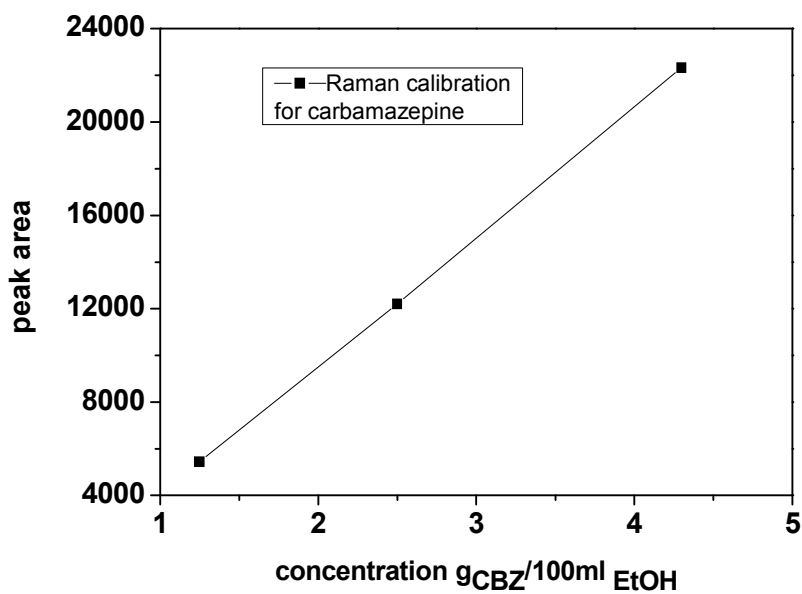
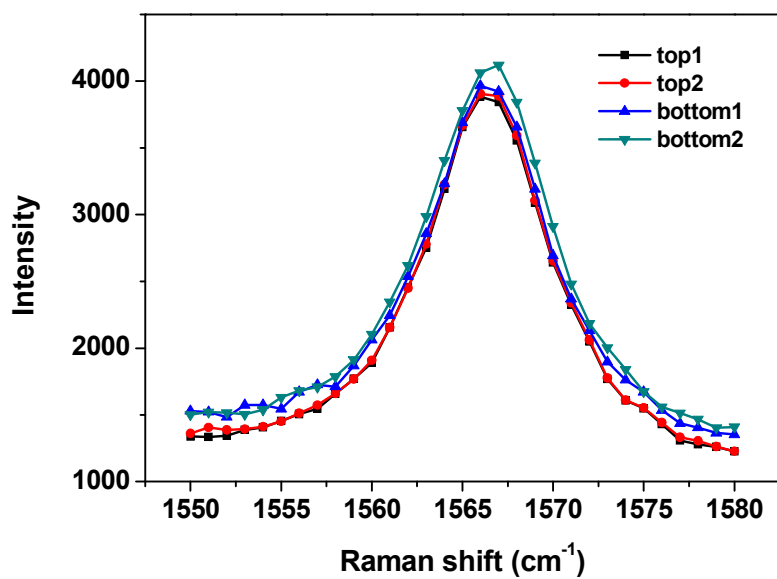


Figure 8.24 Calibration of Raman shift for CBZ in EtOH solutions.

Measurement of centrifuged solution of 4.8g/100ml (18ml total) centrifuged and samples taken from the top and bottom



**Figure 8.25** Results of centrifugation of 4.8g/100ml CBZ in EtOH solution.

Calculated concentrations (from derivative): T=4.84g/100ml, B=4.98g/100ml.

Calculated densities from weight T=0.784g/ml, B=0.819g/ml.

Unfortunately no significant differences were observed.

## 8.6 NIR of ethanol with different water content and CBZ solutions

During induction times studies it has been shown that the effect of recrystallised CBZ used is strongly affected by the presence of water in used ethanol.

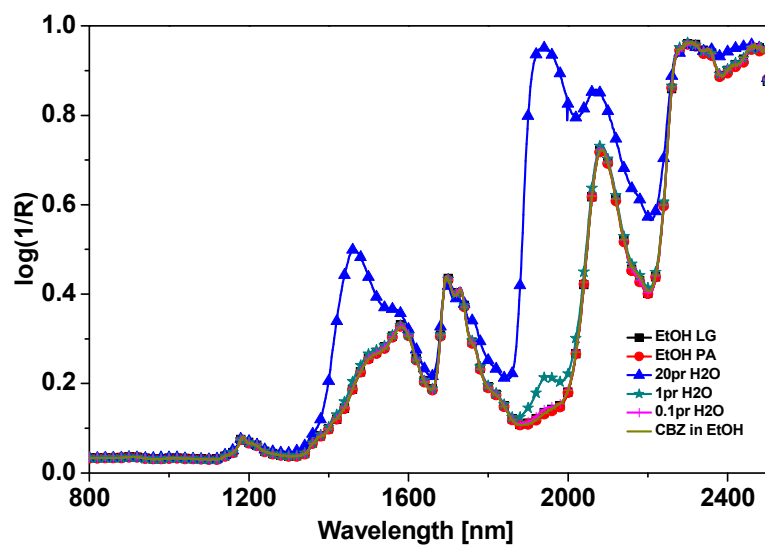


Figure 8.26 NIR spectra of EtOH and CBZ solutions.

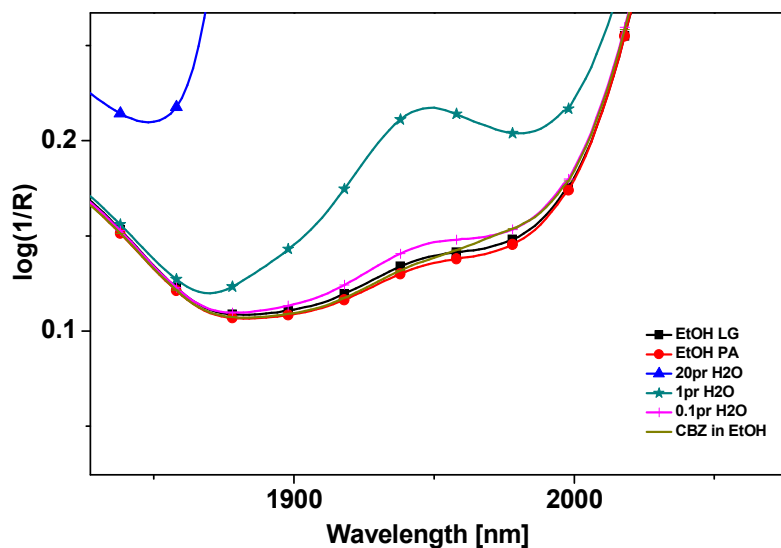


Figure 8.27 NIR spectra of EtOH and CBZ solutions –zoomed peak.

Graphs above show results and possibility of applications of NIR to asses the water content in crystallising CBZ EtOH solutions.

## 8.7 Results of the effect of flow conditions on breakage of tyrosine

Section 5 considering the breakage of tyrosine crystals in flow was relatively extensive and not all data were shown there. The bulk of partial results i.e. stepwise results (showing the kinetics of each process) of breakage in stirring, pumping etc are shown below. Data presented in other way (log etc) than those presented in section 5 are added here.

Obtained results Graphs below are shown in different ways:

No wt results linear scale (sensitive to smaller crystals)

No weighted on logarithmic scale showing the “tale” very sensitive to the biggest crystals (that we are expecting to be broken the most)

Calculated averages in plot (chosen) and table the same (but all)

The range of 190 – 450 $\mu\text{m}$  on logarithmic scale with linear fitting functions and characteristic values of function (the slope and intercept) to shown the trend in data.

Additional plots to results shown in the main chapter.

### Effect of concentration (FBRM specification) while stirring at 700rpm

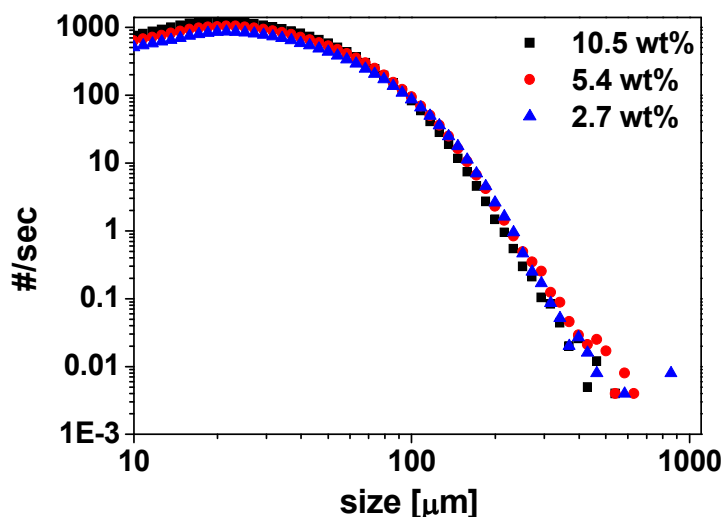


Figure 8.28 Effects of concentrations on logarithmic scale.

	C1/0	C2/1	C3/2	C 4/3	C 5/4	C 6/5
2.7 wt%	25	43	66	95	145	282
5.4 wt%	25	42	64	91	131	200
10.5 wt%	24	39	58	81	110	154

**Table 8.4** FBRM average size for different concentrations.

### FBRM results of breakage of tyrosine

Below results are the partial components of all experiment performed on tyrosine slurries. Results in the chapter 4.3 are the cumulative all those below in this paragraph.

### Representative sample RS

Comparison of measurements after halving of concentration. To see if the pump take representative sample and if the contraction works on representative sample.

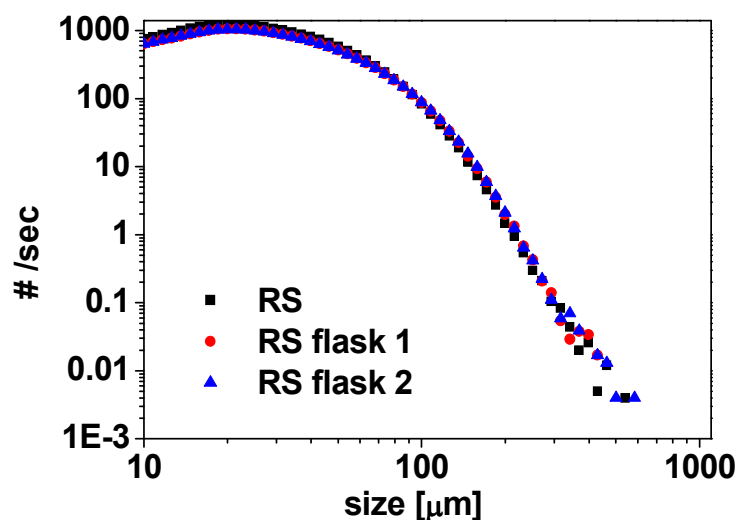


**Figure 8.29** Comparison of results presented on logarithmic scale for stirring in 3 flasks.

	C 1/0	C 2/1	C 3/2	C 4/3	C 5/4	C 6/5
RS	25	43	66	93	125	167
RS flask 1	27	47	72	101	133	172
RS flask 2	27	46	71	100	132	173

**Table 8.5** Average sizes for RS test.

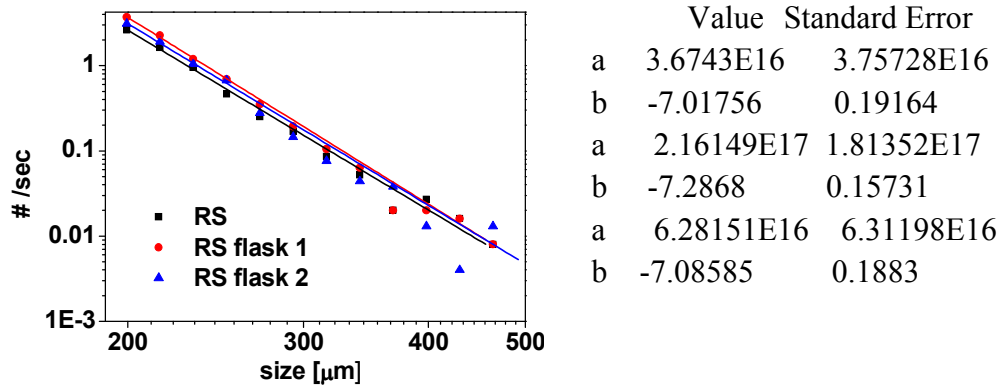


**Figure 8.30** Fitting functions for RS test.

### Effect of stirring of tyrosine.

#### 2.7 wt% stirr 700

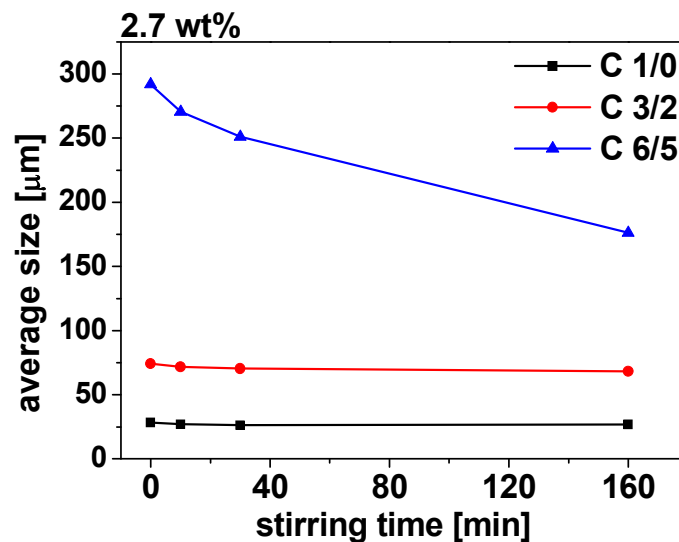
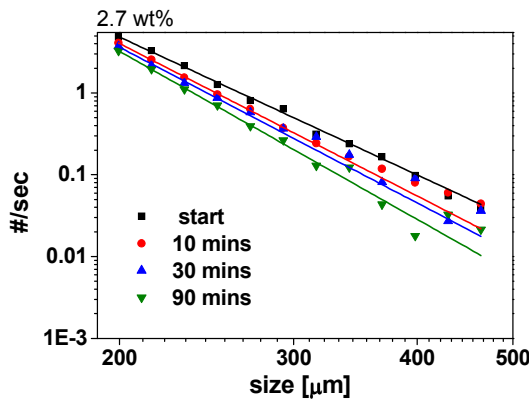


**Figure 8.31** Change in average sizes for weighted functions of stirring of 2.7 wt% of tyrosine at 700rpm.

	C 1/0	C 2/1	C 3/2	C 4/3	C 5/4	C 6/5
start	28	48	74	111	175	292
10 mins	27	47	72	106	164	271
30 mins	26	46	70	103	156	251
90 mins	27	45	68	96	131	176

**Table 8.6** Percentage changes in average sizes of stirring of 2.7 wt% of tyrosine at 700rpm.



	Value	Standard Error
a	3.75827E13	2.15563E13
b	-5.60186	0.10715
a	7.17714E14	2.12023E14
b	-6.19328	0.05527
a	1.30765E15	1.14354E15
b	-6.32624	0.16366
a	1.6247E16	7.31183E15
b	-6.82375	0.0843

Figure 8.32 Fitting functions for stirring of 2.7 wt% of tyrosine.

5.4 wt% stirr 700

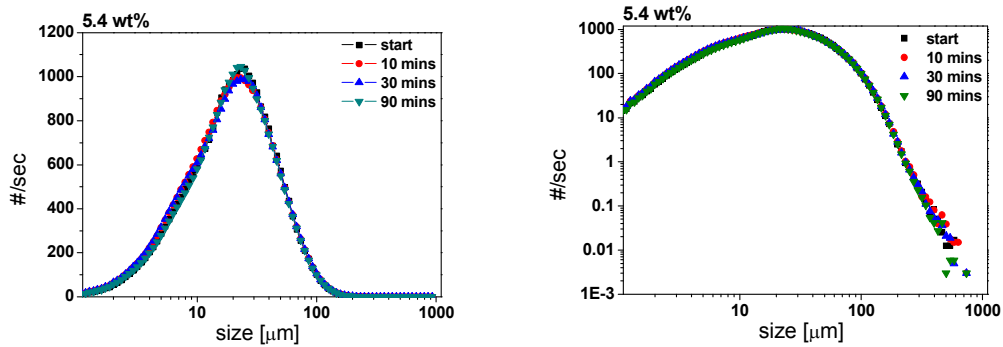


Figure 8.33 Stirring of 5.4 wt% tyrosine at 700rpm plotted on linear and logarithmic scale

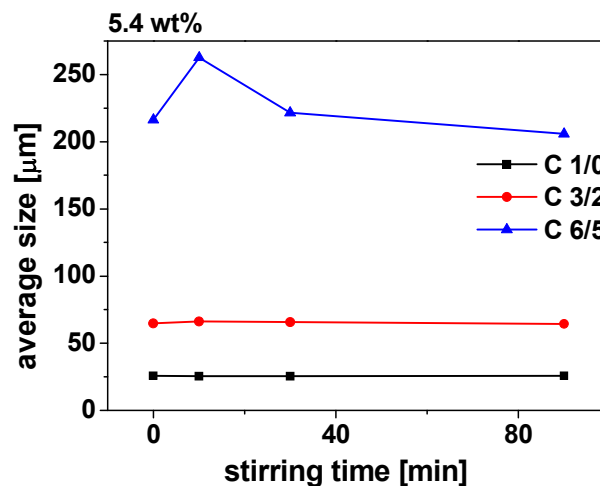
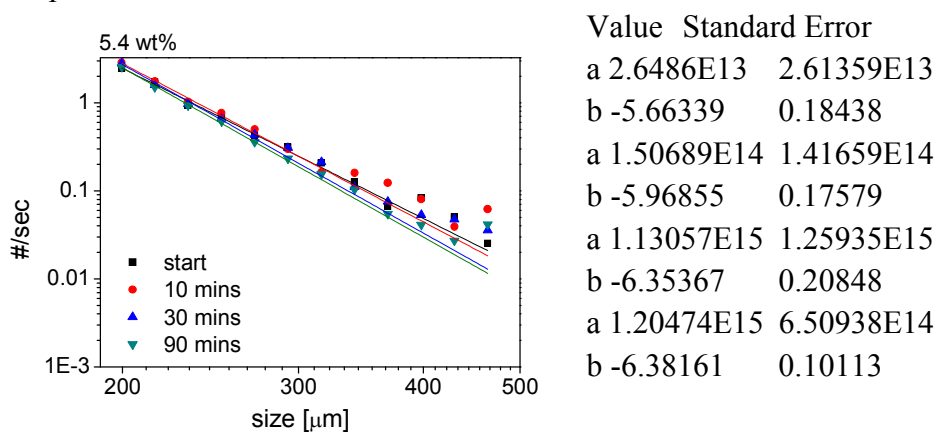


Figure 8.34 Change in average sizes for weighted functions of stirring of 5.4 wt% of tyrosine at 700rpm.

	C1/0	C2/1	C3/2	C 4/3	C 5/4	C 6/5
start	26	43	65	93	139	216
10 mins	25	44	66	98	155	263
30 mins	25	44	66	94	140	222
90 mins	26	43	64	92	133	206

**Table 8.7** Percentage changes in average sizes of stirring of 5.4 wt% of tyrosine at 700rpm.



**Figure 8.35** Fitting functions for stirring of 5.4 wt% of tyrosine.

### 9.0 wt% stirr 700

17.5g of tyrosine has been suspended in 175 ml deionised water and stirred for 160 minutes at 700rpm.

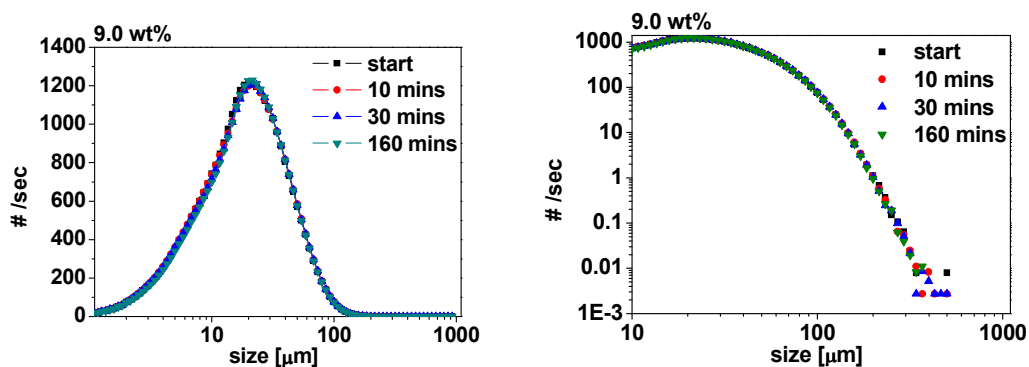


**Figure 8.36** Stirring of 9.0 wt% tyrosine at 700rpm plotted on linear and logarithmic scale.

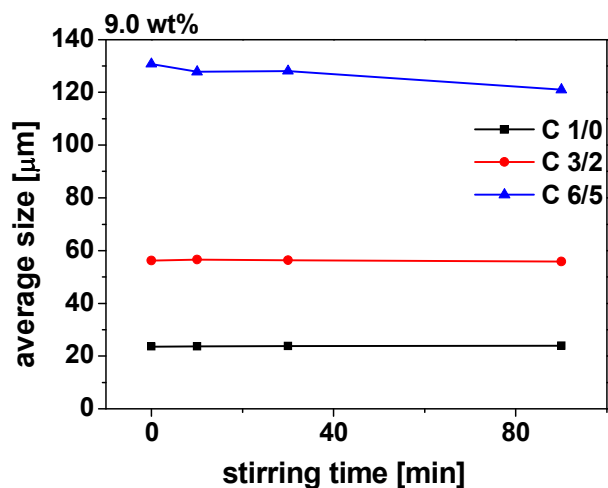
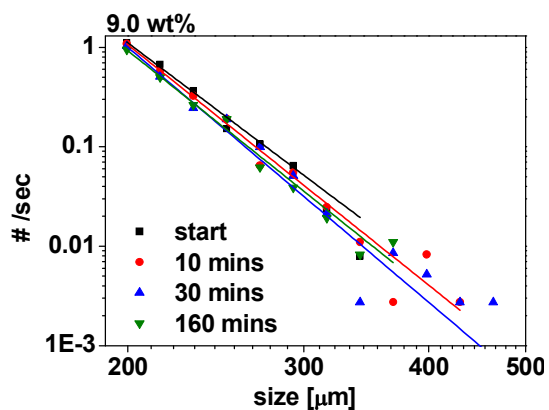


**Figure 8.37** Change in average sizes for weighted functions of stirring of 9.0 wt% of tyrosine at 700rpm.

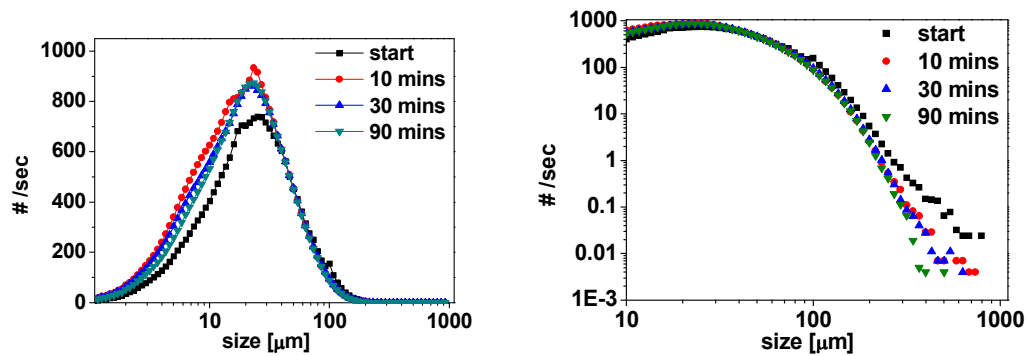
	C1/0	C2/1	C3/2	C 4/3	C 5/4	C 6/5
start	24	39	56	76	100	131
10 mins	24	39	57	76	99	128
30 mins	24	39	56	76	99	128
90 mins	24	39	56	75	96	121

**Table 8.8** Percentage changes in average of stirring of 9.0 wt% of tyrosine at 700rpm.



	Value	Standard Error
a	2.79687E17	4.73704E17
b	-7.56234	0.31769
a	3.27787E18	3.00625E18
b	-8.0349	0.17214
a	4.00707E19	6.93991E19
b	-8.51896	0.32526
a	2.78659E18	4.14208E18
b	-8.03042	0.27899

**Figure 8.38** Fitting functions for stirring of 9.0 wt% of tyrosine.

*Effect of pumping.***2.7 wt% n 200 (MP200)**

**Figure 8.39** Pumping of 2.7 wt% of tyrosine at 200rpm plotted on linear and logarithmic scale.

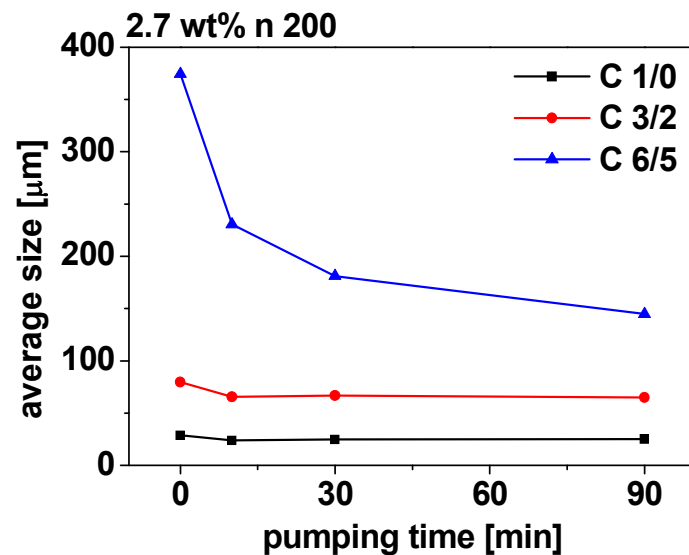


**Figure 8.40** Change in sizes for weighted functions for pumping of 2.7wt% of tyrosine at 200rpm.

	C 1/0	C 2/1	C 3/2	C 4/3	C 5/4	C 6/5
start	29	51	80	125	217	374
10 mins	24	43	66	95	140	231
40 mins	25	44	67	94	129	181
90 mins	25	43	65	90	116	145

**Table 8.9** Changes in average sizes for pumping of 2.7 wt% of tyrosine at 200rpm.

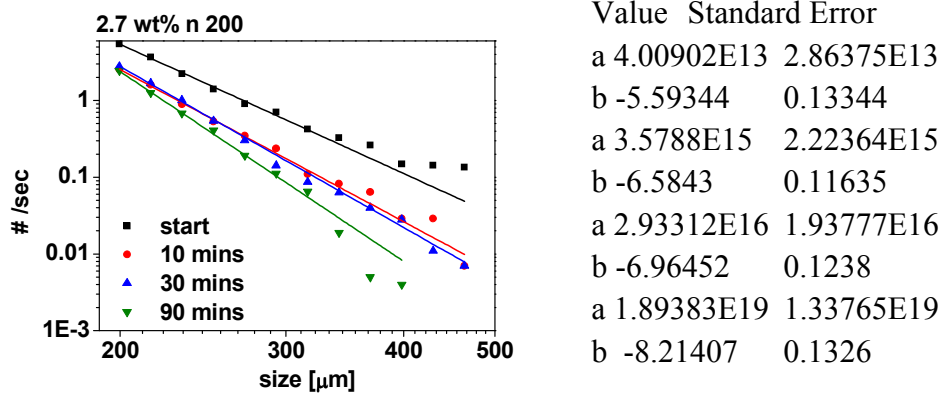


Figure 8.41 Fitting functions for pumping of 2.7wt% of tyrosine at 200rpm.

### 2.7 wt% n 400 (MP400)

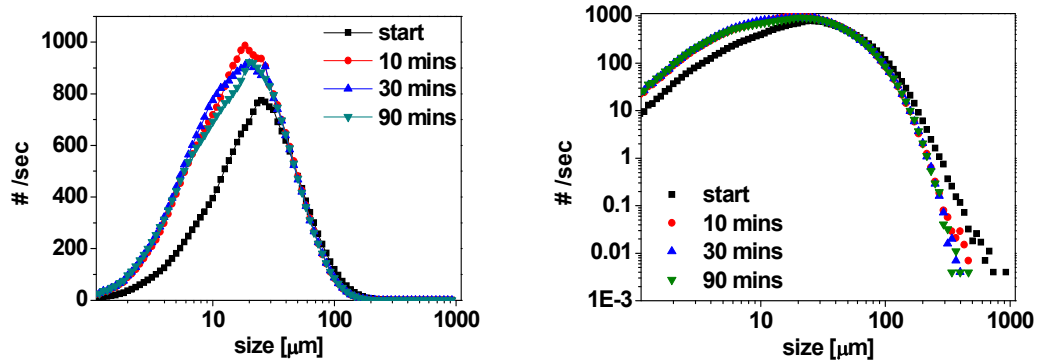


Figure 8.42 Pumping of 2.7wt% of tyrosine at 400rpm plotted on linear and logarithmic scale.

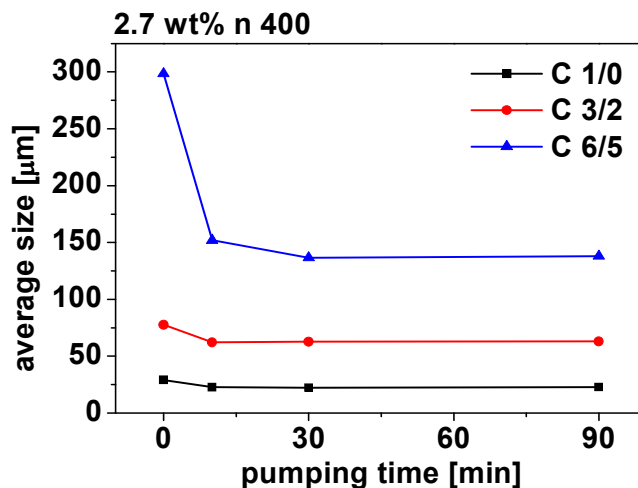
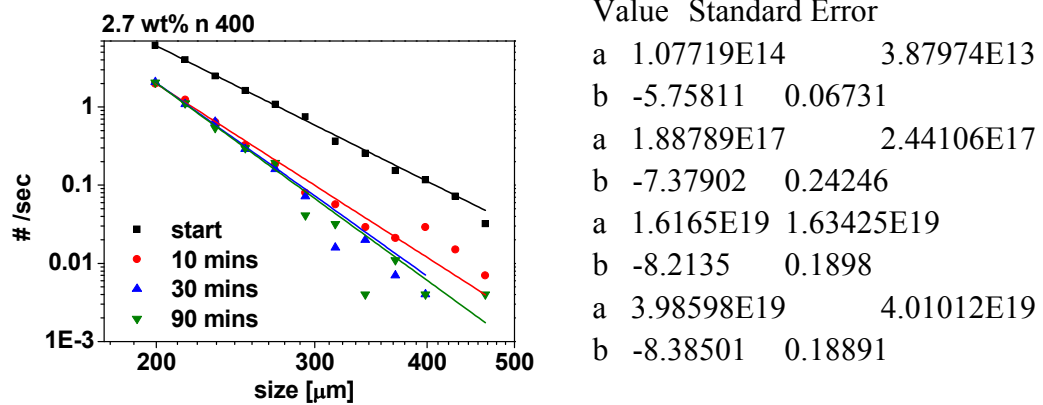


Figure 8.43 Change in average for weighted functions for pumping of 2.7 wt% of tyrosine.

	C 1/0	C 2/1	C 3/2	C 4/3	C 5/4	C 6/5
start	29	50	78	115	178	299
10 mins	23	41	62	87	115	152
40 mins	22	41	63	86	111	137
90 mins	23	41	63	86	111	138

**Table 8.10** Changes in average sizes for pumping of 2.7wt% of tyrosine at 400rpm.



**Figure 8.44** Fitting functions for pumping of 2.7wt% of tyrosine at 400rpm.

#### 5.4 wt% n 200 (MP 200)

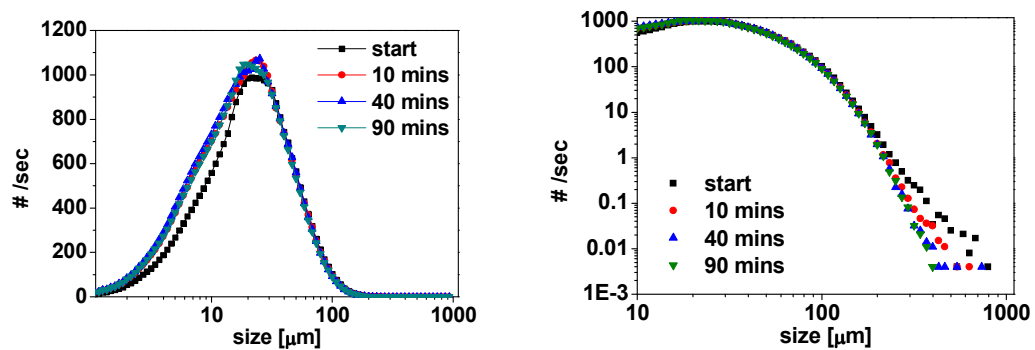


**Figure 8.45** Pumping of 5.4wt% of tyrosine at 400rpm plotted on linear and logarithmic scale.

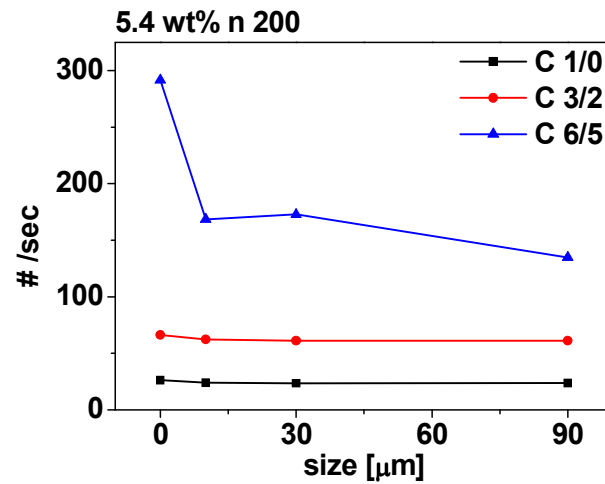


**Figure 8.46** Change in average sizes for functions of pumping of 5.4 wt% of tyrosine.

	C 1/0	C 2/1	C 3/2	C 4/3	C 5/4	C 6/5
Start	26	44	66	99	162	292
10 mins	24	42	62	87	118	169
30 mins	24	41	61	84	115	173
90 mins	24	41	61	84	108	135

**Table 8.11** Changes in average sizes of pumping of 5.4 wt% of tyrosine at 200rpm.

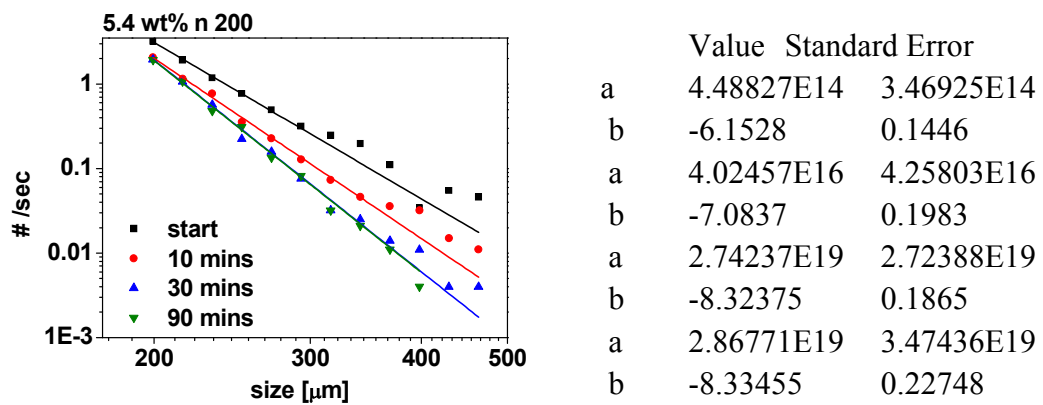


**Figure 8.47** Fitting functions for pumping of 5.4 wt% of tyrosine at 200rpm.

## 5.4 wt% n 400 (MP400)

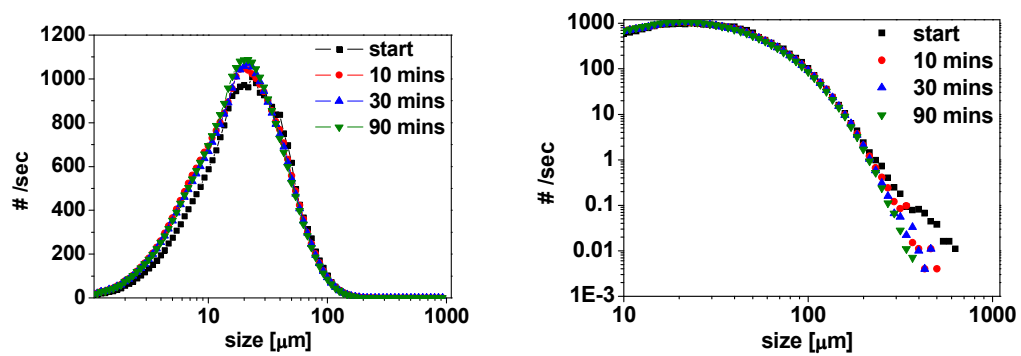


**Figure 8.48** Pumping of 5.4 wt% of tyrosine at 400rpm plotted on linear and logarithmic scale.

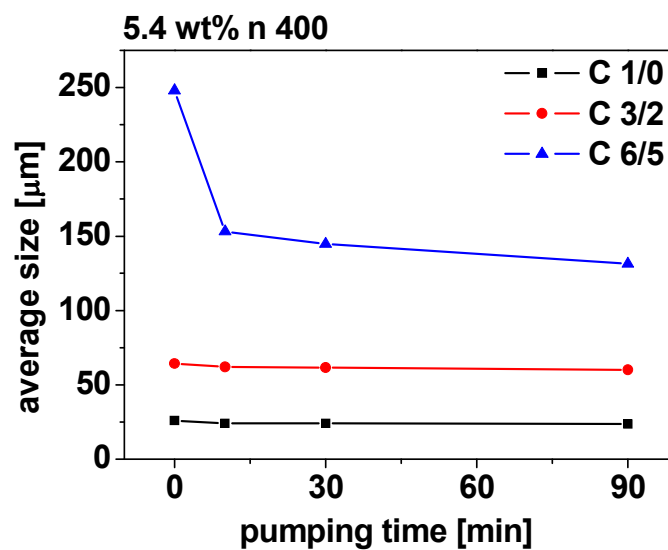


**Figure 8.49** Change in average sizes for functions of pumping of 5.4 wt% of tyrosine at 400rpm.

	C 1/0	C 2/1	C 3/2	C 4/3	C 5/4	C 6/5
Start	26	43	64	94	148	248
10 mins	24	42	62	86	115	153
30 mins	24	41	62	85	111	145
90 mins	24	40	60	82	106	131

**Table 8.12** Changes in average sizes of pumping of 5.4 wt% of tyrosine at 400rpm.

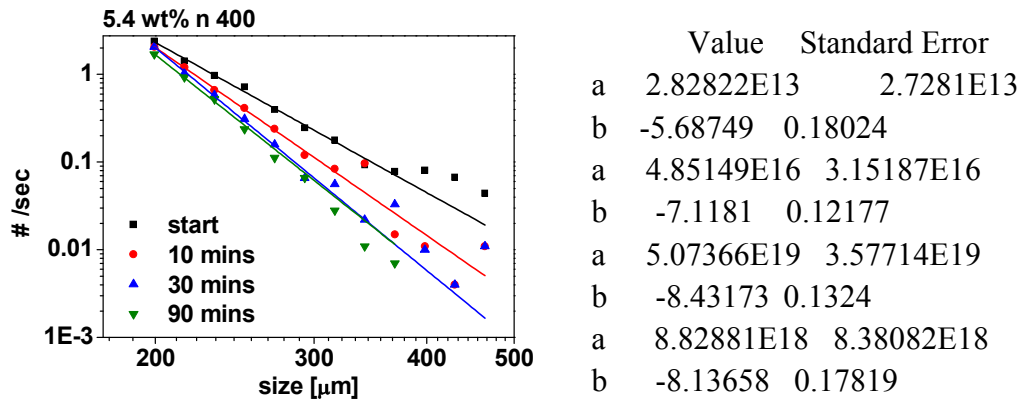


**Figure 8.50** Fit for change in average sizes for of pumping of 5.4 wt% of tyrosine at 400rpm.

### 9.0 wt% n 200 (MP 200)

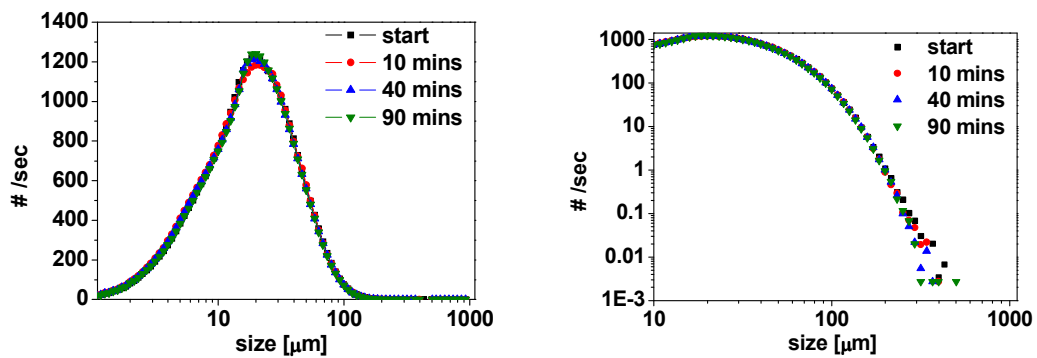


**Figure 8.51** Pumping of 9.0 wt% of tyrosine at 200rpm plotted on liner and logarithmic scale.

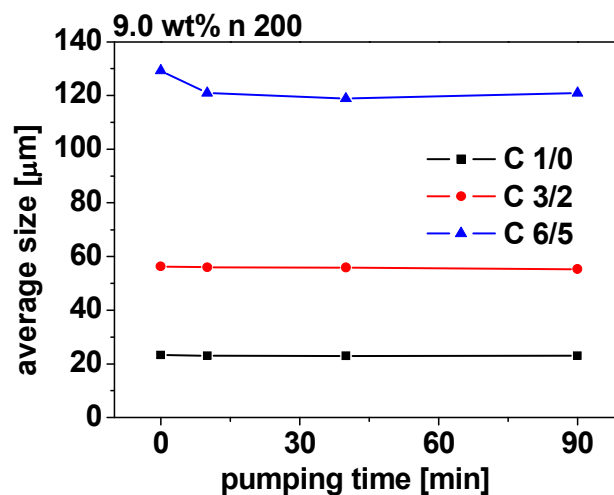


**Figure 8.52** Change in average sizes for functions of pumping of 9.0 wt% of tyrosine at 200rpm.

	C 1/0	C 2/1	C 3/2	C 4/3	C 5/4	C 6/5
start	23	39	56	76	100	129
10 mins	23	38	56	75	97	121
40 mins	23	38	56	75	96	119
90 mins	23	38	55	75	96	121

**Table 8.13** Changes in average sizes of pumping of 9.0 wt% of tyrosine at 200rpm.

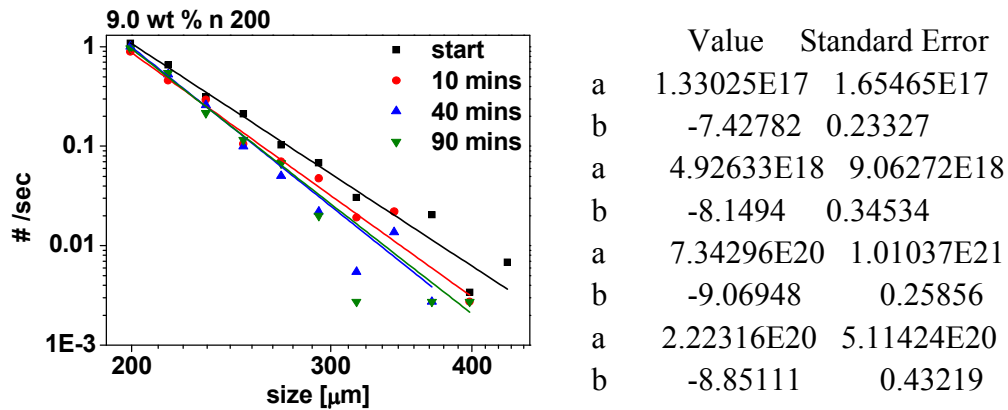


**Figure 8.53** Fitting functions for pumping of 9.0 wt% of tyrosine at 200rpm.

#### 9.0 wt% n 400 (MP 400)

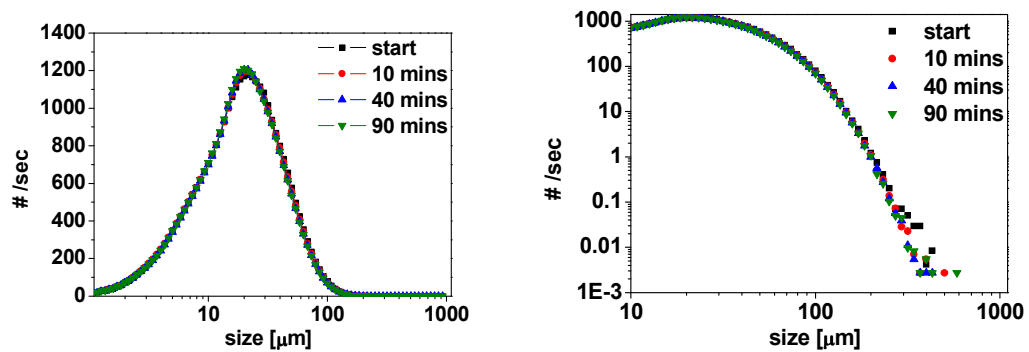


**Figure 8.54** Pumping of 9.0 wt% of tyrosine at 40rpm plotted on linear and logarithmic scale.

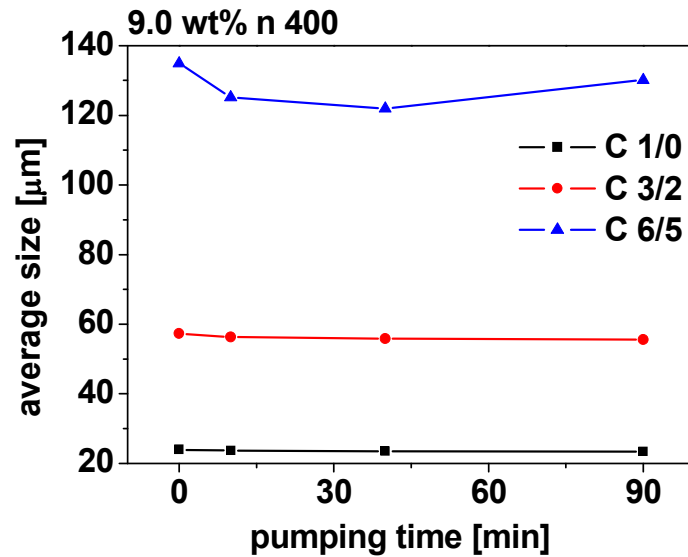


**Figure 8.55** Change in average sizes for functions of pumping of 9.0 wt% of tyrosine at 400rpm.

	C 1/0	C 2/1	C 3/2	C 4/3	C 5/4	C 6/5
start	24	39	57	78	103	135
10 mins	24	39	56	76	98	125
40 mins	24	38	56	75	97	122
90 mins	23	38	56	75	98	130

**Table 8.14** Changes in average sizes of pumping of 9.0 wt% of tyrosine at 400rpm.

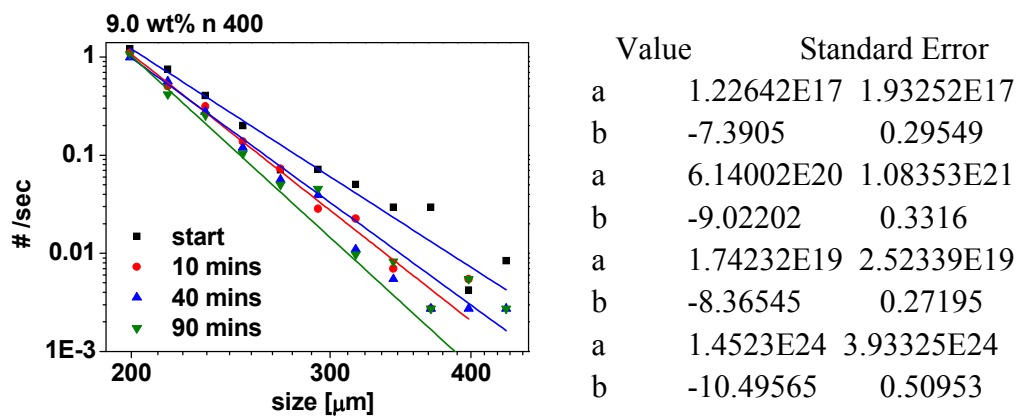


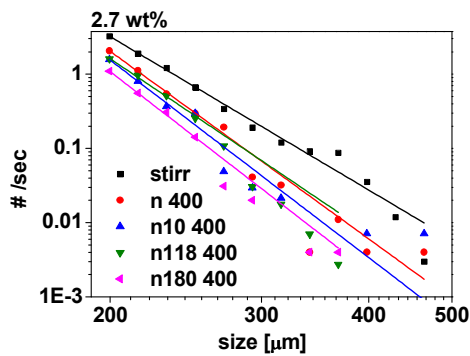
**Figure 8.56** Fitting functions for pumping of 9.0 wt% of tyrosine at 400rpm.

### Effect of pumping with nozzles

Comparison of end values for stirring and pumping at 400rpm tests of suspensions of 2.7 wt% of tyrosine.

	stirr 700	n 400	n10 400	n118 400	n180 400
C 1/0	27	23	24	24	23
C 2/1	45	41	40	41	39
C 3/2	68	63	60	61	58
C 4/3	96	86	83	85	79
C 5/4	131	111	108	110	102
C 6/5	176	138	136	134	125

**Table 8.15** Average sizes for 2.7 wt% tests at 400rpm.



Value Standard Error

a	1.90658E16	1.37018E16
b	-6.85613	0.13464
a	3.98598E19	4.01012E19
b	-8.38501	0.18891
a	3.14799E20	7.69134E20
b	-8.82656	0.45901
a	1.29074E18	2.39343E18
b	-7.78079	0.34793
a	3.87147E20	6.50865E20
b	-8.9329	0.315888

**Figure 8.57** Fitting functions for 2.7wt% for different nozzles at 400rpm

Comparison of end values for stirring and pumping at 200rpm tests of suspensions of 2.7 wt% of tyrosine.

	stirr 700	n 200	n10 200	n118 200
C 1/0	27	25	24	24
C 2/1	45	43	41	42
C 3/2	68	65	61	63
C 4/3	96	90	85	87
C 5/4	131	116	111	113
C 6/5	176	145	138	139

**Table 8.16** Average sizes for 2.7 wt% tests at 200rpm.

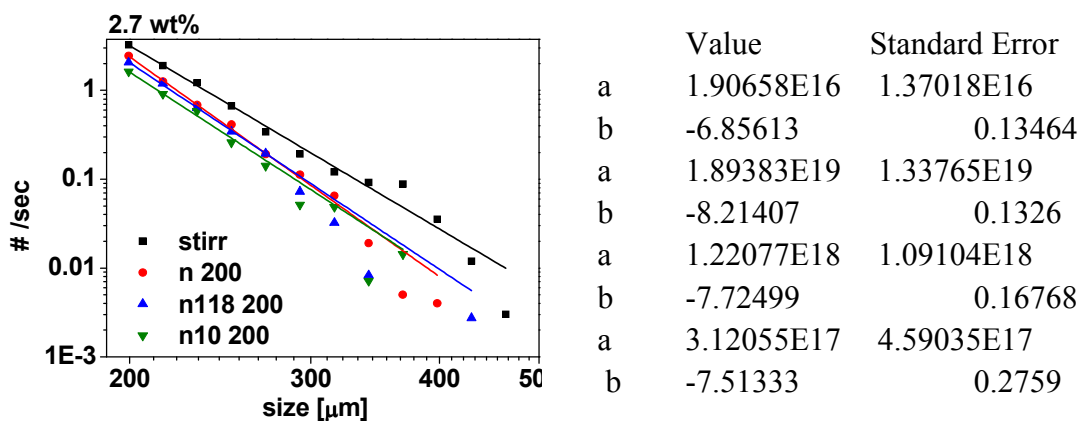


**Figure 8.58** Fitting for comparison of end values for 2.7 wt% of tyrosine at 200rpm.

Comparison of end values for stirring and pumping at 400rpm tests of suspensions of 5.4 wt% of tyrosine.

	stirr	n 400	n10 400	n118 400
C 1/0	26	24	23	23
C 2/1	43	40	39	38
C 3/2	64	60	58	56
C 4/3	92	82	79	77
C 5/4	133	106	102	98
C 6/5	206	131	125	120

**Table 8.17** Average sizes for 5.4 wt% tests at 400rpm.

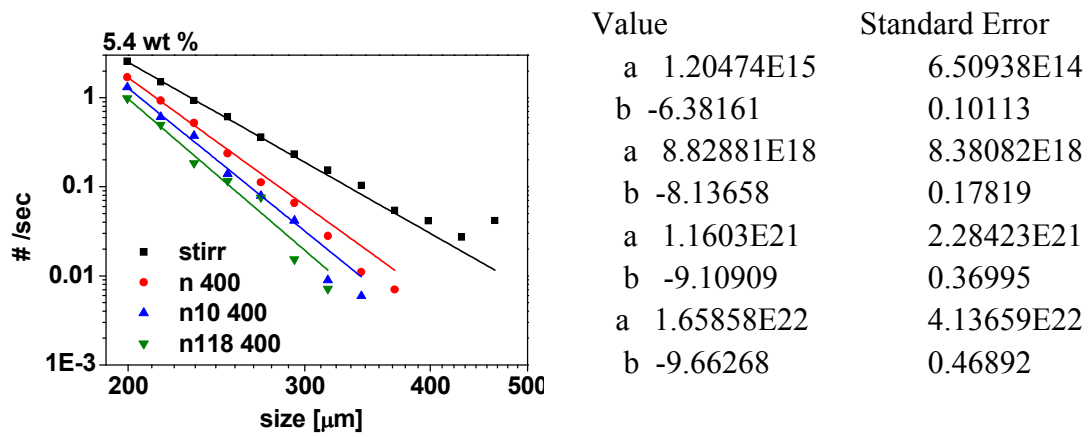


**Figure 8.59** Fitting for comparison of end values for 5.4 wt% at 400rpm.

Comparison of end values for stirring and pumping at 200rpm tests of suspensions of 5.4 wt% of tyrosine.

	stirr	n 200	n10 200	n118 200
C 1/0	26	24	23	24
C 2/1	43	41	39	40
C 3/2	64	61	58	59
C 4/3	92	84	79	82
C 5/4	133	108	102	108
C 6/5	206	135	127	143

**Table 8.18** Average sizes for 5.4wt% tests at 200rpm.

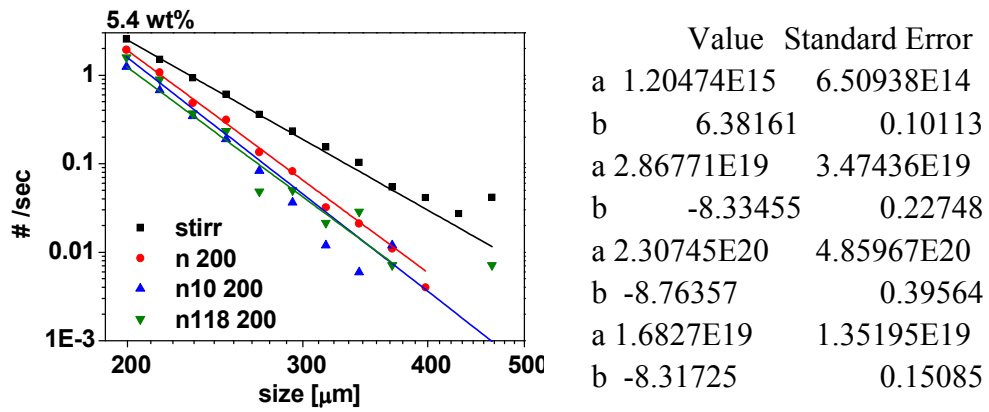


**Figure 8.60** Fitting for comparison of end values for 5.4 wt% at 200rpm.

Comparison of end values for stirring and pumping at 400rpm tests of suspensions of 9.0 wt% of tyrosine.

	stirr	n 400	n10 400	n118 400
C 1/0	24	23	22	22
C 2/1	39	38	38	37
C 3/2	56	56	55	55
C 4/3	75	75	75	74
C 5/4	96	98	95	94
C6/5	121	130	118	115

**Table 8.19** Average sizes for 9.0wt% tests at 400rpm.

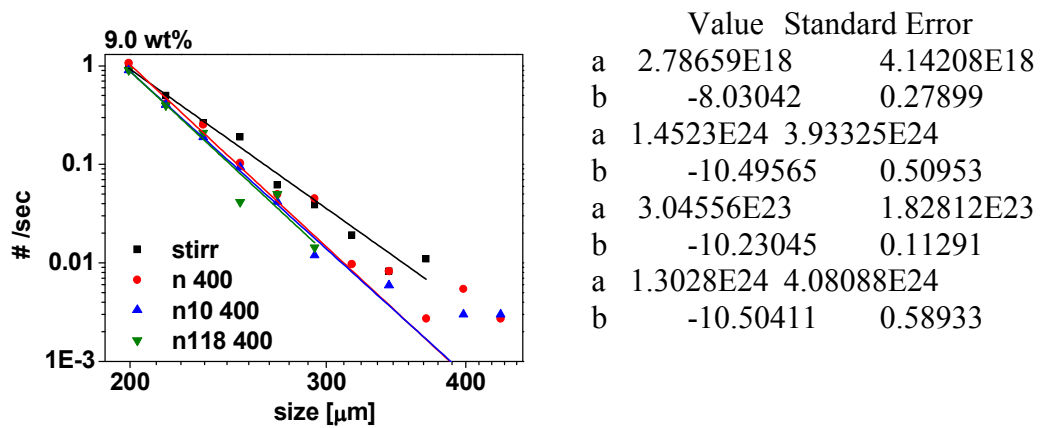


**Figure 8.61** Fitting for comparison of end values for 9.0 wt% at 400rpm.

Comparison of end values for stirring and pumping at 200rpm tests of suspensions of 9.0 wt% of tyrosine.

	stirr	n 200	n10 200	n118 200
C 1/0	24	23	23	23
C 2/1	39	38	39	39
C 3/2	56	55	57	57
C 4/3	75	75	78	77
C 5/4	96	96	100	99
C 6/5	121	121	125	123

**Table 8.20** Average sizes for 9.0wt% tests at 200rpm.

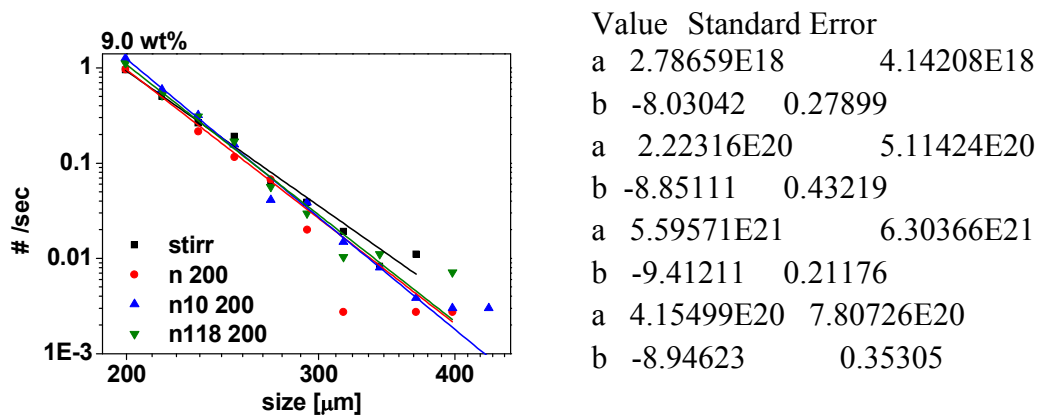


**Figure 8.62** Fitting for comparison of end values for 9.0 wt% at 200rpm.

## 8.8 Viscosity of tyrosine in water slurries

The breakage experiments of tyrosine have lead to interesting conclusions that more concentrated slurries are less prone to breakage. In order to investigate this phenomenon we want to know more about the properties of slurries therefore viscosity measurements were carried. ARI000-N Rheometer (Rheolyst TA instruments) was used to investigate the viscosity. In all tests flat plate with 40.0mm diameter was used. 25°C.

First viscosity results were obtained with conditions: 250 $\mu$ m gap, shear rate range: 1-1000 and then to compare from 10 to 1001/s.

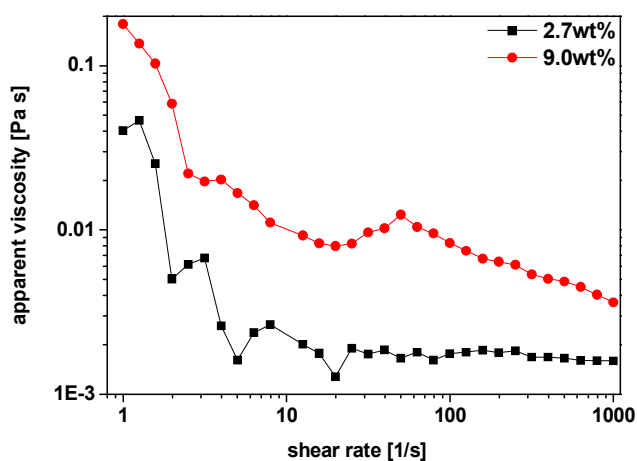


**Figure 8.63** Viscosity of tyrosine for 250 $\mu$ m gap in the 1-1000 [1/s] shear rate range.

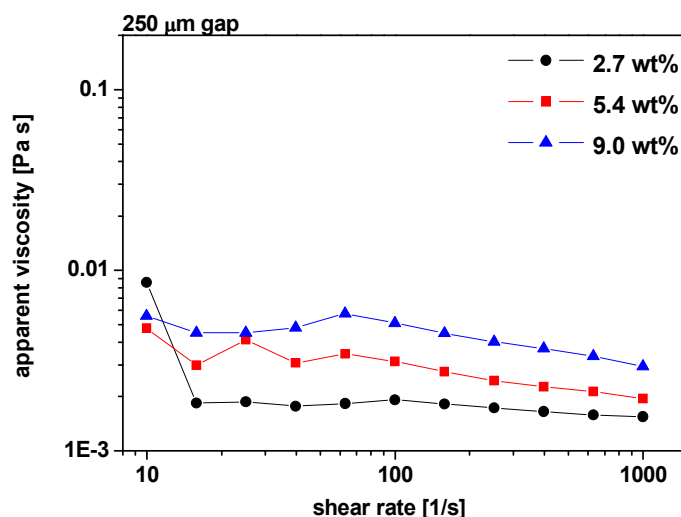


**Figure 8.64** Viscosity of tyrosine for 250 $\mu$ m gap in the 10-100 [1/s] shear rate range.

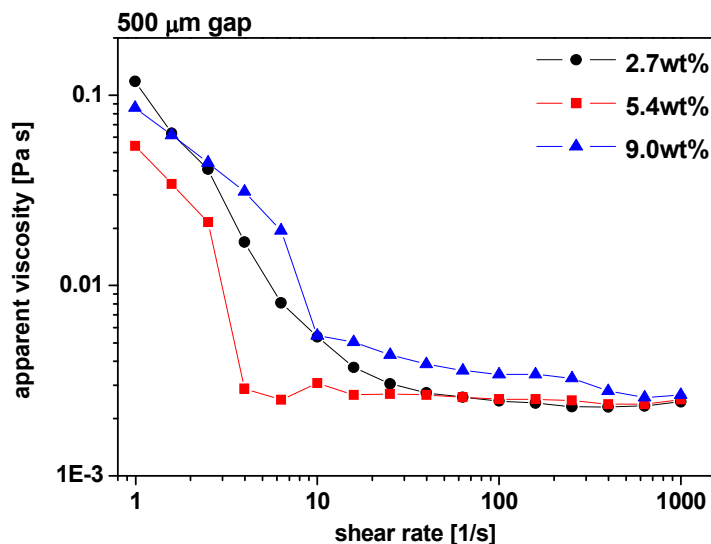


**Figure 8.65** Viscosity of tyrosine for 500 $\mu\text{m}$  gap in the 1-1000 [1/s] shear rate range.

Results show that measured apparent viscosity of tyrosine/water suspensions in the lower shear rates values changes substantially. In higher values of shear rates significant change of viscosity with the concentration is observed. This behaviour is called shear thinning. From the value of shear more than  $10\text{s}^{-1}$  the apparent viscosity is constant. Comparing results of measurement for 250 $\mu\text{m}$  gap started at  $1\text{ s}^{-1}$  and  $10\text{s}^{-1}$  it is thought that the sedimentation effect is not significant and not influencing obtained results. Results show different values obtained while using different gap values. This feature is the most remarkable at lower shear stresses  $1 - 10\text{s}^{-1}$ . This complicated relationship between shear stress and shear rate says that tyrosine – water suspensions are Non-Newtonian fluids.